Xiangwei Zhao
Meng Lu *Editors*

Nanophotonics in Biomedical Engineering

Springer

Nanophotonics in Biomedical Engineering

Xiangwei Zhao • Meng Lu
Editors

Nanophotonics in Biomedical Engineering

Springer

Editors
Xiangwei Zhao
State Key Laboratory of Bioelectronics
Southeast University
Nanjing, Jiangsu, China

Meng Lu
Electrical and Computer Engineering
Iowa State University
Ames, Iowa, USA

ISBN 978-981-15-6136-8 ISBN 978-981-15-6137-5 (eBook)
https://doi.org/10.1007/978-981-15-6137-5

This Springer imprint is published by the registered company Springer Nature Singapore Pte Ltd.
The registered company address is: 152 Beach Road, #21-01/04 Gateway East, Singapore 189721, Singapore

Contents

Chapter 1
Photonic Crystals for Biomolecule Sensing Applications

Le Wei, Shirin Pavin, Xiangwei Zhao, and Meng Lu

Abstract Photonic crystal (PhC) sensors offer important advantages in molecular diagnostic applications, such as detection of disease-related proteins, genes, and pathogenic viruses, and bacteria. This chapter briefly explains the operation principles of three-dimensional (3D) and two-dimensional (2D) photonic crystals, presents how the PhC structures can be fabricated inexpensively, and demonstrate several key applications as for the detection of biomolecules. These applications are based on four main sensing modalities: reflectometry, fluorescence emission, surface-enhanced Raman scattering, and photoacoustic detection. The chapter discusses the implementations of PhC sensors to facilitate the detection of biomolecules via these venues. For each detection modality, we will elaborate the advantages provided by the PhC sensors in the context of specific applications and sensing performances, such as sensitivity and limit of detection. The PhC-based biosensors not only offer new ways to detect biomolecule with low cost and high throughput but also enable researchers and clinicians to improve exiting lab-based assays to achieve better assay sensitivities.

Keywords Photonic crystals · Optical sensors · Surface-enhanced Raman scattering · Fluorescence · Nanofabrication

L. Wei
Department of Electrical and Computer Engineering, Iowa State University, Ames, IA, USA

S. Pavin · M. Lu (✉)
Department of Electrical and Computer Engineering, Iowa State University, Ames, IA, USA

Department of Mechanical Engineering, Iowa State University, Ames, IA, USA
e-mail: menglu@iastate.edu

X. Zhao (✉)
State Key Laboratory of Bioelectronics, School of Biological Science and Medical Engineering, Southeast University, Nanjing, China

National Demonstration Center for Experimental Biomedical Engineering Education, Southeast University, Nanjing, China
e-mail: xwzhao@seu.edu.cn

X. Zhao, M. Lu (eds.), *Nanophotonics in Biomedical Engineering*,
https://doi.org/10.1007/978-981-15-6137-5_1

1.1 Introduction

Recent research has demonstrated that photonic crystals (PhCs), which are capable of manipulating light and molecule interactions at the nanometer scale, can be harnessed as a new type of analytical chemistry tool for the detection of a variety of analytes, including volatile organic compounds, DNAs, proteins, and even cells. A vast array of PhC structures have been developed to fulfill the chemical and biomolecule sensing [1–4]. Among them, there are two major categories of PhC structures: the three-dimensional (3D) PhCs with the periodical modulation of dielectric material's refractive index in 3D space and the PhC slabs, whose lattice structure is confined in a two-dimensional (2D) plane. The 3D PhC and 2D PhC slabs can be engineered to exhibit unique optical phenomena, such as photonic bandgap, high Q-factor cavity, and guided-mode resonance. In conjunction with a specific analytical assay, the PhC structures can be exploited for the quantitative analysis of an analyte in complex samples, such as blood, urine, saliva, and many more. Fundamentally, the PhC can sense target molecules in one of the three different ways: (1) Measuring the change of refractive index of the PhC or its surrounding medium; (2) Detecting the change of PhC geometry owing to the absorption of chemicals; and (3) Enhancing the scattering or emission of analyte immobilized on PhCs. Based on these mechanisms, a number of PhC-based detection assays have been introduced for the analysis of the direct absorptions of the gas molecule, virus, and cells or the bindings between ligand and analyte. Such PhC-based assays have great potential in many molecular diagnostic applications, such as disease biomarker detections, nucleic acid tests, identification of pathogens, and many others.

This chapter first explains the underlining physics of PhCs and shows how the PhCs are designed and fabricated. Then, the sensing mechanisms using PhCs for the label-free, fluorescence, Raman-based, and photoacoustic detections of biomolecules are described. Finally, the chapter presents several examples of PhC-based assays with a specific focus on the multiplexed detection of disease biomarkers. This chapter aims to serve as a review for demonstrating the design of PhC devices, methods of fabrication, and assay capabilities. For full details, the reader is directed to full articles published on each topic.

1.2 Fundamental Principle of PhC for Sensing

1.2.1 2D and 3D PhC Structures

The idea of PhC was first demonstrated in 1987 by Yablonovitch, who showed that the periodic structures with alternating refractive indices can be analogous to semiconductor crystals with the forbidden gap [5]. Light propagation with its wavelength in the photonic bandgap is prohibited by the periodic structure. Later,

the concept of PhCs was successfully realized in 3D to achieve PhCs with full bandgaps [6–9]. The bandgap of PhCs can be considered as a result of destructive interference of light reflection by the photonic lattice of refractive index (n). The 3D PhCs can strongly reflect light whose wavelength (λ) falls in the range of the forbidden gap. The lattice constant, also known as period (Λ), of a PhC is approximately half of the wavelength of the light to be reflected. In general, the material refractive indexes and the geometry parameters, including Λ and duty cycle, of PhCs determine the spectral position of the photonic bandgap. For the PhC with a photonic bandgap in the visible or near-infrared range, its period is on a scale of several hundred nanometers. The 3D PhCs have been utilized to reflect, guide, and localize light on a subwavelength scale (Fig. 1.1a, b). For sensing applications, the 3D PhC-based sensor can be applied to measure a wide range of signals, such as pressure, temperature, humidity, pH value, ions, gas molecules, and biomolecules [10]. For example, a selective absorption of target disease biomarkers via the ligand–analyte binding can cause the change of refractive index around the PhC, and thus shift the color displayed by the 3D PhC structure. In addition, the 3D PhC structure can also change its color when the absorption of a target analyte, such as organic compounds results in the change of its period. The colorimetric detection upon 3D PhC sensors have enabled the development of compact and low-cost sensor systems for point-of-care diagnostics [2].

The PhC slab integrates the periodic modulation of material refractive index into a slab waveguide, as shown in Fig. 1.1c. The PhC slab uses the waveguide to confine light in the direction perpendicular to the slab's surface and adopt the PhC structure to control light propagation along the waveguide. Two main types of 2D PhC slabs, the in-plane confined PhC slab and out-of-plane coupled PhC surface, have been extensively studied [11–15]. The in-plane PhCs can be designed to form optical

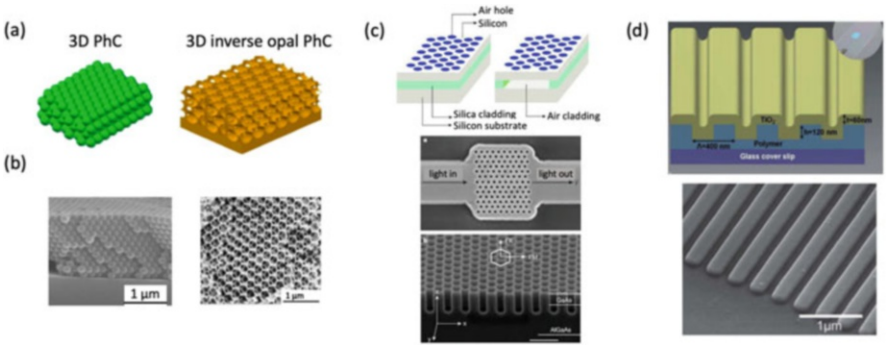

Fig. 1.1 3D PhCs and PhC slabs. (**a**, **b**) show the schematic and SEM images of the 3D PhC and inverse opal PhC structures, respectively (reproduced with permission from [10]. Copyright 2013, MDPI Switzerland). (**c**) Schematic (top panel) and SEM image (bottom panel) of in-plane confined 2D PhC slabs (reproduced with permission from [13] Copyright 2000, Springer Nature and from [14] Copyright 2018, Intech Open). (**d**) Out-of-plane coupled PhC slab structure (top panel) and SEM image (bottom panel). (Reproduced with permission from [34]. Copyright 2013, The Royal Society for Chemistry)

waveguides, interferometers, and high Q-factor (high-Q) resonators. When light is coupled into an in-plane PhC, the light is confined and cannot escape from the surface of the slab. The PhC slab-based interferometers and high Q cavities can be implemented to develop refractive index-based sensors. For example, the ligand–analyte binding occurring around a PhC cavity can cause a shift of the resonance wavelength (λ_r) [4]. The capability of measuring the change of λ_r allows the PhC cavity to be used as a refractometric sensor. It is also possible to achieve a high-Q optical resonance with a significantly enhanced nearfield on the surface of a 2D PhC slab. The features of enhanced nearfield can be exploited to improve the signal-to-noise ratio (SNR) for fluorescence or Raman scattering-based assays.

Unlike the highly confined modes of in-plane confined PhCs, the out-of-plane coupled PhCs mode can be coupled from its surface. Such 2D PhC slabs are also known as leaky mode resonance waveguides, high-contrast gratings, or guided-mode resonance (GMR) filters. The underlying principle of leaky mode resonance was first reported by Magnusson's group in the early 1990s [15]. Most out-of-plane coupled PhCs consists of a grating coupler and a dielectric waveguide, which can support resonance modes with the signature of narrowband reflections or transmissions. The grating coupler can also be integrated into the waveguide to form the leaky mode waveguide. When light is coupled into a resonance mode via the grating coupler, the constructive interference between the backward leaked and reflected light yields a nearly 100% reflection (as shown in Fig. 1.1d). The spectral characteristics of reflection, such as its resonance wavelength, peak reflection efficiency, and linewidth, are determined by the materials and geometry of the 2D PhC slab [16]. The resonance mode supported by the out-of-plane coupled PhC can be exploited for both refractive index-based biosensor and nearfield-enhanced sensing. The examples of the GMR-based sensor are shown in Sect. 1.3 of this chapter.

1.2.2 Fabrication Processed for PhCs

For the PhCs that operate in the visible wavelength region, the critical feature size could be as small as 100 nm. The subwavelength feature size presents a great challenge for PhC fabrication, in particular, the lithography step. Nanoscale patterns of the 2D PhC slabs have been successfully fabricated using conventional lithography approaches, such as deep UV (DUV) lithography, electron beam lithography (EBL), focused ion beam lithography (FIB), and helium ion beam lithography (HIL) [17]. Following the lithography process, the pattern can be transferred into the substrate layer using dry etching, such as ion milling or reactive ion etching. These methods can provide excellent resolution but also have constrains of low throughput and high cost. Fabrication of 3D PhCs is particularly difficult using these conventional approaches because of the requirement of patterning and alignment between multiple layers. Unconventional approaches, including interference lithography, nanoimprint lithography (NIL), and self-assembly method, have been successfully exploited to fabricate subwavelength gratings for the PhC slabs with high

throughput, high fidelity, uniformity, and low cost [18]. Details of the self-assembly, NIL, and interference lithography processes for the PhC fabrication are reviewed below.

Self-Assembly Method The self-assembly method uses colloidal solutions to form a variety of PhCs through the ordered arrangement of nanobeads. Using self-assembly, large-area and high-quality PhC can be fabricated on a substrate with low cost and high throughput. Many 3D PhC structures have been successfully self-assembled using colloidal solutions of silica, polymer, or hydrogel nanobeads. The simplest self-assembly method is to naturally precipitate the nanobeads using a diluted colloidal solution, followed by a sintering process to improve the PhC's stability (Fig. 1.2a) [19, 20]. Alternatively, in vertical deposition, which is the most widely used method upon evaporation of the solution, the nanobeads are forced to line up on the substrate, as shown in Fig. 1.2b. The Langmuir-Blodgett method is another alternative, where a single-layer film of nanobeads can be formed at the interface between air and liquid surface [21]. The single layers can be built up to form 2D and 3D PhC patterns.

Imprint Lithography For 2D PhC slabs, it is possible to form large-area and single-layer periodic structures using nanoimprint lithography (NIL). The NIL process is a contact patterning method, which is not limited by the diffraction limit and can produce a feature size below 25 nm. Figure 1.2c illustrates the basic steps of a NIL process [22]. In the first step, a stamp (also known as mold or template) is pressed against a thin layer of imprint resist. After the 1D or 2D grating pattern carried by the mold is transferred to the resist layer, the mold is carefully detached. In the second step, the residual resist is removed and the pattern is transferred onto the substrate material using a dry-etching process. Both thermal and UV light-based NIL processes have been exploited to fabricated 2D PhC slabs.

Interference Lithography The principle of laser interference lithography is based on the interference pattern produced by two or more laser beams, which is translated as physical patterns on a layer of photoresist. The setup shown in Fig. 1.2d is called Lloyd's mirror interferometer [23]. The angle between the Lloyd's mirror can be adjusted to change the period of the interference pattern and thus controls the period of the grating pattern. A two-dimensional grating pattern of a PhC slab can be produced by interfering with three laser beams. Moreover, a variety of 3D PhC structures can be formed with interference of at least four laser beams [24].

1.3 Detection of Biomolecules Using PhC Sensors

The PhC structures can be implemented for sensing applications in a few different ways. The most unique one is the label-free detections, which represent the detection of chemicals and biomolecules based on their intrinsic physical properties. Both 3D PhCs and 2D PhC slabs have been successfully demonstrated as label-free

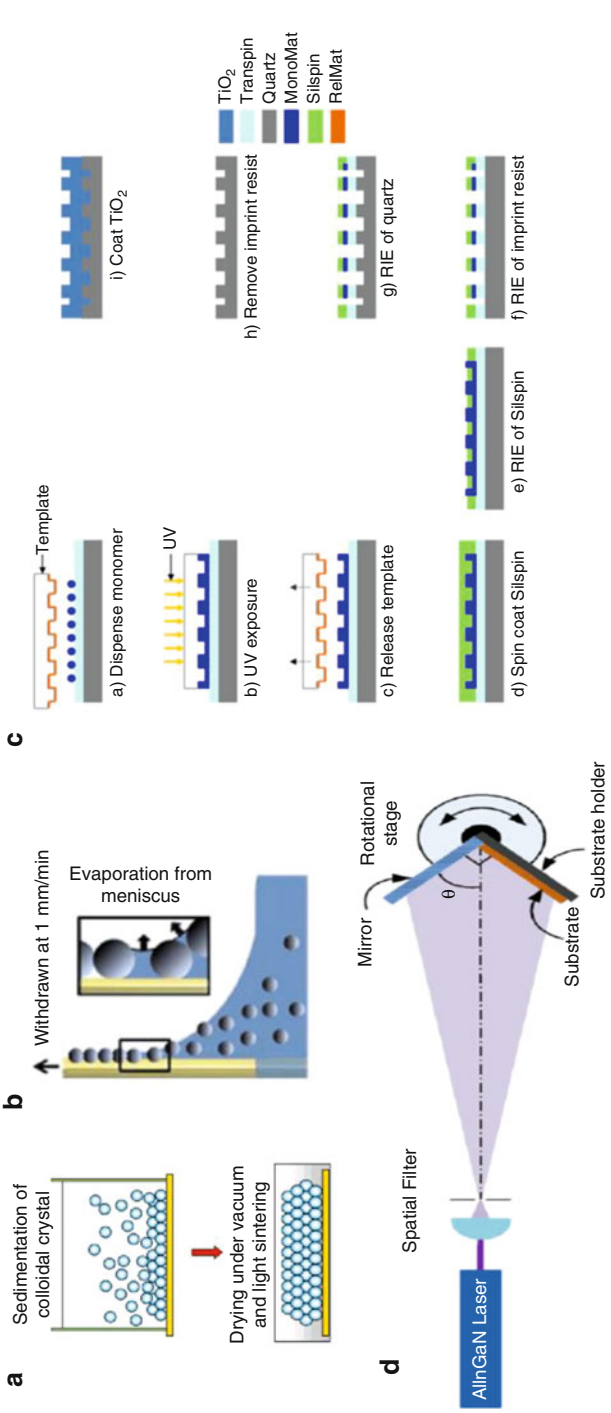

Fig. 1.2 Fabrication of PhC structures. Self-assembly of colloidal 3D PhCs by precipitation (**a**) and vertical dipping deposition (**b**) (**a**: Reproduced with permission from [20]. Copyright 2002, WILEY-VCH, and **b**: Reproduced with permission from [19]. Copyright 2014, IOP Publishing). (**c**) Imprint lithography of 2D PhC slabs (reproduced with permission from [22]. Copyright 2010, Optical Society of America). (**d**) Interference lithography for 3D and 2D PhCs. (Reproduced with permission from [23]. Copyright 2010, IOP Publishing)

biosensors [2]. In addition to the label-free detections, the PhCs can also benefit the label-based assays, such as fluorescence and photoacoustic immunoassays. This section reviews the PhC-based label-free biosensors as well as the fluorescence, Raman, and photoacoustic sensors that use PhC structures for improved sensing performances.

1.3.1 Refractive Index-Based PhC Sensors: Detection of Ligand–Analyte Bindings

By and large, there are two major categories of PhC-based refractometric detections, including the colorimetric and spectroscopic methods. The colorimetric PhC biosensors manifest the sensing results as color changes that can be observed by naked eyes. The spectroscopic PhC biosensors measure the subtle change of reflection or transmission spectrum for quantitative analysis. The examples of colorimetric and quantitative PhC biosensors are discussed below.

1.3.1.1 Semi-Quantitative Analysis: Colorimetric Detection

The colorimetric analysis uses colloidal 3D PhC films that can be fabricated using the self-assembly method discussed in Sect. 1.2. A colloidal PhC sensor (Fig. 1.3a), consisting of closely packed hydrogel nanoparticles, can absorb analyte and change its dimension [25]. As a result, the bandgap of the PhC shifts and thus the reflection color of the PhC film changes. This phenomenon is mainly caused by the swelling or shrinking of elastic PhCs. In case of a swelling event, the lattice constant of PhC increases and changes the PhC reflection peak to a longer wavelength as illustrated in Fig. 1.3b. Based on this feature, the colorimetric 3D PhC sensors have been demonstrated for the detections of volatile organic compounds [26].

By modifying the 3D PhC material with an analyte-specific agent, a large variety of colorimetric sensors have been developed. For example, by adding a glucose-responsive hydrogel, Nakayama et al. showed the colorimetric glucose sensor that provides the desired monitoring of glucose levels by the naked eye (Fig. 1.3c). Zhao et al. demonstrated the hydrogel PhC sensor for DNA as shown in Fig. 1.3d by adding a single-stranded DNA probe into the colloidal PhC [27–29]. The colloidal hydrogel 3D PhC sensor can also be engineered to detect proteins (Fig. 1.3c, d), drugs, and other chemicals. The colorimetric PhC sensors have enabled unprecedented assays to perform with regard to the assay time, cost, and ease of use.

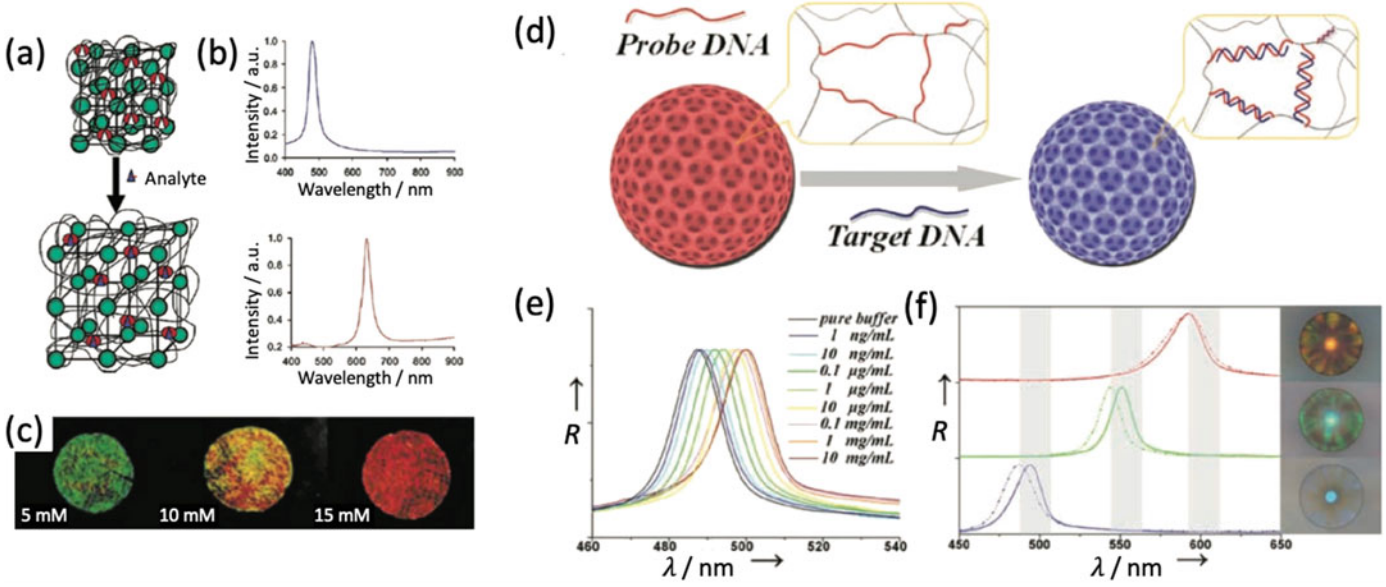

Fig. 1.3 Colorimetric sensing using colloidal 3D PhCs. (**a**) Scheme diagram of the geometric change of 3D PhC lattice constant caused by the absorption of an analyte (reproduced with permission from [45]. Copyright 2004, Oxford University Press). The corresponding change of the reflection spectrum is shown in (**b**) (reproduced with permission from [45]. Copyright 2004, Oxford University Press). (**c**) Colorimetric detection of glucose in tear fluid with different glucose concentrations of 5, 10, and 15 mM (reproduced with permission from [46]. Copyright 2003, WILEY-VCH). (**d**) Schematic diagram of colorimetric detection of DNA using a hydrogel 3D PhC (reproduced with permission from [47]. Copyright 2003, WILEY-VCH). (**e**) Reflection spectra of 3D PhC with different DNA concentrations (reproduced with permission from [27]. Copyright 2009, WILEY-VCH). (**f**) Detection of hemoglobin, horseradish peroxidase, and bovine serum albumin using the 3D PhC beads. (Reproduced with permission from [27]. Copyright 2009, WILEY-VCH)

1.3.1.2 Quantitative Analysis of Optical Resonance

In order to obtain highly quantitative results, the analysis of the reflection spectrum from PhCs are needed. In particular, for the PhC slabs, which supports narrowband and high-Q resonance modes, the spectral analysis can be exploited for the label-free detections of a range of biomaterials from drug compounds to cells. These PhCs slabs were designed to quantify the binding of ligand and analyte via measuring the binding-induced refractive index (RI) change. The sensitivity of these label-free sensors is evaluated by the value of nm/RI unit, which represents the wavelength shift of a PhC resonance as a response to the change of RI. Cunningham et al. reported the label-free detection using PhC slabs with a 1D grating structure as shown in Fig. 1.4a, b [30, 31]. The PhC slab sensors were fabricated inexpensively using the NIL method on a plastic substrate by roll-to-roll manufactures [32]. These plastic-based sensors can be attached to the bottom of 96- or 384-microwell plates for high-throughput screening of analyte (Fig. 1.4c). Figure 1.4d shows the optical setup used for microscopic measurement of reflectance from the label-free PhC sensor [33, 34]. In addition to the low cost and high throughput, label-free PhC senor can also output binding results in real time as shown in Fig. 1.4e. The binding dynamics can be analyzed to determine the binding affinity or dissociation constant of analyte and ligand pairs [35]. Recently, Cunningham's group demonstrated the label-free imaging capability of the PhC sensor for the analysis of cell adhesion and signal nanoparticles as shown in Fig. 1.4f, g [34, 36].

1.3.2 Nearfield-Enhanced Spectroscopy on PhC Surfaces

In addition to the label-free assays, the PhCs can also be exploited by the existing spectroscopic approach to detect chemicals and biomolecules. In particular, the PhC structures can enhance the fluorescence and Raman-based detection to achieve a higher detection sensitivity and lower detection limit. The enhancement can be explained from three main aspects: (1) strengthened local electric field when the excitation light is coupled with a specific resonance mode; (2) directional emission when the scattered or fluorescent light is trimmed by a PhC cavity mode; (3) large surface area provided by the nanostructured PhCs. The section reviews the PhC-enhanced fluorescence emission, Raman scattering, and photoacoustic detection, respectively. Several examples are shown to elaborate on how the PhC structure can boost the performance of the existing protein, DNA, and chemical sensing technologies.

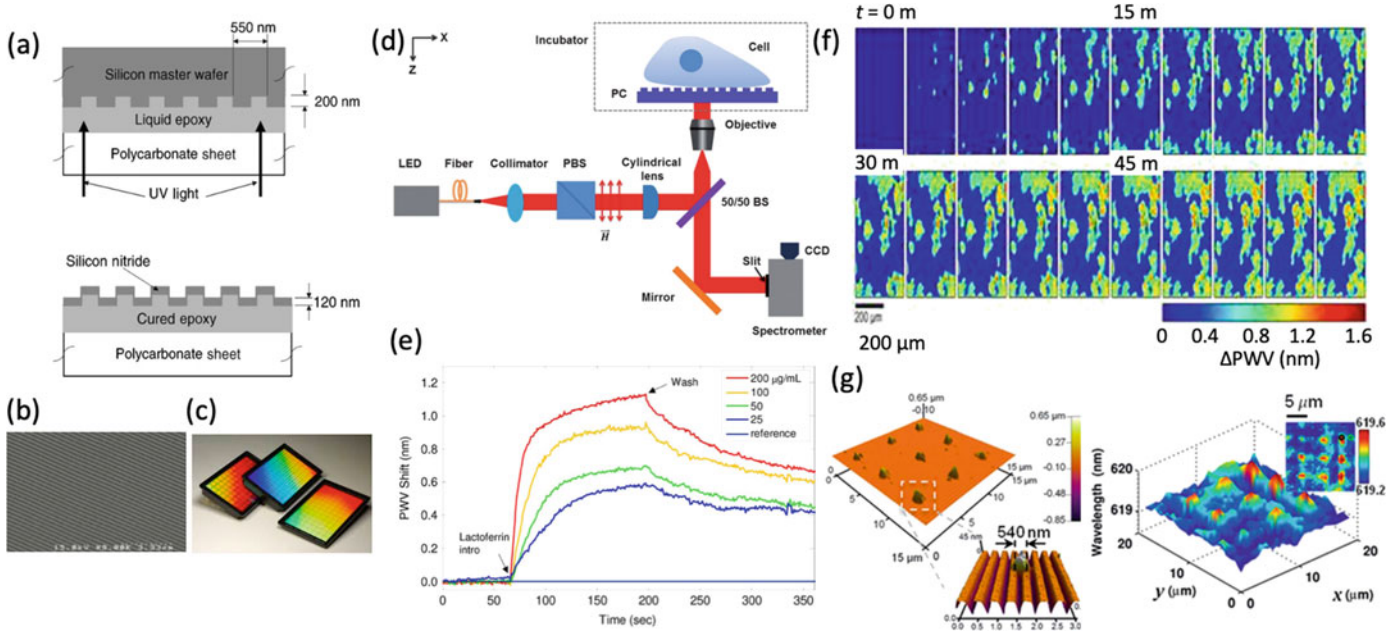

Fig. 1.4 Label-free detection of chemicals, cells, and nanoparticles using the 2D PhC slab. (**a**) Scheme diagram of the PhC sensor fabricated using the NIL process (reproduced with permission from [30]. Copyright 2002, Elsevier). The SEM image in (**b**) shows the 1D grating structure (reproduced with permission from [48]. Copyright 2006, American Institute of Physics). (**c**) Microwell plates with the PhC sensors on the bottom (reproduced with permission from [32]. Copyright 2008, SPIE). (**d**) Microscopic label-free imaging setup for high throughput and high-resolution analysis (reproduced with permission from [34]. Copyright 2013, The Royal Society of Chemistry). (**e**) Kinetic detection of lactoferrin at different concentrations (reproduced with permission from [49]. Copyright 2009, IEEE). (**f**) Label-free images of cellular attachment of dental epithelial stem cells on a PhC sensor (reproduced with permission from [34]. Copyright 2013, The Royal Society of Chemistry). (**g**) Detection of plastic nanodots deposited on a PhC surface. (Reproduced with permission from [36]. Copyright 2014, The Royal Society of Chemistry)

1.3.2.1 PhC-Enhanced Fluorescence Detection

Cunningham's group demonstrated that the PhC slabs with 1D or 2D grating patterns can provide higher signal-to-noise ratios (SNRs) for the detection of fluorescent emitters, and thus can reduce the limits of detection of fluorescence-based assays [37]. In contrast to the aforementioned label-free assays, the fluorescence-based assays are suitable for the detection of low concentration analytes in complex biological samples, owing to the high specificity. The PhC-enhanced fluorescence takes advantage of two phenomena: enhanced excitation and enhanced extraction, which are associated with PhC resonances, as shown in Fig. 1.5a [38]. The *enhanced excitation* represents the coupling of the excitation light to a PhC resonance and resulting in a strengthened electric field, which can be in orders of magnitude higher than the amplitude of excitation radiation. The enhanced field is highly confined near the PhC surface and can cause stronger emission from the fluorophores immobilized on the PhC as illustrated in Fig. 1.5a. Such an enhancement effect is limited to the molecules within approximately 100 nm of the PhC surface. Background signals from substrate or superstrate materials, which are in a distance from the near-field region, are not increased. Therefore, the signal-to-noise ratio of the fluorescence analysis can be improved. The *enhanced extraction* mechanism involves a spectral and directional redistribution of the emission from the fluorophores. When the fluorophores emit from the PhC surface, the fluorescent photons are first coupled into specific optical resonances and are then radiated towards a narrow set of angles. The combination of PhC-enhanced excitation and emission makes the PhC surface a better substrate for fluorescence-based biomolecule detection assay compared to a flat glass substrate.

Figure 1.5b shows the PhC-enhanced fluorescence images of Cy-5-labeled DNA microarray with the signal enhancement factor of approximately 60 times [39]. The signal enhancement factor was calculated as spot intensity subtracted by the background and divided by the net fluorescence intensity measured on a glass substrate. For the detection of biomarkers at low concentrations, it is particularly important to improve the SNR and limit of detection for a given detection assay. Figure 1.4d shows the results of an antibody microarray, which was used to quantify a panel of protein biomarkers that may indicate breast cancer as shown in Fig. 1.5c–e [40]. The enhancement effect provided enhanced signal for all the spots when the PhC mode was utilized for the on-resonance case. The dose-response curve, also known as the standard curve, for TNFα with and without the PhC enhancement are compared in Fig. 1.5e. It can be seen that the PhC surface exhibited a greater sensitivity with a larger slope in the linear region and the tenfold reduced limit of detection. In addition to TNFα, the EGFR and uPAR antigens were detected at concentrations as low as 3.6 ng/mL and 7.1 ng/mL, respectively. Without the PhC enhancement, the fluorescent spots representing the EGFR and uPAR antigens at these concentrations were at the noise level (SNR < 3) and could not be differentiated from the local background noise.

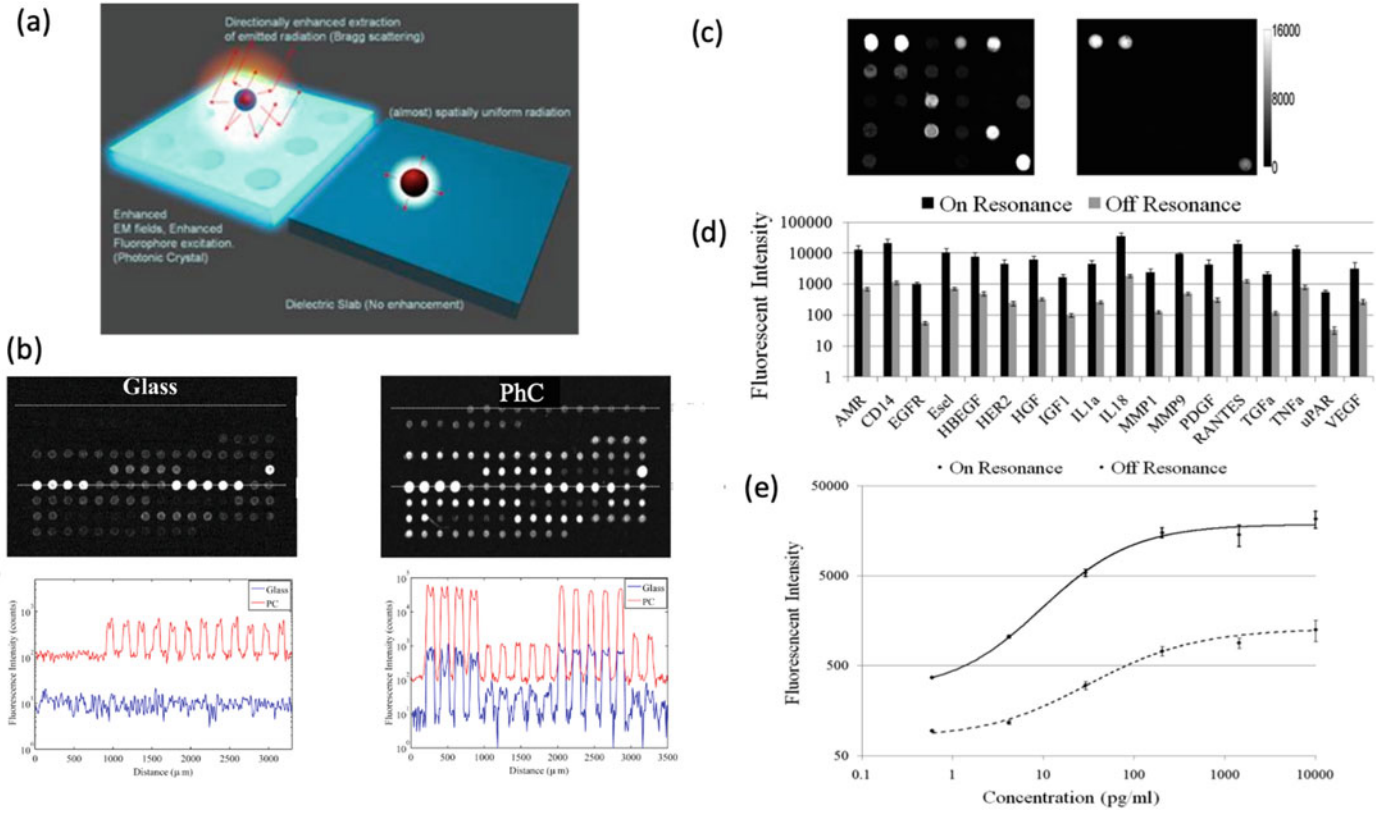

Fig. 1.5 PhC-enhanced fluorescence detection of DNA and protein biomarkers. (**a**) Scheme diagram of PhC-enhanced excitation and extraction phenomena (reproduced with permission from author: Dr. Brian T. Cunningham). (**b**) PhC-enhanced fluorescence emission from a DNA microarray (reproduced with

permission from [39]. Copyright 2010, American Chemical Society). (**c**) Fluorescence images of a protein microarray with (left) and without (right) PhC enhancement, respectively (reproduced with permission from [40]. Copyright 2011, American Chemical Society). (**d**) Enhancement of fluorescence signals for a panel of protein biomarkers (reproduced with permission from [40]. Copyright 2011, American Chemical Society). (**e**) Dose-response curves of TNFα detection on and off the PhC surface. (Reproduced with permission from [40]. Copyright 2011, American Chemical Society)

1.3.2.2 PhC-Enhanced Raman Spectroscopy

As a vibrational spectroscopy method, the Raman analysis detects target analytes via their structural fingerprints, which are known as the Raman shifts. Based on Raman scattering, the surface-enhanced Raman spectroscopy (SERS) can dramatically enhance Raman signal by target analytes adsorbed on surfaces of metal nanostructures. It is believed that the localized surface plasmon resonance (LSPR) modes supported by the metal nanostructures contribute to SERS signals. The strength of the SERS signal depends on the density of plasmonic hot spots, which represent the strong and localized electric fields around the metal nanostructure. However, the density, distribution, and accessibility of the LSPR hot spots are difficult to control. To maximize the performance of SERS assay, recent research efforts aim to integrate the plasmonic nanoparticles and 3D PhC structure. The 3D PhC can function as an ordered 3D nanoporous substrate to optimize the spatial distribution and accessibility of the SERS hot spots. In addition, the LSPR modes can be coupled with the PhC resonance locating at the edge of the PhC bandgap to further improve the SERS signal from analyte around the metal nanoparticles [41].

Zhao's group reported a flow-through SERS sensor that incorporated an inverse opal PhC (IO PhC) and gold nanoparticles inside a capillary tube (Fig. 1.5a). The 3D IO PhC structure was formed inside the capillary tube by the self-assembly of plastic nanobeads followed by the infusion of sol-gel glass and removal of the plastic nanospheres. Then, the gold nanoparticles were synthesized on the surface of IO PhC in the capillary tube. Figure 1.5b shows the colorimetric reflection from the IO PhCs with different periods. The Raman spectra of creatinine at different concentrations (Fig. 1.5c) demonstrated a detection limit as low as 0.9 mg/dL. The PhC-SERS capillary tube enabled rapid and simple delivery and analysis of analyte. Such an optofluidic sensor can be adopted for point-of-care testing applications.

The PhC-SERS can also be used for the detection of multiple analytes whose concentrations range from pg/mL to sub mg/mL. With the wide linear dynamic range of SERS analysis, a sample can be measured without being diluted to avoid signal saturation. Mu et al. reported the use of hydrogel IO-PhC with silver nanoparticles to detect three proteins: mouse myoglobin (MB), Cyt C, and human hemoglobin (Hb), simultaneously as shown in Fig. 1.5d [28]. Due to the high-density hot spots and local electromagnetic field at the bandgap of IO PhC (Fig. 1.5e), the 3D PhC structure offered an enhancement of nine times compared to Ag nanoparticles without the PhC structure. Recently, SERS encoded nanotags have shown great potential in the multiplex capacity as well as a sensitivity down to a single molecule. Due to the limited number of available Raman dyes, the SERS encoding capacity is limited. Liu et al. demonstrated the 3D PhC tags that had different lattice constants and exhibited unique reflection signatures, as shown in Fig. 1.5f [29]. The 3D PhC tags can increase the encoding capacity of multiplexed detection and improve the limits of detection for all analytes.

1.3.2.3 PhC-Enhanced Photoacoustic Immunoassay

As shown in Fig. 1.6a, the modulated absorption of light by analyte can generate an acoustic signal, which can be measured using a low-cost acoustic detector. In particular, the LSPR resonance supported by metal nanoparticles can be exploited to produce a strong photoacoustic signal. Based on the strong photoacoustic effect of metal nanoparticles, a photoacoustic immunoassay was developed to improve the detection of sandwich immunoassays. Recently, Zhao et al. demonstrated the use of the leaky mode PhC slabs to enhance photoacoustic sensing of metal nanoparticles [42] The intensified evanescent field of a PhC resonance, as shown in Fig. 1.6b, has successfully enhanced light absorption of gold nanoparticles and resulted in a stronger photoacoustic signal. The PhC substrate was also applied to gold nanorod, which exhibited over 40 times stronger photoacoustic signals compared to a flat glass substrate (Fig. 1.6c). The PhC-enhanced photoacoustics is capable of detecting a single gold nanoparticle within an area of 100 μm^2. The photoacoustic immunoassay was applied to detect the human interleukin 8 chemokine [43, 44]. Compared to the gold standard enzyme-linked immunosorbent assay, the PA immunoassay showed a decrease of the limit of detection from 23 to 0.16 pg/mL, which corresponded to an improvement of the limit of detection by a factor of 143 times. The PhC-enhanced photoacoustic immunoassay enabled a new path towards single-molecule absorption spectroscopy with greater performance, long-term assay stability, and inexpensive instrumentation (Fig. 1.7).

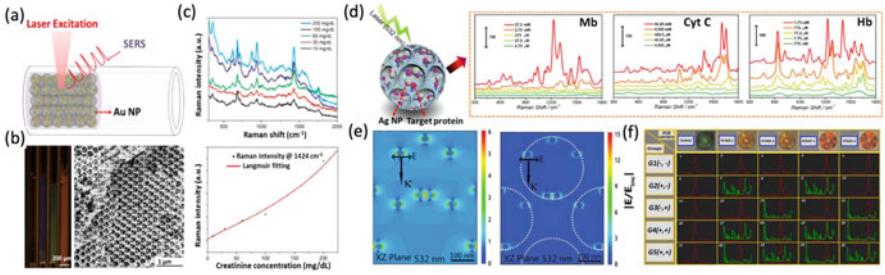

Fig. 1.6 3D PhC-enhanced SERS. (**a**) Scheme diagram flow-through SERS sensor consisting of the 3D IO PhC inside a capillary tube (reproduced with permission from [41]. Copyright 2015, Elsevier). (**b**) Reflection images (left panel) of the 3D IO PhC-filled capillary tubes with different lattice constants. The right panel shows the SEM image of the 3D IO PhC structure (reproduced with permission from [41]. Copyright 2015, Elsevier). (**c**) Raman spectra of creatinine with different concentrations (top panel) and a Raman intensity at 1424 cm^{-1} (reproduced with permission from [41]. Copyright 2015, Elsevier). (**d**) Multiplexed SERS analysis of three different proteins (reproduced with permission from [28]. Copyright 2015, WILEY-VCH). (**e**) The simulated $|E/E_{inc}|$ distributions inside the IO PhC with silver nanoparticle hotspots (reproduced with permission from [28]. Copyright 2015, WILEY-VCH). (**f**) Multiplexed bioassay of qualitative detection of mouse IgG and rabbit IgG by PhC beads. (Reproduced with permission from [29]. Copyright 2016, The Royal Society of Chemistry)

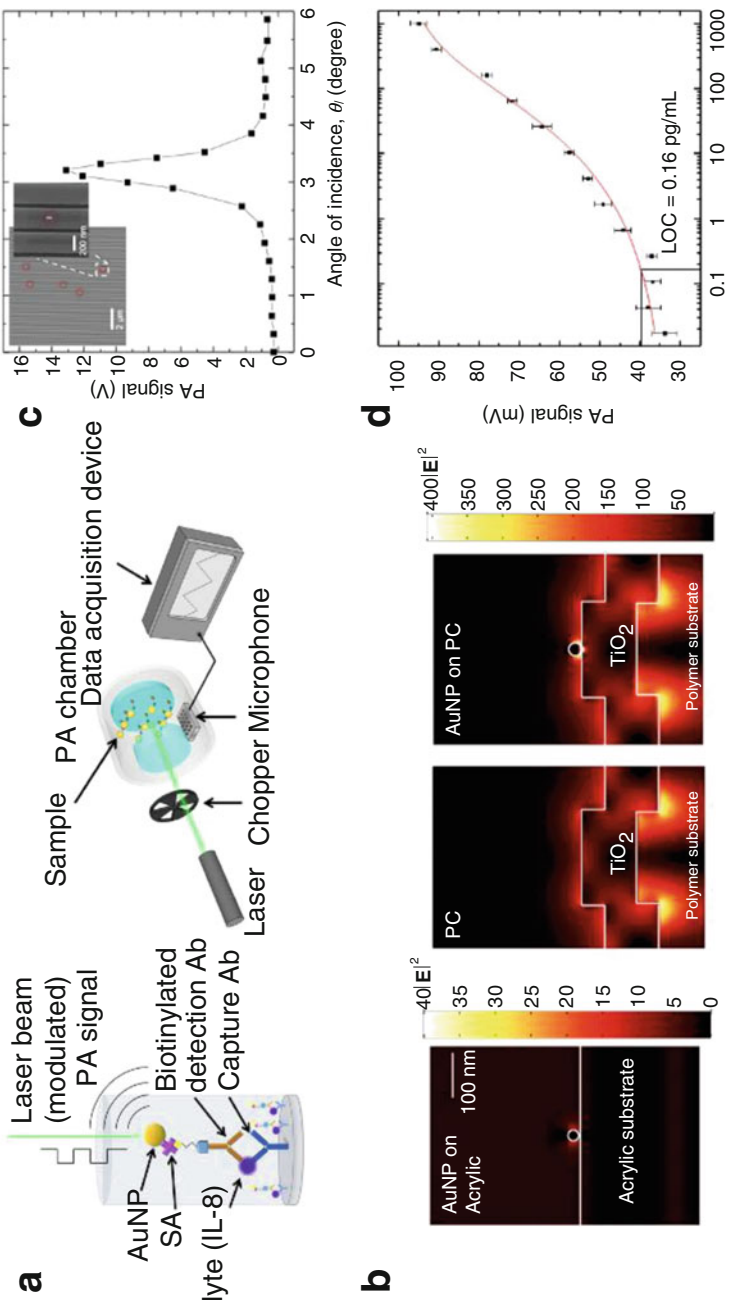

Fig. 1.7 Photoacoustic immunoassay. (**a**) Schematic diagram of the photoacoustic detection of protein biomarker (reproduced with permission from [43]. Copyright 2016, Elsevier). (**b**) Electromagnetic simulation of nearfield distributions of a gold nanoparticle on a 2D PhC slab (reproduced with permission from [42]. Copyright 2014, AIP Publishing). (**c**) Enhanced photoacoustic detection of gold nanoparticles (reproduced with permission from [42]. Copyright 2014, AIP Publishing). (**d**) Dose-response curve of photoacoustic detection of IL-8. (Reproduced with permission from [43]. Copyright 2016, Elsevier)

1.4 Summary

In summary, this chapter reviewed 3D PhC structures and 2D PhC slabs for their applications in the detections of chemicals and biomolecules. As shown in the preceding examples, the PhC-based biosensor offers the capability of label-free detection of analytes without using a signal tag. In addition, the PhC structures can also be combined with spectroscopy methods, including but not limited to fluorescence detection, Raman scattering, and photoacoustic method to offer improved sensitivity and a lower limit of detection. We expect that future developments in this field will produce PhC-based biosensors with lower cost, higher sensitivity, and higher throughput. A particular intesting direction is to integrate the PhC sensors with the mobile or internet of things technologies to develop point-of-care systems for disease diagnosis, food and water quality analysis, and environmental monitoring applications.

References

1. Inan H, Poyraz M, Inci F, Lifson MA, Baday M, Cunningham BT, Demirci U. Photonic crystals: emerging biosensors and their promise for point-of-care applications. Chem Soc Rev. 2017;46(2):366–88.
2. Zhao Y, Zhao X, Gu Z. Photonic crystals in bioassays. Adv Funct Mater. 2010;20(18):2970–88.
3. Pitruzzello G, Krauss TF. Photonic crystal resonances for sensing and imaging. J Opt. 2018;20 (7):073004.
4. Chow E, Grot A, Mirkarimi LW, Sigalas M, Girolami G. Ultracompact biochemical sensor built with two-dimensional photonic crystal microcavity. Opt Lett. 2004;29(10):1093–5.
5. Yablonovitch E. Inhibited spontaneous emission in solid-state physics and electronics. Phys Rev Lett. 1987;58(20):2059.
6. Joannopoulos JD, Meade RD, Winn JN. Photonic crystals. Molding the flow of light. Princeton, NJ: Princeton University Press; 1995.
7. Ho KM, Chan CT, Soukoulis CM. Existence of a photonic gap in periodic dielectric structures. Phys Rev Lett. 1990;65(25):3152.
8. Fan S, Villeneuve PR, Meade RD, Joannopoulos JD. Design of three-dimensional photonic crystals at submicron lengthscales. Appl Phys Lett. 1994;65(11):1466–8.
9. Lin S-y, Fleming JG, Hetherington DL, Smith BK, Biswas R, Ho KM, Sigalas MM, Zubrzycki W, Kurtz SR, Bur J. A three-dimensional photonic crystal operating at infrared wavelengths. Nature. 1998;394(6690):251–3.
10. Wang H, Zhang K-Q. Photonic crystal structures with tunable structure color as colorimetric sensors. Sensors. 2013;13(4):4192–213.
11. Chutinan A, Noda S. Waveguides and waveguide bends in two-dimensional photonic crystal slabs. Phys Rev B. 2000;62(7):4488.
12. Johnson SG, Fan S, Villeneuve PR, Joannopoulos JD, Kolodziejski LA. Guided modes in photonic crystal slabs. Phys Rev B. 1999;60(8):5751.
13. Chow E, Lin SY, Johnson SG, Villeneuve PR, Joannopoulos JD, Wendt JR, Vawter GA, Zubrzycki W, Hou H, Alleman A. Three-dimensional control of light in a two-dimensional photonic crystal slab. Nature. 2000;407(6807):983–6.

14. Rajan R, Babu PR, Senthilnathan K. The dawn of photonic crystals: an avenue for optical computing. In: Theoretical foundations and application of photonic crystals. Rijeka: InTech; 2018. p. 119.
15. Wang SS, Magnusson RJAO. Theory and applications of guided-mode resonance filters. Appl Opt. 1993;32(14):2606–13.
16. Liu J-N, Schulmerich MV, Bhargava R, Cunningham BT. Sculpting narrowband Fano resonances inherent in the large-area mid-infrared photonic crystal microresonators for spectroscopic imaging. Opt Express. 2014;22(15):18142–58.
17. Zhuo Y, Hu H, Wang Y, Marin T, Lu M. Photonic crystal slab biosensors fabricated with helium ion lithography (HIL). Sensors Actuators A Phys. 2019;297:111493.
18. Liu L, Khan HA, Li J, Hillier AC, Lu M. A strain-tunable nanoimprint lithography for linear variable photonic crystal filters. Nanotechnology. 2016;27(29):295301.
19. Armstrong E, Osiak M, Glynn C, O'Dwyer C. Investigations into structure and chemistry of 1D, 2D and 3D structured vanadium oxide nanomaterials for Li-ion batteries. ECS Trans. 2014;58 (14):3–12.
20. Lee W, Pruzinsky SA, Braun PV. Multi-photon polymerization of waveguide structures within three-dimensional photonic crystals. Adv Mater. 2002;14(4):271–4.
21. Kohoutek T, Parchine M, Bardosova M, Pemble ME. Controlled self-assembly of Langmuir-Blodgett colloidal crystal films of monodispersed silica particles on non-planar substrates. Colloids Surf A Physicochem Eng Asp. 2020;593:124625.
22. Pokhriyal A, Lu M, Chaudhery V, Huang C-S, Schulz S, Cunningham BT. Photonic crystal enhanced fluorescence using a quartz substrate to reduce limits of detection. Opt Express. 2010;18(24):24793–808.
23. Byun I, Kim J. Cost-effective laser interference lithography using a 405 nm AlInGaN semiconductor laser. J Micromech Microeng. 2010;20(5):055024.
24. Burrow GM, Gaylord TK. Multi-beam interference advances and applications: nano-electronics, photonic crystals, metamaterials, subwavelength structures, optical trapping, and biomedical structures. Micromachines. 2011;2(2):221–57.
25. Holtz JH, Asher SA. Polymerized colloidal crystal hydrogel films as intelligent chemical sensing materials. Nature. 1997;389(6653):829–32.
26. Bai L, Xie Z, Cao K, Zhao Y, Xu H, Zhu C, Zhongde M, Zhong Q, Gu Z. Hybrid mesoporous colloid photonic crystal array for high performance vapor sensing. Nanoscale. 2014;6 (11):5680–5.
27. Zhao Y-J, Zhao X-W, Hu J, Li J, Xu W-Y, Gu Z-Z. Multiplex label-free detection of biomolecules with an imprinted suspension array. Angew Chem Int Ed. 2009;48(40):7350–2.
28. Mu Z, Zhao X, Huang Y, Lu M, Gu Z. Photonic crystal hydrogel enhanced plasmonic staining for multiplexed protein analysis. Small. 2015;11(45):6036–43.
29. Liu B, Zhao X, Jiang W, Degang F, Gu Z. Multiplex bioassays encoded by photonic crystal beads and SERS nanotags. Nanoscale. 2016;8(40):17465–71.
30. Cunningham B, Lin B, Qiu J, Li P, Pepper J, Hugh B. A plastic colorimetric resonant optical biosensor for multiparallel detection of label-free biochemical interactions. Sensors Actuators B Chem. 2002;85(3):219–26.
31. Chan LL, Cunningham BT, Li PY, Puff D. Self-referenced assay method for photonic crystal biosensors: application to small molecule analytes. Sensors Actuators B Chem. 2007;120 (2):392–8.
32. Cunningham BT. Photonic crystals utilized for label-free and amplified fluorescence biodetection. In: Micro (MEMS) and nanotechnologies for space, defense, and security II, vol. 6959. Bellingham WA: International Society for Optics and Photonics; 2008. p. 695910.
33. Choi CJ, Cunningham BT. Single-step fabrication and characterization of photonic crystal biosensors with polymer microfluidic channels. Lab Chip. 2006;6(10):1373–80.
34. Chen W, Long KD, Lu M, Chaudhery V, Yu H, Choi JS, Polans J, Zhuo Y, Harley BAC, Cunningham BT. Photonic crystal enhanced microscopy for imaging of live cell adhesion. Analyst. 2013;138(20):5886–94.

35. Choi CJ, Belobraydich AR, Chan LL, Mathias PC, Cunningham BT. Comparison of label-free biosensing in microplate, microfluidic, and spot-based affinity capture assays. Anal Biochem. 2010;405(1):1–10.
36. Zhuo Y, Hu H, Chen W, Lu M, Tian L, Yu H, Long KD, et al. Single nanoparticle detection using photonic crystal enhanced microscopy. Analyst. 2014;139(5):1007–15.
37. Chaudhery V, George S, Lu M, Pokhriyal A, Cunningham BT. Nanostructured surfaces and detection instrumentation for photonic crystal enhanced fluorescence. Sensors. 2013;13 (5):5561–84.
38. Ganesh N, Zhang W, Mathias PC, Chow E, Soares JANT, Malyarchuk V, Smith AD, Cunningham BT. Enhanced fluorescence emission from quantum dots on a photonic crystal surface. Nat Nanotechnol. 2007;2(8):515–20.
39. Mathias PC, Jones SI, Wu H-Y, Yang F, Ganesh N, Gonzalez DO, Bollero G, Vodkin LO, Cunningham BT. Improved sensitivity of DNA microarrays using photonic crystal enhanced fluorescence. Anal Chem. 2010;82(16):6854–61.
40. Huang C-S, George S, Lu M, Chaudhery V, Tan R, Zangar RC, Cunningham BT. Application of photonic crystal enhanced fluorescence to cancer biomarker microarrays. Anal Chem. 2011;83(4):1425–30.
41. Zhao X, Xue J, Zhongde M, Huang Y, Lu M, Gu Z. Gold nanoparticle incorporated inverse opal photonic crystal capillaries for optofluidic surface enhanced Raman spectroscopy. Biosens Bioelectron. 2015;72:268–74.
42. Zhao Y, Liu K, McClelland J, Lu M. Enhanced photoacoustic detection using photonic crystal substrate. Appl Phys Lett. 2014;104(16):161110.
43. Zhao Y, Cao M, McClelland JF, Shao Z, Lu M. A photoacoustic immunoassay for biomarker detection. Biosens Bioelectron. 2016;85:261–6.
44. Zhao Y, Huang Y, Zhao X, McClelland JF, Lu M. Nanoparticle-based photoacoustic analysis for highly sensitive lateral flow assays. Nanoscale. 2016;8(46):19204–10.
45. Alexeev VL, Das S, Finegold DN, Asher SA. Photonic crystal glucose-sensing material for noninvasive monitoring of glucose in tear fluid. Clin Chem. 2004;50(12):2353–60.
46. Nakayama D, Takeoka Y, Watanabe M, Kataoka K. Simple and precise preparation of a porous gel for a colorimetric glucose sensor by a templating technique. Angew Chem Int Ed. 2003;42 (35):4197–200.
47. Zhao Y, Zhao X, Tang B, Xu W, Li J, Gu Z. Quantum-dot-tagged bioresponsive hydrogel suspension array for multiplex label-free DNA detection. Adv Funct Mater. 2010;20 (6):976–82.
48. Ganesh N, Cunningham BT. Photonic cyrstal near-ultraviolet reflectance filters fabricated by nanoreplica molding. Appl Phys Lett. 2006;88(7):071110.
49. Choi CJ, Block ID, Bole B, Dralle D, Cunningham BT. Label-free photonic crystal biosensor integrated microfluidic chip for determination of kinetic reaction rate constants. IEEE Sensors J. 2009;9(12):1697–704.

Chapter 2
Recent Advances in Surface Plasmon Resonance for Biosensing Applications and Future Prospects

Biplob Mondal and Shuwen Zeng

Abstract Surface plasmon resonance (SPR)-based sensors have been widely applied in many applications in the fields of medical research, environment monitoring, food safety, and so on to study and monitor various biomolecular interactions. This chapter is written to provide a comprehensive review on the fundamental techniques for the excitation of surface Plasmon and to employ these recent new techniques in biosensing applications. The first section parts of the chapter introduce different light wave coupling methods for excitation of surface plasmon resonance, and then followed by preliminary study on biomolecular interaction using SPR Bio-chip and a lab-scale measurement system based on Kretschmann's configuration. The protocols discussed here are followed for protein immobilization in sensor fabrication, measurement procedure, optical and fluidic system, etc. Finally, recent developments and future prospects of novel two-dimensional nanomaterials such as graphene and transition metal dichalcogenides targeting towards enhanced sensing performance, for significantly improved ultra-high sensitivity and much narrower full width half maxima of SPR sensors have been discussed in detail.

Keywords Surface plasmon resonance · 2D materials · Biosensing · Optical sensors · Label-free detection

B. Mondal
Department of Electronics and Communication Engineering, Tezpur University, Tezpur, Assam, India

S. Zeng (✉)
XLIM Research Institute, UMR 7252 CNRS, University of Limoges, Limoges Cedex, France
e-mail: shuwen.zeng@unilim.fr

X. Zhao, M. Lu (eds.), *Nanophotonics in Biomedical Engineering*,
https://doi.org/10.1007/978-981-15-6137-5_2

2.1 Introduction

Optical biosensors have been widely applied among the scientific community for different aspects, most commonly in monitoring protein–protein or nucleic acid hybridization interactions and association and determining dissociation kinetics, etc. The application of surface plasmon is recognized widely in recent years as a potential tool for fast screening of bioanalytes where the current main challenge is the detection of nanomolar and picomolar concentration of hard-to-identify biomolecules. Surface plasmon resonance (SPR) interrogation is one of the most advanced and unique optical transduction methods for label-free and real-time detecting biological species in molecular level that uses an optical approach to measure a change in the refractive index unit of target sensing media. The sensing medium is in close vicinity of a metallic surface that consisted of a large number of free electrons to interact with the incident light. Plasmon resonance in this phenomenon can result in extraordinary detection limit due to its capability to give extremely high sensitivity towards even a tiny change in refractive index at the sensing interface. This chapter presents a brief review on Kretschmann configuration-based surface plasmon resonance technique for the biosensing areas. Here, we will present the latest trend to design and fabricate portable setup for SPR measurement along with discussions related to target antibody immobilization, choice of metal for improved sensitivity, and accuracy of measurement. The chapter also provides insights on the future trends of SPR technology for superior sensing performance.

2.2 History of SPR Technology

In 1902, R.W. Wood observed anomaly spectra of dark and light bands that occurred in the reflected light when polarized light is incident on a mirror with diffraction grating at the surface [1]. This appeared to be a remarkable physical phenomenon that took nearly four decades to be physically interpreted with the excitation of surface plasmons by attenuated total reflection (ATR) by Otto [2], Raether, and Kretschmann [3] independently in 1968. The fundamental principles of their demonstration were based on the studies made by Zenneck [4] in 1907 theoretically proving the existence of radio frequency surface electromagnetic (EM) waves at the boundary of a metal (lossy) and dielectric (loss-free) medium, Ritchie [5] in 1957 theoretically demonstrating the existence of surface plasma at metal surface, while Swan and Powell's [6] work on the excitation of surface plasmons at metallic interfaces with electrons, and later by Stern and Ferrell [7] to show surface electromagnetic waves at a metallic surface involved the coupling between electromagnetic radiation and surface plasmons.

In its early stage, the unique property of surface plasmon resonance (SPR) being very sensitive to its boundary conditions was utilized in determining the optical properties of cadmium arachidate thin films deposited on metal surface by Pockrand

[8] and Wahling [9] independently. In 1982, Nylander [10] has demonstrated the utility of SPR in gas sensing. Later, Liedberg et al. [11] working at the laboratory of applied physics in Linkoping University, Sweden, reported biosensing with surface plasmon resonance for the first time. They reported immunosensing of anti-IgG (anti-immunoglobulin G) down to the concentration of 0.2 μg/mL using 60 nm thick silver films deposited on microscopic slide. Since then, an increasing number of the SPR approaches are developed in health-care research, fundamental biological studies, drug design/screening, clinical diagnosis, food and environmental monitoring, defense security, and agricultural insecticide research [12–14]. Over the years, several generations of instrumentation for SPR biosensing have been witnessed from prism and grating coupled [15] instrumentation to fiber-coupled SPR sensing for point-of-care application [16–18].

Current trends in SPR technology directed towards improving the sensitivity and accuracy of measurements with the application of multilayer graphene or molybdenum disulfide (MoS_2) coating, achieving oxidization resistance of the sensitive element, and developing methods for regeneration of receptors for multiple use [19–21]. SPR imaging with integrated Microfluidics lab-on-a-chip (LOC) for point-of-care (POC) application in medical and clinical theranostics appears to be the promising technology of near future [22].

2.3 Fundamental Theory and Principle of Surface Plasmon Resonance

Surface plasmon resonance (SPR) is an optical phenomenon that induces a charge density oscillation wave that could propagate along the metal dielectric interface (metal and dielectric layer having opposite sign for their dielectric constants) when excited by p-polarized light. These surface plasmons also referred to as surface plasmon wave (SPW) can only be excited by a longitudinal (TM or p-polarized) electric field (along the direction of light propagation), which would exponentially decay in the hybrid layer of metal and dielectric. The propagation constant of a SPW is defined as [23]:

$$K_{sp} = \frac{w}{c}\sqrt{\frac{\varepsilon_m \varepsilon_d}{\varepsilon_m + \varepsilon_d}} \tag{2.1}$$

Where c is the speed of light in vacuum, w is angular frequency, and ε_m and ε_d are respectively the dielectric constants of metal layer and dielectric layer. Here, the real part of ε_m must be negative, and its absolute value smaller than ε_d to promise the metals could supports SPW. The surface plasmon waves (SPWs) have maximum field intensities at the metal-dielectric interface with limited propagation length, usually 200–400 nm. The electromagnetic field decreased exponentially in both

the media and the majority of which is concentrated in the dielectric [17] indicating SPW is highly sensitive to the changes in properties of the dielectric.

The propagation constant of a light wave propagating with a frequency w in free space is given by

$$K_{\mathrm{d}} = \frac{w}{c}\sqrt{\varepsilon_{\mathrm{d}}} \tag{2.2}$$

Based on Eqs. (2.1) and (2.2), the dielectric constants of metal and dielectric being negative and positive respectively infers that the wave propagation constant of SPW should be always higher than that of wave propagating in dielectric. Direct light therefore cannot excite surface plasmon at metal-dielectric interface, and hence to satisfy the condition of resonance the momentum of the incident wave propagating through the dielectric that has to be enhanced. At resonance the wave vector of the incident and surface plasmon wave (SPW) matches with each other leading to a reduced intensity of the reflected light. To date, three methods are popularly used for matching the momentum that uses high refractive index material for momentum matching: Attenuated total reflection (ATR) in prism coupler, diffraction at the surface of diffraction grating, and optical waveguides.

2.4 Light Wave Coupling Techniques

In prism coupling configuration, surface plasmons (SPs) are usually excited with an evanescent wave from a high-refractive index glass prism under attenuated total reflection (ATR) condition [17]. When p-polarized is passed through a prism coated with metal at its base which remains in contact with dielectric media of low refractive index and θ_{inc} is greater than or equal to critical angle for total internal reflection, evanescent wave is generated at the prism metal interface. This facilitates the excitation of surface plasmons (SPs), which occurs when the wave vector of the propagation constant of incident light through the prism matches with that of the surface plasmon with same frequency and polarization state. This occurs at a specific angle of incidence θ_{res} and the resonance condition is given as

$$\frac{w}{c}\sqrt{\varepsilon_{\mathrm{p}}}\sin\theta_{\mathrm{res}} = \frac{w}{c}\sqrt{\left(\frac{\varepsilon_{\mathrm{m}}\varepsilon_{\mathrm{d}}}{\varepsilon_{\mathrm{m}}+\varepsilon_{\mathrm{d}}}\right)} \tag{2.3}$$

Where the left side of the Eq. (2.3) is the wave propagation constant of the incident light in the direction parallel to the metal surface and ε_{p} is the refractive index of prism. The propagation constant of evanescent wave and SPW can be matched by controlling the angle of incidence and frequency of the incident beam. This method is schematically depicted in Fig. 2.1a. The ATR method is conventionally implemented in two different configurations proposed by Otto and

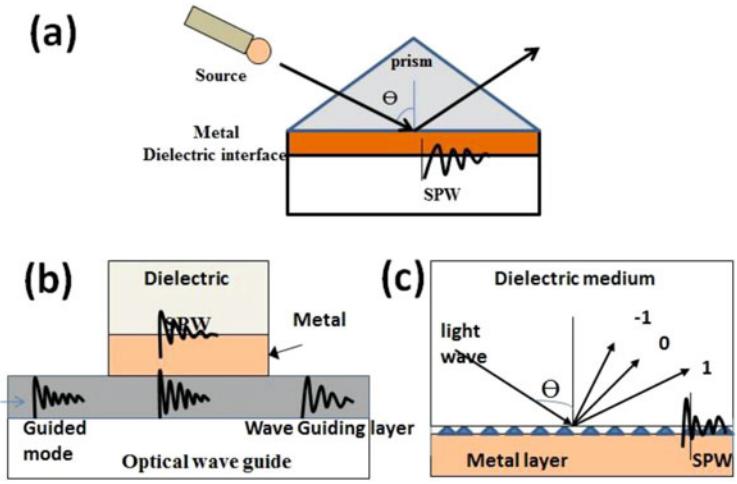

Fig. 2.1 Excitation of surface plasmon waves (SPWs) based on: (**a**) prism coupling (**b**) optical waveguide (**c**) diffracting grating

Kretschmann. The core of an optical waveguide (for example, optical silica fiber) can be used to replace the bulky prism used in ATR method to get the benefit of simple and flexible design and miniaturized sensor system. Evanescent waves are excited at the core-cladding interface when light is guided through optical fiber. If a portion of the cladding is removed and deposited with thin metal layer, light entering the region can evanescently penetrate through the metal layer exciting SPW at the core-metal interface. The method is depicted in Fig. 2.1b. It is worth noting that the coupling of the evanescent field with SPs depends strongly on the wavelength of incident light, and the dielectric constants of the fiber/metal layer. Momentum enhancement to compensate the wave vector mismatch between the incident light waves and SPWs can also be achieved with the diffraction of the light at the surface of metallic diffraction grating as shown in Fig. 2.1c. Conventionally a sinusoidal grating is used with which the wave vector enhancement of the diffracted wave proportional to the period of the grating can be achieved [24]. Since fabrication of diffraction grating of given specification is expensive, inexpensive gold-coated diffraction gratings using commercial CD-R type optical storage disk is reported as a low-cost alternative for the fabrication of integrated SPR-based optical sensors [25].

2.5 Sensing with Surface Plasmon Resonance

The interaction of light wave with SPW results in changes in the optical characteristics like intensity, phase etc., of the reflected light,0 which is correlated with the propagation constant of the SPWs. Accordingly, based on the measured

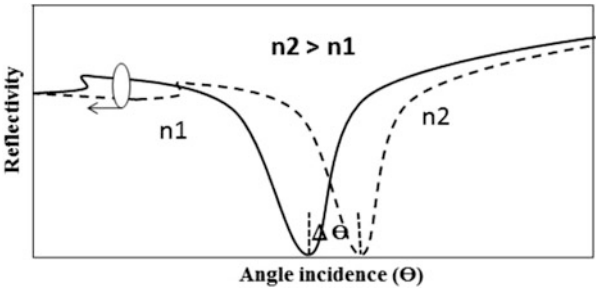

Fig. 2.2 Reflectance spectra as a function of incident angle (θ_{inc}) at the prism–metal interface

characteristics, SPR devices are classified as intensity [26], angular [27], wavelength [28], phase or polarization [29] modulation-based device. Excitation of SPW at metal–dielectric interface results in resonant energy transfer into the SPR form the incident photons reducing the reflected light energy. In the Kretschmann configuration, which is a widely used scheme for SPR sensing, p-polarized light from a light source is directed through a high-refractive index prism with a thin metal layer (~50 nm) deposited at the base. If the reflected light intensity is measured in terms of incident angle, a sharp dip in the reflected intensity could be observed at particular angle of incidence due to resonant transfer of energy to the SPW. The angle at which this resonance condition could be fulfilled is called resonance angle. Optimum coupling between the incident light and the surface Plasmon wave (surface plasmon resonance condition) is strongly dependent on the refractive index of the dielectric medium close to the surface of the metal layer. This is attributed to the fact that the electromagnetic field is strongly concentrated in the dielectric. Thus, the SPR technique is highly sensitive and surface specific experimental for small molecule interactions. If one increased the refractive index of the dielectric sensing media, the resonance angle would have a shift to a larger angle [30–32] as shown in Fig. 2.2.

2.6 SPR-Based Biosensing

Surface plasmon resonance is currently established as a potential optical tool for ultrasensitive detection of bioanalytes that could provide extraordinarily low limit of detection. Compared to other types of electrical and optical sensors, it also showed added unique advantages of real-time and label-free sensing of biological samples in molecular level [27, 33–36]. The development of SPR sensing devices for detection of various chemical and biological molecules has received significant impetus over the last couple of decades, for applications ranging from medical diagnostics [12], environmental monitoring [13] to food safety and defense security [14]. Many researchers are involved in exploring the possibility of the technology for fulfilling the recent demand of extremely high sensitivity of the order nano to picomolar concentration to very specific target which can open up new dimension of research in areas such as drug discovery, food quality and safety, etc. [37, 38]. The SPR

biosensors are sensitive to refractive index changes at the metallic sensing substrate and known to be useful for the study of specificity, affinity, and kinetics of biomolecular interactions, and measurement of the concentration levels of target analytes in complex matrix samples. In the following section, discussion mainly focus on Kretschmann's configuration in the study of SPR signals where the primary components are a prism-based optical coupling system, SPR bio-chip, and analyte handling system.

2.6.1 SPR Bio-Chip

Efficient immobilization and capture of bioreceptor on the sensing substrate is one of the critical steps in the development of optical biosensor. The sensor performance depends significantly on the appropriate surface treatment for effective immobilization of the bio-receptors on sensor surface. Up to date, most of the SPR detection schemes have adopted the self-assembled monolayers (SAMs) to conjugate small biomolecules such as peptides, DNA sequences, and antibodies to the sensor surface. Index-matched cover slips are typically used as the substrate for immobilization of the antibodies. After properly cleaning the cover slips, a thin layer of gold, silver, or other metal supporting surface plasmon resonance is sputtered over it followed by bio-functionalization of the surface with antibody.

2.6.1.1 Immobilization of Antibody: Functionalization, Activation, and Binding of Receptor

Immobilization of properly oriented antibody on the sensor surface is a measure of effectiveness of any immunosensors [39–42]. During immobilization, the antibody must retain their conformation. Moreover, the binding sites of the immobilized antibody should remain exposed to the antigen in order to ensure efficient antigen binding capacity. Direct immobilization on sensor surface results in random orientation of the immobilized antibodies, and thus make binding sites inaccessible for specific interaction with target antigen. This reduces their binding ability resulting in poor sensitivity of the sensors [40, 43]. Availability of highly dense active surface group of immobilized protein also influences the sensitivity of SPR sensor. Immobilization protocol therefore must ensure placement of properly oriented antibody on sensor surface with active binding sites exposed to the target sample. A great variety of immobilization strategies is reported that can be classifies as physical, covalent, and bio-affinity immobilization techniques. Physical adsorption presents the simplest method that utilizes ionic bonds or hydrophobic and polar interactions for immobilization. However, this binding approach yields poor reproducibility due to random orientation and denaturation of immobilized antibody [44, 45]. Contrarily, covalent and bio-affinity-based immobilization method provides higher stability and gently oriented antibody.

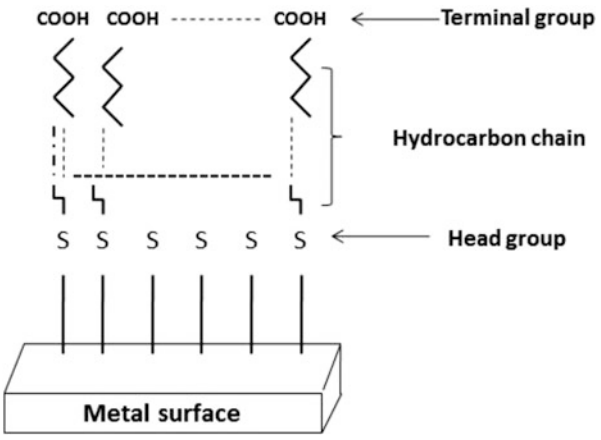

Fig. 2.3 Representation of SAM of alkanethiols on metal

Conventionally used gold-coated SPR substrates generally lack sufficient active groups that are needed for direct attachment of antibody [39]. The inorganic metal surfaces are therefore activated with certain active groups that can efficiently bind with specific moieties (-NH_2, -SH, -COOH, etc.) of the protein to be immobilized. However, before such activation process, the inorganic surfaces are covered with protein-resistant self-assembled monolayer (SAM) in order to maximize the density of active surface groups [46, 47]. In addition, SAM provides stable covalent binding, better control on orientation of immobilized proteins and helps in the minimization of nonspecific protein adsorption on SPR chip [40, 48]. SAMs are ordered molecular assemblies that consist of active functional head group at either end of a hydrocarbon chain and a linear carbon chain that promotes self-assembly, when they are attached to a substrate surface. These active head groups have strong affinities for the binding surface while the other end remains free to bind with moieties of antibody.

Monolayer of alkanethiols on gold is the most extensively studied SAM for protein immobilization [49, 50]. The thiol groups (-SH) are known to exhibit strong binding affinity to the noble metallic surfaces that could allow them to form covalent bonds between the sulfur group in the thiol molecules and the metal atoms as shown in Fig. 2.3. Alkanethiols with acid end group offer excellent chemical modification ability of the SAM surface making them promising for sensing applications [51–53]. SAM formed from 11-mercaptoundecanoic acid (11-MUA) has been reported to form well-ordered monolayers by various research groups and is used for all the studies reported in this chapter [50, 54].

After surface functionalization for target antigen, the monolayer surface is required to be activated for facilitating the covalent attachment of the antibody using moieties such as amine, carboxylic, thiol, and carbohydrate available in the protein. Among these functional groups, amine (-NH_2) groups in the lysine residue of the antibody have been widely used as anchoring points with their presence on the exterior of the antibody. Table 2.1 summarized the common functional groups in antibody used for covalent attachment and the substrate requirement. In the

Table 2.1 Summary of commonly available functional groups for protein immobilization

Functional group in protein	Amino acid	Substrate requirement	Reference
Amine (NH_2)	Lysine	Carboxylic acid active ester	[55–57]
Carboxylic (-COOH)	Aspartate, Glutamate	Amine	[58]
Thiol (-SH)	Cysteine	Maleimide, pyridyil disulfide	[59–61]
Carbohydrate (–COH)	Sugar residue after oxidation	Silane-modified surface	[62]

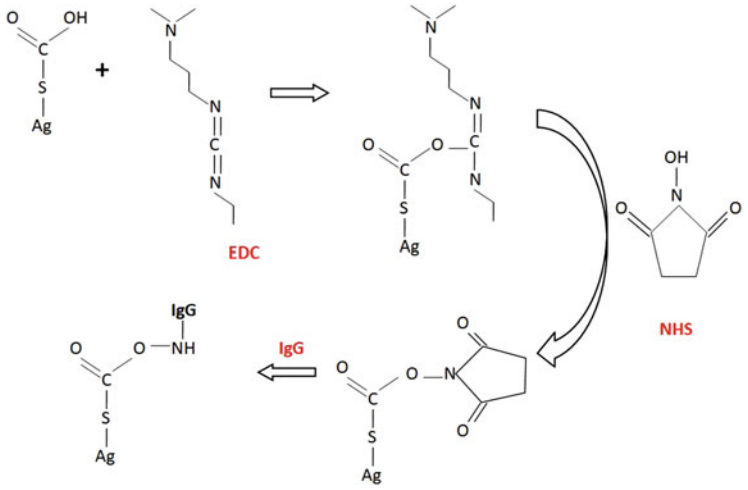

Fig. 2.4 Amine-based coupling chemistry

following section, amine-based chemistry for antibody immobilization is presented which we have used in all further studies presented here.

Amine-based coupling chemistry with carboxylated gold surface is shown in Fig. 2.4. This popularly used carbodiimide chemistry has been applied to produce robust amide bonds between the amine groups and the carboxyl groups of the antibody. Water-soluble carbodiimide reagents 1-ethyl-3-(3-dimethylaminopropyl)-carbodiimides (EDCs) are used to activate the carboxyl group present on the substrate in order to produce a reactive *O*-acylisourea intermediate. When *N*-hydroxy succinimide (NHS) is added, the nucleophile of NHS reacts with the intermediate *O*-acylisourea and forms an NHS ester that is much more stable than the *O*-acylisourea intermediate and leads to their efficient conjugations to primary amines [63, 64]. The conjugation between aldehyde and amine groups realized the immobilization of antibody by a labile Schiff's base formation.

Immobilization Protocol

The following protocol is a standard process used for the preparation of SPR sensor with immobilized antibody [55, 65, 66].

1. **Substrate Preparation**

   (a) The microscopic cover slips (18 × 18 mm^2) were cleaned using acetone vapor at 80 °C followed by treatment with methanol at room temperature for 5 min each. Finally, the slides were rinsed in Deionized (DI) water and then dried in a nitrogen environment.
   (b) Place the samples onto a hotplate facing upwards at 180 °C for about 15 min.
   (c) Sputter deposit ~50 nm gold or silver layer. A thin layer of titanium or chromium (~5 nm) is required to be deposited first before the deposition of Au/Ag layer in order to improve the adhesion capability of Au/Ag with glass.

2. **Functionalization Followed by Activation of Sensor Surface**

   (a) Prepare separate solutions of 1 mM ethanoic solution of 11-MUA, 75 mM EDC, 15 mM NHS and 50 mM ethanolamine solution in water.
   (b) Dip the metal-coated substrates in the ethanoic solution 11-MUA in a close container for 24 h at room temperature.
   (c) Rinse the MUA coated chip in ethanol and dry under nitrogen stream.
   (d) Drop 100 μL of EDC and NHS successively using a micropipette over the sample.
   (e) Incubate the sample for 1 min in a tightly closed petri dish.

3. **Antibody Immobilization**

   (a) The slide is immersed into anti-mouse IgG2b solutions/IgG in 50 μL phosphate buffer solution (PBS) at pH of 7.4 for 2–4 h to form stable monomolecular layer
   (b) The free amine groups of EDC-NHS from the surface functionalization process are blocked through immersing the SPR chip in solutions containing 50 mM ethanolamine (100 μL) for 10–20 min to avoid the unwanted binding of free amine group from EDC-NHS with target molecules.
   (c) Finally, the chip is washed gently with 0.5 mL PBS and then kept at 4 °C for 12 h.

2.6.1.2 Characterization of Sensor Surface

The immobilization protocol for SPR sensor involves a number of steps and the sensor surface consists of a number of layers staked together. The surface composition and structure of the deposited layers viz., thickness of the metal layer, morphology of SAM layer for surface functionalization and NHS-EDC for surface activation is essential for ensuring properly oriented immobilization of antibody. The immobilization of the antibody is usually characterized by spectroscopic measurements such as Fourier-transforms infrared spectroscopy (FTIR) and ultraviolet-visible spectroscopy (UV-Vis) in our studies as other research groups did. However, various other methods can also be used for assessing the state of immobilized

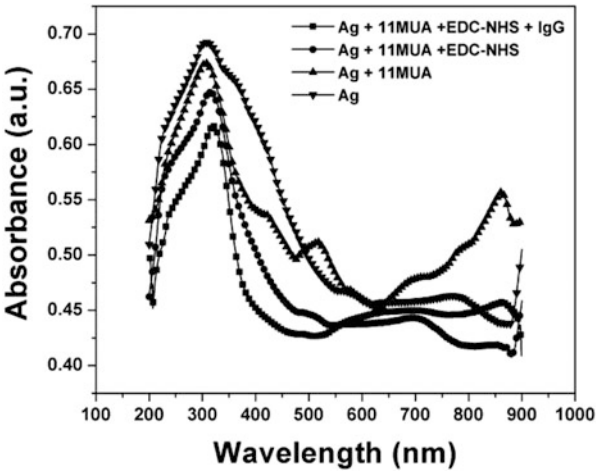

Fig. 2.5 UV-Vis spectra of the pure silver (Ag) thin film deposited sensor surface before and after antibody (IgG) immobilized. (Reprinted with permission form Choudhury et al., Creative Commons Attribution 4.0 International License, http://creativecommons.org/licenses/by/4.0/)

antibody, doing elemental and chemical characterization and studying the surface morphology of the stacked layers. Zhao et al., reported a detailed study on surface composition and structure of self-assembled thiol-monolayer of alkanethiol molecules using X-ray photoelectron spectroscopy (XPS), FTIR and energy dispersive spectroscopy (EDS) [67]. A summary of various characterization techniques is presented by Welch et al. [41].

Figure 2.5 shows the optical absorption spectra using by a UV-Visible spectroscopy of the SPR sensing substrate before/after antibody (IgG) immobilized onto pure silver (Ag) thin film deposited sensor surface. As one can see, the absorbance peak of pure Ag film is centered at 310 nm, and the following deposition of the additional molecular layer on the silver nanofilm results in a red shift in the SPR dip. The surface functionalization with an 11-MUA layer led to the absorption peak with a redshift by ~5 nm that is attributed to the covalent binding of thiol molecules to the metallic surface. While when the antibody is further conjugated, a redshift of 15 nm was induced on the absorbance peak. This is due to the increase of the local dielectric constant of at the metal interface by an additional molecular layer.

The FTIR measurements are performed with Nicolet Impact 410 to characterize the chemical structures of the SPR surface. Figure 2.6 presents the infrared spectroscopy (IR) spectra of the sensing substrate after the monolayer binding with 11-MUA, followed by surface activation with NHS-EDC, and lastly target antibody conjugation. The end chemical groups of 11-MUAs are carboxyl groups of -COOH. The amine groups of NHS conjugated to this group through reaction with EDC finally formed bond of COO-NHS. After the capture process of target antibodies, the end group is then converted to COO-N-IgG as well. Figure 2.6a also showed the band region for carbon inside the IR spectra. This carbon region was characterized through two absorption peaks at wavenumbers 2932 cm^{-1} and 2856 cm^{-1} respectively that generated by the CH_2 symmetric and asymmetric stretches [68]. Figure 2.6b presents the amide and carboxyl region inside the IR spectra. In

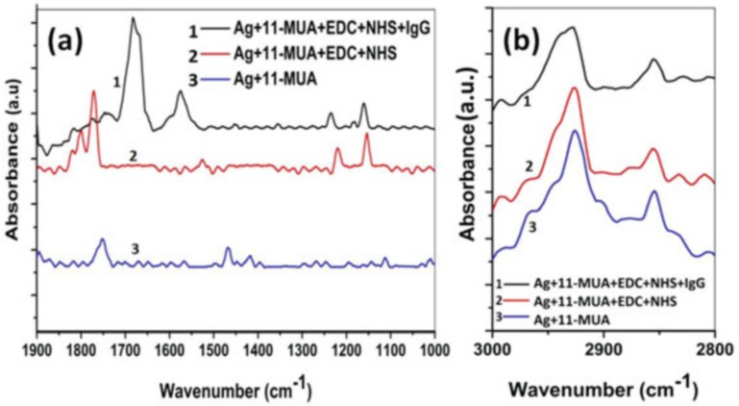

Fig. 2.6 (**a**, **b**) Fourier-transforms infrared spectroscopy (FTIR) spectra of the SPR sensing surface before/after the immobilization of target antibody IgG. (Reprinted with permission form Choudhury et al., Creative Commons Attribution 4.0 International License, http://creativecommons.org/licenses/by/4.0/)

comparison to the 11-MUA molecules-functionalized films, NHS terminated-film showed three characteristic bands centered at 1820, 1798, and 1765 cm^{-1} that are responsible for stretch modes of COO-NHS esters. After the immobilization of the target antibody IgG, there are two new amide bands appearing at 1570 and 1687 cm^{-1} (amide I and amide II), which further confirmed the successful binding of IgG molecules on the substrate [69].

2.6.2 SPR Setup

2.6.2.1 The Optical Assembly

The conventional method of excitation of surface plasmon resonance (SPR) based on Kretschmann's configuration involves focusing laser beam through a prism coated with metal layer, which in turn is placed on a rotating stage. Surface plasmon is excited at the interface between a metal and dielectric layer at a particular incident angle of the light beam. A complex rotation mechanism is needed to adjust the incident angle of the incoming beam and to receive the reflected light. Prof. Mukherji and his group at Indian Institute of Bombay (IITB) have given significant contribution for the development of portable SPR measurement device [70]. At Tezpur University a number of experimental setups were also fabricated by our group and Fig. 2.7 shows a raw version of one [71]. The device comprised of a BK7 prism which was mounted with two supports from its two sides in such a way that it could be easily removed/replaced whenever required. The laser diode (650 nm, 5 mW) was mounted on an "L"-shaped leg and its movement was controlled using a servomotor to adjust the incident angle of the incoming light within an angular span of 45–80° as a reference to the base of the prism. The incoming light from the laser diode went

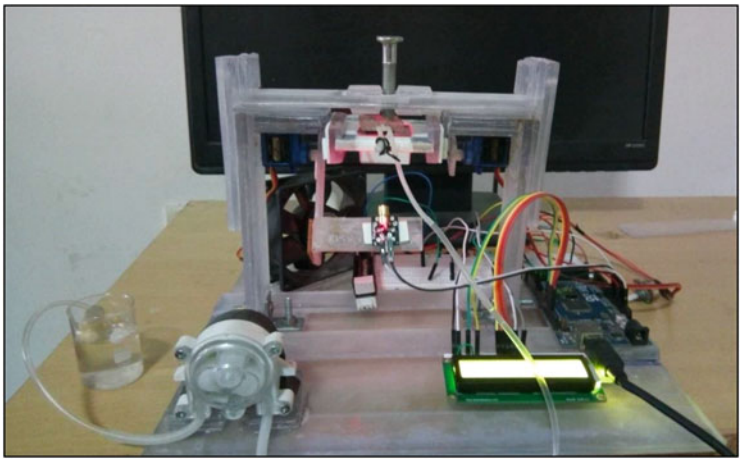

Fig. 2.7 Snapshot of SPR measurement setup

through a linear polarizer to generate a p-polarized light beam and made to fall on the sensor surface at varied angles of incidence. Glycerin having a refractive index unit (RIU) of 1.42 was used as the index-matching layer for sticking the microscopic cover slips on the glass prism (BK7) in order to avoid the any air gaps in between. A detector array from photodiodes is used to collect the light signals reflected from the prism surface. Alternatively, the reflected light from the sensor surface might be converged using a convex lens and collected with a charge-coupled device (CCD) camera based on a universal serial bus (USB) interface.

2.6.2.2 Analytes Handling and Sensor Measurement

The fluid handling system of the device consisted of a specially designed flow cell (~280 mm^3) regulated by peristaltic pump which was used to pass stream of test samples through the sensor surface. The flow cell could be readily attached to the sensor surface using O-ring to prevent leakage of test fluid. A schematic arrangement of fluid handling system is shown in Fig. 2.8. The operation of the pumping system was controlled using an Arduino microcontroller. Before the protein conjugation studies, the phosphate buffer solution (PBS) with a pH of 7.4 is flowed onto the self-assembled monolayer (SAM) for establishing a baseline signals for the following tests. For the subsequent measurement steps, the sensor head is reacted with target IgGs in different concentrations of (0.05–0.35 mg/mL) diluted in the PBS solution for 10 min. The antigen-antibody binding is depicted in Fig. 2.8. For the final step, PBS is then injected to the sensing substrate to initiate the dissociation binding of protein molecules.

In modern biotechnology particularly for drug discovery, clinical and proteomic research, multiple proteins detection is becoming increasingly important where

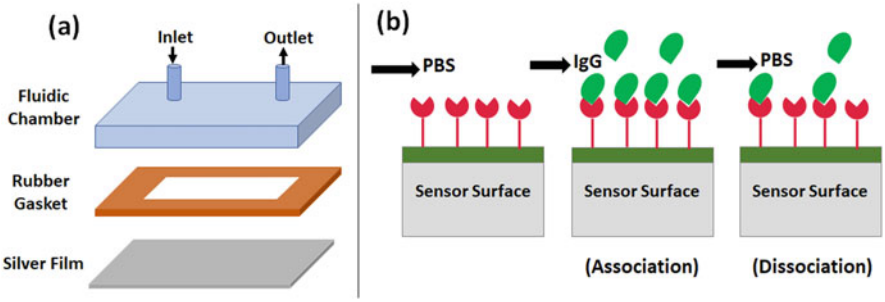

Fig. 2.8 Schematic of fluid handling system (**a**) and sensor measurement procedure (**b**)

sophisticated fluidic systems for precise delivery of various fluids to the sensor surface is essential. In this direction Piliarik et al. have reported a SPR sensor with high sensitivity that consisted of a SPR Disperser (SPRCD) and a coupler. The sensor head is integrated with a set of microfluidic channels enabling the device for multiple measurements [72]. Using this compact system designed at the Institute of Photonics and Electronics, Prague (Czech Republic), portable SPR immunosensors with six channels for simultaneous detection of antibiotics in milk sample was reported by Fernandez et al. [73]. Recently Liu et al. also demonstrated multi-analyte detection capability of a compact multichannel SPR biosensor even on a cell mobile device as an effective platform for in situ measurement [74].

2.6.3 Experimental Result

The value of intensities of the light reflected from the SPR sensing chip as a function of the incident angles are plotted in Fig. 2.9 below. Protein IgG in a concentration of 0.05 mg/mL is flowed and reacted with the capture antibody (monoclonal anti-IgG) immobilized sensor surface. The redshift of the SPR resonance dip with successive additional deposition of layers over the sensor surfaces indicates binding between the stacked layers.

To systematically study the antigen–antibody interactions, antibody proteins with different concentrations were flowed and reacted with the IgG-functionalized sensing substrate. All of the measurements are carried out by immersing the sensor head with the protein diluted in the PBS buffer. The output data with dip angle in terms of the IgG concentrations are plotted in Fig. 2.10a, b. The flow of protein of higher concentration results in higher degree of refractive index change in the medium close to the sensor interface. This is due to more binding events between antigen–antibody. The binding process made the resonance dip to shift towards right with increasing concentration of the target protein as can be from Fig. 2.10a. It is worth noting that the SPR characteristic curve is not much affected by change in the concentration of the sample, as the full width half maxima (FWHM) remain nearly identical for all the different samples.

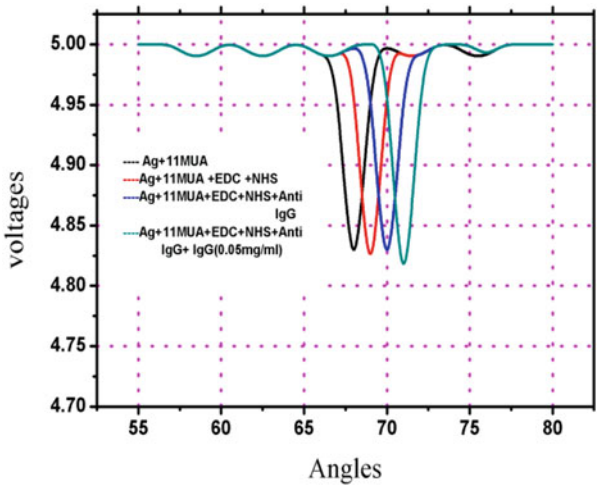

Fig. 2.9 SPR measurements on the stacking sandwich layers

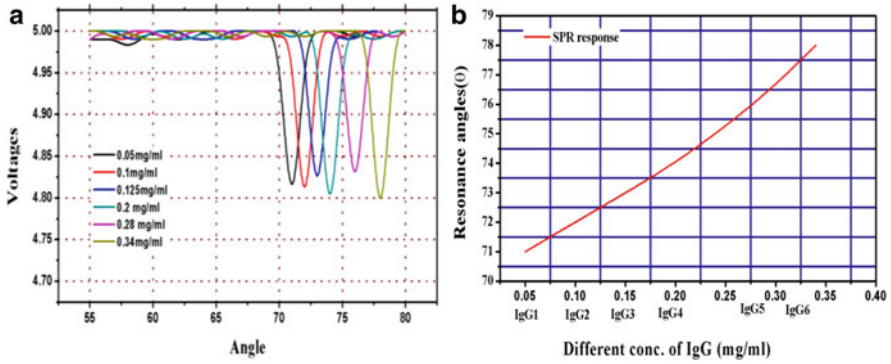

Fig. 2.10 (**a**, **b**) Experimentally measured SPR data with varied protein concentration

The SPR sensorgrams depicting association and dissociation for the sensor is shown in Fig. 2.11. The baseline was initially measured by flowing PBS through the monoclonal anti-IgG functionalized sensor surfaces for a period of 5 min. While the continuous flow of protein, the sensor signal reaches a maximum and the sensor is defined in the association phase during this period. A relatively low concentration (0.05 mg/mL) target protein is initially exposed to the sensor resulting in the shift of the resonance tip towards right. After 12 min when the injection of protein is stopped, the sensor slowly goes to a steady state (saturate) level. Later, the sensing signal returns to a value close to the one of baseline the during the dissociation phase when a stream of PBS is passed through the sensor surface. Subsequently, the cycle is repeated by increasing the concentration of the target protein that shows good repeatable behavior of the sensor.

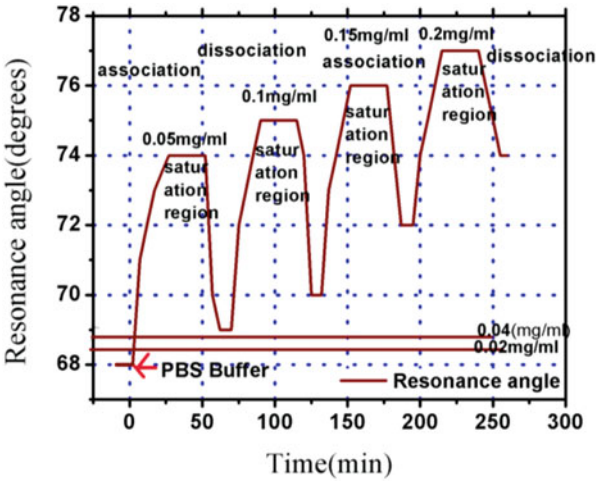

Fig. 2.11 SPR sensorgrams showing binding kinetic with protein IgG of different concentrations

2.7 Performance Characteristics of SPR-Based Sensing

The performance parameters of a SPR sensing device are generally investigated by: its sensitivity, accuracy of measurement and limit of detection. The SPR sensitivity with angular interrogation is defined as: $S = \delta\theta_{res}/\delta n_s$, where $\delta\theta_{res}$ is the resonance angle shift due to the refractive index change of the sensing medium by δn_s. Sensitivity enhancements with various methods such as the integration of plasmonic nanostructures coupled onto SPR chip [75], use of nanogratings [76] and graphene [77] have been reported. The characteristics of the SPR curve including its shape, full width at half maxima (FWHM), and position of the SPR resonance dip are of significant importance for sensing applications. A smaller value of FWHM implies a high signal-to-noise (S/N) ratio signifying better accuracy/resolution of measurements [78]. Figure-of-merit (FOM) is known as the ratio between sensitivity (S) and the FWHM. Various research groups also use it as a key parameter to evaluate sensing performance of SPR sensor. Uses of absentee layer, or high-refractive index thin dielectric layer, bimetallic layers were found suitable for FOM enhancement [79–81]. Limit of detection (LOD) is another key parameter and is usually termed as the minimum input quantity measured with higher than 99% fidelity. The LOD could be calculated by $3\in/S$, in which $\in$ is the uncertainty of output [82].

2.7.1 Choice of Metal for SPR Sensor

The choice of the metal layer and its film thickness has significant impact on the performance characteristics of the SPR sensor. Silver and gold are usually the preferred choices for the metal layer due to their unique properties such as the high

Table 2.2 Sample ID with specifications

Sample ID	Name of the metallic film	Thickness of film
I	Silver	50 nm
II	Gold	50 nm
III	Silver-Gold	35 nm (Silver) and 15 nm (Gold)

efficiency in the electron resonance at the conduction band for specific excitation wavelength, thermal/chemical stability, and ability to conjugate organic molecule for surface functionalization. It has been observed that silver film yields a more distinct SPR spectrum than gold. A thin film of silver with thickness around 50 nm produces a sharp SPR signal supporting precise determination of the resonance angle [83]. Gold on the other hand produces a larger shift of the resonance angle than that of silver for a fixed change of refractive index unit of the sensing layer, while it is much more stable in the ambient environment and more resistant to the oxidization [84]. However, a bimetallic film of silver-gold can combine the advantages of both materials thereby accounting for better SPR sensing. Zynio et al. were the first research group to propose bimetallic films of gold and silver. In their designed structures, gold was deposited on top of silver to for the excitation of SPR. It was reported that the bimetallic films displayed a large shift of resonance angle due to the changes of refractive index similar to gold thin films as well as showed a narrow resonance curve like silver, thereby leading to a high detection accuracy of measurements. In addition to it, the silver was protected against oxidation by the outer gold layer [85]. Yuan et al. also presented a bimetallic configuration of silver-gold. In their results, the obtained value of full width at half maximum (FWHM) with the bimetallic film was found to be much smaller than that of the pure gold film, while the stability of the bimetallic film was found to be better than that of the pure silver film [86]. In our recent study, we also emphasized on parameters such as full width at half maxima (FWHM) and sensitivity of a set of three bimetallic sensors are prepared by varying the metal film type and thickness [87]. The samples and their specifications are indicated the Table 2.2.

Figure 2.12 shows the SPR responses of the silver, bimetallic, and gold-based sensor chips towards three test samples (Water, Acetone and Butanol). The experimental results of FWHM obtained from the graphs in Fig. 2.12 are listed in Table 2.3. From the FWHM values it was seen that pure silver had the least FWHM due to its narrowest width of the curve, thus providing the highest resolution of detection of the resonance angle. In comparison, the width of the pure gold-based sensor chip is the largest among these three configurations. As far as the bimetallic sensor chip was investigated, it exhibited a small value of FWHM (approximately six times less than the pure gold-based sensor chip) indicating reasonably better detection resolution of the resonance angle. As mentioned above, the SPR sensitivity parameter is dependent on the value of the resonance dip (angular shifts) for a fixed refractive-index change of the surrounding sensing media. If the angular shift is a larger signal change, the SPR sensitivity is considered to be relatively higher.

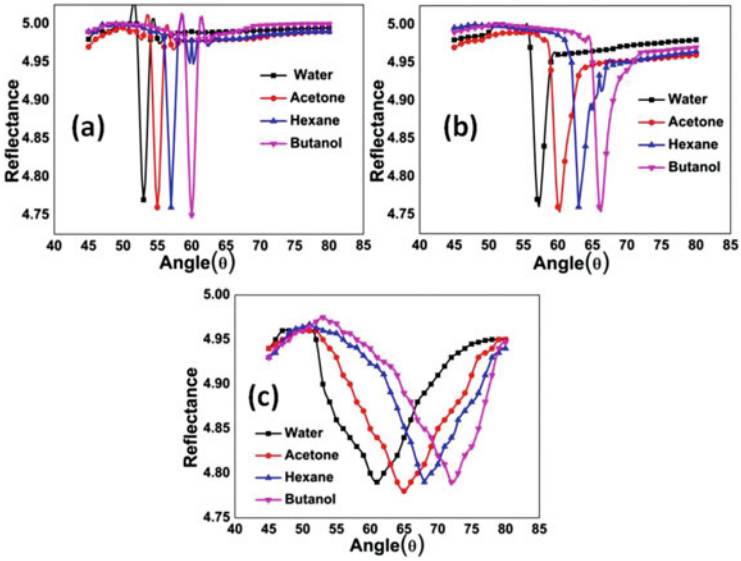

Fig. 2.12 SPR responses of the silver (**a**), bimetallic (**b**) and gold (**c**) sensor chip towards Water, Acetone, hexane and Butanol

Table 2.3 Experimental results of FWHM (in degrees) for different configurations

Test samples	Silver (degree)	Silver-gold (degree)	Gold (degree)
Water	1	2	12
Acetone	1	2.5	12
Hexane	1	2	11
Butanol	1	2	11

Table 2.4 Shift of the resonance angle due to change in refractive index of the sensing layer

	Shift in resonance angle (in degree) For sensor with		
Refractive index unit (RIU)	silver	Silver-gold	Gold
0.0261	2	3.5	4

Table 2.4 lists the experimental measurement results showing the signal change of the resonance dip angle (in degrees) due to the corresponding refractive index change of the sensing layer extracted from the graphs in Fig. 2.12.

2.7.2 *Sensitivity Enhancement with Graphene, MoS_2, and 2D Perovskite Nanolayers*

As introduced in the previous sections, plasmonic sensors are known as an efficient tool for real time monitoring biomolecular interactions. The detection mechanism is based on the field perturbation at the plasmonic sensing interface induced by the binding of molecules. This molecular binding process could be recorded through reflected light signal when the surface plasmon is excited by the incident light. In recent studies, we have presented the use of hybrid 2D nanomaterial-based metasurface nanostructures as a plasmonic sensing substrate. The thickness of the sensing substrate is tuned in an atomic scale and optimized to obtain an enhanced sensing effect. More specifically, a sharp phase signal change and phase-related Goos-Hänchen signal shift was achieved that results from the strong resonance. The improved sensitivities of 2D nanostructures were investigated. It is worth noting that the atomic layer design led to the sensing substrate optimized with a tuning scale less than 1 nm. By precisely design the metasurface substrates, more than 4 orders of magnitude improvement of the sensitivity (900,000 μm/RIU) were obtained in comparison to the one with pure gold sensing substrate (400 μm/RIU).

Figure 2.13 illustrates the configuration of our designed 2D graphene/MoS_2-enhanced plasmonic biosensors. A single layer of graphene is deposited on the top of the sensing substrate to capture the target biomolecules. The hexagonal carbon ring structure of graphene could enhance the adsorption rate of the analyte due to pi-stacking force. It is worth noting that monolayer hexagonal boron nitride (hBN, known as white graphene) could also be coated on the silver thin film to protect the

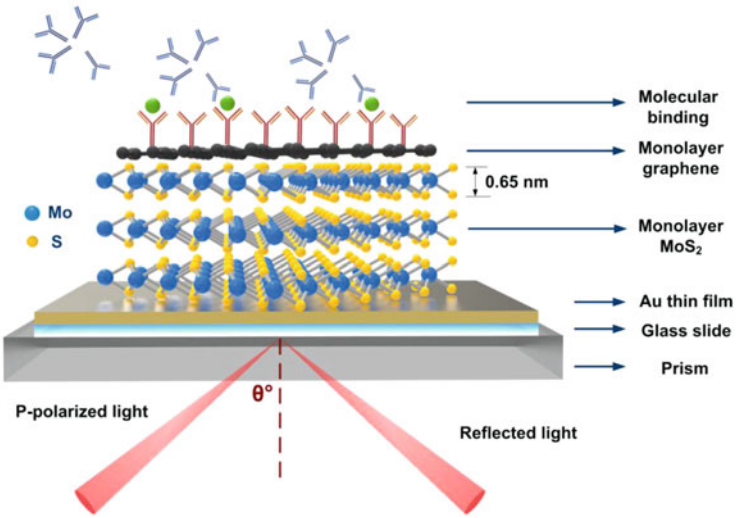

Fig. 2.13 Schematic configuration of the designed graphene/MoS_2 nanolayers on 45 nm gold sensing substrate for protein detection [88]

surface from oxidization during the detection process. It is known that under the similar resonance condition (e.g., excitation wavelength, thickness of metallic thin film, SF11 prism coupling), the silver thin film exhibited a better sensing performance with high sensitivity and high detection resolution than that of gold ones, in terms of a lower minimum reflectivity and narrower width of the reflectance spectra. Graphene is measure to be the thinnest two-dimensional nanomaterial so far in the world. Since its first report in 2004 by Andre Geim and Kostya Novoselov, their unique optical and electronic properties have been demonstrated such as its zero bandgap with high electrical conductivity, and zero effective mass at the Dirac point. The high charge carrier mobility of graphene up to 10^6 cm^2 V^{-1} s^{-1} makes it an attractive candidate for the next generation of substrate for SPR sensors. By designed the graphene layers on the gold or silver SPR sensor head, strong electric field enhancement at the hybrid interface would be generated through an effective charge transfer process. The drastic concentration of plasmon electric field in this 2D plane provides a novel sensing functionality and makes it fit to the definition of "metasurfaces." In our recent studies, we have demonstrated an ultrasensitive graphene-based surface plasmon resonance sensing device with a detection limit as low as attomolar 1 aM (10^{-18} M) for target single-stranded DNA (ssDNA) analytes as shown in Fig. 2.14 was demonstrated by our group [89].

2.8 Summary and Outlook

Two-dimensional (2D) transition metal dichalcogenides (TMDCs) nanolayers have become intriguing to the SPR community and showed their potential to improve the performances of different optoelectronic devices such as solar cells and photo detection arrays [90–93]. It is worth noting that absorption rate (~5%) is the much higher for TMDC nanomaterials than that of monolayer graphene (2.3%). The thickness is also with the atomic thickness range. 2D TMDCs showed a tunable bandgap characteristic that is different from that of graphene. Their bandgaps could be tuned from indirect to the direct ones when their thicknesses are down to the nanoscale. This feature promises them to be complementary with graphene for the design of next-generation integrated flexible optoelectronic devices. The physical structure of TMDCs nanomaterials are similar to the graphene in which the metal atom M and the chalcogen atoms X were bonded in a hexagonal plane. As of the TMDC in the bulk forms, the stacking of each layer was achieved by van der Waals forces. Thus, monolayer TMDC can be obtained by exfoliation. Up to date, the atomic thin TMDC with large size have been fabricated through vapor deposition growth. To achieve multiple layer substrates, one could transfer the single layer and repeatedly stack them on the target sensing substrate. Several research groups have reported that depositing a thin layer of dielectric materials could significantly vary the SPR resonance condition and thus may facilitate on the integration process of the current prism-based plasmonic sensors [94, 95]. The fabrication of atomically thin 2D nanomaterials has been reported in recent literatures [90–93]. There are different

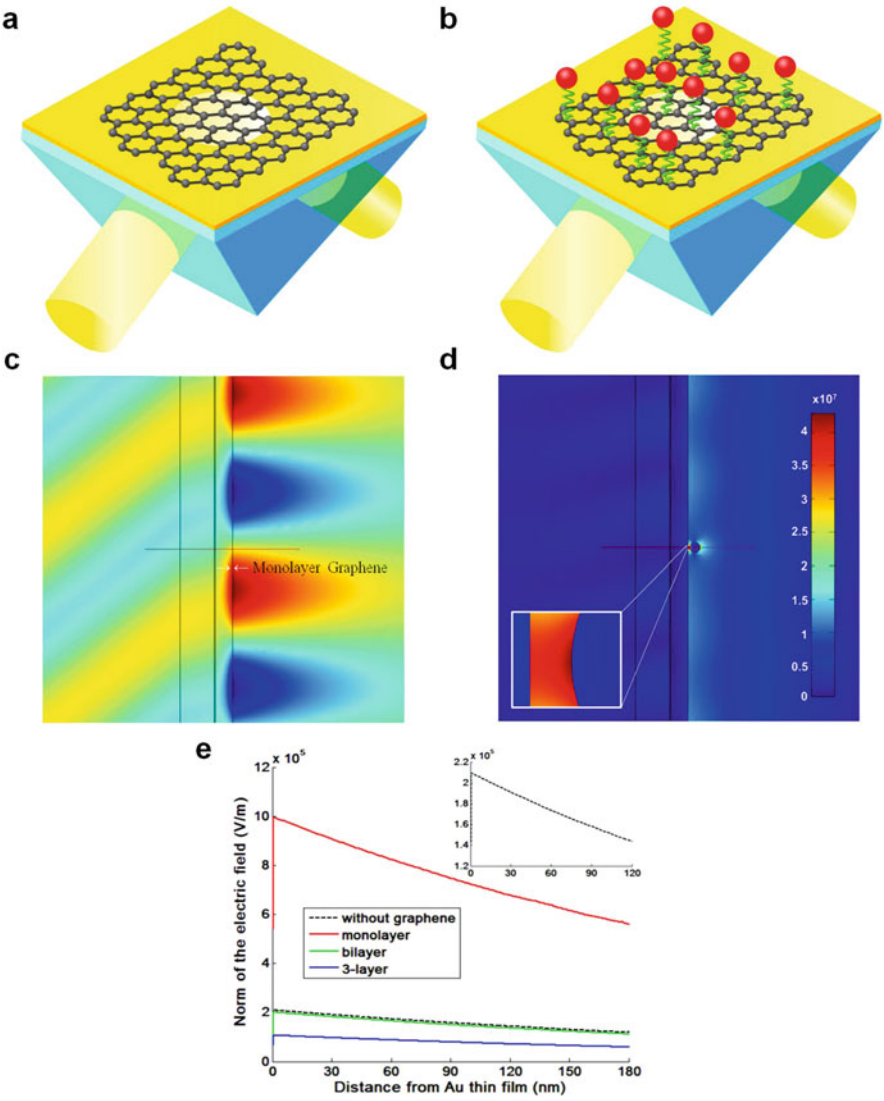

Fig. 2.14 (**a**–**e**) Designs and sensing results of graphene–gold metasurface architectures [89]

types of TMDC materials including MoS_2, $MoSe_2$, WS_2, and WSe_2, which depend on the combination of its metal and chalcogen elements. The presence of 2D TMDC metasurface layers could enhance the transmission loss, which provides stronger surface plasmon resonance.

In addition to the novel 2D nanomaterials as enhanced sensing substrate, the SPR detection schemes could also be step into the next generation instead of the traditional angular and wavelength scanning method. Since Surface plasmon resonance

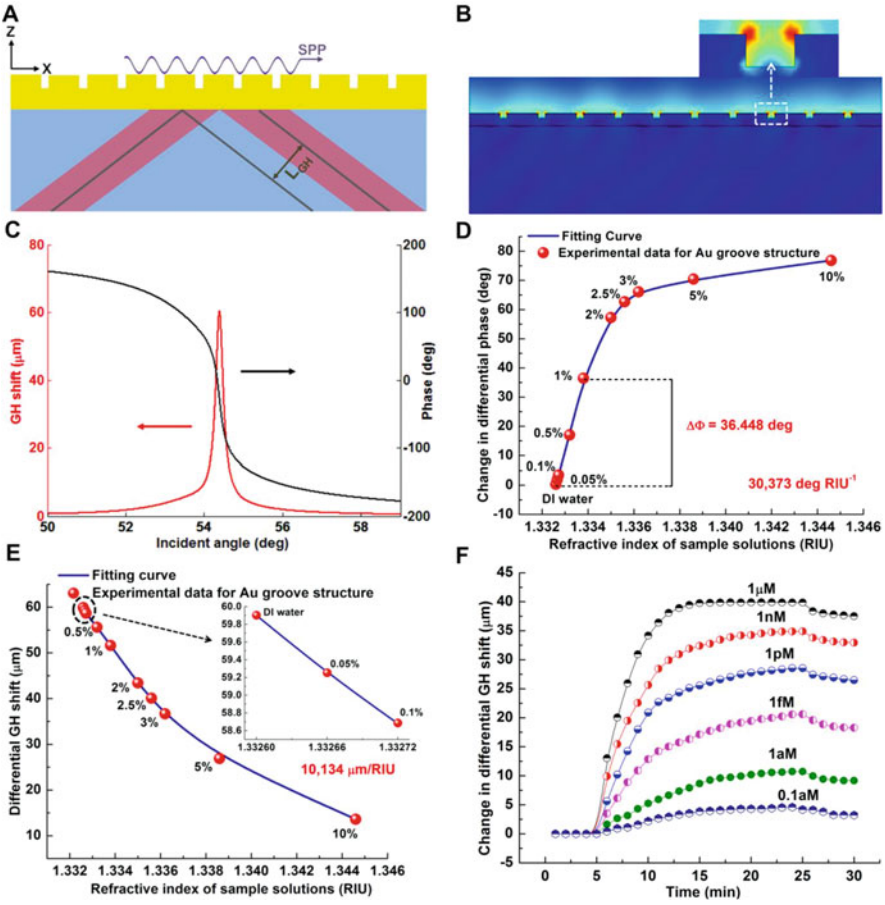

Fig. 2.15 (**a**–**f**) Phase-sensitive and Goos-Hänchen (GH)-sensitive plasmonic sensing platform based on the groove metasurface structures [96]

(SPR) only affects p-polarized light, which is parallel to the propagation direction. Therefore s-polarized light can be used as a reference signal. Based on this mechanism, we could extract the differential signal between the two polarized light beams from the reflected side simultaneously. The environmental noise and the stability of the setup can be significantly improved during experimental measurement. The signals that we collect are phase-related Goos-Hänchen signals reflected from the sensing substrate, which is a lateral position shift of the light beams at the sensing interface. The GH detection is different from the angular measurement of the conventional method, which suffers from the loss of the metallic and graphene materials. The phase and GH jumps are only corresponding to the dip value of the SPR reflectance curves. With gold nanoarray in Fig. 2.15, the field coupling of localized SPR and SPP waves would further improve the detection sensitivity. As the concentration of sensing medium increases, groove metasurface-based SPR

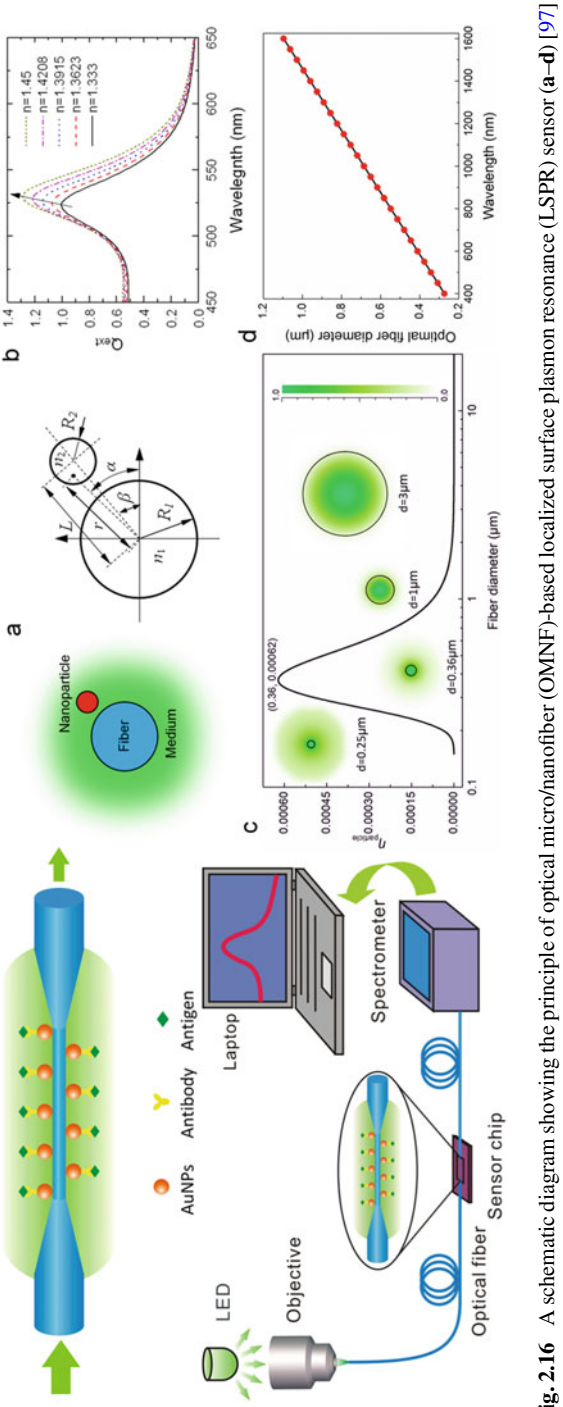

Fig. 2.16 A schematic diagram showing the principle of optical micro/nanofiber (OMNF)-based localized surface plasmon resonance (LSPR) sensor (**a**–**d**) [97]

sensor undergoes larger GH signal shift. Integration of fiber-device based on nanostructure-metasurface (e.g. transverse Anderson localization and Fano resonance) for enhanced plasmonic sensing and image transport is another future trend for the development of portable SPR biomedical devices. One of the highlights is our study [97] on the integration of functional gold nanoparticles with optical micro/nanofibers (OMNFs) as a versatile platform for sensing of streptavidin biomolecules with a low detection of 1 pg/mL in Fig. 2.16.

References

1. Wood RW. On a remarkable case of uneven distribution of light in a diffraction grating spectrum. Phil Mag. 1902;4:396–402.
2. Otto A. Excitation of nonradiative surface plasma waves in silver by the method of frustrated total reflection. Z Phys. 1968;216:398–410.
3. Kretschmann E, Reather H. Radiative decay of non-radiative surface plasmons excited by light. Z Naturforsch. 1968;23:2135–6.
4. Zenneck J. Uber die Fortpflanztmg ebener elektro-magnetischer Wellen langs einer ebenen Leiterflache und ihre Beziehung zur drahtlosen Telegraphie. Annals der Physik. 1907;23:846–66.
5. Ritchie RH. Plasma losses by fast electrons in thin films. Phys Rev. 1957;106:874–81.
6. Powell CJ, Swan JB. Effect of oxidation on the characteristic loss spectra of aluminum and magnesium. Phys Rev. 1960;118:640–3.
7. Stern EA, Ferrell RA. Surface plasma oscillations of a degenerate electron gas. Phys Rev. 1960;120:130–6.
8. Pockrand I, Swalen JD, Gordon JG, Phllpott MR. Surface plasmon spectroscopy of organic monolayer assemblies. Surf Sci. 1977;74:237–44.
9. Wahling G. Arachldate layers on Ag and Au substrates detected by the ATR method. Z Nuturforsch. 1978;33a:536–9.
10. Nylander C, Liedberg B, Lind T. Gas detection by means of surface plasmons resonance. Sensors Actuators. 1982;3:79–88.
11. Liedberg B, Nylander C, Lundstrom I. Surface plasmons resonance for gas detection and biosensing. Sensors Actuators. 1983;4:299–304.
12. Lijie H, Quentin P, Iban L, Aritz YS, Amaia P, Amaia Z, Daniel M, Rabah B, Sabina S. Label-free femtomolar cancer biomarker detection in human serum using grapheme coated surface plasmon resonance chip. Biosens Bioelectron. 2017;89:606.
13. Mauriz E, Calle A, Manclus JJ, Montoya A, Lechuga LM. Multi-analyte SPR immunoassays for environmental biosensing of pesticides. Anal Bioanal Chem. 2012;387:1449–58.
14. Li Y, Liu X, Lin Z. Recent developments and applications of surface plasmon resonance biosensors for the detection of mycotoxins in foodstuffs. Food Chem. 2012;132:1549–54.
15. Seo M, Lee J, Lee M. Grating-coupled surface plasmon resonance on bulk stainless steel. Opt Express. 2017;25(22):26941.
16. Bremer K, Roth B. Fibre optic surface plasmon resonance sensor system designed for smartphones. Opt Express. 2015;23:17179.
17. Sharma AK, Jha R, Gupta BD. Fiber-optic sensors based on surface plasmon resonance: a comprehensive review. IEEE Sensors J. 2007;7(8):1118–29.
18. Chandra S, Bharadwaj R, Mukherjia S. Label free ultrasensitive optical sensor decorated with polyaniline nanofibers: characterization and immunosensing application. Sensors Actuators B Chem. 2017;240:443–50.

19. Dorozinska H, Lyapin O, Dorozinsky G, Maslov V. Current trends in technology and materials of sensors based on surface plasmon resonance. Adv Mater Sci Eng. 2018;2:1.
20. Ouyang Q, Zeng S, Jiang L, Junle Q, Dinh X-Q, Qian J, He S, Coquet P, Yong K-T. Two-dimensional transition metal dichalcogenide enhanced phase-sensitive plasmonic biosensors: theoretical insight. J Phys Chem C. 2017;121(11):6282–9.
21. Jiang L, Zeng S, Ouyang Q, Dinh XQ, Coquet P, Qu J, He S, Yong KT. Graphene-TMDC-graphene hybrid plasmonic metasurface for enhanced biosensing: a theoretical analysis. Phys Stat Solid A Appl Mater Sci. 2017;214:1–15.
22. Gerardo A, Lopez M-CE, Solera M, Lechuga LM. Recent advances in nanoplasmonic biosensors: applications and lab-on-a-chip integration. Nanophotonics. 2017;6(1):123–36.
23. Homola J. Present and future of surface plasmon resonance biosensorm. Anal Bioanal Chem. 2003;277:528–39.
24. Melo EF, Fontana E. Optimization of metal gratings for SPR sensing applications. In: SBMO/IEEE MTT-S International Microwave and Optoelectronics Conference (IMOC 2011); 2011.
25. Fontana E. Theoretical and experimental study of the surface plasmon resonance effect on a recordable compact disk. Opt Soc Am. 2004;43(1):79.
26. Lee J-S, Huynh T, Lee S-Y, Lee K-G, Lee J, Tame M, Rockstuhl C, Lee C. Quantum noise reduction in intensity-sensitive surface-plasmon-resonance sensors. Phys Rev A. 2017;96:033833.
27. Hong DG, Kim TW, Kim KB, Yuk JS, Ha KS. Development of an immunosensor with angular interrogation-based SPR spectroscopy. Meas Sci Technol. 2007;18:1367–71.
28. Zhang Z, Lu D-f, Liu Q, Qi Z-m, Yang L, Liu J. Wavelength-interrogated surface plasmon resonance sensor with mesoporous-silica-film-enhanced sensitivity to small molecules. Analyst. 2012;137:4822.
29. Deng S, Wang P, Yu X. Phase-sensitive surface plasmon resonance sensors: recent progress and future prospects. Sensors. 2017;17:2819.
30. Miyazaki CM, Shimizu FM, Ferreira M. 6 - Surface plasmon resonance (SPR) for sensors and biosensors. In: Nanocharacterization techniques, micro and nano technologies. Cambridge, MA: William Andrew; 2017. p. 183–200.
31. Hong LH, Yahaya A, Munajat Y. Simulation of surface plasmon resonance sensor. AIP Conf Proc. 2015;1674:020015.
32. Filion-Côté S, Roche PJR, Foudeh AM, Tabrizian M, Kirk AG. Design and analysis of a spectro-angular surface plasmon resonance biosensor operating in the visible spectrum. Rev Sci Instrum. 2014;85:093107.
33. Homola J. Surface plasmon resonance sensors for detection of chemical and biological species. Chem Rev. 2008;108:462–93.
34. Yokoyama K, Oishi M, Oshima M. Development of an enhanced surface plasmon resonance sensor substrate by investigating a periodic nanohole array configuration. J Appl Phys. 2015;118:023101.
35. Boruah R, Mohanta D, Choudhury A, Nath P, Ahmed GA. Surface plasmon resonance-based protein bio-sensing using a Krestschmann configured double prism arrangement. IEEE Sensors J. 2015;15:6791–6.
36. Fen YW, Yunus WMM, Talib ZA, Yusof NA. Development of surface plasmon resonance sensor for determining zinc ion using novel active nanolayers as probe. Spectrochem Acta A Mol Biomol Spectrosc. 2015;134:48–52.
37. Sim HR, Wark AW, Lee HJ. Attomolar detection of protein biomarkers using biofunctionalized gold nanorods with surface plasmon resonance. Analyst. 2010;135:2528–32.
38. Wang Y, Knoll W, Dostalek J. Bacterial pathogen surface plasmon resonance biosensor advanced by long range surface plasmons and magnetic nanoparticle assays. Anal Chem. 2012;84(19):8345–50.
39. Yu Q, Wang Q, Li B, Lin Q, Duan Y. Technological development of antibody immobilization for optical immunoassays: progress and prospects. Crit Rev Anal Chem. 2015;45:62–75.

40. Kausaite-Minkstimiene A, Ramanaviciene A, Kirlyte J, Ramanavicius A. Comparative study of random and oriented antibody immobilization techniques on the binding capacity of immunosensor. Anal Chem. 2010;82:6401–8.
41. Welch NG, Scoble JA, Muir BW, Pigram PJ. Orientation and characterization of immobilized antibodies for improved immunoassays (Review). Biointerphases. 2017;12:02D301.
42. Lee JM, Park HK, Jung Y, Kim JK, Jung SO, Chung BH. Direct immobilization of protein G variants with various numbers of cysteine residues on a gold surface. Anal Chem. 2007;79:2680–7.
43. Lee JE, Seo JH, Kim CS, Kwon Y, Ha JH, Choi SS, Cha HJ. A comparative study on antibody immobilization strategies onto solid surface. Korean J Chem Eng. 2013;30(10):1934–8.
44. Tomizaki K, Usui K, Mihara H. ChemBioChem. 2005;6:782–99.
45. Ma X-X, Liu H-Z, Tang J-J, Guo L, Xie J-W. Comparison of three enzyme-linked immunosorbent assay methods for quantitative determination of ricin. Chin J Anal Chem. 2011;39:685–9.
46. Rusmini F, Zhong Z, Feijen J. Protein immobilization strategies for protein biochips. Biomacromolecules. 2007;8:1775–89.
47. Sanchez JLA, Fragoso A, Joda H, Suarez G, McNeil CJ, O'Sullivan CK. Anal Bioanal Chem. 2016;408:5337.
48. Uchida K, Otsuka H, Kaneko M, Kataoka K, Nagasaki Y. Anal Chem. 2005;77:1075–80.
49. O'Dwyer C, Gay G, Viaris de Lesegno B, Weiner J. The nature of alkanethiol self-assembled monolayer adsorption on sputtered gold substrates. Langmuir. 2004;20:8172–82.
50. Stettner J, Winkler A. Characterization of alkanethiol self-assembled monolayers on gold by thermal desorption spectroscopy. Langmuir. 2010;26(12):9659–65.
51. Czanderna AW, King D, Spaulding D. J Vac Sci Technol A. 1991;9:2607.
52. Frey BL, Corn RM. Anal Chem. 1996;68:3187.
53. Duevel RV, Corn RM. Anal Chem. 1992;64:337.
54. Lebec V, Boujday S, Poleunis C, Pradier CM, Delcorte A. J Phys Chem C. 2014;118:2085.
55. Choudhury SN, Konwar B, Kaur S, Doley R, Mondal B. Study on snake venom protein-antibody interaction by surface plasmon resonance spectroscopy. Photon Sensors. 2018;8 (3):193–202.
56. Yam CM, Deluge M, Tang D, Kumar A, Cai CJ. Colloid Interface Sci. 2006;296:118–30.
57. Goddard JM, Hotchkiss JH. Prog Polym Sci. 2007;32:698.
58. Fernandez-Lafuente R, Rosell CM, Rodriguez V, Santana C, Soler G, Bastida A, Guisan GM. Enzyme Microb Technol. 1993;15:546–50.
59. Viitala T, Vikholm I, Peltonen J. Langmuir. 2000;16:4953–61.
60. Trilling AK, Beekwilder J, Zuilhof H. Analyst. 2013;138:1619.
61. Sharma H, Mutharasan R. Anal Chem. 2013;85:2472.
62. Qian W, Xu B, Yao D, Lin Y, Wu L, Wang C, Yu F, Lu Z, Wei Y. Site-directed immobilization of immunoglobulin G on 3-aminopropyltriethoxylsilane modified silicon wafer surfaces. Mater Sci Eng C. 1999;8:475–80.
63. Staros JV, Wright RW, Swingle DM. Enhancement by N-hydroxysulfosuccinimide of water-soluble carbodiimide-mediated coupling reactions. Anal Biochem. 1986;156:220–2.
64. Thermo Scientific crosslinking technical handbook.
65. Konwar B. Fabrication of surface plasmon resonance biosensor for snake venom protein detection. Dissertation, Department of ECE, Tezpur University; 2017.
66. Swarnakar S. Fabrication of surface plasmon resonance biochip to study interaction of IgG with monoclonal anti IgG. Dissertation, Department of ECE, Tezpur University; 2018.
67. Zhao X, Cai Y, Wang T, Shi Y, Jiang G. Preparation of alkanethiolate-functionalized core/shell Fe_3O_4@Au nanoparticles and its interaction with several typical target molecules. Anal Chem. 2008;80:9091–6.
68. Amoli BM, Gumfekar S, Hu A, Zhou YN, Zhao B. Thiocarboxylate functionalization of silver nanoparticles: effect of chain length on the electrical conductivity of nanoparticles and their polymer composites. J Mater Chem. 2012;22(37):20048–56.

69. Goormaghtigh E, Ruysschaert JM, Raussens V. Evaluation of the information content in infrared spectra for protein secondary structure determination. Biophys J. 2006;90(8):2946–57.
70. Mukherji S, Hussain MI, Kundu T, Chandratre D. Development of a surface plasmon resonance based biosensing system. In: Vinoy KJ, et al., editors. Micro and smart devices and systems. New Delhi: Springer; 2014. p. 49–72.
71. Chakraborty S. Development of surface plasmon resonance based portable refractometer. Dissertation, Department of ECE, Tezpur University; 2018.
72. Piliarik M, Vala M, Tichý I, Homola J. Compact and low-cost biosensor based on novel approach to spectroscopy of surface plasmons. Biosens Bioelectron. 2009;24:3430–5.
73. Fernández F, Hegnerová K, Piliarik M, Sanchez-Baezaa F, Homola J, Marco MP. A label-free and portable multichannel surface plasmon resonance immunosensor for on-site analysis of antibiotics in milk samples. Biosens Bioelectron. 2010;26:1231–8.
74. Liu Y, Chen S, Liu Q, Masson J-F, Peng W. Compact multi-channel surface plasmon resonance sensor for real-time multi-analyte bio-sensing. Opt Express. 2015;23:20540–8.
75. Zeng S, Baillargeat D, Ho H-P, Yong K-T. Nanomaterials enhanced surface plasmon resonance for biological and chemical sensing applications. Chem Soc Rev. 2014;43:3426–52.
76. Jang YH, Chung K, Quan LN, Špačková B, Šípová H, Moon S, Cho WJ, Shin H-Y, Jang YJ, Lee J-E. Configuration-controlled Au nanocluster arrays on inverse micelle nano-patterns: versatile platforms for SERS and SPR sensors. Nanoscale. 2013;5:12261–71.
77. Yang C-T, Wu L, Liu X, Tran NT, Bai P, Liedberg B, Wang Y, Thierry B. Exploiting surface-plasmon-enhanced light scattering for the design of ultrasensitive biosensing modality. Anal Chem. 2016;88(23):11924–30.
78. Jiang Y-X, Liu B-H, Zhu X-S, Tang X-L, Shi Y-W. Long-range surface plasmon resonance sensor based on dielectric/silver coated hollow fiber with enhanced figure of merit. Opt Lett. 2015;40:744–7.
79. Chen Z, Zhao X, Lin C, Chen S, Liang Y, Ding Y. Figure of merit enhancement of surface plasmon resonance sensors using absentee layer. Appl Opt. 2016;55:6832–5.
80. Shalabney A, Abdulhalim I. Figure-of-merit enhancement of surface plasmon resonance sensors in the spectral interrogation. Opt Lett. 2012;37:1175–7.
81. Jha R, Sharma AK. High-performance sensor based on surface plasmon resonance with chalcogenide prism and aluminum for detection in infrared. Opt Lett. 2009;34:749–51.
82. Guider R, Gandolfi D, Chalyan T, Pasquardini L, Samusenko A, Pederzolli C, Pucker G, Pavesi L. Sensitivity and limit of detection of biosensors based on ring resonators. Sens Bio-Sens Res. 2015;6:99–102.
83. Nelson SG, Johnston KS, Yee SS. High sensitivity surface plasmon resonance sensor based on phase detection. Sensors Actuators B Chem. 1996;35(1-3):187–91.
84. Chen X, Jiang K. Effect of aging on optical properties of bimetallic sensor chips. Opt Soc Am. 2010;18(2):1105–12.
85. Zynio SA, Samoylov AV, Surovtseva ER, Mirsky VM, Shirshov YM. Bimetallic layers increase sensitivity of affinity sensors based on surface plasmon resonance. Sensors. 2002;2 (2):62–70.
86. Yuan X-C, Ong BH, Tan YG, Zhang DW, Irawan R, Tjin SC. Sensitivity–stability - optimized surface plasmon resonance sensing with double metal layers. J Opt A Pure Appl Opt. 2006;8 (11):959–63.
87. Kashyup R, Chakraborty S, Swarnikar S, Humbert G, Zeng S, Mondal B. FWHM and sensitivity study of bimetallic SPR sensor chip. In: 2019 IEEE International Conference on Electrical, Computer and Communication Technologies (IEEE ICECCT 2019). Washington, DC: IEEE; 2019.
88. Zeng S, Hu SY, Xia J, Anderson T, Dinh XQ, Meng XM, Coquet P, Yong KT. Graphene-MoS2 hybrid nanostructures enhanced surface plasmon resonance biosensors. Sens Actuat B Chem. 2015;207:801–10.

89. Zeng S, Sreekanth KV, Shang JZ, Yu T, Chen CK, Yin F, Baillargeat D, Coquet P, Ho HP, Kabashin AV, Yong KT. Graphene-gold metasurface architectures for ultrasensitive plasmonic biosensing. Adv Mater. 2015;27(40):6163–9.
90. Novoselov KS, Mishchenko A, Carvalho A, Castro Neto AH. 2D materials and van der Waals heterostructures. Science. 2016;353(6298):aac9439.
91. Azizi A, Eichfeld S, Geschwind G, Zhang K, Jiang B, Mukherjee D, Hossain L, Piasecki AF, Kabius B, Robinson JA, Alem N. Freestanding van der Waals Heterostructures of graphene and transition metal dichalcogenides. ACS Nano. 2015;9(5):4882–90.
92. Ouyang Q, Zeng S, Jiang L, Hong L, Xu G, Dinh X-Q, Qian J, He S, Qu J, Coquet P, Yong K-T. Sensitivity enhancement of transition metal dichalcogenides/silicon nanostructure-based surface plasmon resonance biosensor. Sci Rep. 2016;6:28190.
93. Britnell L, Ribeiro RM, Eckmann A, Jalil R, Belle BD, Mishchenko A, Kim YJ, Gorbachev RV, Georgiou T, Morozov SV, Grigorenko AN, Geim AK, Casiraghi C, Neto AHC, Novoselov KS. Strong light-matter interactions in heterostructures of atomically thin films. Science. 2013;340(6138):1311.
94. Bahauddin SM, Robatjazi H, Thomann I. Broadband absorption engineering to enhance light absorption in monolayer MoS_2. ACS Photon. 2016;3(5):853–62.
95. Mishra AK, Mishra SK, Verma RK. Graphene and beyond graphene MoS2: a new window in surface-plasmon-resonance-based fiber optic sensing. J Phys Chem C. 2016;120:2893–900.
96. Jiang L, Zeng S, Xu Z, Ouyang Q, Zhang D-H, Chong PHJ, Coquet P, He S, Yong K-T. Multifunctional hyperbolic nanogroove metasurface for submolecular detection. Small. 2017;13(30):1700600.
97. Li K, Zhou W, Zeng S. Optical micro/nanofiber-based localized surface plasmon resonance biosensors: fiber diameter dependence. Sensors. 2018;18(10):3295.

Chapter 3
Surface-Enhanced Raman Scattering for Detection in Biology and Medicine

Jie Sun, Chenyan Pan, and Jian Dong

Abstract Raman and surface-enhanced Raman scattering (SERS) were introduced briefly, and shortcoming and detection strategies of the application of SERS for detection in biology and medicine were summarized. SERS detection of redox state was used as an example to introduce the detection strategies in cell, surface of tissues, superficial layer of tissues, and deep tissues in biology and medicine.

Keywords Raman · SERS · Redox detection · In vitro analysis · In vivo analysis

3.1 Introduction

The various spectroscopies have been employed in biology and medicine. The optical properties of molecules or their derivatives provide qualitative or quantitative information. Raman scattering is a vibrational spectrum of molecules, which was widely used to provide chemical and physical information of molecules. As an analytical tool for detection in biology and medicine, Raman-related techniques have many advantages. The most important advantage is that the biological samples do not need a step of pretreatment and can be examined in their native states, by which the collected spectra can provide real information of the molecules or their native. Thus, the techniques are widely introduced into the researches in biology and medicine, which have provided effective solutions to solve various challenging analytical problems.

J. Sun · C. Pan · J. Dong (✉)
State Key Laboratory of Bioelectronics, School of Biological Science and Medical Engineering, Southeast University, Nanjing, China
e-mail: dongjian@seu.edu.cn

X. Zhao, M. Lu (eds.), *Nanophotonics in Biomedical Engineering*,
https://doi.org/10.1007/978-981-15-6137-5_3

3.1.1 Raman Scattering

The inelastic scattering of light was first proposed by Smekal in 1923 and first observed experimentally in 1928 by Raman and Krishnan. Since then, the phenomenon was named after Raman. When light interacts with molecules, the photons would be absorbed or scattered. If the energy of the scattered photon was equal to that of the incident photon, the scattered event was elastic scattering, or Rayleigh scattering, and if the energy of the scattered photon was lower or higher than that of the incident photon, the scattered event, inelastic scattering, was stocks scattering or anti-stocks scattering, and also called Raman scattering. The Raman scattering is a fingerprinting characteristic spectrum, and each molecule has its specific Raman scattering spectrum. But most of the scattered events are Rayleigh scattering, and only one in a million or less is Raman scattering.

Both infrared and Raman spectra are vibrational spectra of molecules, but the interactions between the photon and molecules are different. In infrared spectroscopy, the photons with energies covering a wide range interact with molecules, and part photons are absorbed specifically by the molecule. The infrared spectrum is absorbance light. In Raman spectroscopy, the photons with a single energy are used to interact with molecules, and only very few proportions of the photons are scattered inelastically. The change of the scattered photons in energy is specific for a molecule. The Raman spectrum is the inelastically scattered light.

3.1.2 The Development of Surface-Enhanced Raman Scattering (SERS)

Due to the weak normal Raman signal, since the phenomenon of Raman scattering was found, it has been a challenge to collect strong Raman signal. In the 1960s, the use of laser, instead of mercury lamp, made it easier. In the 1970s, SERS phenomenon was discovered accidentally on rough silver electrode surface, and the collected Raman signal was six orders of magnitude higher than a normal Raman signal. Since then, more and more work has been focused on the pursuit of fabricating SERS substrates with high enhancement factors in material fields. First, rough substrates of coin metals, such as Au, Ag, and Cu, were used. Then, coin metal nanoparticles were fabricated as novel SERS substrates. It is easy to control their shape and size, which strongly affect the enhancement effect of the nanoparticles. These nanoparticles can be used to further assemble advanced materials. Aggregated nanoparticles always provide higher enhancement effect than an isolated nanoparticle. Coupling effects (hotspot) among them were proposed to explain the greatly SERS intensity. Constructing dimers based on various strategies has attracted many attentions to form hotspots. In previous reports on dimers, the field strength in the “hotspot” can reach $\sim 10^{14}$ or more.

There are two different theories to explain the enhancement effect of the surface of metal. One is called electromagnetic enhancement, in which the molecule is adsorbed onto or close to the metal surface, and an interaction occurs between the molecule and the plasmons of free electrons resonated with the incident light. The enhancement effect of electromagnetic enhancement is about 10^4, which decreases with the increase of the distance between molecule and particle. It is important to match the wavelength of incident light, the peak of plasmon resonance of SERS substrates, and the absorbance peak of the molecule. For detection of biomolecules, since the absorbance peak of biomolecules is always located in the ultraviolet region, it is common to adjust the peak of plasmon resonance of metal nanoparticles to match the wavelength of incident light. The other is charge transfer or chemical enhancement, in which the molecule chemically bonds to the metal surface. The enhancement effect of chemical enhancement is about 10^2. In detection, the molecules chemically attached on particle have higher Raman signal. Thus, only the first layer has chemical enhancement and electromagnetic enhancement, whereas a second and subsequent layers have electromagnetic enhancement. About the real mechanism of enhancement effect, there are still other different explanations.

3.2 SERS for Detection in Biology and Medicine

It is critical for researches and applications of biology and medicine to detect biological processes. In addition, the specific detection of metabolites contributes to a better understanding of biological processes and has a huge impact on disease diagnosis and treatment. Therefore, it is essential to develop effective methods for specifically detecting metabolites or biological processes in complex biological samples. As a fast and powerful tool for fingerprint characterization, SERS has advantages over fluorescence methods due to its non-destructiveness and sensitivity [1–3]. Due to these significant advantages, SERS has been developed for detection in many biological fields.

In general, the biological applications of SERS include direct detection and indirect detection. The direct detection is to directly detect SERS spectra of the biological samples, the Raman signals of which were magnified by adding them on SERS substrates. The indirect detection refers to the use of probes or substrates labeled with Raman signal molecules to reflect the occurrence of molecules.

The SERS studies depend to a certain extent on the nature of the selected SERS substrate. Therefore, a brief introduction to the SERS substrate was provided before introducing SERS for detection in biology and medicine. In general, the SERS substrate consists of the noble metal nanomaterials with strong signal enhancement effects and repeatability. In addition, for indirect detection, it is required to improve stability, biocompatibility, and targeting of SERS substrates. Although not all components are required for a given SERS research, the properties of noble metal nanomaterials are critical in different SERS applications.

3.2.1 *Direct SERS Detection in Biology and Medicine*

In this section, the SERS substrates were directly used for the analysis of molecules of cells or tissues. In this way, the living cells or tissues could be identified and investigated according to obtained SERS signals. S. Mahajan et al. successfully used SERS and gold nanoparticle (AuNP) pulse depletion to realize the differentiation of nanoparticles into different endocytic pathways (Fig. 3.1) [4]. In their research, the Raman spectra of the cells at different stages of endocytosis of AuNPs in them were collected, and the obtained SERS data were analyzed by developing a suitable methodology of reference-based principal component analysis-linear discriminant analysis. Their method was validated and exemplarily used to extract spectral features characteristic of the endocytic compartment inside cells, which can characterize intracellular components. The developed analytical approach was generic and enabled the application of reporter-free SERS to identify unknown components in different biological matrices and materials.

Bone marrow mesenchymal stem cells (BMSCs) are multipotent stem cells, which play an important role in the repair of bone injury, angiogenesis, immune diseases, cancer invasion, and metastasis. Therefore, increasing attention has been

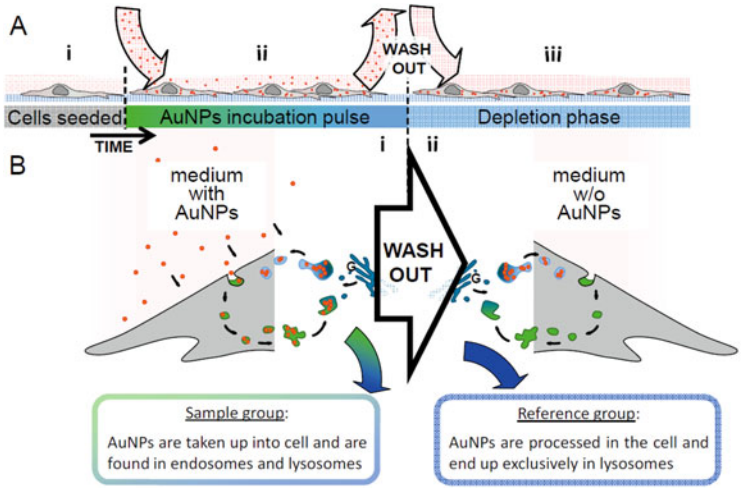

Fig. 3.1 Schematic of experimental design. (**a**) Full experimental procedure involves AuNPs (red spheres) being added to the cell culture environment after (**a**.i) cells have sufficiently attached to the culture dish. (**a**.ii) Following uptake of the particles into the cell via endocytosis during the incubation pulse, extracellular particles were washed out. (**a**.iii) Fresh culture medium without AuNPs was added, and the cells were left until incorporated particles were processed into lysosomes (depletion phase). (**b**.i) During the incubation phase, cells constantly internalize AuNPs, which accumulate inside endosomes (green vesicles) and lysosomes (blue vesicles). Their acquired SERS map data serves as the sample group for analysis. (**b**.ii) Following the wash-out, vesicular AuNPs are processed along the endo-lysosomal pathway and are eventually found exclusively in lysosomes. SERS maps of fixed cells with only lysosomal AuNPs serve as the reference group for the data analysis. Golgi apparatus (G) [4]

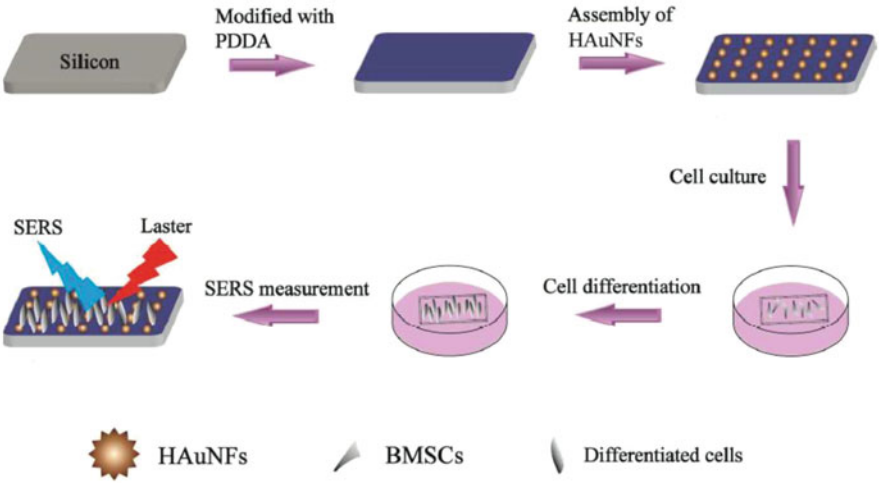

Fig. 3.2 Schematic diagram of the procedures for the preparation of the HAuNF substrates and the SERS identification and discrimination of BMSC differentiation [5]

focused on the study of BMSCs. However, the identification and discrimination of the undifferentiated and differentiated BMSCs, which are closely related and morphologically similar, is still a challenge by traditional methods. Through the assembly of the hollow gold nanoflower substrate and the use of the difference spectrum analysis method, Cao et al. successfully realized the identification and discrimination of the differentiation of bone marrow mesenchymal stem cells (Fig. 3.2) [5], which achieved the investigations of biological processes and cellular functions at a cellular level. They reported a novel SERS substrate based on hollow gold nanoflower (HAuNF)-decorated silicon wafers for distinguishing the differentiation of BMSCs. The fabricated HAuNF substrates had very good reproducibility, homogeneous SERS activity, and high SERS effect, which were necessary for direct SERS application. The HAuNF substrate was used to monitor the changes of cellular biochemical composition during the differentiation of BMSCs. The collected SERS spectra were analyzed using principal component analysis, which successfully segregated the subtypes of BMSCs. Furthermore, they demonstrated that adipogenic inductor and osteogenetic inductor could induce the differentiation of BMSCs into adipocytes and osteocytes, respectively. Their work suggested that the SERS technique based on SERS-active substrates provides a sensitive, efficient, and noninvasive detection method for studying the differentiation of stem cells.

It remains a challenge in biology and medicine to probe the cellular environment and further to discover the signaling mechanism of biological activities of cell. To identify biomarkers of specific pathologies, up- or downregulation of pathways or cellular response to changes in the environment is helpful for researching signaling pathways. However, it is necessary to develop measurement tools for chemical measurement at the length scale and in proximity of cells. The secretion of various molecules is an indicator of intercellular signaling pathways, the concentration of

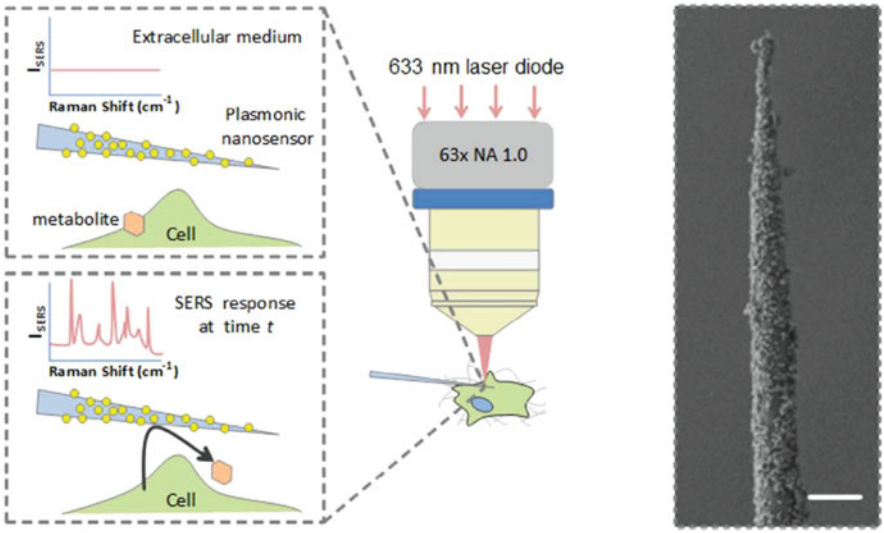

Fig. 3.3 (Left) Representation of the concept of a SERS nanosensor to monitor cellular secretion. The SERS nanosensor is located near cells and continuously monitors molecules diffusing in the hotspots of nanoparticles aggregated on the tip of the nanosensor. The cells and the nanosensors are positioned under a Raman microscope. (Right) SEM image of a typical SERS nanosensor on a pulled glass capillary with gold nanoraspberries. The scale bar of the SEM image is 1 μm [6]

which reaches zepto- to attomoles of chemical messengers, in a very short period of time. To monitor the secretion activities, it requires that the developed analytical tools can collect biological signal with high temporal resolution and high selectivity during the cellular secretion events.

J. F. Masson et al. achieved cell secretion process evaluation by assembly of nanomaterials on the capillary after the taper treatment (Fig. 3.3) [6]. They developed a nanosensor by decorated Au nanoparticles (served as a SERS substrate) on borosilicate nanopipettes. When the nanosensor approached to a cell, the decorated Au nanoparticles at different domains on the nanopipettes can provide spatial signals of the cell in a short time. The plasmonic nanosensor was used to monitor metabolite secretion near living Madin-Darby canine kidney (MDCKII) epithelial cells. Multiple metabolites, such as pyruvate, lactate, ATP, and urea, were detected simultaneously. The nanosensors can also be used to monitor metabolites in the extracellular medium. This SERS technique for the sensitive and non-destructive monitoring of extracellular metabolites secreted from living cells is broadly applicable to varied cellular and tissue models and should therefore provide a powerful tool for cellular studies.

It is crucial for advancements in biology and medicine to understand biological processes on a molecular level. Based on the combination of Raman and other analytical technologies, direct SERS applications have also been used to monitor dynamical cellular activities, such as apoptosis, mitosis, differentiation, and stress [7–11].

For example, cell apoptosis is one of the most studied cellular processes because it plays an important role in normal tissue development and the advancement of many acquired diseases. The apoptosis process is highly regulated by various molecular signals that involved a large number of proteins and nuclear acids in cellular and molecular events. During an apoptosis process, cells undergo a series of morphological and molecular events such as blebbing, cell shrinkage, proteolysis, and nuclear DNA fragmentation. It is crucial for gaining a more complete understanding of the intricate mechanism of apoptosis by investigating these events on a molecular level. But it still remains a challenge for observing morphological and monitoring molecular events in real-time on a single living cell scale simultaneously.

M. A. El-Sayed et al. developed a SERS-related method to monitor morphological and molecular events during cellular apoptosis in real-time simultaneously (Fig. 3.4) [7]. The analysis of Raman spectra indicated the DNA/protein composition in the cell nucleus to reveal the occurrence and dynamics of apoptotic events: protein denaturation, proteolysis, and DNA fragmentation. A temporal profile of apoptotic events was drawn: first, protein denaturation was induced by hydrogen peroxide addition; second, protein unraveled with hydrophobic amino acid exposure; and finally, protein degraded. These results demonstrate the developed technique can be used to study the mechanism of other apoptosis molecular pathways.

Mitosis, an important biological process, is a highly coordinated process, which involves complex and dynamic change of biomolecules. That any mistake happened in this process may lead to appearance of abnormal cells. Understanding dynamic change of biomolecules of mitosis in abnormal cells can enhance our knowledge about the survival of the abnormal cells and develop more efficient therapeutic techniques against diseases from the abnormal cells. As the abovementioned, it is difficult to monitor the change in morphology of cells and cell components simultaneously. Many events take place during the mitosis process, and there is a need for high temporal resolution methods for collecting morphological and molecular signals of each step.

The above method of plasmonically enhanced light scattering properties of functionalized gold nanoparticles together with SERS to monitor the complex and dynamic biological processes was involved in mitosis of normal and abnormal cells (Fig. 3.5) [8]. SERS spectra of various stages of mitosis indicated that most α-helix structure of mitotic proteins was converted into β-sheet conformation in the cancer cells during meta-, ana-, and telophases. Unique biochemical modifications to the lipid and amino acid moieties played important roles in conformational conversation of protein of cancer cells. However, in healthy cells, the existence of proteins was largely in the α-helix form. From the biological view of biology, there is a difference between normal and abnormal cells in the profile of proteins in the nucleus and the content of proteins in the cytoplasm. The reason of abnormal conformational modifications of mitotic proteins was unclear. Their researches suggested that conformational conversation of proteins can be monitored using SERS in real-time in live cells, and the SERS-related technologies can provide new tools to research the role of protein conformation dynamics during biological activities.

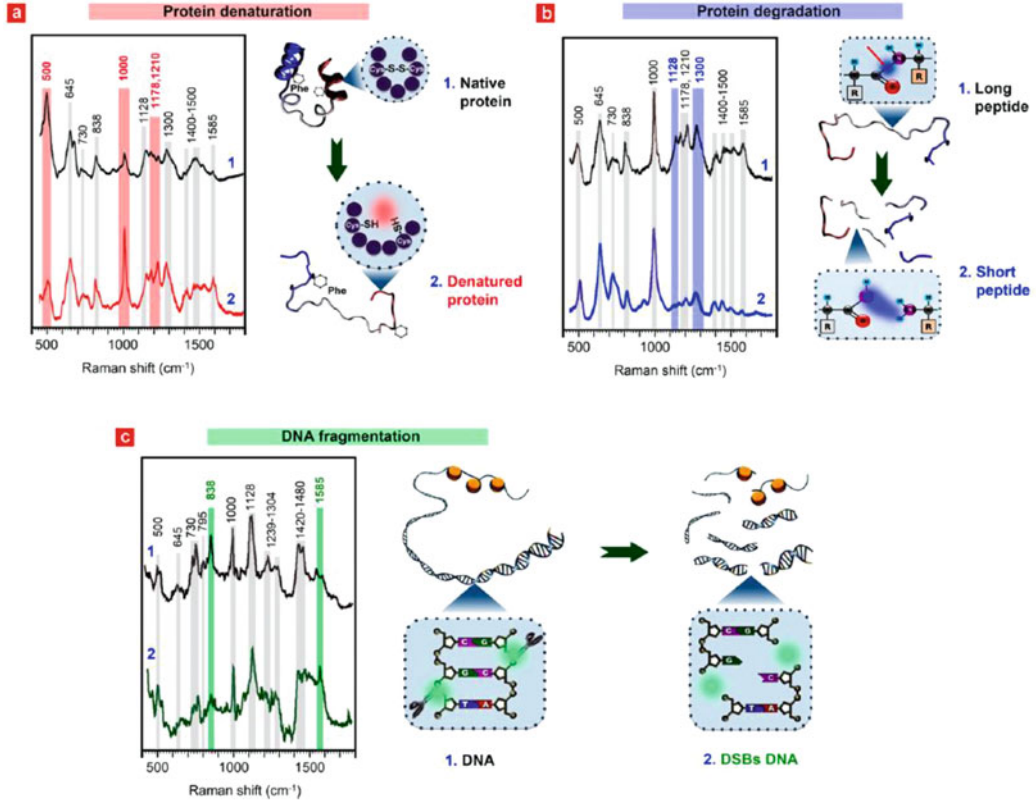

Fig. 3.4 In situ reference spectra of apoptotic molecular events. (**a**) Protein denaturation: plasmonically enhanced Raman spectrum of highly ordered, folded proteins extracted from HSC-3 cells (top) and denatured proteins treated by β-mercaptoethanol (bottom). (**b**) Protein degradation: plasmonically enhanced Raman spectra of long, intact peptides (top) and short peptides treated by trypsin (bottom). (**c**) DNA fragmentation: plasmonically enhanced Raman spectra of undamaged, extracted DNA from cells (top) and damaged DNA in the form of double-strand breaks (DSBs) after 4 h treatment with UV light (bottom) [7]

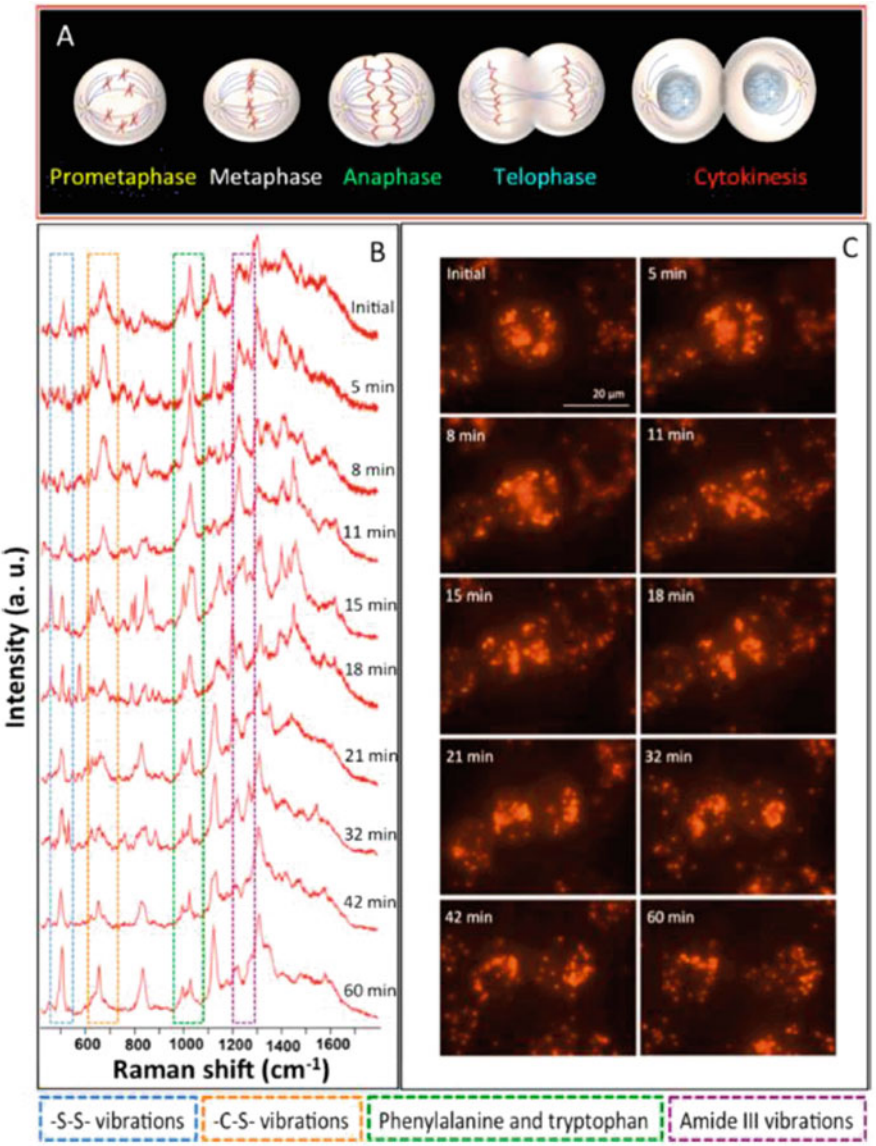

Fig. 3.5 (**a**) Schematic representation of various stages of mitosis. (**b**) Time-dependent SERS spectra collected from the HSC cells at different stages of mitosis. DF images collected at respective time are also given (**c**) [8]

Plasmonic photothermal therapy (PPT) is a promising cancer treatment by rapid conversation from NIR light to heat by plasmonic nanoparticles. The converted heat of the gold nanoparticles increased the temperature of their environment, higher than body temperature, and induced death of cells near the nanoparticles. Therefore, PPT

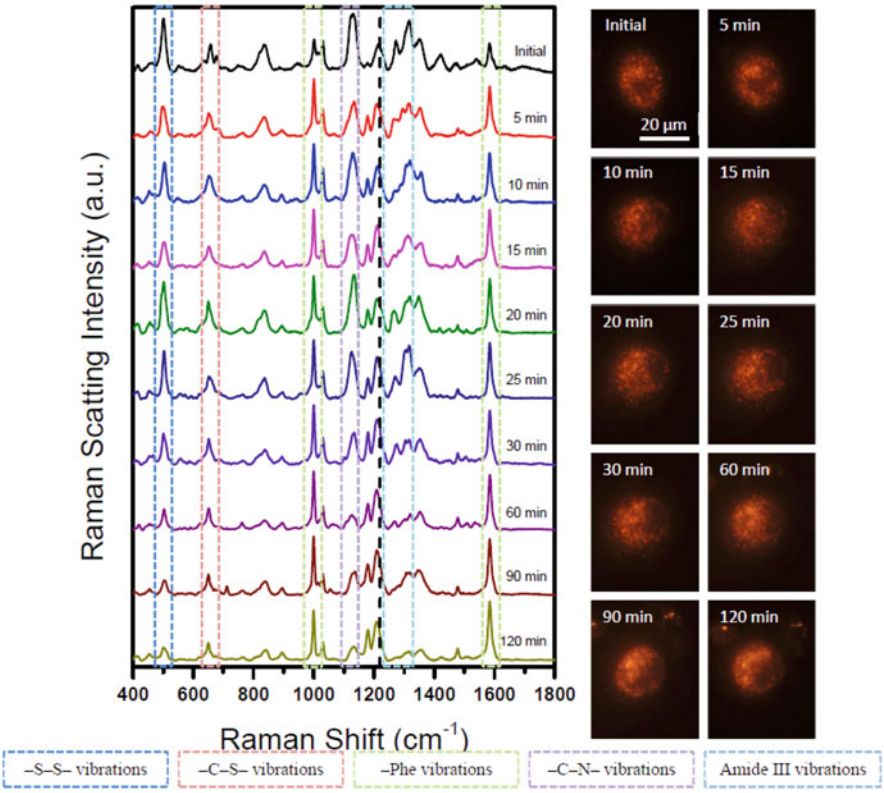

Fig. 3.6 Time-dependent SERS spectra collected from a single HSC-3 cell during PPT cell death induced by continuous laser exposure at lower power (6.2 mW). The vertical line at 1225 cm^{-1} serves as a visual guide to highlight the shift in this vibrational peak from the amide III β-confirmation at 1225 cm^{-1} to the aromatic amino acid residue peaks at 1209 cm^{-1}, which in conjunction with the disappearance of additional vibrations around 500 cm^{-1} and in the 1250–1350 cm^{-1} range signals cell death. Corresponding darkfield images for each spectrum are also shown [10]

relies on how to deliver plasmonic nanoparticles into or around the cells of interest, which can be achieved through passive or active targeting.

M. A. El-Sayed et al. reported the use of actively targeted spherical gold nanoparticles, both to induce PPT cell death and to monitor the associated molecular changes through time-dependent surface-enhanced Raman spectroscopy within a single cell (Fig. 3.6) [10]. When absorbing near-infrared (NIR) laser light of sufficient powers, the aggregated nanoparticles produced heat which caused modifications in the protein and lipid structures within the cell and ultimately led to cell death, which were monitored in real-time. The same molecular changes were observed using different plasmonic nanoparticle, indicating the consistency of the molecular changes throughout PPT-induced cell death from actively targeted AuNPs. Their researches suggested that Raman-related technologies not only

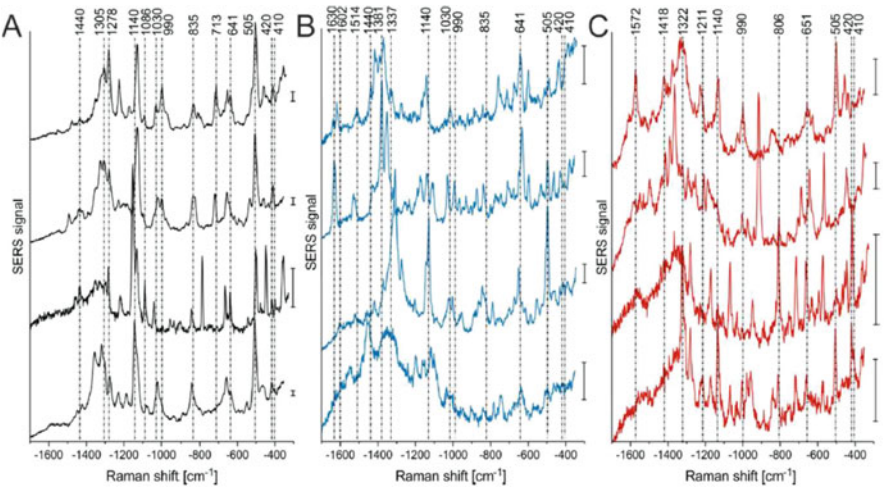

Fig. 3.7 SERS spectra, extracted from the mapping datasets of several *L. mexicana*-infected primary macrophage cells from the areas of (**a**) parasite, (**b**) the parasitophorous vacuole, and (**c**) endo-lysosomes located in the cytoplasmic regions. Excitation wavelength, 785 nm; acquisition time, 1 s; excitation intensity, 2×10^5 W cm^{-2}. Scale bar: 50 cps [11]

obtained the morphological and molecular signals simultaneously but also adjusted the cells and monitored the change of molecules simultaneously.

Leishmania are protozoan parasites, causing cutaneous and deadly visceral leishmaniasis worldwide. From insects to host, they are extracellular flagellated forms, and their intracellular forms called amastigotes that replicate in vertebrate cells. Amastigotes replicate in an endo-lysosomal compartment, the parasitophorous vacuole (PV). To date, morphological methods such as immunofluorescence microscopy and molecular destructive approaches such as proteomics and mass spectrometry can't be carried out simultaneously. The researches are needed for a more complete understanding of parasite replication. J. Kneipp et al. reported the direct probing of the molecular composition of *Leishmania*-infected macrophage cells in vitro by SERS (Fig. 3.7) [11]. In their research, Raman data showed spatiotemporal information of various infection-related molecules simultaneously, and their results of electron microscopy revealed the gold nanoprobes accessed to the parasitophorous vacuoles (PV) through the endosomal system, which suggested that SERS nanoprobes located in the direct proximity to the parasite and infection-related molecules were induced by the parasite event. Their work suggested that the combination of Raman and other analytical methods could obtain dynamically morphological and molecular information at high spatiotemporal resolution.

Thyroid cancer is an endocrine tumor, and due to the evolution of biotope and the change of lifestyle, the incidence of cancer in young people increased rapidly. For cancer, the combination of early diagnosis and surgery was the most effective way to improve the survival rate of cancer patients. Computerized tomography and magnetic resonance imaging can provide the morphological information of solid cancer,

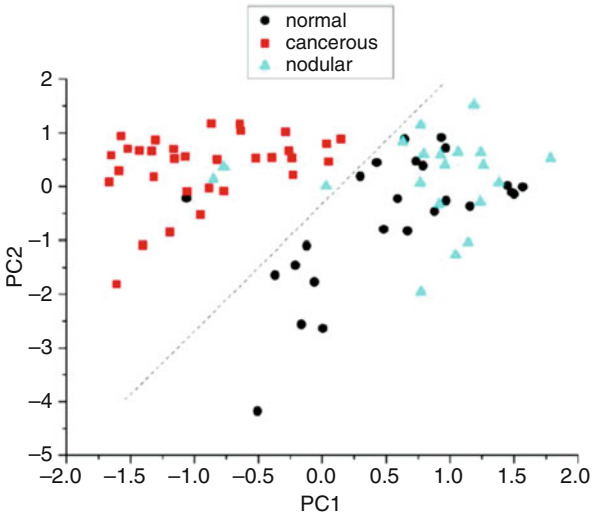

Fig. 3.8 Plot of the first principal component (PC1) versus the second principal component (PC2) for normal group, nodular group, and thyroid cancer group [12]

but the clinical process to assess pathological changes in tissue still relies on the histopathology tests, which can provide well-defined morphologic features of tissue. Methods of rapidly distinguishing histopathological information are needed for further surgery. R. Chen et al. have enabled the tumor margins identification with SERS (Fig. 3.8) [12]. In the report, silver nanoparticles were synthetized to collect Raman information of human thyroid tissues to discriminate their different types, including thyroid cancers, nodular goiters, and normal thyroid tissues. Raman data were analyzed using the principal component analysis and linear discriminant analysis together. The results showed that collected data can provide diagnostic sensitivities of 92%, 75%, and 87.5% and specificities of 82.6%, 89.4%, and 84.4%, respectively, for differentiation among normal, nodular, and malignant thyroid tissue samples. Their work suggested that analysis results of tissue SERS spectroscopy would have potential for diagnosing cancers on the molecular level.

3.2.2 Indirect SERS Detection in Biology and Medicine

In the body, many biomarkers have a weak intrinsic Raman activity. On the physiological or pathological levels, these biomarkers cannot be detected by SERS. For this case, the common strategy was to use a reactive molecule as a probe, which has three moieties: anchor group for attaching on SERS substrates such as thiol, high Raman activity group for strong Raman signals such as aromatic rings, and the responsive part to respond the molecules of interest.

Under normal circumstances, the internal physiological parameters of the organism remain within a certain range. After the balance is broken, the physiological parameters will change significantly, and the organism itself will produce the

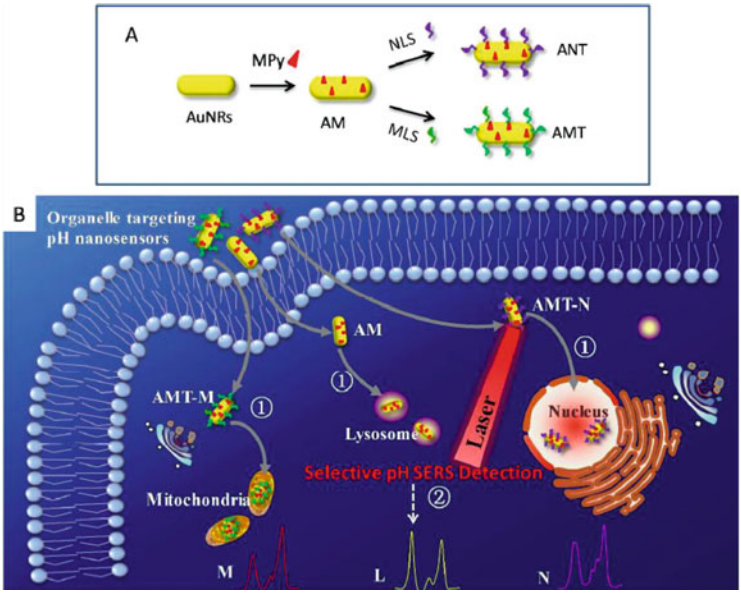

Fig. 3.9 (**a**) The preparation of organelle targeting pH nanosensors. (**b**) The procedure of selective determinations of pH in specific organelles by SERS spectroscopy with organelle targeting pH nanosensors [13]

corresponding diseases. Of course, for cells, the impacts of these changes are relatively greater. Intracellular pH homoeostasis plays a pivotal role in all cellular processes such as cell proliferation, differentiation, apoptosis, etc. In general, subtle pH changes of subcellular components are involved in various abnormal functions of cells and tissue, such as cancer and Parkinson's and Alzheimer's disease. Thus, detections of subcellular dynamical pH in living cells can promote understanding on physiology and pathology processes.

SERS is widely used in this area due to its non-destructive, fast, and sensitive characteristics. Xu et al. developed a series of SERS nanosensors with high sensitivity and targeting function for the quantification and monitoring of pH values in the mitochondria, nucleus, and lysosome (Fig. 3.9) [13]. The nanosensors were composed of gold nanorods (AuNRs) functionalized with pH-responsive molecule (4-mercaptopyridine, mercapto moiety as an anchor group, pyridine ring as a strong intrinsic Raman activity part, and nitrogen of the pyridine ring as a responsive element to pH) and targeted peptides that can specifically deliver the probe to the targeting subcellular organelles. Due to the targeting ability of the targeted peptides, once these nanosensors are incubated with the cells, they enter the lysosome, nucleus, and mitochondria, respectively, so that the pH of different organelles can be detected by monitoring the Raman spectral changes of MPy along with different pH values. In this way, the local pH changes in different organelles can be also

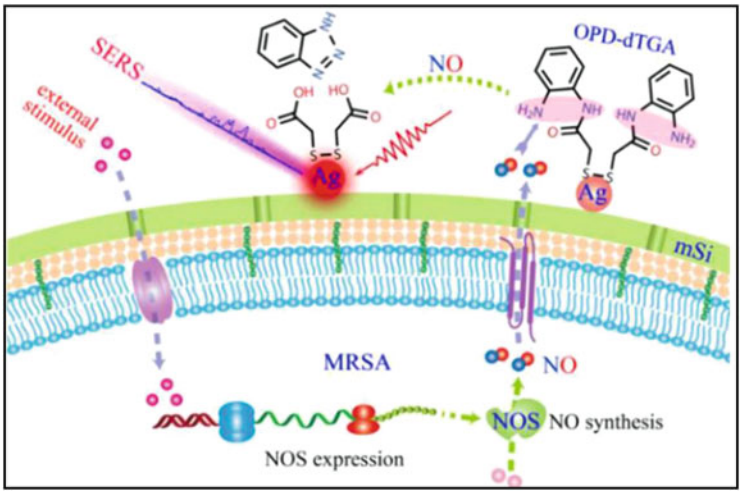

Fig. 3.10 Illustration of the working principle of the live bacteria SERS platform [14]

detected. The SERS nanosensors can be used to detect pH values of subcellular microenvironments and organelle pH values of organelle-related diseases.

Nitric oxide (NO), carbon monoxide (CO), and hydrogen sulfide (H_2S) are the three significant gaseous signaling molecules in various pathological and physiological pathways, drawing more and more attentions as important physiological regulators for various human diseases. The three are typical small molecules, and they have no strong intrinsic Raman activity, but they have high reactivity. They can react with the responsive part of probe molecules and be detected indirectly by monitoring the change in Raman spectra of the probe molecules.

Since it was first identified as the endothelium-derived relaxation factor, NO has been recognized as a ubiquitous intra- and intercellular messenger involved in diverse physiological and pathophysiological processes. Xing et al. developed a simple and unique SERS platform for the precise and sensitive in situ monitoring of NO by using a SERS reporter, 2,2′-disulfanediylbis(*N*-(2-aminophenyl)acetamide), and the relative radio of the SERS intensity at 1446 and 960 cm^{-1} was used to the amount of NO (Fig. 3.10) [14]. Once the Raman reporter is exposed to the NO, the value of I_{1446}/I_{960} changed. In this way, the amount of the NO can be confirmed.

Certain Gram-positive bacteria, such as *Staphylococcus* and *Bacillus* species, were discovered to have a bacterial NO synthase (bNOS) gene, similar to eukaryotic NOSs. Due to the resistance to antibiotics, among these NOS-producing bacterial species, *methicillin-resistant Staphylococcus aureus* (MRSA) has drawn much attention. There is increasing evidence that NO plays a crucial role in MRSA antibiotic resistance. To better understand the roles of NO in bacterial physiology, the authers used the SERS reporter for the precise and sensitive in situ monitoring of nitric oxide (NO) release from the individual bacteria and evaluated the stress of antibiotics and co-infected bacteria.

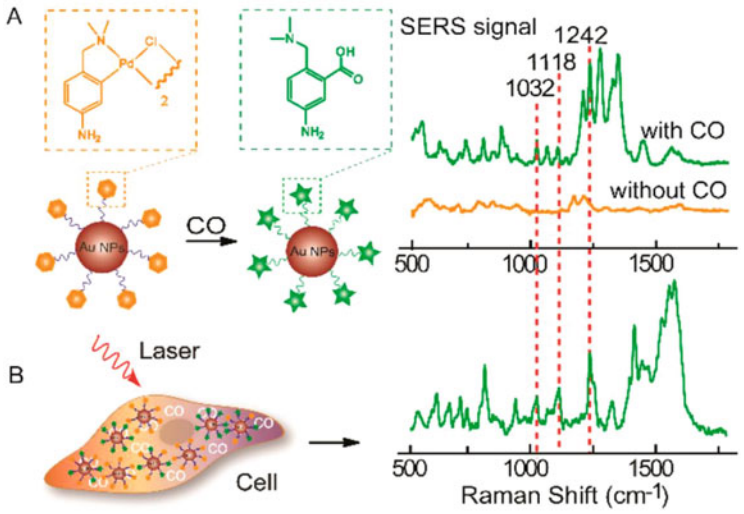

Fig. 3.11 Illustration of SERS nanosensors for the detection of intracellular CO. (**a**) SERS response and sensing mechanism of palladacycle carbonylation on AuNP/PC nanosensors for CO. (**b**) SERS detection of CO in living cells using AuNP/PC nanosensors [15]

The second gaseous messenger, CO, has been increasingly recognized as an important messenger in mammalian cells. Emerging studies demonstrate that, similar to nitric NO and H_2S, CO plays a significant role in signaling pathways involved in a number of pathophysiological processes, due to its status as a second messenger in the cells. Consequently, CO have diverse biological effects in the body, and many aspects of its functions are still indistinct. To detect the amount of CO in the biological processes, several techniques, such as infrared absorption, chromatography, chromogenic detection, and electrochemical assays, have been developed. These methods are difficult to implement for the detection of CO in biological circumstances in a noninvasive way. Li et al. explored a novel nanosensor for the highly selective detection of intracellular carbon monoxide (CO) by SERS on the basis of palladacycle carbonylation (Fig. 3.11) [15]. The SERS nanosensors (AuNP/PC) with high SERS activity and reactivity with CO were prepared. When the AuNP/PC nanosensors contacted with CO, carbonylation of the PC was triggered by CO, and the consequent SERS spectra of AuNP/PC changed, which indicated the concentration of CO indirectly in situ. Their studies further indicated that the CO concentrations in normal human liver cells and HeLa cells were as low as 0.5 μM.

The third gaseous messenger, H_2S, also is a significant endogenous gaseous signaling molecule involved in biological events. To better understand the physiological and pathological functions of H_2S, several methods have previously been developed for H_2S detection. As mentioned above, these methods often require the destruction of specimens. Long et al. reported a novel SERS nanosensor (Fig. 3.12) [16]. 4-Acetamidobenzenesulfonyl azide was used as a SERS reporter, functionalized gold nanoparticle (AuNPs/4-AA) for detecting the endogenous H_2S

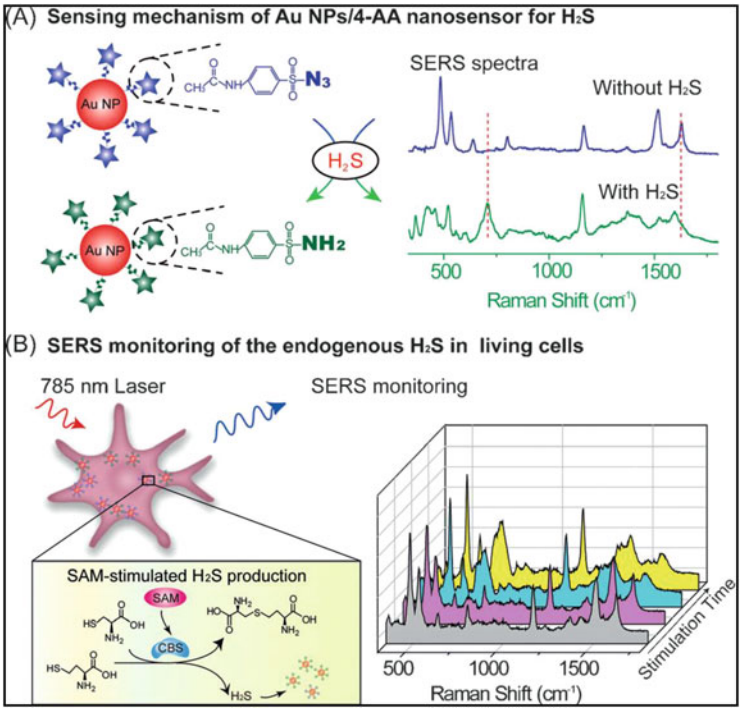

Fig. 3.12 (**a**, **b**) SERS nanosensors for monitoring endogenous H_2S in living cells [16]

in living cells. The change in collected SERS spectra of AuNPs/4-AA indicated the amount of H_2S indirectly. The SERS nanosensor responded to H_2S within 1 min with a 0.1 mm level of sensitivity. They also used the SERS nanosensor to monitor the endogenous H_2S of living glioma cells.

In the body, the change in redox state is involved in many physiological and pathological processes (such as the behaviors of cells and states of biomolecules), and the favorite redox states are varied for different physiological and pathological processes. It is mainly dependent on the reaction of reactive oxygen species (ROS), reactive nitrogen species (RNS), antioxidant molecules, and corresponding enzymes. For this case, the used SERS reporters should respond to all involved molecules instead of one given molecule. C. J. Campbell et al. report a SERS technique using targeted nanosensors to detect redox state (Fig. 3.13) [17].

The microenvironment and biochemical events of cancer are complex and different to that of normal tissues. Oxygen gradients are common, and hypoxia is often a feature of the tumor microenvironment due to the lack of blood vessel and high consumption of energy and oxygen gas, which caused different metabolic pathways and products in cancer tissues. The microenvironment induced by abnormal metabolic pathways promoted the cancer development further. So, monitoring the microenvironment of cancer tissue is better than that of a single cell or a layer of cells for

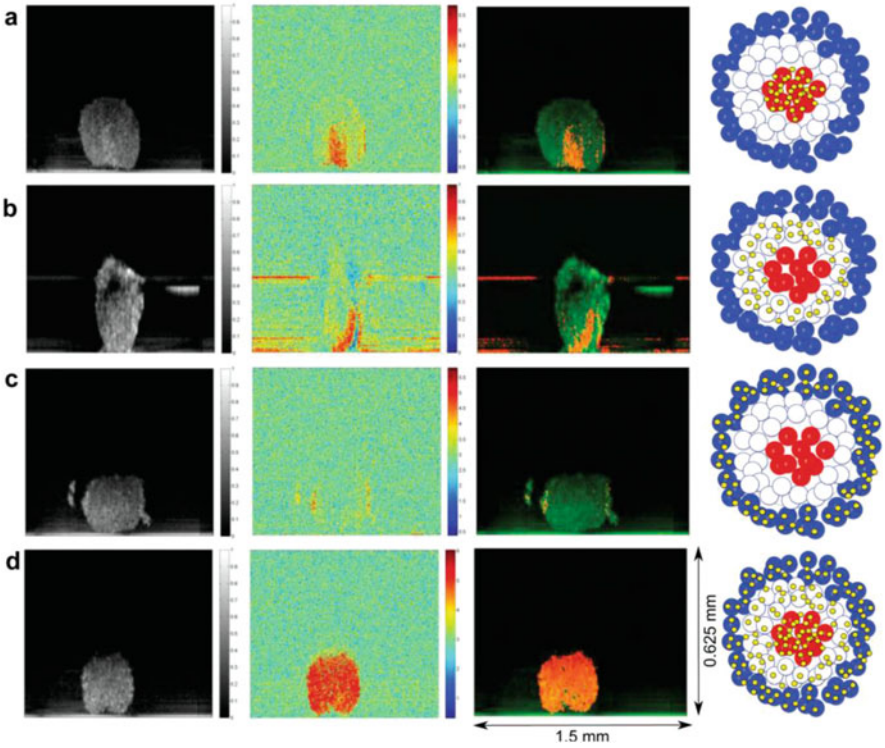

Fig. 3.13 (**a–d**) Targeted SERS nanosensors in MTS imaged using PTOCT. OCT signals (far left column), photothermal signals (central left column), an overlay of photothermal on OCT signal (central right column), and a schematic of the NS distribution that each condition represents (far right column). Dimensions apply to all photothermal and OCT images [17]

understanding cancer biology. C. J. Campbell used their targeted nanosensors to show redox potential of 3D tissues. In their report, the formation of multicellular tumor spheroids (MTS) was used as a model of tumor structure. The targeted nanosensors were located in all the MTS, and SERS spectra of different domains of the MTS indicated their redox potential indirectly. The developed technique indicated spatiotemporally redox distribution of MTS, which can provide more effective information to understand cancers.

Besides the above direct detection methods of molecules using SERS, based on the influence of the molecules of interest on a molecule with strong intrinsic Raman activity adsorbed on SERS substrates. The strategy can also be used to detect molecules of interest indirectly and to monitor the molecule-involved events in cells.

The liver plays major roles in regulating various metabolic functions of the body such as glycolysis and detoxification. Liver injury, usually induced by toxic molecules, viral infection, or drug abuse, is a common clinical symptom. Acute liver injury is one of the leading causes of death in clinics, and liver injuries need to be rapidly and efficiently diagnosed and remedied. Based on gold nanoflowers (GNFs)

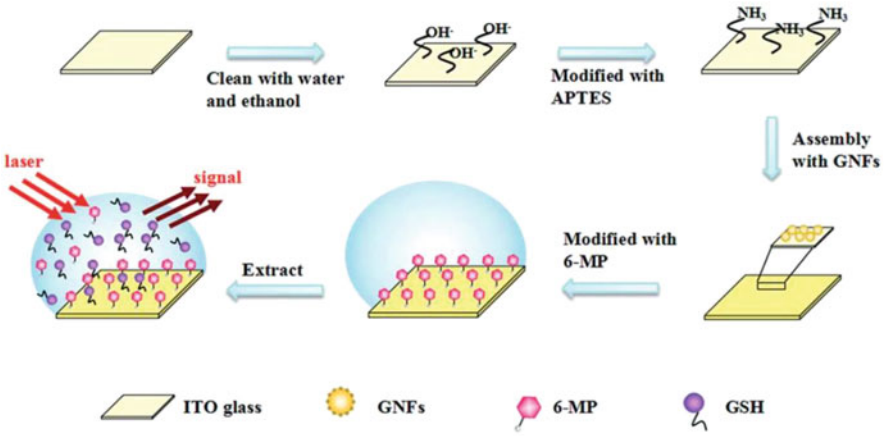

Fig. 3.14 Schematic illustration of fabrication of GNF substrate and 6-MP loading and detection procedures of the SERS system [18]

and 6-mercaptopurine (6-MP) as a SERS signal molecule, Wang et al. developed a novel method for monitoring carbon tetrachloride (CCl_4)-induced acute liver injury of mice (Fig. 3.14) [18]. Wang et al. found the GSH-triggered GST-accelerated turn-off behavior of 6-MP in buffer systems. In the liver tissue extracts from CCl_4-induced acute liver injury mice without adding GST, the turn-off behavior of 6-MP was also accelerated, but the detection intensity from 10^5 down to 10^3 counts for 6-MP. The SERS results confirmed that GNF substrate exhibited excellent stability in complex biological environment and response in clinical sample. This study provided a rapid and sensitive approach for analysis of trace amounts detection based on their SERS probe.

The indirect SERS methods not only detect endogenous molecules but also detect drugs in cells. For tracking the intracellular dynamical drug release process, which was triggered by molecules of interest, to design and fabricate responsive nanocarriers is relatively easy, but how to monitor their release behavior in cells remains a challenge. Until now, the fluorescence technique was widely employed in these researches. However, the fluorescence-traceable nanocarriers met some undesirable problems, such as quenching, overlapping, and covering the fluorescence of molecules of interest. Cui et al. developed a redox-responsive drug carrier based on nanoscale graphene oxide (NGO) loaded with Ag nanoparticles (Fig. 3.15) [19]. Their intracellular release behavior was monitored by SERS-fluorescence combined spectroscopy. In the drug carrier, the redox-responsive property is from the disulfide linkages between the load drug molecules and NGO. In the body, the existence of glutathione (GSH) cleaves the disulfide linkage and releases the loaded drug. In their report, the intracellular real-time drug release dynamics can be monitored by the combined SERS-fluorescence technique.

What's more, SERS was used as a label method, in which molecules with strong intrinsic Raman activity were adsorbed on a SERS substrate to form a SERS tag and

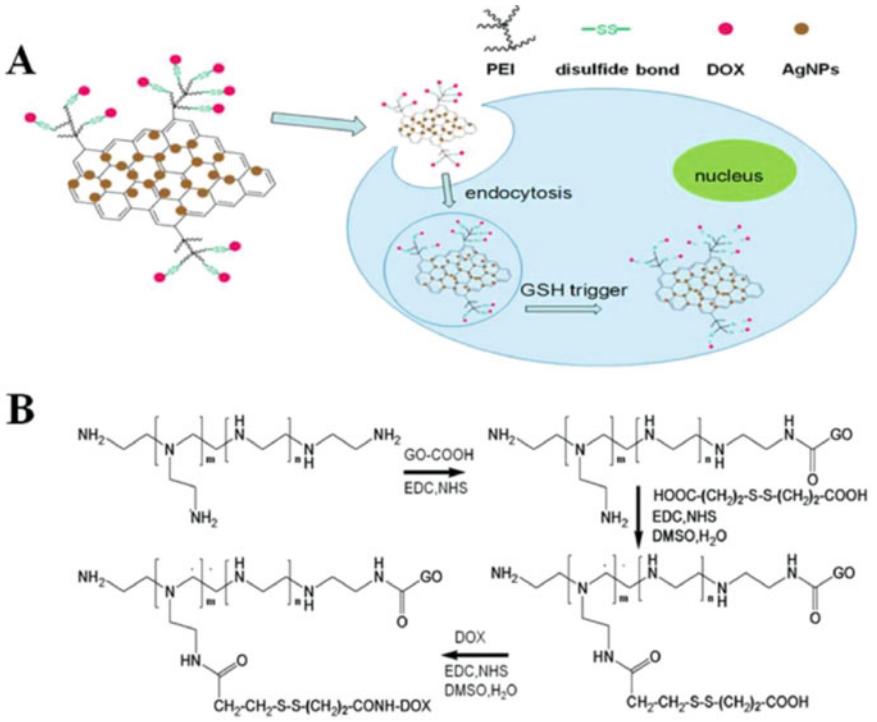

Fig. 3.15 (**a**) Intracellular drug delivery of redox-responsive DOX-loaded NGO-Ag and (**b**) synthesis pathway of disulfide-based drug delivery system [19]

antibody, ligand, or other recognizable elements were attached on the SERS tag to form a SERS probe. The SERS probes can be used to detect biomolecules, cells (exosomes), and tissues.

Respiratory tract infections (RTIs) are severe acute infectious diseases. Any time delay in RTI diagnosis will exacerbate the patient's condition and can even lead to their death. However, it is still a challenge for accurate clinical diagnosis in RTIs because one, two, or more pathogens may be involved, including bacteria and atypical pathogens. A single clinical symptom can be caused by different pathogens, and conversely, one pathogen can induce various clinical symptoms. It has been documented that 80% of upper respiratory tract infections (URTIs) and a proportion of lower respiratory tract infections (LRTIs) are caused by atypical pathogens, such as influenza A, influenza B, parainfluenza 1, parainfluenza 2, parainfluenza 3, adenovirus, respiratory syncytial virus, *Chlamydophila pneumoniae*, *Coxiella burnetii*, *Mycoplasma pneumoniae*, and *Legionella pneumophila*. Various combinations of these pathogens appeared when RTI occurs. In clinics, traditional methods for identifying the viral pathogens are mostly dependent on laboratory examination following pathogen isolation and culture, which is complicated, time-consuming, difficult, and with a low limit of detection (LOD).

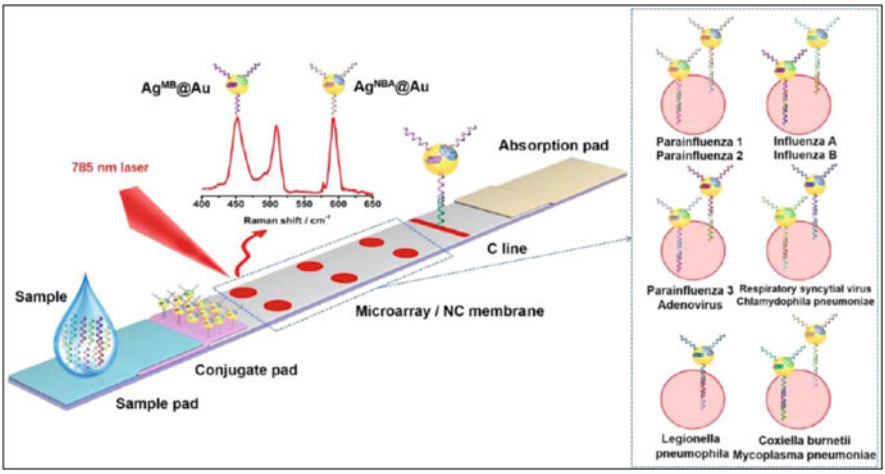

Fig. 3.16 Schematic illustration of SERS LFM for the detection of the nucleic acids of 11 RTI pathogens with RDs encoded core-shell SERS nanotags [20]

Zhao et al. developed a SERS lateral flow microarray (LFM) that achieves ultrasensitive and high-throughput diagnosis of the nucleic acids of RTI pathogens (Fig. 3.16) [20]. Core-shell nanoparticles encoded with 2 Raman dyes were chosen as SERS nanotags and combined on a microarray immobilized on a nitrocellulose membrane for rapid quantification of the nucleic acids of 11 RTIs on a single strip simultaneously, in which the amount of sample required, reagent consumption, material cost, and duration of assay preparation and detection have been reduced because of the multiplex assays. The LOD for these nucleic acids were at the level of pM.

The lethal reason of most cancer is related to metastasis in the body due to the hematogenous dissemination of circulating tumor cells (CTCs). Clinical data have proved that the CTCs were markers of metastatic development, survival time, cancer recurrence, and therapeutic efficacy. A variety of assays have been developed to detect CTCs from a sample of peripheral blood, but most of these methods have limit to large-scale clinical applications. A. S. Biris et al. developed a technique to increase both the molecular and spectral specificity of cancer diagnosis by using tunable silver-gold nanorods with narrow SERS and high photothermal contrast (as shown in Fig. 3.17) [21]. In their report, the silver-gold nanorods were functionalized with four Raman-active molecules and four antibodies specific to breast cancer markers and with leukocyte-specific CD45 marker. Using an antibody rainbow cocktail can realize highly specific detection of single breast cancer cells. By integrating multiplex targeting, multicolor coding, and multimodal detection, the approach has the potential to improve multispectral imaging of individual tumor cells in complex biological environments.

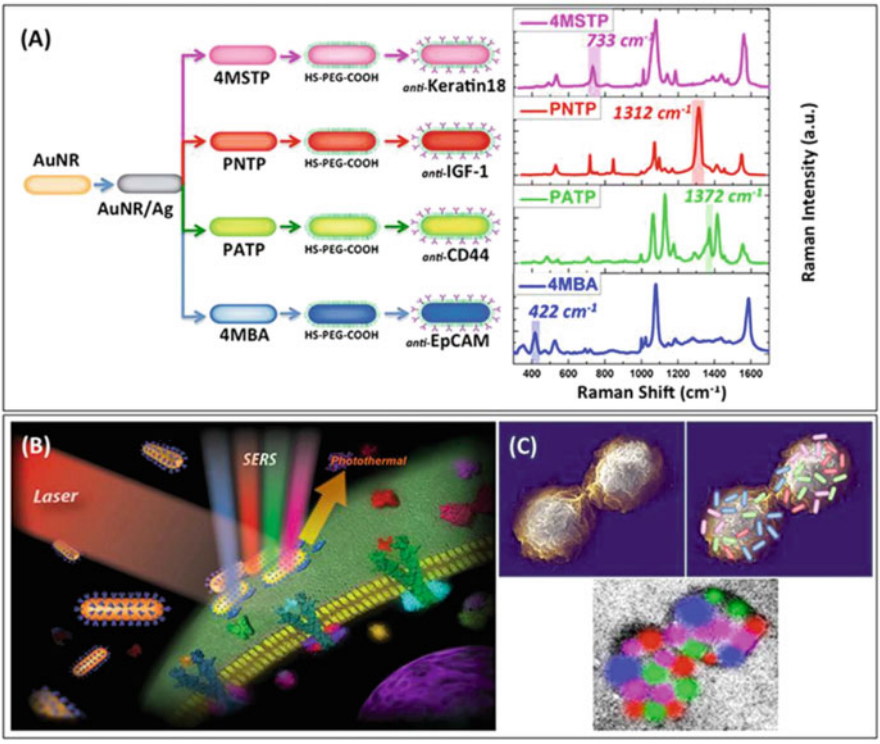

Fig. 3.17 (**a**) Schematic diagram (preparation steps) and Raman spectra (acquisition time 50 s) for the four families of SERS nano-agents. A color was assigned to a non-overlapping peak from each SERS spectrum as follows: blue, AuNR/Ag/4MBA/anti-EpCAM; red, AuNR/Ag/PNTP/*anti*-IGF-1 receptor β; green, AuNR/Ag/PATP/anti-CD44; and magenta, AuNR/Ag/4MSTP/*anti*-Keratin18. *4MBA* 4-mercaptobenzoic acid, *PNTP* *p*-nitrobenzoic acid, *PATP* *p*-aminobenzoic acid, *4MSTP* 4-(methylsulfanyl)thiophenol. (**b**) Schematics of breast cancer cell surface targeting by four nano-agents and SERS/PT detection technique. (**c**) Schematics of 2D multicolor SERS data correlation with nano-agents' distribution on cell surface [21]

A SERS-based method for the detection of multiple exosomes was presented by taking the advantages of the excellent multiplexing ability of the SERS spectra and particularly designed aptamers [22].

Multimodality imaging agents are often needed in tumor diagnosis because they can provide more alternative and reliable information for the accurate detection and therapy of diseases than single imaging technique. But, most conventional imaging agents cannot meet the requirements of multimodality imaging. Therefore, exploring a composite with various modality characteristics has a great impact on the diagnosis of cancer. Zhang et al. reported mesoporous silica gadolinium-loaded gap-enhanced Raman tags (Gd-GERTs) specifically for surgery imaging (Fig. 3.18) [23], which can be used as agents of computed X-ray tomography (CT), magnetic resonance (MR), and SERS simultaneously. They exhibit strong attenuation property for CT

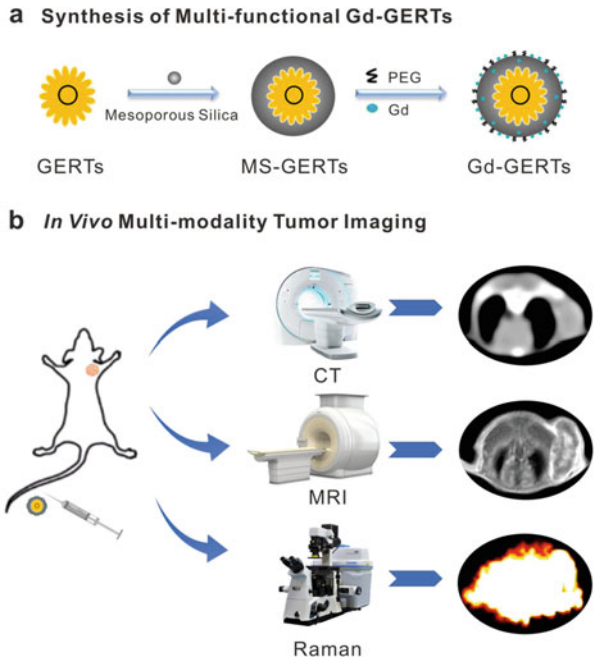

Fig. 3.18 Schematic illustration of multifunctional nanoprobes and preoperative/intraoperative imaging. (**a**) The synthesis process of Gd-loaded gap-enhanced Raman tags (Gd-GERTs) and (**b**) their application for in vivo CT/MRI/Raman multimodality tumor imaging [23]

imaging, high T_1 relaxivity for MR imaging capability, and SERS signal with good dispersity and stability, which presents three-mode imaging performance of the tumor. In their report, in vivo biodistribution and long-term toxicity studies revealed that the Gd-GERTs have good biocompatibility and bio-safety.

All in all, SERS has a strong application capability in biology and medicine. However, SERS still has defects, which limits the further development of SERS. In the next part, the shortcoming of SERS will be discussed.

3.3 Shortcoming of SERS Application and Corresponding Strategies

Firstly, since SERS requires high-sensitivity detection by means of a signal-enhanced substrate, the uniformity, stability, repeatability, and biocompatibility of the material determine the effect of SERS detection. In order to overcome these questions, many noble metal nanomaterials with different morphologies emerged as the time require [24–26].

Secondly, with the wide application of SERS, semi-quantitative methods are difficult to meet the demand, and accurate quantification has become popular. To achieve quantitative detection, a single peak intensity calculation method was

eliminated, and multiple Raman peaks were selected for some calculations to accurately quantify [27].

Thirdly, SERS detection depth has certain limitations, which requires the introduction of other technologies, such as embedding a visualization window in the body [28], combining SERS with an endoscope [29], performing in vivo reactions and in vitro detection with acupuncture needles [30], etc.

Last but not least, after nanomaterials enter the organism or cells, they cannot be metabolized. This is another problem that needs to be solved.

3.4 Biological Effects of Redox Potential and the Strategies of SERS Detection on Various Levels

The change of redox state is involved into many biological processes, including auxesis, metabolism, cell differentiation, apoptosis, and necrocytosis, which is affected by the proportion of antioxidants and oxidants (such as reactive oxygen species and reactive nitrogen species). Oxidant stress will occur when the proportion of oxidants is higher than physiological threshold. Excessive oxidants would disturb the normal physiological process and bring some physiological and pathological responses, or even cellular damage and death, which are the leading reason of some diseases, such as cardiovascular diseases, neurodegenerative disease, and cancer. The detection of redox state in cells and tissues is needed for indicating their biological processes.

It is very critical for keeping health to regulate the redox state. Drugs or foods are important supplements of external antioxidants. Botanical foods are parts of daily diets, which are rich in reductive materials such as starch and natural antioxidants, like phenols, flavonoids, flavanols, and vitamin C. Therefore, the detection of the redox state of the materials is essential and attracts more and more attention in the daily life, food processing, and so on.

In the nature, plants synthetize reductive materials using CO_2, H_2O, and light, while animals decompose the materials using O_2. The conversions of the materials are redox reactions, and redox state is an indicator for all the reactions of biological processes. Colin J. Campbell of the University of Edinburgh has established a new approach to monitor intracellular redox potential based on the use of SERS nanosensors comprising redox-sensitive reporter molecules assembled on gold nanoshells (Fig. 3.19) [31].

Redox potential is an important indicator of cell state. It is a challenge for quantitatively monitoring intracellular redox potentials. Based on the use of SERS probes, redox-sensitive molecules assembled on a gold nanoshell. Since the Raman spectrum of the molecule changes depending on its oxidation state and is enhanced by the gold nanoshell, the SERS probes can enter into the cytoplasm by endocytosis process, to monitor intracellular redox potential dynamically.

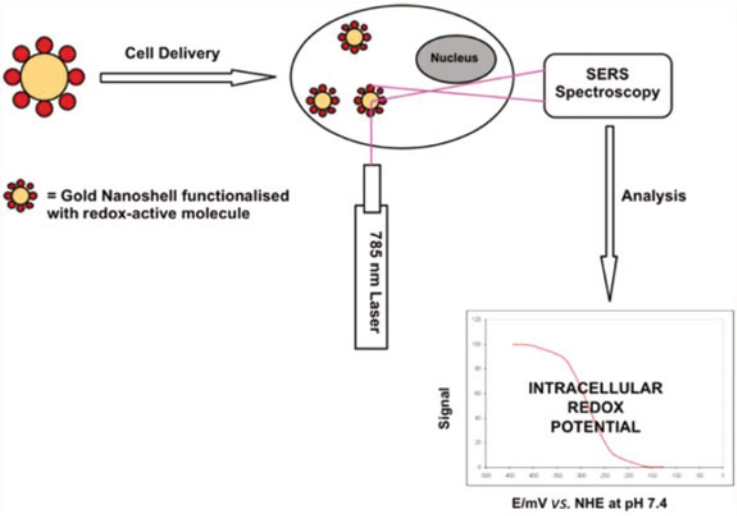

Fig. 3.19 Illustration of a redox SERS probe for monitoring the intracellular redox potential [31]

The method of monitoring intracellular redox potential is used to carry out some fundamental researches, which can't be done due to the lack of suitable tools or methods. Hypoxia can change gene expression and cause many dysregulations of metabolic pathways, which induces many diseases including stroke and cancer. The SERS probes are suitable tools to research the relationship among hypoxia, redox potential, gene expression, and metabolic pathways.

Fruits and vegetables are parts of daily diets, which are rich in natural antioxidants, like phenols, flavonoids, flavanols, and vitamin C. Therefore, the detection of the antioxidants of fruits and vegetables is essential and attracts more and more attention in the daily life, food processing, and so on. For traditional methods to detect samples in vitro, it is necessary to extract the juices or antioxidant compositions from fruits and vegetables before detection. Obviously, the extraction processes are time-consuming. More importantly, it is inevitable that the antioxidant compositions would be exposed to air during the extraction processes.

It is simple for monitoring their redox potentials using SERS probes. A redox SERS probe and a pH SERS probe were fabricated and dropped onto the flesh of the fresh incision of fruits and vegetables, respectively (Fig. 3.20) [32]. The SERS spectra of redox probes were collected to indicate the redox states of the fruits and vegetables, and the SERS spectra of pH probes were collected to indicate their pH values. The order of redox states (redox potential) of the detected fruits and vegetables is as follows: potato carrot > Golden marshall apple > crystal pear > Fuji apple > Chinese royal pear > Xinjiang kuerle fragrant pear > Green delicious apple. Compared with traditional methods, the developed SERS method is simple without any pretreatments and consumption of additional chemicals, which would become a

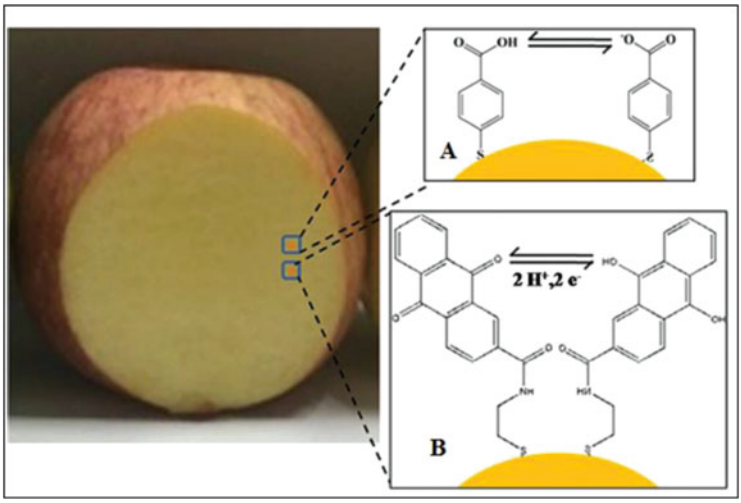

Fig. 3.20 (**a**, **b**) Illustration of a redox SERS probe and a pH SERS probes for monitoring the redox potential and pH of fruits and vegetables [32]

popular evaluation methodology during growth and storage stages of fruits and vegetables.

Wound healing is a complicated and ordered biological process involving hemostasis, inflammatory reactions, cellular proliferation, and wound remodeling. In previous reports, the outbreak of ROS from neutrophils during early stage of wound healing process changed the redox states of the wound, and the redox states varied at different pathophysiological stages and triggered related cellular signaling pathways, autonomous defense, and antibacterial radicals for wound healing. However, the evolution of redox states during wound healing process is unclear because no given method can detect the native redox states. For invasive detection, the sampling of wound fluids would destroy the healing wound and make a new wound on the old wound, immediately changing the wound states and redox state of the wound. For noninvasive detection, electrochemical methods provided the redox states of only one dot of the wound and can't provide information of the whole process, and electron paramagnetic resonance spectroscopy provided only the redox states of the whole wound, lacking the spatial resolution.

To detect the redox state evolution during wound healing process, the redox SERS probes were integrated on one surface of a chitosan membrane as a redox-sensitive wound dressing (Fig. 3.21) [33]. The redox-sensitive wound dressing was used to cover on an acute wound as both a wound dressing and a redox sensor. The spatiotemporal evolution of the redox states of the healing wound was obtained by spatiotemporally collecting the SERS spectra of the SERS probes covered on the wound. The data showed that the domains with the lowest redox potential shifted from the edge to the center of a wound during healing process and high concentration of glucose blocked the shift of the domains and the healing process.

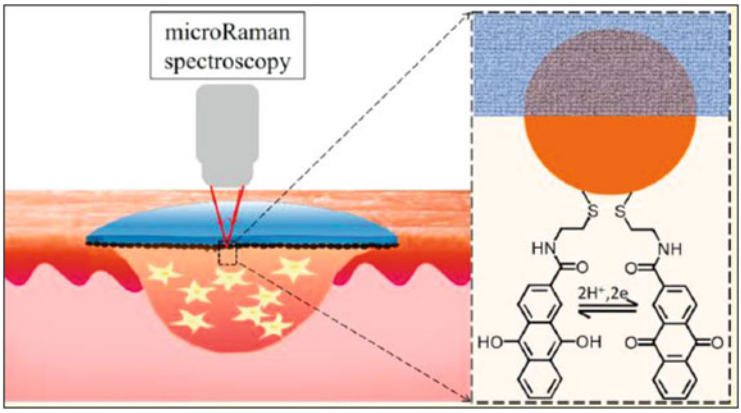

Fig. 3.21 Illustration of a redox SERS probe for monitoring the evolution of redox potential during the process of wound healing [33]

The redox-sensitive wound dressing and the method of detecting redox states of the wound provide a new path for the detection the spatiotemporal evolution of the redox states of the wound healing, which would provide more data to the understanding and therapy of wound healing.

The redox-sensitive wound dressing can sense the redox potential of the superficial tissues. But it is still a great challenge to detect redox potential of internal parts of tissues, such as skin and muscle, let alone bone joint and cartilage. Obviously, to detect SERS signals in vivo, SERS probes should be introduced into internal parts of tissues, usually by surgery or injection; however, it is difficult either to collect SERS signals or to take the SERS probes out. Acupuncture needles, used in Chinese traditional medicine, are minimally invasive tools into and out of the body. In previously reports, SERS-active microneedles were structured by adsorbed SERS probes on an acupuncture needle to achieve minimally invasive sampling in vivo and direct Raman detection ex vivo. Various ingenious design and fabrication allowed the SERS-active microneedles to become ideal miniaturized SERS detection elements to avoid adverse effects of common SERS substrates used in vivo.

To detect redox potential and pH simultaneously in rat joints, a SERS-active microneedle was structured with two separate grooves containing redox and pH SERS probes into muscles with minimal invasion to assess their response in tissues (Fig. 3.22) [34]. The multiplexed SERS-active microneedles were inserted into rat joints to sense their redox status and pH simultaneously. The strategy of one SERS probe in one groove would allow SERS-active microneedles to become a multiplexed analytical tool for minimally invasive multi-sampling in vivo and direct Raman multi-detection ex vivo, and the multiplexed SERS-active microneedles would become a versatile analytical tool to promote novel researches in biology and medicine.

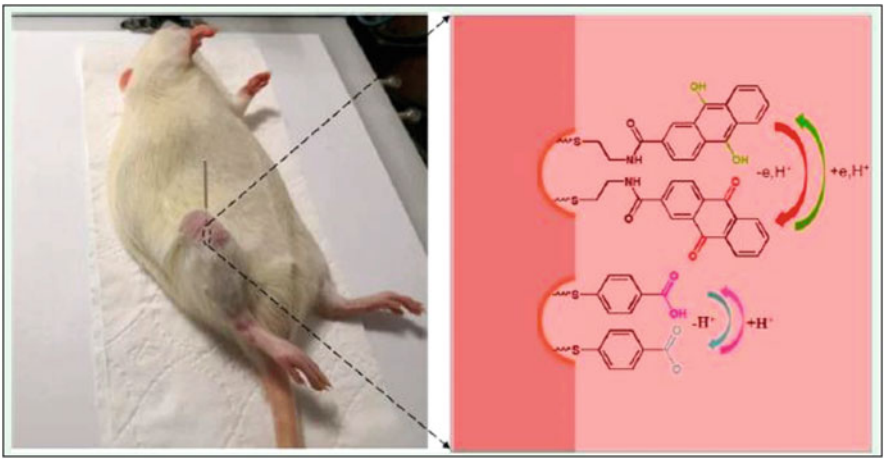

Fig. 3.22 Illustration of a redox SERS probe for monitoring the redox potential in rat joint [34]

By various strategies, the redox SERS probes can be used to monitor the redox potentials in cell, surface of tissues, superficial layer of tissues, and deep domain of tissues, which suggest that SERS-related methods can be used in all soft tissues.

3.5 Summary and Outlook

Bioanalytical technologies have always been key pushers for the progress of biology and medicine. Raman spectroscopy is widely used to provide chemical and physical information based on vibrations in molecules. It is also a qualitatively or semi-quantitatively analytical tool for ultrasensitive detection benefited from the design and fabrication of nanostructures with high SERS activities. The Raman-related techniques are desirable for monitoring biological samples in situ and real time because their applications are performed without considering physical states of samples such as states, temperature, morphology, and size. Many attempts have been carried out to use Raman spectroscopy to detect target molecules in vivo. Along with the further combination of Raman-related techniques, biology, and medicine, Raman spectroscopy would be a key to open ultimate mystical doors of biology and medicine.

References

1. Smith E, Dent G. Modern Raman spectroscopy: a practical approach. Hoboken, NJ: John Wiley & Sons; 2005. p. 135–79.

2. Alvarez-Puebla RA, Liz-Marzán LM. Traps and cages for universal SERS detection. Chem Soc Rev. 2012;41:43–51.
3. Nie SM, Emory SR. Probing single molecules and single nanoparticles by surface-enhanced Raman scattering. Science. 1997;275:1102–6.
4. Huefner A, Kuan WL, Muller KH, Skepper JN, Barker RA, Mahajan S. Characterization and visualization of vesicles in the endo-lysosomal pathway with surface-enhanced Raman spectroscopy and chemometrics. ACS Nano. 2016;10:307–16.
5. Cao X, Shan Y, Tan L, Yu X, Bao M, Lia W, Shi H. Hollow Au nanoflower substrates for identification and discrimination of the differentiation of bone marrow mesenchymal stem cells by surface-enhanced Raman spectroscopy. J Mater Chem B. 2017;5:5983–95.
6. Lussier F, Brule T, Vishwakarma M, Das T, Spatz JP, Masson JF. Dynamic-SERS optophysiology: a nanosensor for monitoring cell secretion events. Nano Lett. 2016;16:3866–71.
7. Kang B, Austin LA, El-Sayed MA. Observing real-time molecular event dynamics of apoptosis in living cancer cells using nuclear-targeted plasmonically enhanced Raman nanoprobes. ACS Nano. 2014;8:4883–92.
8. Panikkanvalappil SR, Hira SM, Mahmoud MA, El-Sayed MA. Unraveling the biomolecular snapshots of mitosis in healthy and cancer cells using plasmonically-enhanced Raman spectroscopy. J Am Chem Soc. 2014;136:15961–8.
9. El-Said WA, Kim SU, Choi JW. Monitoring in vitro neural stem cell differentiation based on surface-enhanced Raman spectroscopy using a gold nanostar array. J Mater Chem C. 2015;3:3848–59.
10. Aioub M, El-Sayed MA. A real-time surface-enhanced Raman spectroscopy study of plasmonic photothermal cell death using targeted gold nanoparticles. J Am Chem Soc. 2016;138:1258–64.
11. Zivanovic V, Semini G, Laue M, Drescher D, Aebischer T, Kneipp J. Chemical mapping of leishmania infection in live cells by SERS microscopy. Anal Chem. 2018;13:8154–61.
12. Li ZF, Li C, Lin D, Huang ZF, Pan JJ, Chen GN, Lin JQ, Liu NR, Yu Y, Feng SY, Chen R. Surface-enhanced Raman spectroscopy for differentiation between benign and malignant thyroid tissues. Laser Phys Lett. 2014;11:045602.
13. Shen YT, Liang LJ, Zhang SQ, Huang DS, Zhang J, Xu SP, Liang CY, Xu WQ. Organelle-targeting surface-enhanced Raman scattering (SERS) nanosensors for subcellular pH sensing. Nanoscale. 2018;10:1622–30.
14. Zhang Z, Han X, Wang Z, Yang Z, Zhang W, Li J, Yang H, Ling XY, Xing B. Chem Commun. 2018;54:7022–5.
15. Cao Y, Li DW, Zhao LJ, Liu XY, Cao XM, Long YT. Highly selective detection of carbon monoxide in living cells by palladacycle carbonylation-based surface enhanced Raman spectroscopy nanosensors. Anal Chem. 2015;87:9696–701.
16. Li DW, Qu LL, Hu K, Long YT, Tian H. Monitoring of endogenous hydrogen sulfide in living cells using surface-enhanced Raman scattering. Angew Chem Int Ed. 2015;54:12758–61.
17. Jiang J, Auchinvole C, Fisher K, Campbell CJ. Quantitative measurement of redox potential in hypoxic cells using SERS nanosensors. Nanoscale. 2014;6:12104–10.
18. Wang Y, Yang Q, Sun J, Nie M, Dong J, Qian W. Gold nanoflowers modified ITO glass as SERS substrate for carbon tetrachloride-induced acute liver injury in vitro detection. RSC Adv. 2016;6:115189–95.
19. Chen H, Wang Z, Zong S, Wu L, Chen P, Zhu D, Wang C, Xu S, Cui Y. SERS-fluorescence monitored drug release of a redox-responsive nanocarrier based on graphene oxide in tumor cells. ACS Appl Mater Interfaces. 2014;6:17526–33.
20. Zhang D, Huang L, Liu B, Ge Q, Dong J, Zhao X. Quantification of multiplex respiratory tract infection pathogen via lateral flow microarray based on SERS nanotags. Theranostics. 2019;9:4849–59.
21. Nima ZA, Mahmood M, Xu Y, Mustafa T, Watanabe F, Nedosekin DA, Juratli MA, Fahmi T, Galanzha EI, Nolan JP, Basnakian AG, Zharov VP, Biris AS. Circulating tumor cell

identification by functionalized silver-gold nanorods with multicolor, super-enhanced SERS and photothermal resonances. Sci Rep. 2014;4:4752.
22. Wang Z, Zong S, Wang Y, Li N, Li L, Lu J, Wang Z, Chen B, Cui Y. Screening and multiple detection of cancer exosomes using an SERS-based method. Nanoscale. 2018;10:9053–62.
23. Shi B, Zhang B, Zhang Y, Gu Y, Zheng C, Yan J, Chen W, Yan F, Ye J, Zhang H. Multifunctional gap-enhanced Raman tags for preoperative and intraoperative cancer imaging. Acta Biomater. 2020;104:210–20.
24. Huang Y, Zhang X, Ringe E, Ma L, Zhai X, Wang L, Zhang Z. Detailed correlations between SERS enhancement and plasmon resonances in subwavelength closely spaced Au nanorod arrays. Nanoscale. 2018;10:4267–75.
25. Li H, Yang Q, Hou J, Li Y, Li M, Song Y. Bioinspired micropatterned superhydrophilic Au-Areoles for surface-enhanced Raman scattering (SERS) trace detection. Adv Funct Mater. 2018;28:1800448.
26. Bai S, Serien D, Hu A, Sugioka K. 3D microfluidic surface-enhanced Raman spectroscopy (SERS) chips fabricated by all-femtosecond-laser-processing for real-time sensing of toxic substances. Adv Funct Mater. 2018;28:1706262.
27. Goodacrea R, Grahamb D, Faulds K. Recent developments in quantitative SERS: moving towards absolute quantification. Trends Anal Chem. 2018;102:359–68.
28. Stuart DA, Yuen JM, Shah NC, Lyandres O, Yonzon CR, Glucksberg MR, Walsh JT, van Duyne RP. In vivo glucose measurement by surface-enhanced Raman spectroscopy. Anal Chem. 2006;78:7211–5.
29. Garai E, Sensarn S, Zavaleta CL, Loewke NO, Rogalla S, Mandella MJ, Felt SA, Friedland S, Liu JTC, Gambhir SS, Contag CH. A real-time clinical endoscopic system for intraluminal, multiplexed imaging of surface-enhanced Raman scattering nanoparticles. PLoS One. 2015;10: e0123185.
30. Dong J, Chen Q, Rong C, Li D, Rao Y. Minimally invasive surface-enhanced Raman scattering detection with depth profiles based on a surface-enhanced Raman scattering-active acupuncture needle. Anal Chem. 2011;83:6191–5.
31. Auchinvole CAR, Richardson P, McGuinnes C, Mallikarjun V, Donaldson K, McNab H, Campbell CJ. Monitoring intracellular redox potential changes using SERS nanosensors. ACS Nano. 2012;6:888–96.
32. Jie S, Dong J, Shuyan H, Wang Y, Yang Q, Weiping Q. Redox state detection of fruits and vegetables by a simple surface-enhanced Raman scattering method. J Nanosci Nanotechnol. 2018;18:4891–7.
33. Sun J, Han S, Wang Y, Zhao G, Qian W, Dong J. Detection of redox state evolution during wound healing process based on a redox-sensitive wound dressing. Anal Chem. 2018;90:6660–5.
34. Pan C, Li X, Sun J, Li Z, Zhang L, Qian W, Wang P, Dong J. A multiplexed SERS-active microneedle for simultaneous redox potential and pH measurements in rat joints. ACS Appl Bio Mater. 2019;2:2102–8.

Chapter 4
Nanophotonic Techniques for Single-Cell Analysis

Muhammad Shemyal Nisar and Xiangwei Zhao

Abstract Single-cell analysis is an essential tool with numerous applications in biological and medical analyses. Nanophotonic techniques are emerging methods that use nanoscale devices and electromagnetic waves to extract information from a single cell. These techniques generally use the visible spectrum or the near-IR region of the electromagnetic spectrum. Various techniques have been developed by researchers, each for a specific purpose. These methods include mass spectrometry, quantum dots, nanolasers and spasers, optofluidics, zero-mode waveguides, nanoantennas, etc. This chapter gives an overview of these techniques when applied for single-cell analysis. Their basic working principles, key variants, and benefits are explained in detail.

Keywords Single-cell analysis · Spectroscopy · Resolution · Nanophotonics

4.1 Introduction

A cell is a basic unit of any biological organism. It was first visualized in the seventeenth century using an optical microscope. Lamarck claimed at the time that the matter contained in the cell has liquid phase and that all organisms were composed of cells. The later works of Schleiden and Schwann proved these claims. A cell is of central importance for the fields of cell biology, electrophysiology, and even molecular biology [1]. A single cell is depicted in Fig. 4.1, showing the different components of the cell, including the nucleus, cytoplasm, and plasma membrane.

The application of single-cell analysis includes, but is not restricted to, transcriptomics, metabolomics, single-cell genomics, and proteomics at the level of an individual cell. Transcriptomics is the study of transcriptomes and their

M. S. Nisar · X. Zhao (✉)
State Key Laboratory of Bioelectronics, School of Biological Science and Medical Engineering, Southeast University, Nanjing, China
e-mail: xwzhao@seu.edu.cn

X. Zhao, M. Lu (eds.), *Nanophotonics in Biomedical Engineering*,
https://doi.org/10.1007/978-981-15-6137-5_4

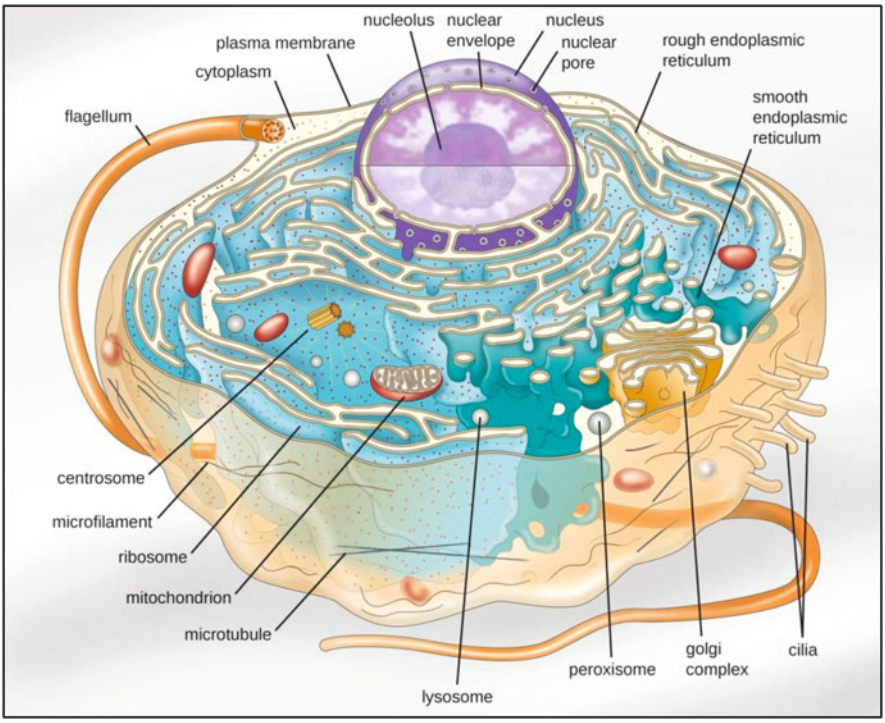

Fig. 4.1 Schematic of a eukaryotic cell [2]

functions. Transcriptomes are the sets of RNA molecules in a single cell [3, 4]. Transcriptomics analyzes which genes expressed in each cell are useful for RNA splicing, cell typing, and studying gene dynamics. Transcriptomics is also useful for understanding embryonic development [5]. Specific cellular processes leave behind uniquely characteristic chemical fingerprints. The scientific method of analyzing such prints is known as metabolomics [6]. Metabolomics at a single cell level gives access to a molecular-level understanding of cancer, stem cells, drug resistance, and aging, as well as cellular response to environmental stress and cellular functions [7]. Proteomics quantitatively and comprehensively analyzes and describes the cellular mappings of proteins and the changes which they undergo [8, 9]. Understanding the proteome at a single cell level can lead to an understanding of how a cell operates and how the gene expression changes with different stimuli [10]. Genomics tracks the changes occurring in the population of the bacteria. The second primary focus of genomics is to understand the genetic evolution of cancer cells, which can only be achieved by single-cell analysis [5, 11]. Single-cell analysis is a robust method that has enabled mapping of the distribution of biomolecules with subcellular resolution [12]. The single-cell analysis is essential because a single cell holds transcribed in itself the architectural blueprint of the genome, which is of central importance to all life.

The single-cell analysis has been a powerful tool in making promising breakthroughs. It provides unique insights into the variability of diseases and their treatments, highlighting the differences and the causes of those differences [13]. It has improved our understanding of mutations leading to brain cancer [14, 15]. Patti and colleagues used single-cell analysis for understanding neuropathic pains [16]. A study conducted by Qiu et al. identified the profiles of transcription from the hippocampus of the mouse and its neocortical neurons through single-cell RNA sequencing [17, 18]. One of the first studies on the topic of germline transmission analyzed single sperm cells. The analysis revealed an average of 22.8 events of recombination, 5–15 events of gene conversion, and 25–36 de novo mutations in each sperm cell [19]. Although most of the studies on germline are conducted using sperms, a study by Hou et al. used Multiple Annealing and Looping Based Amplification Cycles (MALBAC) for the analysis of oocytes [20]. MALBAC has the advantage of lower error rate in the reduction of amplification bias during genome analysis.

Progress in the field of embryogenesis has provided a better understanding of the transcriptional regulations and the reprogramming of the epigenome at the earliest stages of the embryogenesis [21–24]. Single-cell sequencing can answer a host of challenging questions. These questions have been aptly alluded to in the works of Eberwine: "How many distinct cell types exist in the 100 trillion cells of the human body? What is the role of somatic DNA alteration in cell identity and diversity? If physical changes are prevalent, are they random or part of a genomic program? Is the phenotype of a cell programmed by its genome or the result of community-coupled cell-state dynamics? That, to use a metaphor, is DNA the program or just informational storage?" [25, 26].

Confounding of genotypic and phenotypic heterogeneity present in bulk samples is of significant concern for the validity of acquired data. In recent work, Macaulay et al. achieved single-cell sequencing without data getting confounding. Future development in this field is bound to refine the prevalent approaches further. With the progress in this field, production of "an atlas of cell states" and their lineages for microorganisms, tissues, and organisms has become a real possibility [27].

The single-cell analysis methods are broadly categorized into three types: fluorescence detection, amperometric detection, and mass spectrometric detection. Isolating a single cell is an essential step for many of the single-cell analysis techniques. Contemporary methods for single-cell isolation include micromanipulation, Raman tweezers, microfluidics, manual methods, and fluorescence-activated cell sorter (FACS) [28, 29].

4.2 Why Nanophotonics?

Nanophotonics is a subject that studies the behavior of light on a nanometer scale. This includes the interaction of light with nanometer-scale objects. Nanophotonics can also involve nanometer-scale metallic components, although it is better referred to as plasmonics.

Researchers of biological and medical sciences want to image cells, their intercellular region, as well as the intracellular region for various purposes elucidated above. Nanophotonics is a suitable method for these research areas because it allows the observation at such a small scale. The communication of cells with each other involves the collaboration of various signaling proteins [30]. Traditional methods measure the average behavior of an ensemble of cells. This averaging results in the concealment of the behavior of an individual cell. The contemporary advancement in the field of nanotechnology has enabled considerable developments in the field of biosensing, leading to single-cell analysis. The details which could not be observed with the earlier technology due to their limited level of resolution can be monitored by incorporating instruments derived from nanotechnology applications.

Nanophotonics can achieve the necessary level of resolution for single-cell analysis because the dimensions of the instruments used for analysis of a cell are comparable to the dimensions of the cell itself. The equivalence of the physical scale enables the system to achieve the necessary resolution to undertake a single-cell analysis. Various tools used in nanophotonics to investigate single cells include nanoparticles, wires, ring resonators, and nanoholes. These elemental nanophotonic particles are the building blocks for the nanophotonic systems for performing single-cell analysis.

4.3 Scanning Near-Field Optical Microscopy (SNOM) for Mass Spectroscopy

The operational principles of scanning near-field optical microscopy (SNOM) are similar to those of scanning tunneling microscopy (STM) [31], as shown in Fig. 4.2. A submicron tip is held close to the surface of the sample. The waves are tunneled from the substrate, through the tip, and across space toward the sample. The received intensity is monitored during the scan, which is then used to build an image of the surface. Typically, SNOM can achieve a lateral resolution of 50 nm and vertical resolution of 5 nm [34, 35].

In recent work, Abeyasinghe proposed a combination of near-field optical microscopy and two-photon excited fluorescence to investigate gold quantum dots with a 30 nm point resolution. The method has potential applications in ultrasensitive sensing, disease diagnostics, cancer treatment, and high-density data storage [36]. The near-field imaging breaks the diffraction barrier through well-established methods of using evanescent waves. Microscopy using evanescent

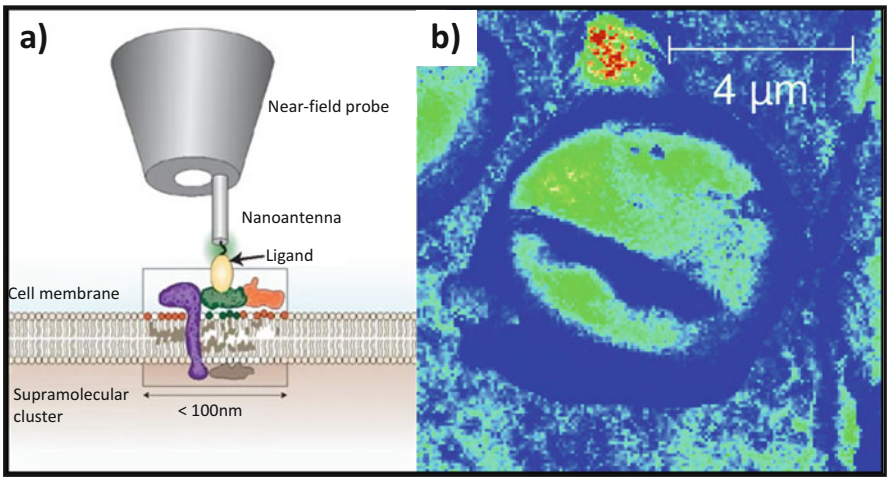

Fig. 4.2 (**a**) Schematic of the SNOM tip operating on a sample [32]; (**b**) s-SNOM third harmonic image, taken at $\lambda = 9.81$ mm, ~20 min scan time and 67 nm pixel resolution. The resolution here is ~140 times better than the diffraction limit at this wavelength and allows imaging of the chemical contrast within the cancer cell [33]

waves implies the presence/fabrication of subwavelength microstructures. In an older study, Raman spectroscopy and SNOM were performed together by assembling a system named as ATR-SNOM-Raman by Futamata et al. [37]. The system was able to perform relatively sensitive imaging at atmospheric pressure using argon-ion laser. The method provided topographic as well as Raman information. The group used this system to analyze thin copper phthalocyanine.

All the studies mentioned above involve non-biological analytes. On the other hand, Butler et al. studied biological analytes using Raman spectroscopy instead of SNOM [38]. As many elements have a unique Raman spectrum, this property is used to obtain information about the Raman spectra of the analyte. The knowledge about the elements can be used to ascertain the biological compounds present. Butler and his team provided a very detailed study about the use of Raman spectroscopy for biological samples along with maps for fresh plant tissues, mammalian tissues, fixed cells, and biocells.

Methods presented by Butler et al. [38] and Futamata et al. [37] are attractive alternatives for performing chemical characterization of the analyte. However, these methods require extensive sample preparation steps which are time-consuming as well as expensive in terms of effort and material costs [39]. Whereas, SNOM is potentially an effective method to achieve very high resolution of the analyte. SNOM operates at atmospheric pressure and requires little or no sample preparation steps, making it an even more desirable alternative. However, until recently, SNOM has not been successful for providing chemical information of the analyte, and it has been used only to obtain topographical information about the sample. Suggestions

have been made to incorporate SNOM with Raman [40] and obtain chemical information from Raman spectra.

Nevertheless, in recent work, SNOM has been used to gain chemical information from a sample of breast cancer cells. This research utilized scattering-type scanning near-field optical microscopy (s-SNOM), which analyzes the backscattered photons, along with quantum cascade diode lasers (QCDL). As the backscattered signal is generally weak, it is more commonly used along with CO_2 laser or, in rare instances, with nonlinear frequency mixing technology [41] for achieving a coherent IR source. The advent of QCDLs has changed that [33]. Therefore, the SNOM device from this group used a tip with a 10 nm radius oscillating at frequencies in the 50–300 kHz range.

4.4 Nanoantennas

Nanoantennas are generally plasmonic nanostructures made of a metal (e.g., gold, silver, and aluminum) on a dielectric substrate. Surface plasmon polaritons (SPP) and strong localized enhancement of the electric field and the magnetic field are known traits of plasmonic structures [42]. The strong localized enhancement of light and the associated optoelectronic response can be tailored according to specific needs by tuning the shape, size, and composition of the plasmonic nanoantenna on the nanoscale [43]. Modern advancements in fabrication technologies have enabled the possibility of tailoring nanoscale plasmonic structures. This ease of fabrication of plasmonic structures and their feasibility as an essential method for nanoscale analysis has led to increased use of nanoantennas for single-cell analysis. Confinement of light to nanoscopic regions enables the detection of single molecules important for single-cell analysis [44]. The only limitation for these nanoantennas is the high ohmic losses of metallic nanostructures, which lead to an increased local temperature at the measurement point [42], apart from the technological limitations in fabrication of such small structures.

In metals, interaction of light with nanostructures gives rise to the oscillation of free electrons. The mechanics of these oscillations are explained by Drude-Sommerfeld model (incorporating the Fermi statistics of quantum mechanics with the classical Drude-Lorentz model) [45–47]. When these free electrons oscillate collectively, it is known as localized surface plasmon resonance (LSPR). LSPRs induce measurable changes in the incident field, making subwavelength resolution possible. This subwavelength resolution is of great value to researchers for single-cell analysis [48].

Researchers have developed numerous structures for generating LSPR necessary for single-cell analysis. These structures can be categorized into two groups called surface-enhanced Raman scattering (SERS) and tip-enhanced Raman scattering (TERS). As apparent from the name, SERS employs nanostructures on the surface of a substrate that acts as an antenna and collects information under the operation conditions. The collected information is then interpreted using a spectrometer or

other digital technologies. On the other hand, TERS is a special type of SERS that uses the nanosurface of tip-like pointed structure for generating LSPR instead of nanostructured colloidal [49]. An additional advantage of the tip is that it can be moved around according to the requirements and is better suited for the in vivo analysis of samples. The topologies of these nanostructures vary from pure spherical nanoparticles to nanowires and rods to slot antennas [32]. These different topologies lead to effects such as photobleaching [50], enhancement [51, 52], confinement of light below the diffraction limit [53], and fluorescence quenching [54, 55]. The analysis of these effects is useful for the detection of single molecules at the concentration level, which is biologically relevant.

Until recently, nanoantennas were mainly used for optical trapping and for sensing through spectroscopy. A surface plasmon polariton (SPP)-based array of monopole antennas was used by a group from MIT to achieve biosensing. The monopoles of gold with 50 nm radius, 100 nm height, and a period of 500 nm were produced on a silica substrate. These monopoles are especially suited for producing strong light localization necessary for achieving near-field enhanced hot spots. The group was able to achieve significant index sensitivities and a reasonable figure of merits for the detection of small molecules [56]. The schematic of the gold nanorods used to achieve SERS is shown in Fig. 4.3a.

A recent study proposed a different topology using a shell-based structure instead of a nanorod. The study used a silica-based shell containing functionalized gold nanostar, as shown in Fig. 4.3b. The platform is named mechanical trap surface-enhanced Raman spectroscopy (MTSERS), which profiles and carries out 3D microscopic mapping of molecular signatures on the cell membrane through trapping of single cells [60]. The purpose of these shells is to amplify the SERS data, which enables label-free 3D molecular analysis.

Using colloidal gold or silver instead of nanorods is another method to conduct surface-enhanced Raman spectroscopy. The colloids are mostly made into near-spherical morphologies, but other shapes have been tried including nano-cylinders [57], nano-cubes [61, 62], nano-prisms [58, 63, 64], and nano-spheres [54, 59, 65, 66].

In a very innovative work, Insub Jung fabricated and used a two-block metal-polymer nanorod colloidal system. The colloidal system consisted of two segments with gold and polypyrrole (Au-PPy) nanorods. This two-block colloidal system showed extended surface plasmon resonance. The addition of doped polypyrrole to Au-nanorod enhanced the coherent electric field because of the distribution of π-electrons over the doped pyrrole section of the nanorod [57]. The schematic is shown in Fig. 4.3c.

Recently, colloidal systems with core-shell topologies have been used by various researchers, which produce better SERS enhancement factor compared to nanoparticles produced from metals. In one such study conducted in South Korea, gold nanoparticle core was used inside a shell made of an alloy of gold and silver. This morphology achieved SERS enhancement factor higher than 1.1×10^8, which was used for DNA detection through an ultrasensitive SERS-based platform

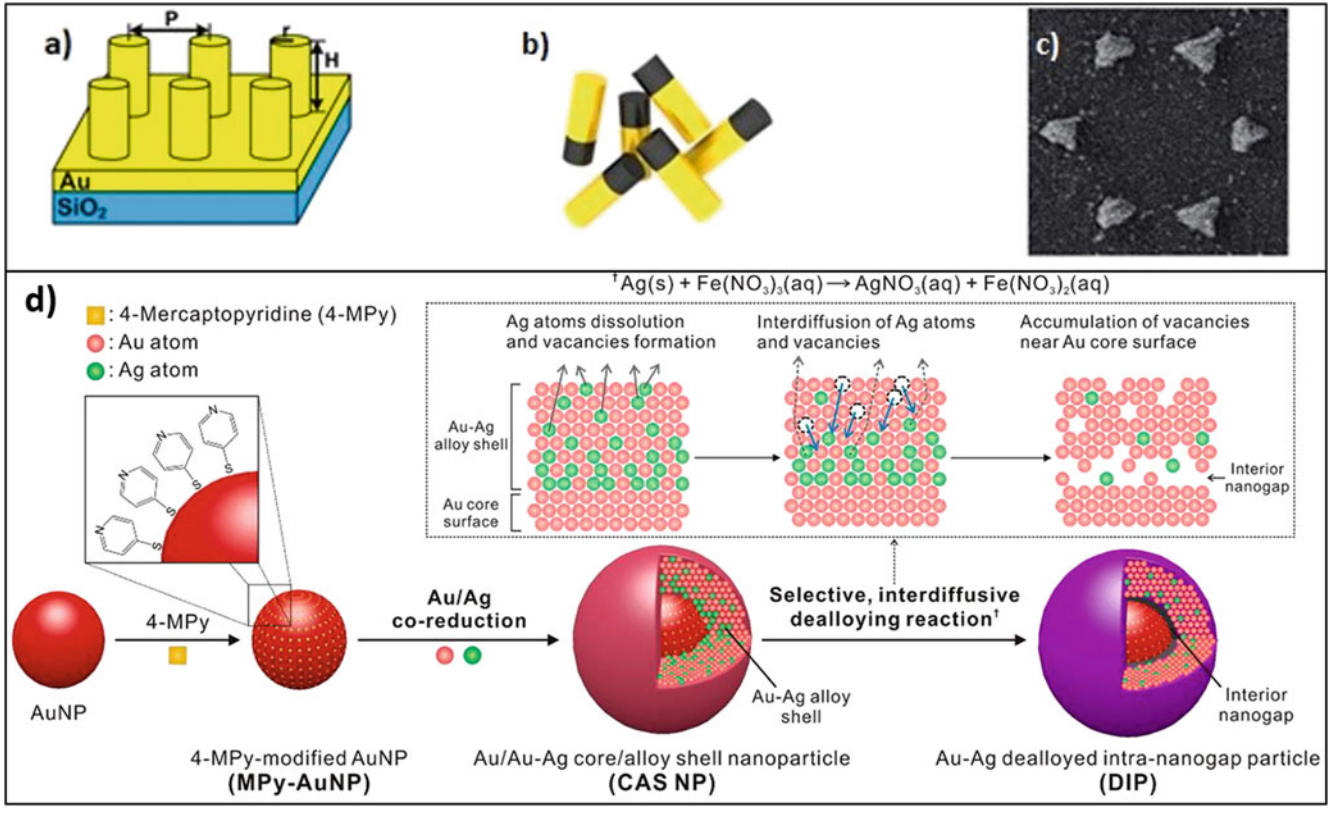

Fig. 4.3 (**a**) Surface plasmon polariton (SPP)-based array of monopole antennas used to achieve biosensing [56]. (**b**) Schematic of gold and polypyrrole (Au-PPy) nanorods used for SERS-based single-cell analysis [57]. (**c**) SEM image showing a nanostructure made from nanoprisms [58]. (**d**) Schematic illustration of the selective, interdiffusive dealloying (SID)-based strategy for the synthesis of Au-Ag dealloyed intra-nanogap particles (DIPs) from Au/Au-Ag core/alloy shell (CAS) NPs. The proposed mechanism of the SID reaction is shown in the black dotted box [59]

[59]. The schematic of these nanoparticles with core-shell structure is given in Fig. 4.3d.

As mentioned earlier, TERS has a unique advantage of the freedom of movement. The TERS-based mechanism has been used for the detection of protein glycosylation, as it can effectively distinguish between glycosylated and normal proteins [67]. TERS has also been used for detecting RGD-integrin binding in the cancer cell [68].

Various kinds of tips have been introduced over the years, such as tips with attached nanoparticles [68], pyramidal tips [69], conical tips [70], and tips with slot antenna [71, 72]. Each of these tips has its unique individual advantages and shortcomings. These various tips show different topologies that can be used to achieve Raman scattering-based spectroscopy. The aperture antennas are discussed in more detail in the next section on "zero-mode waveguide."

4.5 Zero-Mode Waveguide

A waveguide is a photonic structure that enables transmission of optical signals which can be manipulated or guided as and where required [69]. For a waveguide with a given set of dimensions, the cutoff frequency of transverse electric mode is given by [70]:

$$f_{c_{m,n}} = \frac{1}{2\pi\sqrt{\mu\varepsilon}}\sqrt{\left(\frac{m\pi}{a}\right)^2 + \left(\frac{n\pi}{b}\right)^2}$$

where "a" and "b" are the dimensions of two orthogonal sides of a rectangular waveguide such that $a > b$. For a circular waveguide, the cutoff frequency of transverse electric mode is given by [70]:

$$f_{c_{m,n}} = \frac{p'_{mn}}{2\pi a\sqrt{\mu\varepsilon}}$$

The transmitted signal decays exponentially when the aperture of the waveguide is reduced to less than that required by the cutoff frequency. The optical energy forms evanescent waves at the interface. As no mode propagates, the structure is called a zero-mode waveguide. The theoretical basis of ZMWs is well understood through Bethe-Bouwkamp theory [71–73] and Kirchhoff approximation [74, 75].

The schematic of a zero-mode waveguide is shown in Fig. 4.4. The usual choice of substrate is silica because it is transparent in the optical regime. On the other hand, gold or aluminum is used for the metal layer. Gold and aluminum are the metals of choice because of their excellent dielectric constant, while silver is not used because it is not suitable for biological analytes.

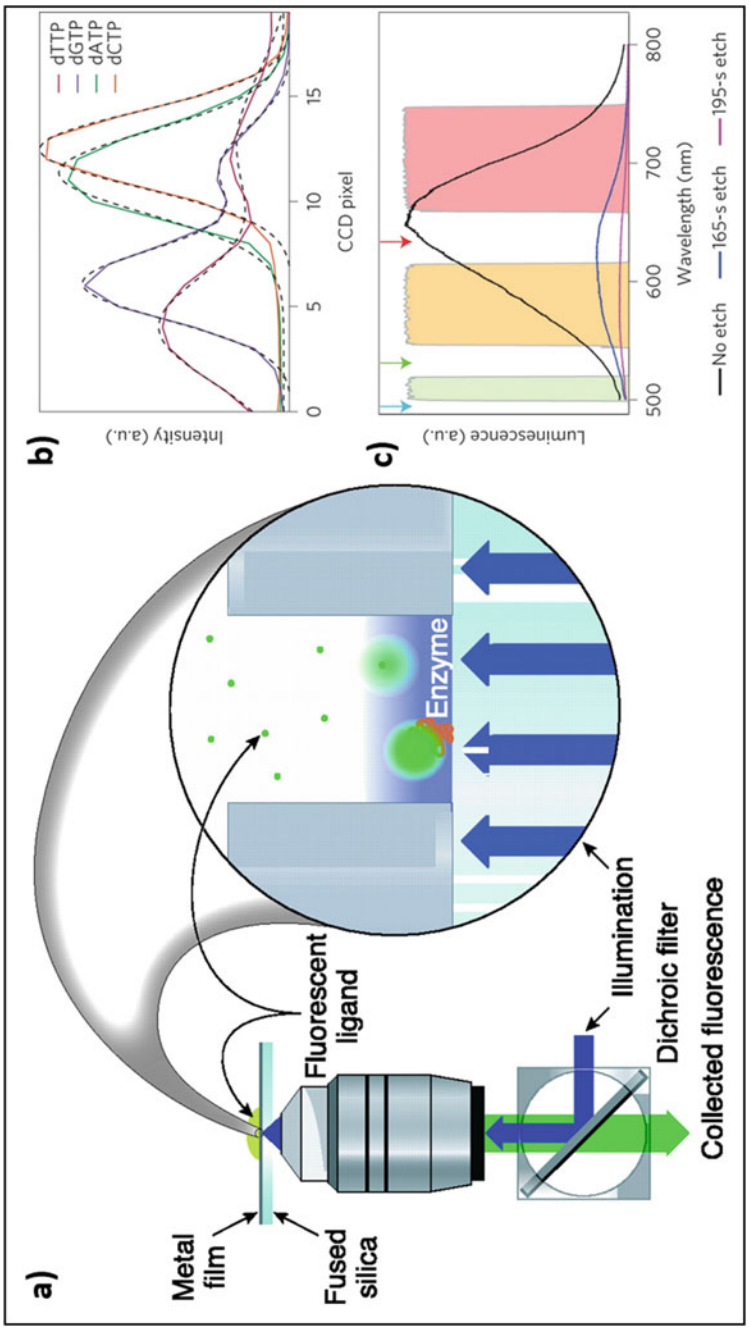

Fig. 4.4 (**a**) Schematic layout of zero-mode waveguide [76]. Typical height of the metal layer is around 100 nm, and the diameter of the nanopore varies from 30 to 300 nm. (**b**) Emission spectra from four nucleotide analogs as imaged on the emCCD, plotted with Gaussian fits for each analog (see dashed lines). Spectra from dT and dG analogs exhibit second minor peaks due to fluorescence rejected by the multiband fluorescence filters necessary for simultaneous 532 and 640 nm illumination [77]. (**c**) Photoluminescence spectra of NZMW devices as fabricated (black), as well as after successive periods of silicon nitride etching (red and blue; all spectra measured using 488 nm illumination). Thinning of the underlying low-stress silicon nitride membrane results in a low-photoluminescence SiO_2 NZMW base that allows single-molecule fluorescence measurements. Arrows illustrate illumination wavelengths. Green, orange, and red spectral bands of the microscope's multiband emission filters are shown [77]

A laser input is applied at the bottom of the substrate, which generates evanescent waves in the nanopore. These evanescent waves interact with the cells of the analyte, causing fluorescence. The fluorescence then travels back through the substrate and is then collected using an objective lens and a spectrometer. Among the methods used for spectrometry, fluorescence correlation spectroscopy (FCS) is a popular method for biological samples. FCS has been used for studying binding kinetics of DNA molecules [78]. As only a small volume of the analyte can be accommodated in a ZMW, it is useful in probing individual interactions by isolating the interactions in a small volume of zeptoliters.

In a study carried out at Cornell University, FCS was used in combination with ZMW to measure transport properties and oligomerization kinetics of repressors at high concentrations. ZMW was fabricated on 170-μm-thick fused silica with aluminum of film thickness 100 nm. The FCS was carried out with a confocal fluorescence microscope in the epi-illumination mode [79]. The same group carried out single-molecule spectroscopy using ZMW made from fused silica and aluminum to study lipid membranes. They fabricated ZMWs with diameters ranging from 50 to 200 nm, which were used to study systems involving ligand-receptor interactions by confining them to attoliter volumes [80]. In another study, a different group of researchers used ZMWs to examine individual receptors of the plasma membrane of a living cell to measure its stoichiometry [81]. One of the major problems faced by the abovementioned systems is very low signal to noise ratio.

By modifying the architecture of the ZMW, a Japanese team improved the SNR. The team used quartz and aluminum to fabricate an array of ZMWs. The modification introduced by them was to make the hole deeper into the quartz layer. This reduced the SNR of the system to half of the SNR of conventional system, enabling them to monitor protein-protein binding in a zero-mode waveguide [82]. In more recent work, Lawrence Zaino and his team from the University of Notre Dame imaged single flavin mononucleotide (FMN) for spectroelectrochemical investigations using zero-mode waveguide arrays. The group fabricated the ZMW with a 100-nm-thick gold layer on top of the glass substrate. For their purpose, they used over-etched ZMW with inclined walls, as shown in the schematic given in Fig. 4.5 [83]. Their system was able to achieve a very good signal to noise ratio due to the use of gold as cladding material. This ensured that only oxidized FMN molecules were stimulated. It was also a major reason for improved performance. This study was instrumental in providing a method for spectroelectrochemical investigation of single enzyme molecules [84].

4.6 Optofluidics

Optofluidics is a branch of microfluidics that uses optical methods in combination with conventional microfluidics to improve the resolution of the system. Microfluidic platforms are gaining popularity because of their ease of use, scalability, and cost reduction in the analysis of biological samples [85]. On the other hand,

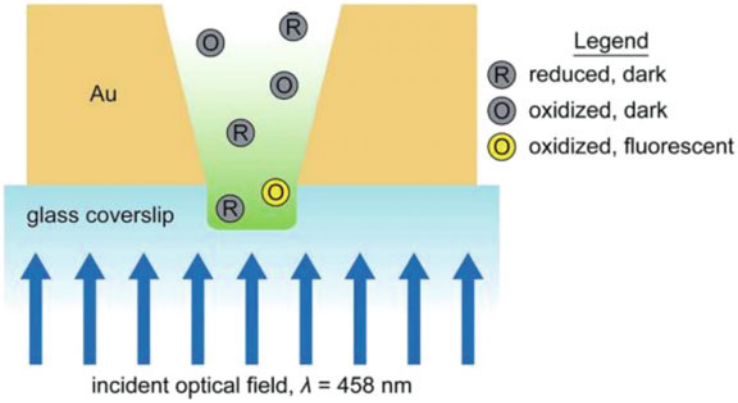

Fig. 4.5 Schematic of over-etched ZMW used by Lawrence and his team to study the redox reaction of FMNs [83]

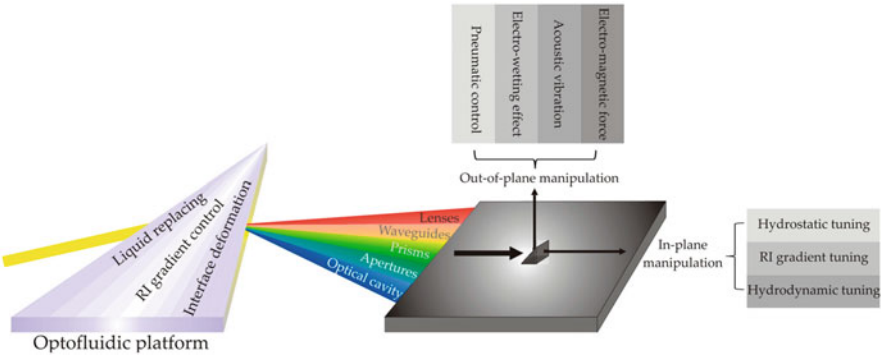

Fig. 4.6 Categorization of optofluidic platforms in terms of their working mechanisms [86]

optofluidics makes use of light for manipulating light on the microscale [86]. This manipulation of light on the micro-/nanoscale can be used to achieve optofluidic interferometry, optofluidic cytometry, optofluidic spectrometry, and on-chip manipulation of micro-objects. Some of these technologies have been commercialized by various companies to provide tunable GRIN lens [86–88] and micro-tweezers [86, 89]. Figure 4.6 presents the categorization of optofluidic platforms in terms of their working mechanisms and the results achievable with them.

As seen from Fig. 4.6, liquid replacing, RI gradient control, and interface deformation are the three main types of optofluidic platforms. These platforms can be used to achieve lenses, waveguides, prisms, apertures, and optical cavities. Out-of-plane manipulation and in-plane manipulation are the two broad categories of desired effects that can be achieved using these platforms. In-plane manipulation includes hydrostatic tuning, RI gradient tuning, and hydrodynamic tuning, whereas

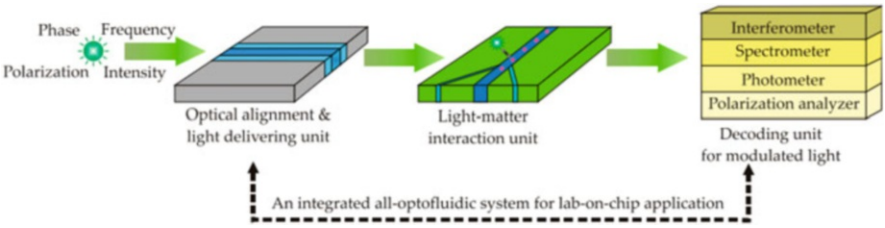

Fig. 4.7 Schematic of the optofluidic system used for lab-on-chip applications [86]

out-of-plane manipulation includes pneumatic control, electro-wetting effect, acoustic vibration, and electromagnetic vibrations.

These platforms are incorporated in the larger scheme for optofluidic analysis, as shown in Fig. 4.6. The platforms (and the effects they achieve) listed in Fig. 4.4 constitute the light-matter interaction unit of an optofluidic system. Figure 4.7 shows the schematic of an optofluidic system. The light is emitted from a source with a particular phase, frequency, polarization, and intensity and then delivered to the platform using "optical alignment and light delivering unit." The light interacts with the analyte at the "light-matter interaction unit" shown in Fig. 4.7. Subsequently, it is collected and then decoded using an interferometer, spectrometer, photometer, or a polarization analyzer according to the requirements of specific experimental designs.

Optofluidics has been used to implement microinterferometric systems for the measurement of dispersive properties of liquids [90], sensing applications [91], label-free detection of liquid bio-samples [92], and single-cell microalgal lipid screening [93]. Baoshan Guo and his multinational group used optofluidic devices along with time-stretch quantitative phase microscopy and achieved a high-throughput of 10,000 cells/s that was label-free and single-cell. The group used this system to characterize the heterogeneous population of *E. gracilis* cells. The heterogeneous population consisted of cells cultured under different conditions, and the system produced an error rate of merely 2.15% [93].

Other groups, such as that of Andy K. S. Lau from Hong Kong, have also used time-stretched microscopy along with an optofluidic platform to conduct high-throughput cytometry of heterogeneous population of yeast cells at the rate of 100,000 cells/s [94]. This technique also enables the identification of biomarkers on individual cells, which has mostly been an unexploited area of research. Single-cell diffraction tomography was conducted by a group led by Paul Muller using an optofluidic platform [95]. The group combined microfluidic flow and optical trappings to rotate single cells along the perpendicular axis.

Optofluidics has been useful for allowing the separation of different chemical species, biochemical species, and cells in the liquid phase. In one such work carried out by a team from South Korea, label-free separation of blood cells was carried out. The cells were distinguished by their optical mobility [96]. The optical mobility of lymphocytes, monocytes, granulocytes, and red blood cells was measured under different conditions [97]. The detection of virus using lab-on-chip optofluidic methods has also been achieved [98]. Similarly, Cai and colleagues developed an

optofluidic system for direct detection of the Ebola virus through on-chip PDMS-based microfluidic chip [99].

DNA sequencing is another vital area of research which has been explored using optofluidic methods. A Dutch team of scientists successfully attempted to sequence and separate DNA with an accuracy of $S = 4 \times 10^{-4}$ [100]. The group created a microfluidic chip through which analyte containing red-labeled and blue-labeled DNA molecules was passed. The fragments were separated according to size using capillary electrophoresis performed using two power modulated femtosecond lasers at different frequencies. The fluorescence was finally detected using a photomultiplier, and the subsequent Fourier analysis helped to distinguish between red- and blue-labeled DNA fragments. DNA sequencing has also been carried out in other studies through photopolymerization in microfluidic devices [101] and using the shift in wavelength of reflected IR waves [102].

4.7 Mass Spectrometric Imaging

Mass spectrometry is a method of identification of chemicals and substances through their ionization and the subsequent sorting of the ions based on the mass-to-charge ratio. Ample attention has been devoted to mass spectrometry in order to improve the existing methods and introduce new methods. The improvements in the framework have been on improving the resolution on the system.

Mass spectrometric imaging is a method that sensitively detects molecules through their ions. Mass spectrometric imaging allows molecular information of the sample to be collected in two or three dimensions depending upon the need or the limitations of the specific method employed [103]. The schematic of the basic principles used for mass spectrometry is given in Fig. 4.8.

The performance attributes of mass spectrometric imaging are lateral spatial resolution, mass resolution, and duty cycle. The figures of merit of a mass spectrometric imaging system are defined by the ionization sources and mass analyzers employed [103].

The advent of mass spectrometry dates back to the beginning of the twentieth century. The early methods for mass spectrometry had numerous limitations where the process was carried out on a sample placed in a container in vacuum. As the analysis was carried out in vacuum, it limited the types of samples that could be tested. Moreover, complicated sample preparation procedures also limited the possible analytes and added extra steps to the process, making it more time-consuming and expensive [105–108].

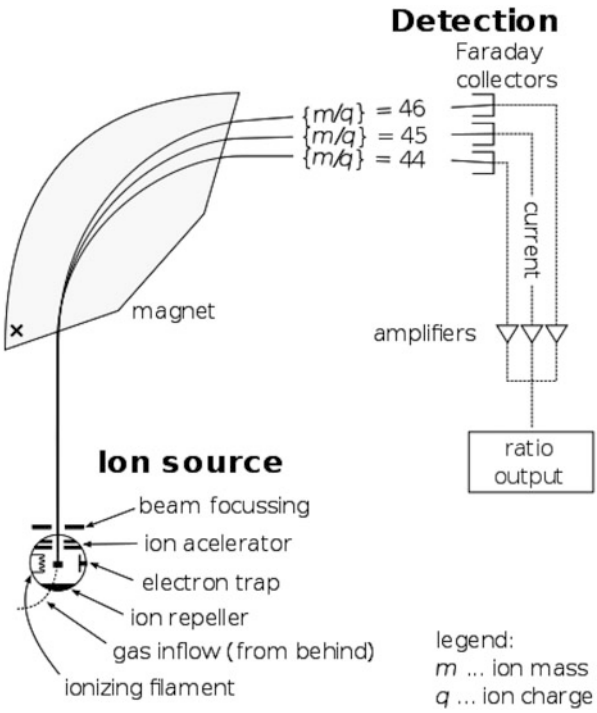

Fig. 4.8 Schematic showing operating principles of mass spectrometry [104]

4.7.1 Ionization Process

The ionization process is the most crucial step in the mass spectrometric system. Various methods of ionization have been adopted over the years, including chemical ionization, electron ionization, electron spray ionization [109], and matrix-assisted ionization [110]. Among these, electron spray ionization and matrix-assisted ionization are considered more suitable ionization methods for biological samples. In laser-based ionization, the interaction of laser radiation with nanostructures results in unique processes and phenomena. The nature of the resulting phenomenon depends on various factors, such as structural dimensions, material properties, and the characteristics of the laser pulse employed for the experiment [111–114].

Various techniques have been developed over the years, with each having its advantages and disadvantages. Among these dozens of techniques, three of the most commonly used techniques are matrix-assisted laser desorption ionization (MALDI) [115], secondary-ion mass spectrometry (SIMS) [116], and desorption electrospray ionization (DESI) [117–119].

MALDI improves the ionization mass of the sample manyfolds by the addition of matrix elements (cobalt nanoparticles and glycerol) in the sample during ionization using a laser-based ionization source [110, 114, 115]. In MALDI, the ionization occurs due to rapid phase transitions induced by using a laser source, which releases

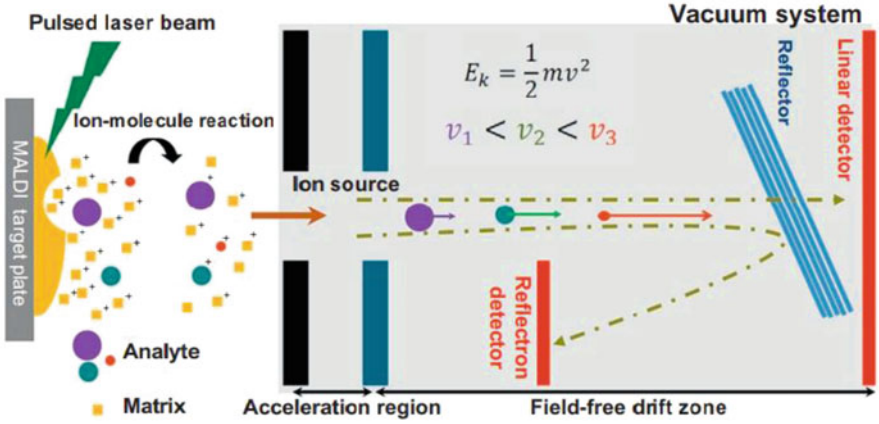

Fig. 4.9 Schematic of AP-MALDI [123]

the biomolecule from the matrix and allows it to be ionized by the plume [120, 121]. This technique quickly became popular as the method of choice for a range of research projects. The cost of this manyfold mass increase is the noise from the matrix elements which affects the results. The noise restricts the observable molecules in the sample, making the analysis of smaller molecules difficult [114]. Subsequently, further methods were developed, which removed the overheads introduced by the steps of sample preparation and vacuum creation. These methods came to be known as atmospheric pressure mass spectrometry (AP-MS).

In AP-MS, the sample is placed at atmospheric pressure rather than in vacuum and with minimum or no sample preparation steps required for the analyte. These developments led Victor et al. to develop MALDI-MS as a technique for conducting mass spectrometry at atmospheric pressure, which was called AP-MALDI [122]. The schematic of AP-MALDI is given in Fig. 4.9.

The advent of MALDI was followed by researchers from across the globe looking for development of methods based on laser desorption and ionization (LDI) but without the disadvantage of matrix noise in the output results. These efforts resulted in the development of numerous other methods. These LDI-based variants of MALDI include the use of graphite-based matrix surface for ionization enhancement often called SALDI [124, 125], use of gold nanowires [126, 127], use of silver nanowires [128], use of germanium nanodots [129, 130], platinum nanoflowers [131], graphite-assisted laser desorption ionization (GALDI) [132], silicon nanowires [133, 134], and nanostructured silicon surfaces [135–137].

In particular, Bennet Walker et al. introduced one of the most novel and successful techniques called nanopost array (NAPA) [138]. This group used nanoposts on a silicon substrate (schematic shown in Fig. 4.10) to enhance the ion production of the system. The silicon nanopost array-based ionization is used along with curved-field reflectron time-of-flight (ToF) mass spectrometer and an ultraviolet nitrogen laser. The height and diameter of these posts are 1 μm and 100 nm, respectively, and the

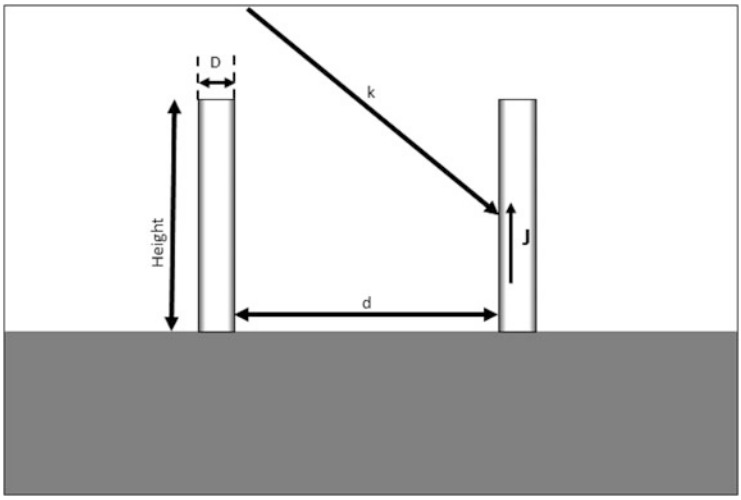

Fig. 4.10 Schematic of nanopost array for mass spectrometry with post diameter, *D*, and the distance between two adjacent posts, *d*. Incident laser beam propagates with wave vector, *k*, and generates current density, *J*

distance between two adjacent posts is 350 nm. This nanostructured surface achieves a mass range of 50 to 1500 Da with the limit of detection being 800 and 20 zmol. This performance is because of the generation of nano-current in the posts, which raises the surface temperature by several orders of magnitude and therefore ionizes the analyte. However, the results from NAPA depend on the polarization of the incident laser beam. The method proved useful for numerous small molecules, including pharmaceuticals, natural products, explosives, and metabolites, with the additional advantage of no background due to the absence of matrix in the analyte composition, unlike MALDI [139].

Later work by the same group combined NAPA with laser desorption and ionization (LDI) to produce NAPA-LDI-MS [140]. They showed that the combination of NAPA with LDI is a powerful method for the detection of small molecules, which is of immense importance for metabolite analysis. NAPA-LDI-MS can detect large metabolic molecules as well as small molecules, thus widening the range of observable molecules. This technique is useful for the detection of many classes of molecules, including nucleotides, amino acids, xenobiotics, carbohydrates, lipids, etc. It was tested on extracted samples of human serum at a metabolite level [140], where the samples were both aqueous and organic extracts.

In more recent work, the group was able to improve the ionization efficiency of the nanoposts by adding triangular chromium features at the top of the nanopost array. The addition of these chromium features on the nanopost changed the geometry of the structure to “elevated bow tie” [141] and improved the ion production approximately by a factor of 17.

4.8 Nanolasers and Spasers

The concept of nanolaser was presented in 2003 by researchers from Georgia State University. These nanolasers are a type of laser with nanoscale dimensions. There are two kinds of nanolasers. The first kind is a photonic nanolaser, which has a photonic cavity at the nanometer scale that amplifies the light through stimulated emission. The photonic nanolasers are composed of dielectric materials. There are two major types of photonic lasers, namely, single-photon pumped lasers and two-photon pumped lasers. The single-photon pumped lasers use ultraviolet light as the source of excitation, while the two-photon pumped lasers use infrared light as the excitation source [142–144]. The second kind of nanolaser is called a spaser or a plasmonic laser. The spasers operate by confining the light into a subwavelength scale through the storage of light energy in electron oscillations called surface plasmon polaritons [145].

The figure of merit of any system used for single-cell analysis, including nanolasers, has to include practicability and sensitivity. The efficiency of all nanophotonic systems, especially that of nanolasers, is strongly related to optical saturation at high laser intensity, blinking effects, and photobleaching. Among the two types of photonic lasers, the use of single-photon pumped laser has certain drawbacks because it employs UV source. These drawbacks include short penetration depth because UV light is better absorbed in biological samples and destruction of the sample due to the high frequency of UV radiation. These drawbacks limit their use as biosensors and, therefore, for single-cell analysis. On the other hand, the two-photon pumped laser uses an infrared source, which is advantageous as it improves penetration depth due to its lower frequency, reduces damage to the biological sample, and avoids photobleaching [146, 147]. However, the two-photon pumped lasers have low quantum yield, smaller two-photon absorption, and faster Auger's recombination rate [147, 148].

A Chinese team of researchers tried to redress these shortcomings of two-photon pumped laser system using perovskite semiconductor nanocrystals. The nanoplates of perovskites, which are naturally formed through recrystallization process, can sustain whispering gallery mode and are advantageous for larger absorption cross section, larger optical gain, and higher fluorescence quantum yields [147].

A researcher from Japan functionalized the photonic lasers of GaInAsP and GaInAsP active layer with a quantum well on InP. This laser was successfully used for biosensing, protein sensing, DNA sensing, biotin sensing, and cell imaging [149]. Another Japanese team introduced a GaInAsP nanoslot nanolaser, which they used for protein sensing. The platform was tested on a standard protein, bovine serum albumin (BSA), and was able to achieve a detection limit as low as 17 pg/mL with a figure of merit of 230 on a sensing area of less than a square micrometer. These results were achieved by making two air holes in a triangular lattice air-bridge photonic crystal slab, which was shifted outward. They incorporated nanoslots with widths ranging from 30 to 70 nm in these holes, which localized the laser mode inside and around the nanoslot. The platform is shown in Fig. 4.11.

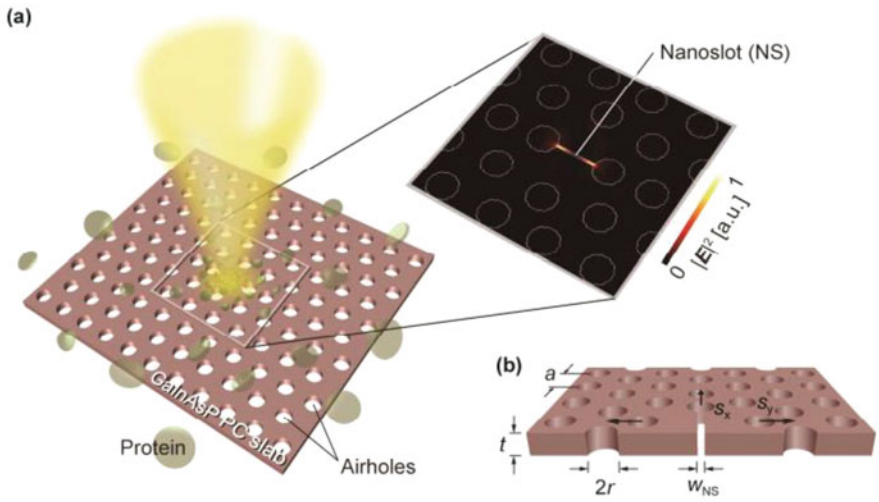

Fig. 4.11 NS nanolaser. (**a**) Schematic of the whole structure with biomolecules adsorbed and modal energy distribution calculated by the 3D finite-difference time-domain (FDTD) method. (**b**) Magnified cross section of NS [150]

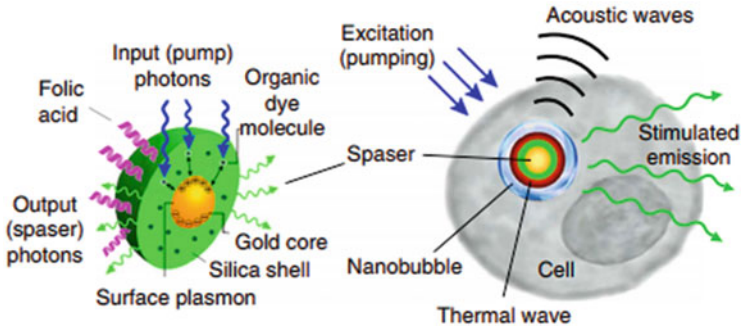

Fig. 4.12 Schematic of a nanospaser and its use as a probe on a cell [142]

Spasers, on the other hand, are plasmonic nanoparticles that are surrounded by a shell of the gain medium. The dimensions of both the plasmonic particle as well as the shell are at the nanometer scale. The spaser can fundamentally produce a bright light of a single-mode that is spectrally tunable and does not saturate. However, the spasers have certain drawbacks as well, which include high optical losses, low solubility, and toxicity [142, 151]. In a recent report, spasers of 22 nm excited by a single nanosecond laser pulse were made biocompatible and were successfully used as a molecular probe with ultrahigh brightness emission and ultranarrow emission spectra. The spaser simultaneously achieved high photoacoustic imaging contrast and photothermal destruction of cancer cells [142]. A schematic of the spaser used as a probe is shown in Fig. 4.12. In another work, spasers were

synthesized using gold nanorods, which were stabilized through CTAB bilayer such that the resonant peak for plasmons was between 680 and 700 nm [152].

However, the nanoparticle-based spasers suffer from low *Q*-factor and strong quenching near the resonator, which undermines the beneficial effects of a high Purcell factor. Furthermore, the near field of the spaser is particularly noisy due to poor β [153].

4.9 Quantum Dots

A quantum dot is a small, only several nanometers, structure of semiconductor material. The small size of quantum dot changes the electrical and optical properties of the material used to make the quantum dot. A quantum dot exhibits properties that lie in between those of bulk material and individual atoms and is also referred to as an artificial atom as it too has discrete electronic bound states like atoms and molecules. A quantum dot can be tuned to emit a specific frequency of light when electricity or light is applied to it. The frequency of the emission is tunable but depends on the size of the dot [154, 155].

The application of quantum dots in biology is based on their property of emitting light. They are used as a replacement for organic dyes because they are about 20 times more stable (significantly less photobleaching) compared to organic dyes and their fluorescence is about a hundred times brighter. The only shortcoming of a quantum dot is its irregular blinking while tracking single particles. Irregular blinking has been addressed by some research groups, and quantum dots that do not blink have been successfully produced [153, 156]. These traits of quantum dots make them an important contender for performing highly sensitive cellular imaging and tracking of cells over a long period. Furthermore, quantum dots can be targeted to specific proteins of a cell through binding them with antibodies, DNA, nucleic acid, or ligands.

Quantum dots have also been used for in vivo targeting of tumors. In vivo targeting of tumors is carried out using two different techniques called active targeting scheme and passive targeting scheme. Active targeting of a tumor is performed by functionalizing the quantum dot in such a way that it attaches to a specific tumor site and a tumor cell. On the other hand, passive targeting uses the better retention ability of tumor cells to deliver the quantum dots. Some of the materials used for quantum dots (such as CdSe under UV light) are toxic for cells. Such quantum dots can be coated with a polymer material to remove their toxicity [157, 158]. Hydrogel and silica are commonly used materials for encapsulating quantum dots. Using hydrogel for encapsulation makes cadmium quantum dots stable in aqueous solution (Fig. 4.13) [160, 161].

Imaging of single genomic loci using transcription activator-like effectors (TALEs) through quantum dot labeling has been successfully used to target HIV-1 proviral DNA sequences. These TALEs can enter the nucleus of a cell to provide fluorescent signals, which can then identify single gene loci. Through this

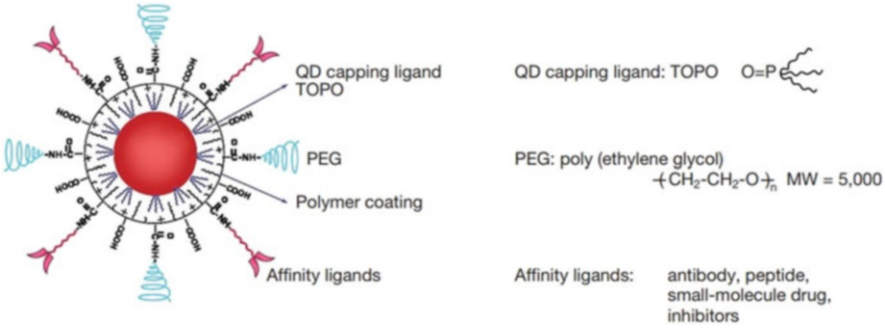

Fig. 4.13 Schematic illustration of quantum dots for in vivo cancer targeting and imaging, which shows the structure of a multifunctional quantum dot probe, consisting of the capping ligand TOPO, encapsulating copolymer layer, tumor-targeting ligands (such as peptides, antibodies, or small molecule inhibitors), and polyethene glycol (PEG) [159]

mechanism, HIV-1 provirus loci in live host cells of human chromosomes were successfully mapped [162]. In another study conducted in China, solid-state zinc-adsorbed carbon quantum dots (ZnCQD) were used as an electrochemiluminescence probe for measuring CD44 expression on breast cancer cells. ZnCQD probes were created by attaching these carbon quantum dots to gold nanoparticles. On this platform, the electrochemiluminescence signal was further amplified by 120-fold using magnetic beads [163].

The cytoplasm is a very complex structure made by the cytoskeleton. A poorly understood subject of cytoskeletal modulation of intercellular dynamics has been addressed by a recent study using nanobody functionalized quantum dots. The quantum dots were adherent cell electroporated and then nanobody functionalized to deliver then to the cytoplasm [164].

4.10 Nanodiamonds

Nanodiamonds, as evident from the name, are diamonds of size less than a micrometer, and are a particular class of carbon nanomaterials. Nanodiamonds are prepared using a variety of methods including electrochemical synthesis, laser bombardment, ion bombardment, ultrasound synthesis, hydrothermal synthesis, chemical vapor deposition, and detonation and by decomposing graphitic C_3N_4 under high temperature and pressure [165]. The industrial production of nanodiamonds is carried out through detonation in an oxygen-less environment of a stainless steel container using a mixture of trinitrotoluene and hexogen, which produces nanodiamonds with an average size of 5 nm [166]. The process of detonation synthesis forms the diamonds at a pressure of 15 GPa and a temperature higher than 3000 K.

Nanodiamonds have numerous biomedical applications because of their inertness and hardness. These properties make them suitable for drug delivery, coat

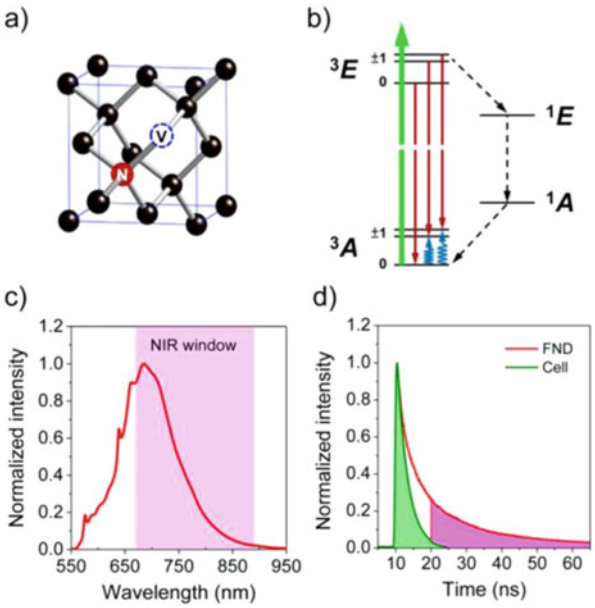

Fig. 4.14 (**a**) The structure of negatively charged nitrogen vacancy in a nanodiamond. The black spheres represent carbon atoms, the red sphere represents a nitrogen atom, and the blue dashed sphere represents a vacancy. (**b**) The energy level diagram of nanodiamond with negatively charged nitrogen vacancy. The green arrow represents optical excitation, red arrows represent fluorescence emission, blue sinusoids are for microwave excitation, and black dashed arrows are intersystem crossing relaxation. (**c**) The graph shows the normalized intensity of the fluorescence spectrum of fluorescent nanodiamonds when excited using 532 nm laser overlapping with the near IR window of biological tissues. (**d**) Comparison between the fluorescence lifetimes of fluorescent nanodiamonds in water and endogenous fluorophores in cells. Time gating at 10 ns is indicated for background-free detection [167]

implantable materials, and biosensors. Various functional groups can be attached to nanodiamonds allowing them to be targeted to some specific location or cells (Fig. 4.14).

In vivo tracking and imaging of cells is vital for carrying out important biological analysis. In recent times, exceptional research focus is being devoted to cancer cells, their identification, and isolation, as cancer is considered to be a major public health issue in today's world. For in vivo tracking and imaging of cancer cells, the stability of fluorescent markers is an essential factor. Due to the importance of cancer research and the inherent advantages that nanodiamonds present, nanodiamonds have been extensively used for cancer research. Quiescent cancer stem cells, the source of tumor initiation, have been successfully found and tracked using nanodiamonds [168, 169].

Fluorescent nanodiamond labeling has been used for wide-field imaging along with flow cytometric analysis of cancer cells in the blood. Nanodiamonds with a high density of negatively charged nitrogen-vacancies were used as fluorescent

biomarkers because of their remarkable photostability and biocompatibility. The nanodiamonds containing an ensemble of negatively charged nitrogen-vacancies are useful for a variety of applications, including long-term cell tracking, super-resolution imaging, and temperature sensing at the nanoscale [167, 170].

4.11 Conclusion and Future Perspectives

Single-cell analysis is an essential tool for numerous biological and medical applications. The scope of single-cell analysis encompasses the vast fields of transcriptomics, genomics, proteomics, and metabolomics. Single-cell analysis holds the key to various studies on cancer and genetics, analysis of DNA and RNA transcription, and the behavior of individual cells under externally applied stimuli. Therefore, single-cell analysis lies at the cutting edge of modern research in the fields of biology and medicine.

When analyzing organisms at the scale of an individual cell, nanophotonics is a clear method of choice as it provides the essential mechanism for improving the resolution of traditional instruments and enables them to image and characterize individual cells. Through the deployment of nanophotonic instruments and tools, such as nanolasers, zero-mode waveguides, nanoparticles, and quantum dots, the medical and biological sciences have made significant and innovative breakthroughs. While tools such as ZMW, optical fibers with nanocrystals, mass spectrometry methods, nanoantennas, and optofluidics have been useful for making breakthroughs in the imaging of single cells leading to valuable insights about the behavior of various types of cells, nanolasers and quantum dots have gained significant importance as tools for elimination of cancerous cells.

Although this field has been explored for several years and researchers have made significant progress in providing solutions, further work is still required for diversification of the existing detection methods and overcoming their limitations, such as resolution and operating accuracy [1].

Many traditional detection methods can be combined with the newest advancement of nanotechnology for in situ detection of single living cells. A few examples of such coupled systems have been highlighted in this chapter [1].

In brief, the development of optoelectronic nanodevices for intracellular studies in single living cells will have a profound impact on the development of future medicine. It is even poised to revolutionize biological medicine. In the future, additional studies will still be needed to further improve the existing resolution levels of these state-of-the-art instruments [1].

References

1. Wang D, Zhao X, Gu Z. Advanced optoelectronic nanodevices and nanomaterials for sensing inside single living cell. Opt Commun. 2017;395:3–15. https://doi.org/10.1016/j.optcom.2016.03.047.
2. Lumen unique characteristics of eukaryotic cells - lumen microbiology.
3. Schwanhüusser B, Busse D, Li N, et al. Global quantification of mammalian gene expression control. Nature. 2011;473:337–42. https://doi.org/10.1038/nature10098.
4. Szabo DT. Transcriptomic biomarkers in safety and risk assessment of chemicals. In: Biomarkers in toxicology. New York, NY: Academic Press; 2014. p. 1033–8.
5. Wang D, Bodovitz S. Single cell analysis: the new frontier in "omics". Trends Biotechnol. 2010;28:281.
6. Daviss B. Growing pains for metabolomics. Scientist. 2005;19:25–8.
7. Zenobi R. Single-cell metabolomics: analytical and biological perspectives. Science. 2013;342:1243259. https://doi.org/10.1126/science.1243259.
8. Anderson NL, Anderson NG. Proteome and proteomics: new technologies, new concepts, and new words. Electrophoresis. 1998;19:1853–61. https://doi.org/10.1002/elps.1150191103.
9. Blackstock WP, Weir MP. Proteomics: quantitative and physical mapping of cellular proteins. Trends Biotechnol. 1999;17:121–7.
10. Wu AR, Wang J, Streets AM, Huang Y. Single-cell transcriptional analysis. Annu Rev Anal Chem. 2017;10:439–62. https://doi.org/10.1146/annurev-anchem-061516-045228.
11. Kalisky T, Quake SR. Single-cell genomics. Nat Methods. 2011;8:311.
12. Passarelli MK, Ewing AG. Single-cell imaging mass spectrometry. Curr Opin Chem Biol. 2013;17:854–9. https://doi.org/10.1016/j.cbpa.2013.07.017.
13. Rubakhin SS, Romanova EV, Nemes P, Sweedler JV. Profiling metabolites and peptides in single cells. Nat Methods. 2011;8:S20–9. https://doi.org/10.1038/nmeth.1549.
14. Mathew AK, Padmanaban VC. Metabolomics: the apogee of the omics trilogy. Int J Pharm Pharm Sci. 2013;5:45–8.
15. Dang L, White DW, Gross S, et al. Cancer-associated IDH1 mutations produce 2-hydroxyglutarate. Nature. 2009;462:739.
16. Patti GJ, Yanes O, Shriver LP, et al. Metabolomics implicates altered sphingolipids in chronic pain of neuropathic origin. Nat Chem Biol. 2012;8:232.
17. Qiu S, Luo S, Evgrafov O, et al. Single-neuron RNA-Seq: technical feasibility and reproducibility. Front Genet. 2012;3:124.
18. Qiu S, Luo S, Evgrafov O, et al. Erratum: single-neuron RNA-Seq: technical feasibility and reproducibility. Front Genet. 2013;4:23.
19. Wang J, Fan HCC, Behr B, Quake SRR. Genome-wide single-cell analysis of recombination activity and de novo mutation rates in human sperm. Cell. 2012;150:402–12. https://doi.org/10.1016/j.cell.2012.06.030.
20. Hou Y, Fan W, Yan L, et al. Genome analyses of single human oocytes. Cell. 2013;155:1492–506.
21. Tang F, Barbacioru C, Bao S, et al. Tracing the derivation of embryonic stem cells from the inner cell mass by single-cell RNA-Seq analysis. Cell Stem Cell. 2010;6:468–78. https://doi.org/10.1016/j.stem.2010.03.015.
22. Xue Z, Huang K, Cai C, et al. Genetic programs in human and mouse early embryos revealed by single-cell RNA sequencing. Nature. 2013;500:593–7. https://doi.org/10.1038/nature12364.
23. Yan L, Yang M, Guo H, et al. Single-cell RNA-Seq profiling of human preimplantation embryos and embryonic stem cells. Nat Struct Mol Biol. 2013;20:1131–9. https://doi.org/10.1038/nsmb.2660.
24. Guo H, Zhu P, Wu X, et al. Single-cell methylome landscapes of mouse embryonic stem cells and early embryos analyzed using reduced representation bisulfite sequencing. Genome Res. 2013;23:2126–35. https://doi.org/10.1101/gr.161679.113.

25. Kim J, Eberwine J. RNA: state memory and mediator of cellular phenotype. Trends Cell Biol. 2010;20:311–8.
26. Eberwine J, Sul JY, Bartfai T, Kim J. The promise of single-cell sequencing. Nat Methods. 2014;11:25–7. https://doi.org/10.1038/nmeth.2769.
27. Macaulay IC, Ponting CP, Voet T. Single-cell multiomics: multiple measurements from single cells. Trends Genet. 2017;33:155–68. https://doi.org/10.1016/j.tig.2016.12.003.
28. Yilmaz S, Singh AK. Single cell genome sequencing. Curr Opin Biotechnol. 2012;23:437.
29. Gross A, Schoendube J, Zimmermann S, et al. Technologies for single-cell isolation. Int J Mol Sci. 2015;16:16897.
30. Cheong R, Wang CJ, Levchenko A. Using a microfluidic device for high-content analysis of cell signaling. Sci Signal. 2009;2:pl2.
31. Binnig G, Rohrer H. Helvetica Phys. Acta 55, 726 (1982). Sci Am. 1985;253:50.
32. Garcia-Parajo MF. Optical antennas focus in on biology. Nat Photonics. 2008;2:201–3. https://doi.org/10.1038/nphoton.2008.37.
33. Amrania H, Drummond L, Coombes RC, et al. New IR imaging modalities for cancer detection and for intra-cell chemical mapping with a sub-diffraction mid-IR s-SNOM. Faraday Discuss. 2016;187:539. https://doi.org/10.1039/c5fd00150a.
34. Dereux A, Vigneron JP, Lambin P, Lucas AA. Theory of near-field optics with applications to SNOM and optical binding. Phys B Phys Condens Matter. 1991;175:65–7. https://doi.org/10.1016/0921-4526(91)90692-8.
35. Dürig U, Pohl DW, Rohner F. Near-field optical-scanning microscopy. J Appl Phys. 1986;59:3318. https://doi.org/10.1063/1.336848.
36. Abeyasinghe N, Kumar S, Sun K, et al. Enhanced emission from single isolated gold quantum dots investigated using two-photon-excited fluorescence near-field scanning optical microscopy. J Am Chem Soc. 2016;138:16299–307. https://doi.org/10.1021/jacs.6b07737.
37. Futamata M, Bruckbauer A. ATR-SNOM-Raman spectroscopy. Chem Phys Lett. 2001;341:425–30. https://doi.org/10.1016/S0009-2614(01)00545-0.
38. Butler HJ, Ashton L, Bird B, et al. Using Raman spectroscopy to characterize biological materials. Nat Protoc. 2016;11:664–87. https://doi.org/10.1038/nprot.2016.036.
39. Liu Z, Lavis LD, Betzig E. Imaging live-cell dynamics and structure at the single-molecule level. Mol Cell. 2015;58:644. https://doi.org/10.1016/j.molcel.2015.02.033.
40. Liang Z, Yin Z, Yang H, et al. Nanoscale surface analysis that combines scanning probe microscopy and mass spectrometry: a critical review. Trends Anal Chem. 2016;75:24–34. https://doi.org/10.1016/j.trac.2015.07.009.
41. Huth F, Govyadinov A, Amarie S, et al. Nano-FTIR absorption spectroscopy of molecular fingerprints at 20 nm spatial resolution. Nano Lett. 2012;12:3973. https://doi.org/10.1021/nl301159v.
42. Albella P, De La Osa RA, Moreno F, Maier SA. Electric and magnetic field enhancement with ultralow heat radiation dielectric nanoantennas: considerations for surface-enhanced spectroscopies. ACS Photon. 2014;1:524. https://doi.org/10.1021/ph500060s.
43. Della Picca F, Berte R, Rahmani M, et al. Tailored hypersound generation in single plasmonic nanoantennas. Nano Lett. 2016;16:1428. https://doi.org/10.1021/acs.nanolett.5b04991.
44. Regmi R, Winkler PM, Flauraud V, et al. Planar optical nanoantennas resolve cholesterol-dependent nanoscale heterogeneities in the plasma membrane of living cells. Nano Lett. 2017;17:6295. https://doi.org/10.1021/acs.nanolett.7b02973.
45. Drude P. Zur Elektronentheorie der Metalle; II. Teil. Galvanomagnetische und thermomagnetische Effecte. Ann Phys. 1900;3:369. https://doi.org/10.1002/andp.19003081102.
46. Sommerfeld A, Bethe H. Elektronentheorie der Metalle. In: Aufbau Der Zusammenhängenden Materie. New York, NY: Springer; 1933.
47. Sommerfeld A. Zur Elektronentheorie der Metalle auf Grund der Fermischen Statistik - I. Teil: Allgemeines. Zeitschrift für Physik. 1928;47:1–32. https://doi.org/10.1007/BF01391052.

48. Giannini V, Fernández-Domínguez AI, Heck SC, Maier SA. Plasmonic nanoantennas: fundamentals and their use in controlling the radiative properties of nanoemitters. Chem Rev. 2011;111:3888.
49. Wang AX, Kong X. Review of recent progress of plasmonic materials and nano-structures for surface-enhanced raman scattering. Materials (Basel). 2015;8:3024.
50. Pellegrotti JV, Acuna GP, Puchkova A, et al. Controlled reduction of photobleaching in DNA origami-gold nanoparticle hybrids. Nano Lett. 2014;14:2831. https://doi.org/10.1021/nl500841n.
51. Yuan H, Khatua S, Zijlstra P, et al. Thousand-fold enhancement of single-molecule fluorescence near a single gold nanorod. Angew Chem Int Ed. 2013;52:1217. https://doi.org/10.1002/anie.201208125.
52. Khatua S, Paulo PMR, Yuan H, et al. Resonant plasmonic enhancement of single-molecule fluorescence by individual gold nanorods. ACS Nano. 2014;8:4440. https://doi.org/10.1021/nn406434y.
53. Huth F, Chuvilin A, Schnell M, et al. Resonant antenna probes for tip-enhanced infrared near-field microscopy. Nano Lett. 2013;13:1065. https://doi.org/10.1021/nl304289g.
54. Puchkova A, Vietz C, Pibiri E, et al. DNA origami nanoantennas with over 5000-fold fluorescence enhancement and single-molecule detection at 25 μm. Nano Lett. 2015;15:8354–9.
55. Dulkeith E, Ringler M, Klar TA, et al. Gold nanoparticles quench fluorescence by phase induced radiative rate suppression. Nano Lett. 2005;5:585. https://doi.org/10.1021/nl0480969.
56. Etin AE, Yanik AA, Yilmaz C, et al. Monopole antenna arrays for optical trapping, spectroscopy, and sensing. Appl Phys Lett. 2011;98:98–101. https://doi.org/10.1063/1.3559620.
57. Jung I, Kim M, Kwak M, et al. Surface plasmon resonance extension through two-block metal-conducting polymer nanorods. Nat Commun. 2018;9:1010. https://doi.org/10.1038/s41467-018-03453-z.
58. Michieli N, Pilot R, Russo V, et al. Oxidation effects on the SERS response of silver nanoprism arrays. RSC Adv. 2017;7:369. https://doi.org/10.1039/c6ra26307k.
59. Kim M, Ko SM, Kim JM, et al. Dealloyed intra-nanogap particles with highly robust, quantifiable surface-enhanced Raman scattering signals for biosensing and bioimaging applications. ACS Cent Sci. 2018;4:277. https://doi.org/10.1021/acscentsci.7b00584.
60. Jin Q, Li M, Polat B, et al. Mechanical trap surface-enhanced raman spectroscopy for three-dimensional surface molecular imaging of single live cells. Angew Chem Int Ed. 2017;56:3822. https://doi.org/10.1002/anie.201700695.
61. Nair AK, Bhavitha KB, Perumbilavil S, et al. Multifunctional nitrogen sulfur co-doped reduced graphene oxide – Ag nano hybrids (sphere, cube and wire) for nonlinear optical and SERS applications. Carbon. 2018;132:380. https://doi.org/10.1016/j.carbon.2018.02.068.
62. Dill TJ, Rozin MJ, Brown ER, et al. Investigating the effect of Ag nanocube polydispersity on gap-mode SERS enhancement factors. Analyst. 2016;141:3916. https://doi.org/10.1039/c6an00212a.
63. Li Y, Ye Y, Fan Y, et al. Silver nanoprism-loaded eggshell membrane: a facile platform for in situ SERS monitoring of catalytic reactions. Crystals. 2017;7:45.
64. Pilipavicius J, Kaleinikaite R, Pucetaite M, et al. Controllable formation of high density SERS-active silver nanoprism layers on hybrid silica-APTES coatings. Appl Surf Sci. 2016;377:134. https://doi.org/10.1016/j.apsusc.2016.03.169.
65. Vitol EA, Orynbayeva Z, Friedman G, Gogotsi Y. Nanoprobes for intracellular and single cell surface-enhanced Raman spectroscopy (SERS). J Raman Spectrosc. 2012;43:817.
66. Altunbek M, Kuku G, Culha M. Gold nanoparticles in single-cell analysis for surface enhanced Raman scattering. Molecules. 2016;21(12):E1617.
67. Cowcher DP, Deckert-Gaudig T, Brewster VL, et al. Detection of protein glycosylation using tip-enhanced Raman scattering. Anal Chem. 2016;88:2105–12. https://doi.org/10.1021/acs.analchem.5b03535.

68. Xiao L, Wang H, Schultz ZD. Selective detection of RGD-integrin binding in cancer cells using tip enhanced raman scattering microscopy. Anal Chem. 2016;88:6547. https://doi.org/10.1021/acs.analchem.6b01344.
69. Balanis CA. Modern antenna handbook. New York, NY: Wiley; 2007.
70. Pozar DM. Microwave engineering. New York, NY: Wiley; 2012.
71. Bethe HA. Theory of diffraction by small holes. Phys Rev. 1944;66:163–82. https://doi.org/10.1103/PhysRev.66.163.
72. Bouwkamp CJ. Diffraction theory. Rep Prog Phys. 1954;17:35. https://doi.org/10.1088/0034-4885/17/1/302.
73. Levine H, Schwinger J. On the transmission coefficient of a circular aperture. Phys Rev. 1949;75:1608.
74. Drezet A, Woehl JC, Huant S. Diffraction by a small aperture in conical geometry: application to metal-coated tips used in near-field scanning optical microscopy. Phys Rev E Stat Phys Plasm Fluid Relat Interdiscip Top. 2002;65:046611. https://doi.org/10.1103/PhysRevE.65.046611.
75. Crouch GM, Han D, Bohn PW. Zero-mode waveguide nanophotonic structures for single molecule characterization. J Phys D Appl Phys. 2018;51:193001.
76. Napoli M, Eijkel JCT, Pennathur S. Nanofluidic technology for biomolecule applications: a critical review. Lab Chip. 2010;10:957.
77. Larkin J, Henley RY, Jadhav V, et al. Length-independent DNA packing into nanopore zero-mode waveguides for low-input DNA sequencing. Nat Nanotechnol. 2017;12:1169–75. https://doi.org/10.1038/nnano.2017.176.
78. Magde D, Elson E, Webb WW. Thermodynamic fluctuations in a reacting system measurement by fluorescence correlation spectroscopy. Phys Rev Lett. 1972;29:705. https://doi.org/10.1103/PhysRevLett.29.705.
79. Samiee KT, Foquet M, Guo L, et al. λ-repressor oligomerization kinetics at high concentrations using fluorescence correlation spectroscopy in zero-mode waveguides. Biophys J. 2005;88:2145. https://doi.org/10.1529/biophysj.104.052795.
80. Samiee KT, Moran-Mirabal JM, Cheung YK, Craighead HG. Zero mode waveguides for single-molecule spectroscopy on lipid membranes. Biophys J. 2006;90:3288. https://doi.org/10.1529/biophysj.105.072819.
81. Richards CI, Luong K, Srinivasan R, et al. Live-cell imaging of single receptor composition using zero-mode waveguide nanostructures. Nano Lett. 2012;12:3690–4. https://doi.org/10.1021/nl301480h.
82. Miyake T, Tanii T, Sonobe H, et al. Real-time imaging of single-molecule fluorescence with a zero-mode waveguide for the analysis of protein-protein interaction. Anal Chem. 2008;80:6018. https://doi.org/10.1021/ac800726g.
83. Zaino LP, Grismer DA, Han D, et al. Single occupancy spectroelectrochemistry of freely diffusing flavin mononucleotide in zero-dimensional nanophotonic structures. Faraday Discuss. 2015;8:535. https://doi.org/10.1039/c5fd00072f.
84. Gooding JJ, Gaus K. Single-molecule sensors: challenges and opportunities for quantitative analysis. Angew Chem Int Ed. 2016;55:11354–66. https://doi.org/10.1002/anie.201600495.
85. Murphy TW, Zhang Q, Naler LB, et al. Recent advances in the use of microfluidic technologies for single cell analysis. Analyst. 2018;143:60–80.
86. Song C, Tan SH. A perspective on the rise of optofluidics and the future. Micromachines. 2017;8:152.
87. Ma Z, Teo AJT, Tan SH, et al. Self-aligned interdigitated transducers for acoustofluidics. Micromachines. 2016;7:216. https://doi.org/10.3390/mi7120216.
88. TAG Optics Inc. TAG lens product family: the world's fastest focusing lenses.
89. Blue-Scientific Optofluidics. http://www.blue-scientific.com/biological-afm-microscopy-jpk-instruments-bruker/. Accessed 1 Nov 2018.
90. Bedoya AC, Monat C, Domachuk P, et al. Measuring the dispersive properties of liquids using a microinterferometer. Appl Opt. 2011;50:2408. https://doi.org/10.1364/AO.50.002408.

91. Testa G, Persichetti G, Sarro PM, Bernini R. A hybrid silicon-PDMS optofluidic platform for sensing applications. Biomed Opt Express. 2014;5:417. https://doi.org/10.1364/BOE.5.000417.
92. Lapsley MI, Chiang IK, Zheng YB, et al. A single-layer, planar, optofluidic Mach-Zehnder interferometer for label-free detection. Lab Chip. 2011;11:1795. https://doi.org/10.1039/c0lc00707b.
93. Guo B, Lei C, Kobayashi H, et al. High-throughput, label-free, single-cell, microalgal lipid screening by machine-learning-equipped optofluidic time-stretch quantitative phase microscopy. Cytometry A. 2017;91:494. https://doi.org/10.1002/cyto.a.23084.
94. Lau AKS, Shum HC, Wong KKY, et al. Optofluidic time-stretch imaging – an emerging tool for high-throughput imaging flow cytometry. Lab Chip. 2016;16:1743. https://doi.org/10.1039/C5LC01458A.
95. Müller P, Schürmann M, Chan CJ, Guck J. Single-cell diffraction tomography with optofluidic rotation about a tilted axis. SPIE Proc. 2015;9548:95480U.
96. Lee KS, Lee KH, Kim SB, et al. Dynamic manipulation of particles via transformative optofluidic waveguides. Sci Rep. 2015;5:15170. https://doi.org/10.1038/srep15170.
97. Lee KH, Lee KS, Jung JH, et al. Optical mobility of blood cells for label-free cell separation applications. Appl Phys Lett. 2013;102:141911. https://doi.org/10.1063/1.4801951.
98. Schmidt H, Hawkins AR. Single-virus analysis through chip-based optical detection. Bioanalysis. 2016;8:867–70. https://doi.org/10.4155/bio-2016-0004.
99. Cai H, Parks JW, Wall TA, et al. Optofluidic analysis system for amplification-free, direct detection of Ebola infection. Sci Rep. 2015;5:14494. https://doi.org/10.1038/srep14494.
100. Pollnau M, Hammer M, Dongre C, Hoekstra HJWM. DNA separation and fluorescent detection in an optofluidic chip with sub-base-pair resolution. SPIE Proc. 2015;9320:93200J.
101. Knob R, Hanson RL, Tateoka OB, et al. Sequence-specific sepsis-related DNA capture and fluorescent labeling in monoliths prepared by single-step photopolymerization in microfluidic devices. J Chromatogr A. 2018;1562:12. https://doi.org/10.1016/j.chroma.2018.05.042.
102. Bertucci A, Manicardi A, Candiani A, et al. Detection of unamplified genomic DNA by a PNA-based microstructured optical fiber (MOF) Bragg-grating optofluidic system. Biosens Bioelectron. 2015;63:248. https://doi.org/10.1016/j.bios.2014.07.047.
103. Petras D, Jarmusch AK, Dorrestein PC. From single cells to our planet—recent advances in using mass spectrometry for spatially resolved metabolomics. Curr Opin Chem Biol. 2017;36:24–31. https://doi.org/10.1016/j.cbpa.2016.12.018.
104. Wikimedia Commons, Fyson D. Mass spectrometer schematic. 2008. https://commons.wikimedia.org/wiki/File:Mass_Spectrometer_Schematic.svg. Accessed 24 Jul 2018.
105. Mukhopadhyay SM. Sample preparation for microscopic and spectroscopic characterization of solid surfaces and films. In: Sample preparation techniques in analytical chemistry. Hoboken, NJ: John Wiley & Sons, Inc.; 2003.
106. Caprioli RM, Suter MJF. Continuous-flow fast atom bombardment: recent advances and applications. Int J Mass Spectrom Ion Process. 1992;118–119:449–76. https://doi.org/10.1016/0168-1176(92)85072-8.
107. Kralj B, Kramer V, Vrščaj V. Fast atom bombardment of molecules in the gaseous state. Int J Mass Spectrom Ion Phys. 1983;46:399–402. https://doi.org/10.1016/0020-7381(83)80136-3.
108. Takayama M. Gas-phase fast-atom bombardment mass spectrometry. Int J Mass Spectrom Ion Process. 1996;152:1–20. https://doi.org/10.1016/0168-1176(95)04298-9.
109. Fenn JB, Mann M, Meng CK, et al. Electrospray ionization for mass spectrometry of large biomolecules. Science. 1989;246:64–71. https://doi.org/10.1126/science.2675315.
110. Tanaka K, Waki H, Ido Y, et al. Protein and polymer analyses up to m/z 100 000 by laser ionization time-of-flight mass spectrometry. Rapid Commun Mass Spectrom. 1988;2:151–3. https://doi.org/10.1002/rcm.1290020802.
111. Vertes A, Irinyi G, Gijbels R. Hydrodynamic model of matrix-assisted laser desorption mass spectrometry. Anal Chem. 1993;65:2389–93. https://doi.org/10.1021/ac00065a036.

112. Wu XW, Sadeghi M, Vertes A. Molecular dynamics of matrix-assisted laser desorption of leucine enkephalin guest molecules from nicotinic acid host crystal. J Phys Chem B. 1998;102:4770–8. https://doi.org/10.1021/jp9806361.
113. Sadeghi M, Wu X, Vertes A. Conformation changes, complexation, and phase transition in matrix-assisted laser desorption. J Phys Chem B. 2001;105:2578–87. https://doi.org/10.1021/jp0032715.
114. Stolee JA, Walker BN, Zorba V, et al. Laser–nanostructure interactions for ion production. Phys Chem Chem Phys. 2012;14:8453. https://doi.org/10.1039/c2cp00038e.
115. Karas M, Bachmann D, Hillenkamp F. Influence of the wavelength in high-irradiance ultraviolet laser desorption mass spectrometry of organic molecules. Anal Chem. 1985;57:2935–9. https://doi.org/10.1021/ac00291a042.
116. Benninghoven A, Rudenauer FG, Werner HW. Secondary ion mass spectrometry: basic concepts, instrumental aspects, applications and trends. New York, NY: John Wiley & Sons; 1987.
117. Perkel JM. LIFE SCIENCE TECHNOLOGIES: mass spec imaging: from bench to bedside. Science. 2013;340:1119–21. https://doi.org/10.1126/science.opms.p1300076.
118. McEwen CN, McKay RG. A combination atmospheric pressure LC/MS:GC/MS ion source: advantages of dual AP-LC/MS:GC/MS instrumentation. J Am Soc Mass Spectrom. 2005;16:1730–8. https://doi.org/10.1016/j.jasms.2005.07.005.
119. McEwen CN, McKay RG, Larsen BS. Analysis of solids, liquids, and biological tissues using solids probe introduction at atmospheric pressure on commercial LC/MS instruments. Anal Chem. 2005;77:7826–31. https://doi.org/10.1021/ac051470k.
120. Knochenmuss R, Zenobi R. MALDI ionization: the role of in-plume processes. Chem Rev. 2003;103:441–52. https://doi.org/10.1021/cr0103773.
121. Knochenmuss R. A quantitative model of ultraviolet matrix-assisted laser desorption/ionization including analyte ion generation. Anal Chem. 2003;75:2199–207. https://doi.org/10.1021/ac034032r.
122. Laiko VV, Baldwin MA, Burlingame AL. Atmospheric pressure matrix-assisted laser desorption/ionization mass spectrometry. Anal Chem. 2000;72:652–7. https://doi.org/10.1021/ac990998k.
123. Cho Y-T, Su H, Wu W-J, et al. Biomarker characterization by MALDI–TOF/MS. In: Advances in clinical chemistry. Amsterdam: Elsevier; 2015. p. 209–54.
124. Dale MJ, Knochenmuss R, Zenobi R. Graphite/liquid mixed matrices for laser desorption/ionization mass spectrometry. Anal Chem. 1996;68:3321–9. https://doi.org/10.1021/ac960558i.
125. Vertes A. Soft laser desorption ionization - Maldi, dios and nanostructures. Springer Ser Opt Sci. 2006;129:505–28. https://doi.org/10.1007/978-0-387-30453-3_20.
126. Colaianni L, Kung SC, Taggart DK, et al. Laser desorption ionization-mass spectrometry detection of amino acids and peptides promoted by gold nanowires. Sens Lett. 2010;8:539–44. https://doi.org/10.1166/sl.2010.1308.
127. Nayak R, Knapp DR. Matrix-free LDI mass spectrometry platform using patterned nanostructured gold thin film. Anal Chem. 2010;82:7772–8. https://doi.org/10.1021/ac1017277.
128. Pyayt AL, Wiley B, Xia Y, et al. Integration of photonic and silver nanowire plasmonic waveguides. Nat Nanotechnol. 2008;3:660–5. https://doi.org/10.1038/nnano.2008.281.
129. Seino T, Sato H, Yamamoto A, et al. Matrix-free laser desorption/ionization-mass spectrometry using self-assembled germanium nanodots. Anal Chem. 2007;79:4827–32. https://doi.org/10.1021/ac062216a.
130. Sato H, Nemoto A, Yamamoto A, Tao H. Surface cleaning of germanium nanodot ionization substrate for surface-assisted laser desorption/ionization mass spectrometry. Rapid Commun Mass Spectrom. 2009;23:603–10.
131. Kawasaki H, Yonezawa T, Watanabe T, Arakawa R. Platinum nanoflowers for surface-assisted laser desorption/ionization mass spectrometry of biomolecules. J Phys Chem C. 2007;111:16278–83.

132. Cha S, Yeung ES. Colloidal graphite-assisted laser desorption/ionization mass spectrometry and MS n of small molecules. 1. Imaging of cerebrosides directly from rat brain tissue. Anal Chem. 2007;79:2373–85.
133. Kang M, Pyun J, Lee J, et al. Nanowire-assisted laser desorption and ionization mass spectrometry for quantitative analysis of small molecules. Rapid Commun Mass Spectrom. 2005;19:3166–70.
134. Go EP, Apon JV, Luo G, et al. Desorption/ionization on silicon nanowires. Anal Chem. 2005;77:1641–6.
135. Chen Y, Vertes A. Adjustable fragmentation in laser desorption/ionization from laser-induced silicon microcolumn arrays. Nature. 2006;78:5835–44.
136. Northen TR, Yanes O, Northen MT, et al. Clathrate nanostructures for mass spectrometry. Nature. 2007;449:1033–6. https://doi.org/10.1038/nature06195.
137. Wei J, Buriak JM, Siuzdak G. Desorption – ionization mass spectrometryonporoussilicon. Nature. 1999;399:243–6. https://doi.org/10.1038/20400.
138. Walker BN, Stolee JA, Pickel DL, et al. Tailored silicon nanopost arrays for resonant nanophotonic ion production. J Phys Chem C. 2010;114:4835–40. https://doi.org/10.1021/jp9110103.
139. Walker BN, Stolee JA, Vertes A. Nanophotonic ionization for ultratrace and single-cell analysis by mass spectrometry. Anal Chem. 2012;84:7756–62. https://doi.org/10.1021/ac301238k.
140. Korte AR, Stopka SA, Morris N, et al. Large-scale metabolite analysis of standards and human serum by laser desorption ionization mass spectrometry from silicon nanopost arrays. Anal Chem. 2016;88:8989–96. https://doi.org/10.1021/acs.analchem.6b01186.
141. Stopka SA, Holmes XA, Korte AR, et al. Trace analysis and reaction monitoring by nanophotonic ionization mass spectrometry from elevated bow-tie and silicon nanopost arrays. Adv Funct Mater. 2018;28:1801730. https://doi.org/10.1002/adfm.201801730.
142. Wang Y, Ta VD, Gao Y, et al. Stimulated emission and lasing from CdSe/CdS/ZnS core-multi-shell quantum dots by simultaneous three-photon absorption. Adv Mater. 2014;26:2954. https://doi.org/10.1002/adma.201305125.
143. Zhu H, Fu Y, Meng F, et al. Lead halide perovskite nanowire lasers with low lasing thresholds and high quality factors. Nat Mater. 2015;14:636. https://doi.org/10.1038/nmat4271.
144. Huang MH, Mao S, Feick H, et al. Room-temperature ultraviolet nanowire nanolasers. Science. 2001;292:1897. https://doi.org/10.1126/science.1060367.
145. Galanzha EI, Weingold R, Nedosekin DA, et al. Spaser as a biological probe. Nat Commun. 2017;8:15528.
146. Li L, Ge J, Wu H, et al. Organelle-specific detection of phosphatase activities with two-photon fluorogenic probes in cells and tissues. J Am Chem Soc. 2012;134:12157. https://doi.org/10.1021/ja3036256.
147. Huang C, Wang K, Yang Z, et al. Up-conversion perovskite nanolaser with single mode and low threshold. J Phys Chem C. 2017;121:10071. https://doi.org/10.1021/acs.jpcc.7b00875.
148. Li M, Zhi M, Zhu H, et al. Ultralow-threshold multiphoton-pumped lasing from colloidal nanoplatelets in solution. Nat Commun. 2015;6:8513. https://doi.org/10.1038/ncomms9513.
149. Baba T. Biosensing using photonic crystal nanolasers. MRS Commun. 2015;5:555. https://doi.org/10.1557/mrc.2015.73.
150. Kita S, Hachuda S, Otsuka S, et al. Super-sensitivity in label-free protein sensing using a nanoslot nanolaser. Opt Express. 2011;19:17683. https://doi.org/10.1364/OE.19.017683.
151. Alix-Panabières C, Pantel K. Biological labels: here comes the spaser. Nat Mater. 2017;16:790.
152. Solowan H-P, Kryschi C. Facile design of a plasmonic nanolaser. Condens Matter. 2017;2:8.
153. Lane LA, Smith AM, Lian T, Nie S. Compact and blinking-suppressed quantum dots for single-particle tracking in live cells. J Phys Chem B. 2014;118:14140. https://doi.org/10.1021/jp5064325.

154. Sabaeian M, Khaledi-Nasab A. Size-dependent intersubband optical properties of dome-shaped InAs/GaAs quantum dots with wetting layer. Appl Opt. 2012;51:4176–85. https://doi.org/10.1364/AO.51.004176.
155. Khaledi-Nasab A, Sabaeian M, Sahrai M, Fallahi V. Kerr nonlinearity due to intersubband transitions in a three-level InAs/GaAs quantum dot: the impact of a wetting layer on dispersion curves. J Opt. 2014;16:55004.
156. Walling MA, Novak JA, Shepard JRE. Quantum dots for live cell and in vivo imaging. Int J Mol Sci. 2009;10:441–91. https://doi.org/10.3390/ijms10020441.
157. Pelley JL, Daar AS, Saner MA. State of academic knowledge on toxicity and biological fate of quantum dots. Toxicol Sci. 2009;112:276–96. https://doi.org/10.1093/toxsci/kfp188.
158. Choi HS, Liu W, Misra P, et al. Renal clearance of nanoparticles. Nat Biotechnol. 2007;25:1165–70. https://doi.org/10.1038/nbt1340.
159. Gao X, Cui Y, Levenson RM, et al. In vivo cancer targeting and imaging with semiconductor quantum dots. Nat Biotechnol. 2004;22:969. https://doi.org/10.1038/nbt994.
160. Yang Y, Jing L, Yu X, et al. Coating aqueous quantum dots with silica via reverse microemulsion method: toward size-controllable and robust fluorescent nanoparticles. Chem Mater. 2007;19:4123. https://doi.org/10.1021/cm070798m.
161. Thoniyot P, Tan MJ, Karim AA, et al. Nanoparticle–hydrogel composites: concept, design, and applications of these promising, multi-functional materials. Adv Sci. 2015;2:1.
162. Ma Y, Wang M, Li W, et al. Live cell imaging of single genomic loci with quantum dot-labeled TALEs. Nat Commun. 2017;8:15318. https://doi.org/10.1038/ncomms15318.
163. Qiu Y, Zhou B, Yang X, et al. Novel single-cell analysis platform based on a solid-state zinc-coadsorbed carbon quantum dots electrochemiluminescence probe for the evaluation of CD44 expression on breast cancer cells. ACS Appl Mater Interfaces. 2017;9:16848. https://doi.org/10.1021/acsami.7b02793.
164. Katrukha EA, Mikhaylova M, Van Brakel HX, et al. Probing cytoskeletal modulation of passive and active intracellular dynamics using nanobody-functionalized quantum dots. Nat Commun. 2017;8:14772. https://doi.org/10.1038/ncomms14772.
165. Fang L, Ohfuji H, Irifune T. A novel technique for the synthesis of nanodiamond powder. J Nanomater. 2013;2013:41. https://doi.org/10.1155/2013/201845.
166. Holt KB. Diamond at the nanoscale: applications of diamond nanoparticles from cellular biomarkers to quantum computing. Philos Trans R Soc A Math Phys Eng Sci. 2007;365:2845. https://doi.org/10.1098/rsta.2007.0005.
167. Hsiao WWW, Hui YY, Tsai PC, Chang HC. Fluorescent nanodiamond: a versatile tool for long-term cell tracking, super-resolution imaging, and nanoscale temperature sensing. Acc Chem Res. 2016;49:400.
168. Lin H-H, Lee H-W, Lin R-J, et al. Tracking and finding slow-proliferating/quiescent cancer stem cells with fluorescent nanodiamonds. Small. 2015;11:4394–402. https://doi.org/10.1002/smll.201500878.
169. Liu KK, Wang CC, Cheng CL, Chao JI. Endocytic carboxylated nanodiamond for the labeling and tracking of cell division and differentiation in cancer and stem cells. Biomaterials. 2009;30:4249. https://doi.org/10.1016/j.biomaterials.2009.04.056.
170. Hui YY, Su LJ, Chen OY, et al. Wide-field imaging and flow cytometric analysis of cancer cells in blood by fluorescent nanodiamond labeling and time gating. Sci Rep. 2014;4:5574. https://doi.org/10.1038/srep05574.

Chapter 5
Biointerface Characterization by Nonlinear Optical Spectroscopy

Wenhua Sun, Shujing Wang, and Xiaofeng Han

Abstract Surface-specific second-order nonlinear optical spectroscopies, such as second harmonic generation (SHG) spectroscopy and sum frequency generation (SFG) spectroscopy, have become well-established tools to investigate biological interfaces because of their sensitivity to broken centrosymmetry. In this chapter, the two techniques of SHG and SFG and their applications in biological research are mainly discussed. The application of SHG in biological imaging and measuring the interaction kinetics of small molecules with living cells are introduced. As a vibrational spectroscopy, SFG spectroscopy has been demonstrated to be an ideal technique to probe and characterize the structures and orientations of peptides/proteins at solid/liquid interfaces. A systematic methodology has been developed to determine interfacial orientations of various secondary structures such as the α-helix, β-sheet, and complex protein by analyzing polarized SFG spectra. Except for planar interface, second-harmonic light scattering (SHS) and SFG scattering (SFS) can also be used to characterize the surface/interface of particles such as liposome, bacteria in solution.

Keywords Nonlinear optical spectroscopy · Second harmonic generation · Sum frequency generation · Biointerface

Interfacial studies are of great scientific significance in biology including interaction between substance and cell membrane, biosurface of biomaterials. The interface represents a unique coordination environment with properties distinct from those of the bulk. However, it is difficult to probe the interface because the interfacial signal tends to be overwhelmed by the bulk signal, and thus not readily discernible. Fortunately, with the advent of pulse laser, we are now able to employ

W. Sun · S. Wang · X. Han (✉)
State Key Laboratory of Bioelectronics, National Demonstration Center for Experimental, Biomedical Engineering Education, School of Biological Science and Medical Engineering, Southeast University, Nanjing, China
e-mail: xfhan@seu.edu.cn

X. Zhao, M. Lu (eds.), *Nanophotonics in Biomedical Engineering*,
https://doi.org/10.1007/978-981-15-6137-5_5

second-order nonlinear optical techniques, sum frequency generation (SFG) and second harmonic generation (SHG), to probe ions and molecules at aqueous interfaces.

5.1 Nonlinear Optical Spectroscopy

Optical spectroscopy and microscopy has many obvious advantages for characterizing biological systems, such as noncontact, in situ measurement and convenient specimen preparation. Optical techniques are so important in biological study that the development of modern biological science and medicine is inseparable from the application of optical technologies. Before the advent of laser, the studies focused on the propagation of weak beams in the medium, and the polarizability of the medium is independent of the light intensity. The polarization intensity of the medium is proportional to the electric field intensity **E** of the light wave. Under the conditions described above, the study of optics is called linear optics. Traditional spectral techniques, such as fluorescence spectroscopy, UV-visible absorption spectroscopy, infrared radiation (IR) absorption spectroscopy, and Raman spectroscopy, are all linear optical spectroscopies.

When the electric field intensity of the laser is equivalent to that of the Coulomb field in the atom, the interaction between the laser and the medium will produce nonlinear effects. The physical quantities that reflect the characteristics of the medium (such as polarization intensity, etc.) are not only related to the first-order power of the field strength **E** but also determined by the higher power term of **E**, resulting in nonlinearity.

Compared with traditional linear optics, there are some obvious advantages for nonlinear optics. One is that nonlinear optics has spatial resolution. Here, we take the mostly used nonlinear optical technique, two-photon fluorescence (TPF) microscope, as an example. Compared with the single-photon fluorescence microscope, the two-photon fluorescence microscope is characterized by the generation of optical signal which is nonlinear. The nonlinear nature of the optical signal leads to the following condition: only a limited area around the focus of the excitation light can satisfy the simultaneous absorption of two photons (as shown in Fig. 5.1), so there is no fluorescence outside the focus. Therefore, the two-photon excitation fluorescence microscope can have natural optical sectioning and three-dimensional (3D) imaging capabilities. Through the focus of the pulsed laser 3D scanning, we can obtain a 3D microscopic image of the sample. In addition, according to its imaging principle, the excitation light used in the two-photon fluorescence microscope is mainly IR pulse light, which can effectively avoid the photobleaching of the focused fluorescent probe. The IR beam has strong penetration ability and low scattering property for biological samples, and is suitable for imaging deep tissues. Generally, the imaging depth of single-photon excited fluorescence in biological samples is only 100–200 μm, while the imaging depth of two-photon excited fluorescence can reach 1–2 mm, which makes the technology widely used in disease diagnosis, physiological process tracking, drug detection, and other fields.

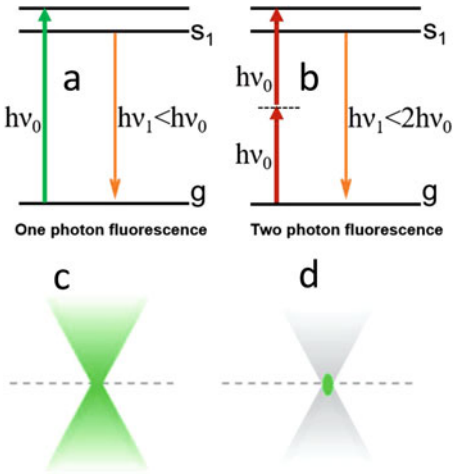

Fig. 5.1 (**a**) Energy diagram of one-photon fluorescence process. (**b**) Energy diagram of two-photon fluorescence process. (**c**) One photon microscopy, fluorescence generated from all profile of incident light passes through the specimen for a spatially uniform sample. (**d**) Two-photon microscopy allows for direct optical excitation at the focus of an optical beam

Another important advantage of nonlinear optics is that, even-order optical nonlinear effects are sensitive to surface/interface, which makes some even-order optical techniques to be ideal tools for characterizing the molecular interactions at biological interfaces. Second-order nonlinear optical spectroscopies, such as second harmonic generation (SHG) spectroscopy and sum frequency generation (SFG) spectroscopy, have become well-established tools to investigate biological interfaces because of their sensitivity to broken centrosymmetry. In this chapter, we mainly discuss the two techniques of SHG and SFG and their applications in biological research.

5.2 Second Harmonic Generation Spectroscopy

SHG is a second-order nonlinear optical phenomenon. When a near-infrared pulsed laser with a frequency of ω interacts with a non-centrosymmetric nonlinear medium or the interface of two centrosymmetric media, photons with a frequency of 2ω would be generated (Fig. 5.2). The SHG phenomenon can only be observed when the intensity of light reaches the threshold. Otherwise, if the intensity of light is too weak, only the linear process of the interaction between light and other substances will be observed.

SHG is with apparent surface and interface sensitivity, capable of detecting the molecular structure of solid–liquid interface in situ. In addition, SHG technique has the advantages of deep detection depth, little damage to biological samples, and high temporal and spatial resolution. These characteristics have made SHG a hot research topic in the field of bio-imaging in recent years. The cell membrane is a barrier between the cell and the external environment, which makes the physiological state on both sides of the interface different, so SHG can be used to detect changes that

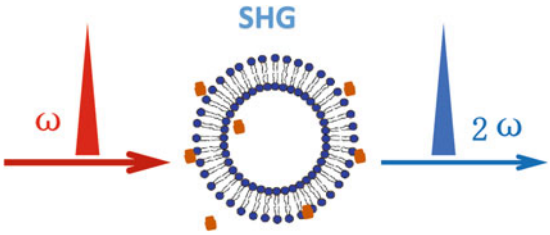

Fig. 5.2 Second harmonic generation. Some non-centrosymmetric nonlinear media, such as membranes randomly absorbed with molecules, can double the frequency of a small number of incident photons

occur on the cell membrane. Additionally, SHG has been used to measure the adsorption of small molecules on nano- and micro-sized particles. Also, SHG has been successfully applied to the measurement of small dye molecules and biomembranes.

5.2.1 History

The phenomenon of SHG was first observed when a strong beam was projected through a crystal quartz by Franken et al. of the University of Michigan in 1961 [1]. They focused the ruby laser at 694.3 nm on a quartz sample, then recorded the spectrum obtained by a spectrometer on the photographic paper, and monitored a strong signal at 347.2 nm. In the next year, Terhune et al. [2] observed the SHG phenomenon on the surface of a center-symmetrical calcite. After that, SHG was also detected in other media, and a series of corresponding basic theories began to develop rapidly in the following years [3].

Early theoretical studies have suggested that the SHG occurring in nonlinear media or on interface is because of the electric quadrupole moment of nonlinear polarization caused by the discontinuity of the electric field. However, by 1969, Brown et al. [4] found that the SHG intensity at the interface decreased significantly due to the adsorption of gas molecules on the Ag surface, which must be explained by the contribution of the electric dipole moment generated at the interface. Subsequently, the theoretical description of surface-sensitive SHG was mainly due to the symmetry-breaking of the surface, rather than the previously believed quadrupole effect [5]. Nevertheless, until that time, SHG could not be well explained, because it is impossible to consider all factors contributing to surface nonlinearity, for example, the structural difference between the surface phase and the medium phase.

Just like every early stage of discovering new fields, researchers at that time had interest only in proving the theoretical predictions of the SHG experiments, yet ignored the applicability of SHG in measuring the nonlinear optical properties of the media. Until 1972, Chen et al. [6] used Na atoms to absorb on the Ge surface, proving that the SHG has high sensitivity to the interface. But this discovery still did

not arouse the scientific community's attention to the measurement characteristics of SHG. It seemed that SHG could not be accepted as a surface detection method because there was still no good interpretation of the surface nonlinearity. Coincidentally and embarrassingly, the development of SHG as a surface-sensitive detection tool has benefited from the discovery of another nonlinear optical phenomenon. In 1974, Fleischman et al. [7] found that the Raman signal generated on rough Ag surface was stronger than the Raman signal generated on smooth Ag surface, which was named surfaced-enhanced Raman scattering (SERS). This was easily reminiscent of the fact that since the Raman scattering, as a nonlinear process, could be enhanced by the local field on the metal surface, could other nonlinear processes be surface-enhanced, as proved by subsequent SHG experiments. More optimistically, SHG could be observed on the bare Ag surface, and the SHG signal was particularly strong when detecting the adsorption and desorption of molecules on the rough metal surface. For pulsed laser, a detectable signal can be obtained without reinforcing the substrate. Since then, SHG has truly developed into a sensitive method for surface/interface detection, such as obtaining the spectrum and orientation information of the molecular monolayer absorbed on a substrate [8], and measuring the surface symmetry of a crystal [9]. In addition, Eisenthal et al. used SHG for the study of liquid interface to obtain the orientation, absorption, and other kinetic information of molecules on it, greatly expanding the research field of SHG.

5.2.2 Theory

As mentioned above, the experimental and theoretical basis of using electric quadrupole moment as the source of SHG had proved unreliable, showing that SHG could be well explained by the electric dipole moment while the contribution of the electric quadrupole moment was almost negligible, which indicated that the SHG method was indeed capable of detecting the molecular information of the interface layer region. In the 1980s, Shen et al. [10–13] considered the contribution of surface/interface to SHG, and proved that SHG was sensitive to submolecular layers. They made a concrete derivation of the SHG occurring on the nonlinear interface using a three-layer model, which was still the basic model we are dealing with today, by treating the interface as a polarized thin layer.

Why is SHG interface-selective? When a near-infrared femtosecond laser with a frequency of ω is irradiated onto a nonlinear medium or interface, linear polarization and high-order polarization terms are generated, which can be expressed by the following formula:

$$P = P^{(0)} + P^{(1)} + P^{(2)} + \cdots = P^{(0)} + \chi^{(1)} \cdot E + \chi^{(2)} : EE + \cdots \tag{5.1}$$

In the above formula, $P^{(0)}$, $P^{(1)}$ and $P^{(2)}$ is zeroth-, first- and second-order polarization strength, respectively; $\chi^{(1)}$ and $\chi^{(2)}$ is first- and second-order polarization

rate tensor; and the effect related to $P^{(2)} = \chi^{(2)}$:EE is called second-order nonlinear optical effect; $P^{(2)}$ and E_ω are vectors; $\chi^{(2)}$ is a 3 × 3 × 3 tensor; and $P^{(2)} = \chi^{(2)}$:EE can be expressed as

$$P_i^{(2)} = \sum_{j,k} \chi_{ijk}^{(2)} E_\omega^j E_\omega^k \tag{5.2}$$

In order to prove that the interface selectivity of SHG is due to the contribution of electric dipole moment generated by noncentral symmetry, the center symmetric inversion is performed on the medium. After the inversion operation, $\chi^{(2)}$ related only to the properties of the medium does not change, that is $\chi^{(2)} = \chi'^{(2)}$; however, the electric field strength E_ω and the second-order polarization strength $P^{(2)}$ will be opposite to the original direction, and the sign changes, so that

$$-P^{(2)} = \chi'^{(2)} : (-E_\omega)(-E_\omega) \tag{5.3}$$

The formula before the inversion is

$$P^{(2)} = \chi^{(2)} : E_\omega E_\omega \tag{5.4}$$

Comparing Formula (5.3) with Formula (5.4), $P^{(2)} = 0$ is calculated and then $\chi^{(2)} = 0$ is concluded. Since the second-order polarizability tensor is zero, it means that the center-symmetric medium does not generate SHG signal. However, for a non-centrosymmetric medium or interface, Formula (5.3) does not hold after inversion, and the result of $-P^{(2)} = P^{(2)}$ cannot be obtained, then $\chi^{(2)}$ is not equal to zero. That is the non-centrosymmetric medium or the interface between two phases can produce SHG signal, so SHG has the characteristic of interface selection. The theoretical analysis of SHG is far from simple, shallow and macro. Many studies have focused on the polarization selection of SHG and the quantitative analysis of interface molecular orientation. Here, we no longer delve into the microscopic theory of SHG, but use more space to describe its application.

5.2.3 Application

5.2.3.1 SHG Imaging

One of the important development directions of spectroscopy technology is optical imaging. In 1986, Freund et al. [14–16] applied SHG to the imaging (Fig. 5.3) of collagen fibers in rat tail lice, which was the beginning of applying SHG to biomedicine. From then on, nonlinear optical technology has been widely used as an emerging microscopic imaging technology in biomedical field. Among nonlinear

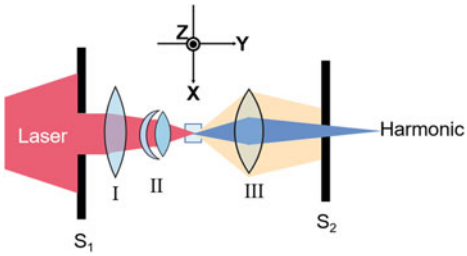

Fig. 5.3 Second harmonic (SH) microscope. Slit S_1, controls the convergence of the incident laser beam, while slit S_2 selects either the coherent or incoherent imaging mode; in the figure, it is set for coherent imaging. The long tendon axis (the *Z* axis) is normal to the plane of the figure, and the sample is scanned raster-fashion under the stationary laser spot. When a low resolution SH scattering curve of a particular sample feature is required, slit S_2 is scanned appropriately. When high-resolution scattering data are needed, condenser II and objective III are slid out of the beam path, and slit S_2 is narrowed and scanned. With the condenser in place the spot size is effectively ~50 μm, and the width of S_2 is normally set to correspond to an angular resolution of 2°. Without the condenser the spot size is ~0.5 mm and S_2 is normally narrowed so that the effective instrumental resolution is ~2 mrad [14]

optical technologies, SHG is best suited for imaging non-centrosymmetric molecules of tissue [17].

The signal intensity of SHG is closely related to the collagen content in biological tissues, and can specifically display the deposition and 3D morphology of fibrous collagen [18–20]. Tai et al. [21] developed a nonlinear optical imaging technique based on SHG and a computer-aided analysis system "Fibro-C-Index" (Fig. 5.4), and successfully applied it to liver fibrosis imaging and scoring in a rat liver cirrhosis model. The evaluation results were consistent with traditional cases and disease progression, confirming that the system could be used to judge the degree of human cirrhosis. "Fibro-C-Index" could subdivide the degree of liver fibrosis into 40 grades, particularly and sensitively reflecting the progress of liver fibrosis.

It was also found that the SHG signals of fibrosis caused by different causes also showed different 3D structures, providing a new reference for the etiological diagnosis [22]. Strupler et al. [23] used SHG-based nonlinear optical imaging and pathological section staining techniques to evaluate renal interstitial fibrosis in a mouse kidney disease model (Fig. 5.5). It was found that there was a certain deviation in the traditional pathological section staining techniques while the SHG-based nonlinear optical imaging technology did not have the problem of staining deviation, and the latter could specially display the deposition of renal interstitial fibrous collagen. In addition, they also scored through the average value of SHG signal, the SHG pixel density of the fibrous collagen deposition image and the ratio of the former two, which could accurately distinguish normal mice and kidney disease model mice, and the score was consistent with the disease progression in the mice model.

Wu et al. [24] used SHG-based nonlinear optical imaging technology to clearly observe the morphological changes and spatial distribution of collagen in the tail

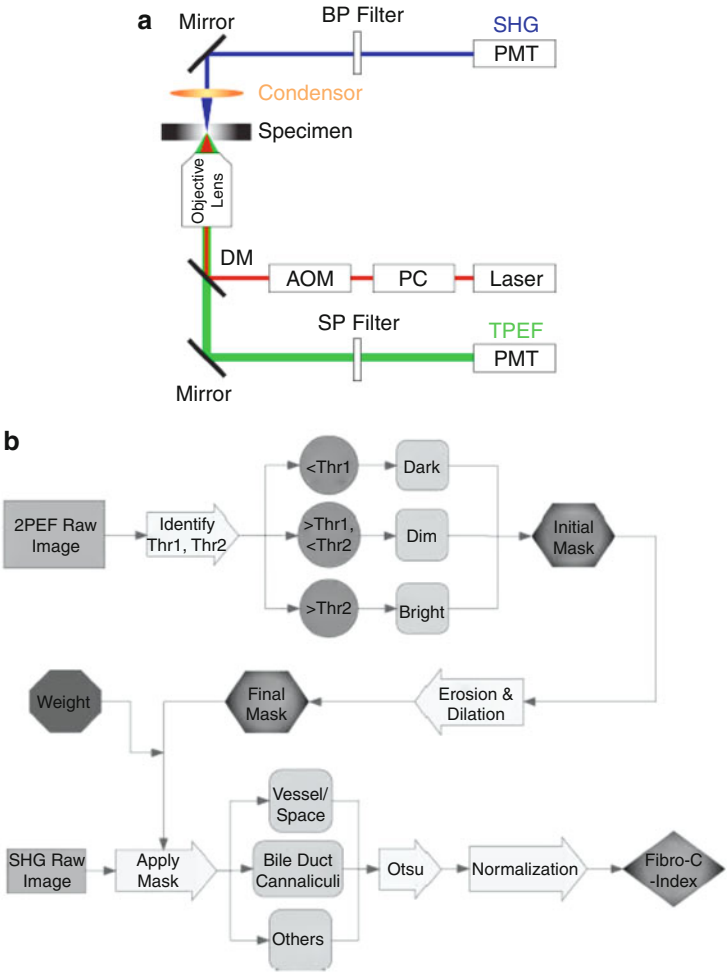

Fig. 5.4 (**a**) Schematic illustration of the optical configuration: excitation laser is a tunable mode-locked laser (710–990 nm) with a pulse compressor (PC) and an acousto-optic modulator (AOM) for power control. The laser go through a dichroic mirror (DM, 490 nm), an objective lens, and reached tissue specimen. SHG signal is collected at the opposite side the laser source, in the transmitted mode, by a high numerical aperture (NA) condenser, through a field diaphragm, and a 450 nm band-pass (BP) filter, before being recorded by a photomultiplier tube (PMT). Two-photon excited fluorescence (TPEF) is collected by the objective lens, filtered by a 700-nm short-pass (SP) filter, before being recorded by another PMT. (**b**) Flow chart of the adaptive quantification algorithm. TPEF images are first differentiated into three groups, depending on the pixel intensity level, into dark, dim, and bright regions. Different weights are added to these groups before applying Otsu segmentation. After segmentation, remaining grainy noises are removed using erosion and dilation algorithms, and the final mask is created. This mask is applied on SHG images for adaptive weighting adjustment on collagens in different areas. Finally, collagen content is quantified to generate Fibro-C-Index [21]

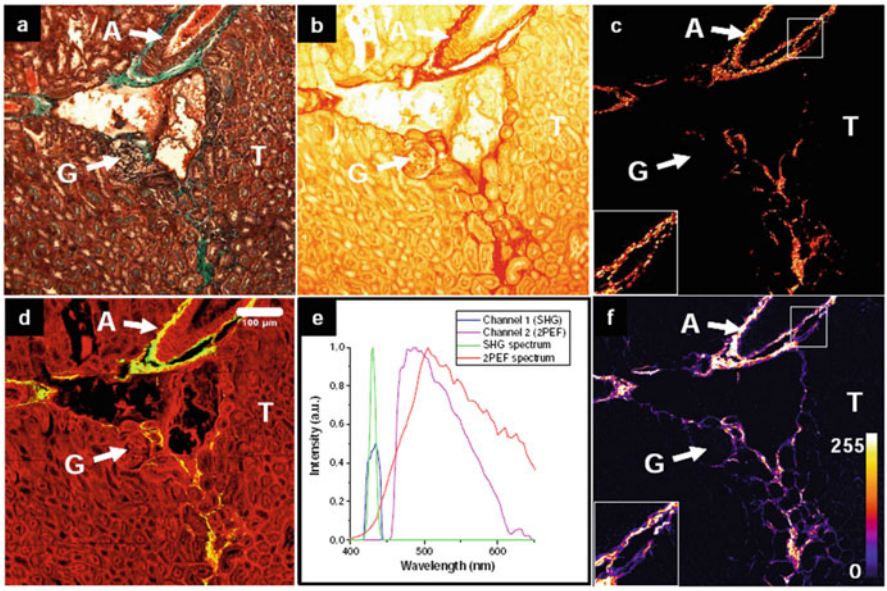

Fig. 5.5 Comparison of histological staining and endogenous SHG in fibrotic kidney tissue: serial sections of mouse kidney (4 µm thick) visualized by (**a**, **b**) transmitted light microscopy, (**c**) polarized light microscopy, and (**d**, **f**) multiphoton microscopy (20 mW excitation at 860 nm, circular polarization, NA 0.9). G: glomerulus, A: artery, T: tubules, scale bar: 100 µm. (**a**) Masson's trichrome staining; (**b**, **c**) Picrosirius red staining. (**d**) Multiphoton image showing SHG from collagen fibers (green) and endogenous 2PEF underlining the kidney morphology (red). (**e**) Spectra of these nonlinear endogenous signals (2PEF: red, and SHG: green), superimposed to the spectral transmittance of the SHG (blue) and 2PEF (pink) detection channels. (**f**) SHG image only (zoomed-in view in inset) [23]

skin of mice with lymphedema, and dynamically observed the collagen change during the progression of lymphedema, indicating that the used technique had the potential for clinical biopsy diagnosis and could monitor the therapeutic effect of lymphedema. Pena et al. [25] applied SHG-based nonlinear optical imaging technology to study lung tissue fibrosis, and observed the characteristics of pulmonary fibrosis by comparing normal lung tissue with bleomycin-induced pulmonary fibrosis specimens. They then demonstrated the micro-scale 3D spatial distribution of fibrous collagen, and proposed a phenomenological-based pulmonary fibrosis score which could clearly distinguish normal lung tissue from pulmonary fibrosis. The scoring method was highly sensitive and reproducible for pulmonary fibrosis in the subpleural region, and it was easy to generalize and could be applied to evaluate other organ fibrosis.

SHG imaging is a high-resolution, noninvasive imaging technology that can be used to diagnose not only fibrosis of tissues or organs but also tumors, especially in the early diagnosis and judgment of benign or malignant. Mucosal tissues, including the cervix, ears, nose, mouth, and esophagus, have tumor lesions that begin hundreds

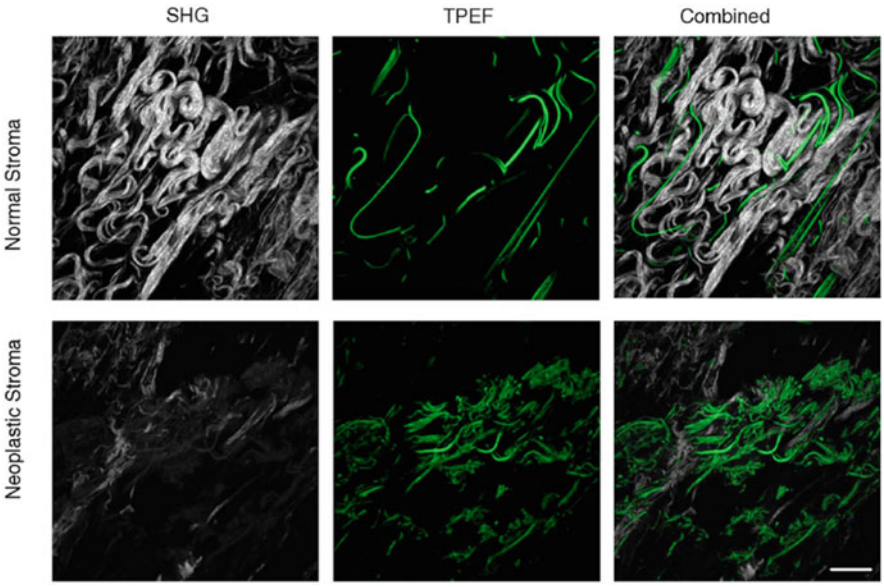

Fig. 5.6 From left to right: SHG, TPEF, and combined SHG (gray) and TPEF (green) images of the human esophageal stroma. Top to bottom: normal stroma and neoplastic stroma. The excitation wavelength λ_{ex} was 850 nm. Scale bar = 20 μm [26]

of microns under the skin, and SHG imaging can reach this depth without the need for traditional slicing. By comparing the SHG signal in the normal esophageal tissue and esophageal tumor tissue matrix (Fig. 5.6), Zhou et al. [26] found that these two showed distinct tissue characteristics, proving that SHG signal could exhibit biomorphological phenomena, such as the related changes of collagen, elastin, and proportional changes of matrix molecules, which were important markers of tumor progression. In monitoring the therapeutic effect of tumors, SHG can also play a pivotal role. Steele et al. performed SHG imaging of tumor cells stained with collagen and eGFP, and clearly observed the different effects of C6001 and GM6001 on osteosarcoma, respectively.

As a new disease diagnosis method, SHG imaging is still in the stage of experimental research and is mainly applied to animal disease models and a small number of clinical specimens. Its accuracy, specificity, sensitivity, and reproducibility for disease diagnosis still require extensive clinical studies to further validate.

The measurement of cell membrane voltage plays an important role in understanding the process of cell signaling. After labeling with a suitable membrane dye, the change in signal intensity can reflect the magnitude of the membrane voltage through SHG imaging of the dye molecules. In recent years, a major area of SHG imaging is the development of optical measurement methods, which can be used for transmembrane voltage across living cells, with high spatiotemporal resolution and high sensitivity. In 1993, Bouevitch et al. [27] demonstrated that the applied electric

field can strongly modulate SHG intensity. In 1999, Campagnola et al. [28] proved that SHG signal varies with membrane voltage. In 2003, Millard et al. [29] found that SHG was more sensitive to membrane voltage than TPEF. When the excitation wavelength was 850 nm, the sensitivity of SHG to the membrane voltage was 18/100 mV, while that of TPEF was only 10/100 mV. One year later, they further studied the sensitivity of the SHG signal generated by the styrene-based dye to the membrane voltage [30]. Their experiments showed that at an excitation wavelength of 850–910 nm, the dye made SHG sensitive to membrane voltage as high as 20/100 mV, and due to the resonance enhancement, the sensitivity reached 40/100 mV when the excitation wavelength of 950–970 nm was used. These findings further consolidated the significance of SHG in functional imaging of membrane voltage in living cells.

SHG imaging provides a new method for in vivo measurement due to its high sensitivity to microstructure, high spatial resolution, and low biocidal properties, and is expected to be a powerful tool for histomorphology and physiology research. At present, SHG has made some progress in neuroscience, pharmacology, and early diagnosis of diseases. However, SHG imaging is still an immature technology, and its application still needs further development with the deepening of research. With the development of optical fiber technology, SHG imaging can also be combined with fiber optics for human endoscopy to achieve imaging at the molecular level in deep tissues of living organisms. Assisted with signal detection technology and computer technology, SHG imaging can also be used to observe biological activity in real time. It is foreseeable that in the near future, SHG imaging will become a powerful tool in biomedical research and clinical diagnosis.

5.2.3.2 Second-Harmonic Light Scattering (SHS)

In addition to SHG imaging, another important research area based on the SHG phenomenon is SHS, which has proved to be one of the best techniques for studying surface molecular information in various colloidal solutions. SHG has inherent surface/interface specificity because it is inhibited in centrosymmetric medium under dipole approximation. When molecules are freely dispersed in a large amount of liquid, no coherent SHG signal can be generated, because SHG emitted from adjacent molecules can destructively interfere, only incoherent super-Rayleigh scattering left. When molecules are absorbed onto the surface of the particles, the molecules are connected to each other, and the second harmonic emitted by the molecules can coherent to contribute to the SHG signal. If the particle is larger than the excitation wavelength and the center symmetry of the particle surface is broken, SHS can be generated. In micron-scale colloidal solutions, the SHG sensitivity is proportional to the number of molecules adsorbed on the colloidal surface, so SHS can be used to measure the kinetics of adsorption.

In 2005, Eckenrode et al. [31] analyzed the effect of surface charge and composition on molecular adsorption kinetics by adsorbing cationic nonlinear optical probe, the dye molecule malachite green (MG, Fig. 5.7), on an aqueous solution

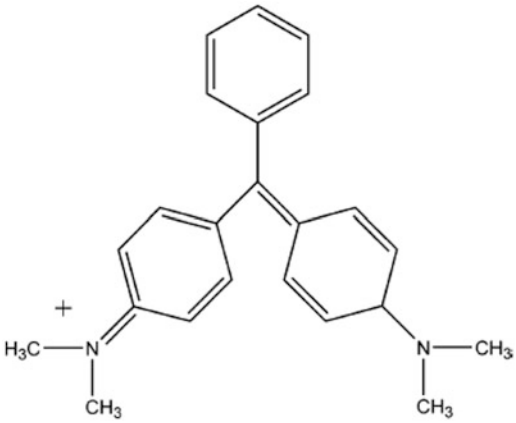

Fig. 5.7 Malachite green cation structure. The equivalent resonance structures with the positive charge on either one of the N atoms result in a C_{2v} symmetry. The Cartesian coordinates in the molecular frame are set to have the z' axis parallel to the C_2 rotation axis and the y' axis out of the molecular plane

with pH $\leq$ 5 (Fig. 5.8). MG is an SHG-active molecule, and its presence can increase the SHG signal intensity of the bulk solution. They used three types of polystyrene particles with different surface compositions: (1) sulfate-terminated anionic surfaces, (2) neutral surfaces terminated without any functional groups, and (3) an amine-terminated cationic surfaces. The result was that, regardless of the surface potential, the cationic dye can be adsorbed on the surfaces of all the above three kinds of particles. It indicated that the generation of optical second harmonic can be used to characterize the absorption of cationic dye molecules on anionic, neutral, or cationic colloidal surface in aqueous solution. The nonlinear optical method allows measurement of adsorption free energy, adsorption density, and even adsorption configuration. The adsorption density of the dye molecules on the above three kinds of surface was independently measured using a centrifugal separation technique, and the results obtained were in agreement with the SHG measurements.

Although SHG is inherently sensitive to interface, rigorous theoretical processing is still required in order to determine the interfacial properties of the colloidal particles and to explain the experimental observations. Gonella et al. [32] have developed a framework for calculating the intensity of SHS produced by monolayers absorbed on spherical particles using nonlocal mean (NLM) theory and appropriate boundary conditions (Fig. 5.9). It has been shown that the NLM theory can be applied to fit experimental scattering plots of second harmonic generated from particles of any size, and such an analysis can determine the adsorption configuration and the hyperpolarizability of the molecules absorbed on the particle surface.

Understanding the complexity of the interaction among molecules, ions, and phospholipid bilayers is important to advance application of drug delivery. In 2017, Kumal et al. [33] realized the real-time study on the adsorption and transport kinetics of MG molecules on the surface of liposomes under different buffer and salt ion conditions by applying SHS (Figs. 5.10 and 5.11). In citrate buffer without adding other salt ions, the transport of MG on 1,2-dioleoyl-*sn*-glycero-3-[phospho-rac-(1-glycerol)] (DOPG) and 1,2-dioleoyl-*sn*-glycero-3-phospho-L-serine (DOPS)

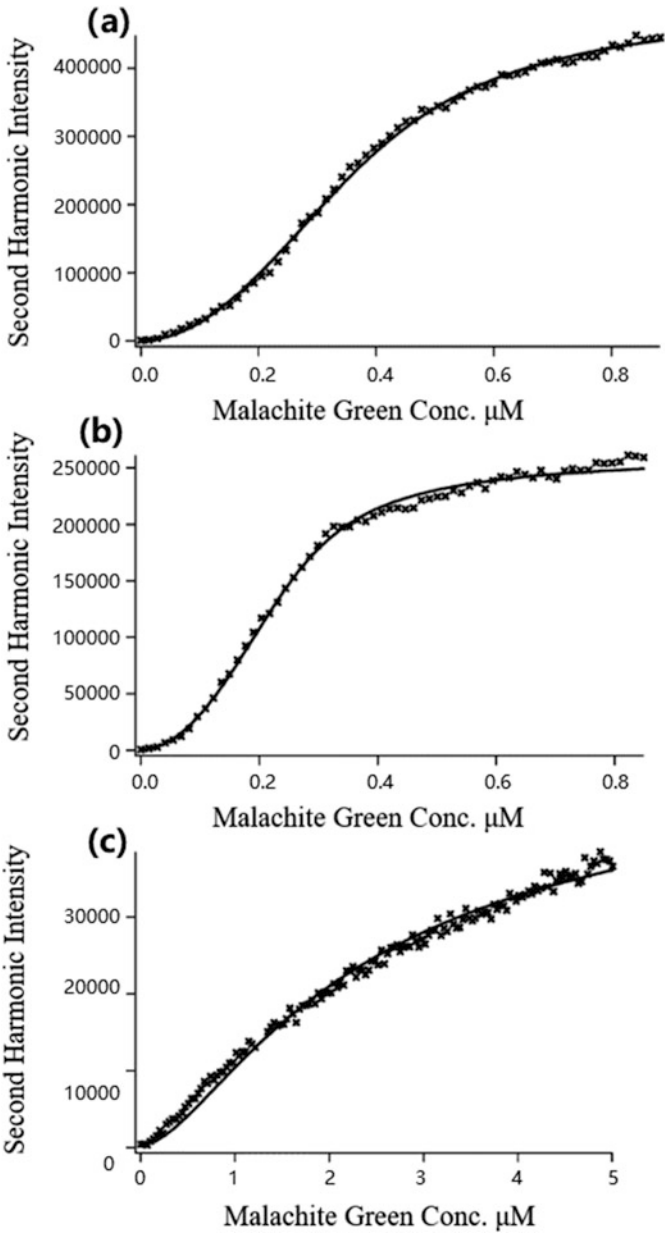

Fig. 5.8 Second harmonic intensity detected as a function of the added concentration of malachite green dye in the colloid solutions of (**a**) plain polystyrene microspheres (PPS); (**b**) polystyrene sulfate microspheres (PSS); and (**c**) polystyrene amino microspheres (PSA). The SH intensity is expressed in number of photon counts per second [31]

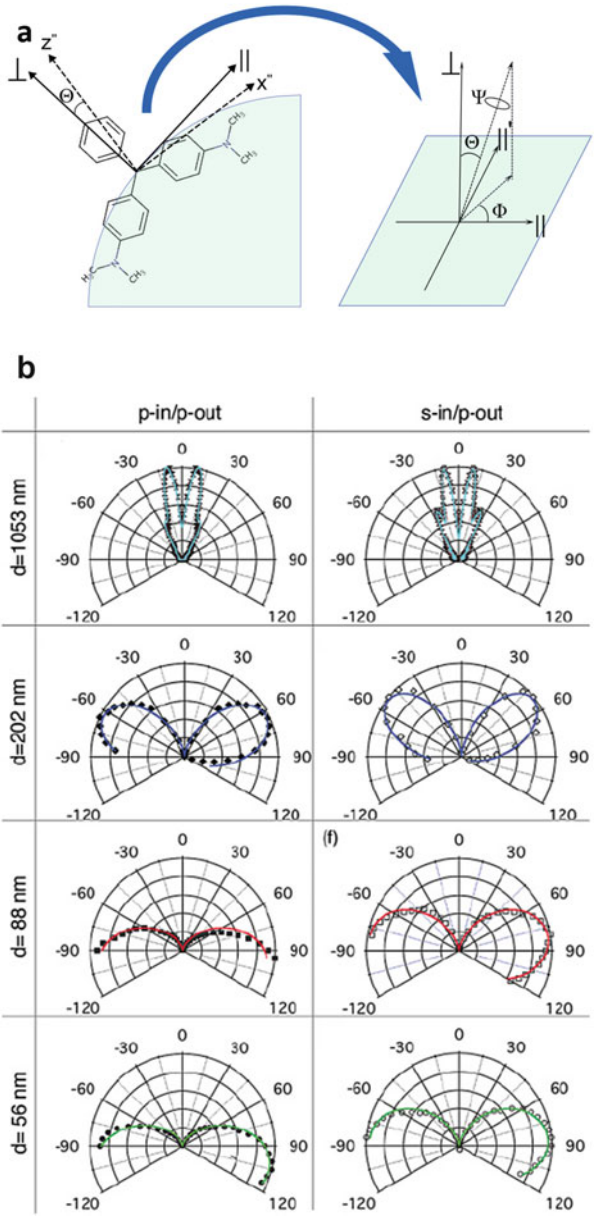

Fig. 5.9 (**a**) MG structure and relation between the surface local coordinate system ($\|$, $\|'$, $\perp$) and the molecular reference frame (x'', y'', z'') (blown up on the right-hand side). Given the isotropicity of the surface $\|\equiv\|'$. (**b**) The best NLM model fit to the experimental data (SH intensity vs. scattering angle Θ) for different particle diameters and polarization combinations. $\Theta = 0$ indicates the fundamental propagation direction. The fundamental wavelength is 840 nm [32]

liposomes was faster, whereas no adsorption and transport of MG on trimethyl quinone-1,2-dioleoyl-*sn*-glycero-3-phosphoethanolamine (QPADOPE) and 1,2-dioleoyl-*sn*-glycero-3-phosphocholine (DOPC) liposomes was observed. The transport rate constant of MG molecules in DOPG liposomes increased linearly with MG concentration, but that in DOPS liposomes was much less dependent on

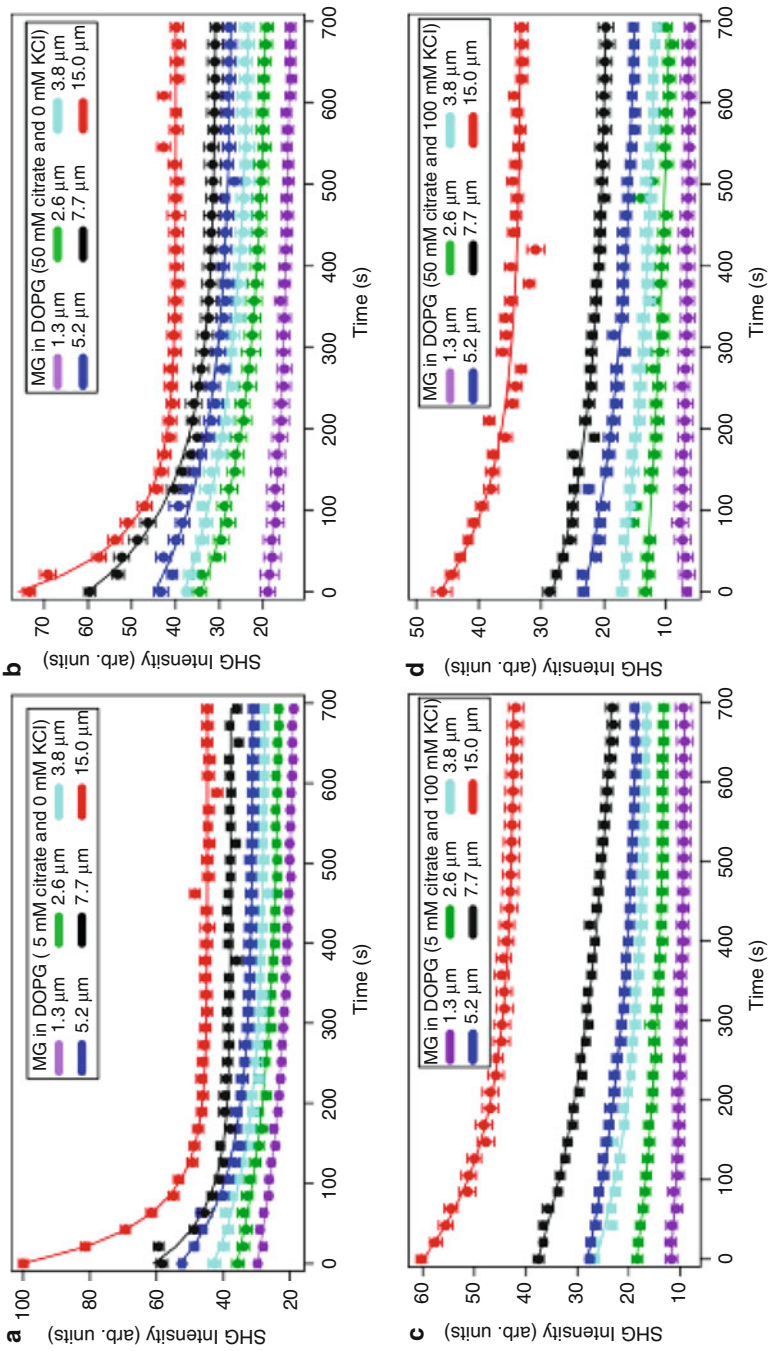

Fig. 5.10 SHG time profiles of DOPG liposomes (50 µM lipid) with various MG concentrations in aqueous (pH 4.0) buffer solutions composed of (**a**) 5 mM citrate and 0 mM KCl, (**b**) 50 mM citrate and 0 mM KCl, (**c**) 5 mM citrate and 100 mM KCl, and (**d**) 50 mM citrate and 100 mM KCl [33]

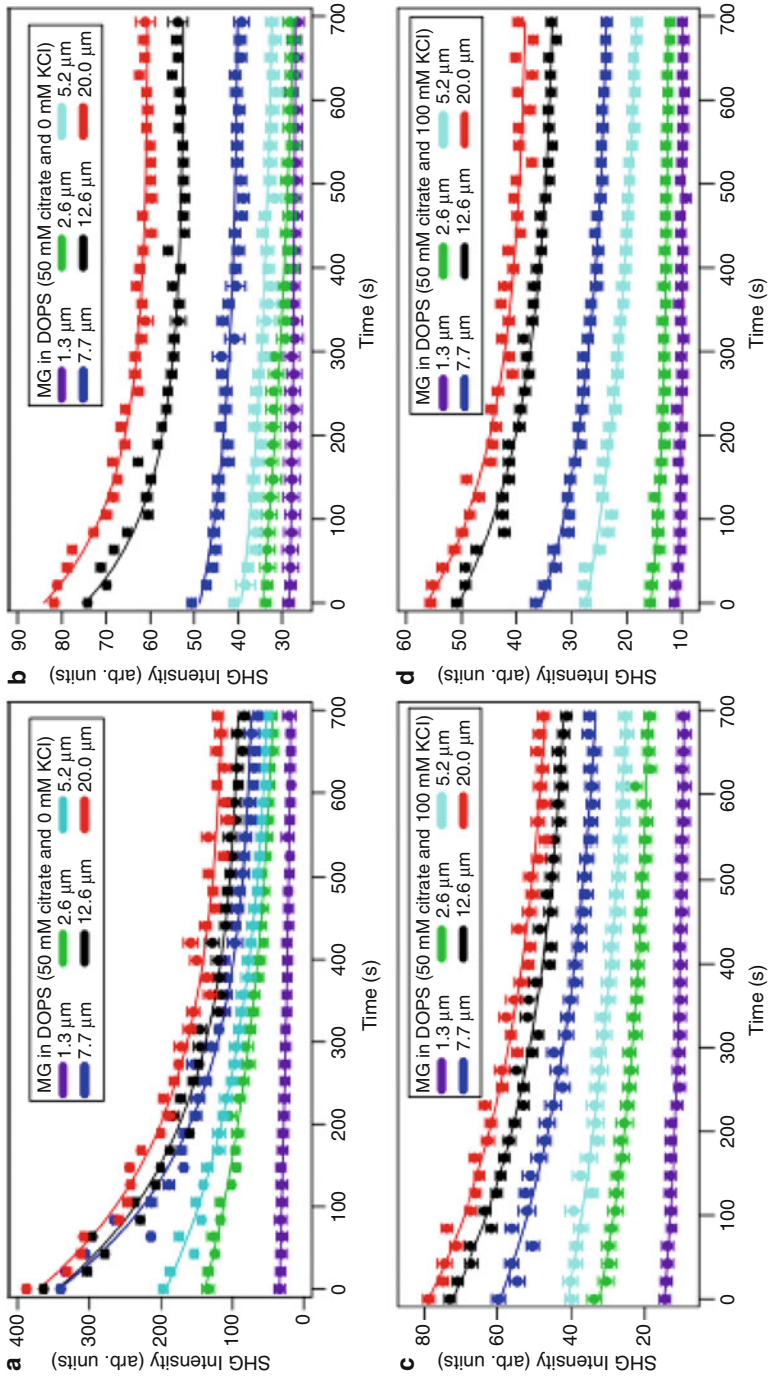

Fig. 5.11 SHG time profiles of DOPS liposomes (50 μM lipid) with various MG concentrations in aqueous (pH 4.0) buffer solutions composed of (**a**) 5 mM citrate and 0 mM KCl, (**b**) 50 mM citrate and 0 mM KCl, (**c**) 5 mM citrate and 100 mM KCl, and (**d**) 50 mM citrate and 100 mM KCl [33]

MG concentration. The adsorption site density and the adsorption free energy were determined by fitting a modified Langmuir adsorption isotherm model. As a result, the free energy generated by the adsorption of MG on the liposome surface was higher without the addition of salt ions due to the increased electrostatic. However, due to the formation of ion pairs and decreased repulsive force between the cation adsorbates, the corresponding adsorption site density increased in the presence of other salt ions. Comparative experiments with different citrate buffers and KCl concentrations showed that the adsorption and transport of MG in liposomes were affected by several interrelated factors, including the molecular structure of the lipid head group, the electrostatic interaction between the charged liposomes and the ion adsorbates, the electrolyte, and the formation of ion pairs. These findings highlight important considerations for potential application of liposome-based drug delivery and transport of small molecule drugs across the plasma membrane.

In addition to model cells—liposomes, SHS has also been used to detect the kinetics of interaction between molecules and living cells. Dai et al. [34] utilized SHS technology to observe the adsorption and transport of MG on *Escherichia coli* (*E. coli*) membrane (Fig. 5.12). The SHG signal intensity I is proportional to the square of the molecular adsorption number N. In the single-layer membrane model, N is equal to the difference between the number of particles inside and outside the membrane, $N = (N_o - N_i)$. In the two-layer membrane model, N is equal to the sum of the difference between the number of particles inside and outside the inner membrane and the outer membrane, $N = (N_{1o} - N_{1i} + N_{2o} - N_{2i})$. When there are only MG molecules in the bulk solution, only High Rayleigh Scattering (HRS) phenomenon occurs. After the cells are added to the bulk, the positively charged MG is rapidly adsorbed to the outer layer of the negatively charged cell membrane, and a peak appears when it reaches saturation. After that, the MG molecules gradually begin to adhere to the inner layer of the cell membrane, and the SHG signals emitted by the inner and outer MG molecules cancel each other out, so the signal intensity decreases until the difference in the number of molecules in the inner and outer layers reaches an equilibrium state. As a typical Gram-negative bacterium, there is a loose outer membrane outside the peptidoglycan cell wall of E. coli in addition to a layer of cytoplasmic membrane. The obtained SHS signals recorded the transport of MG across the above two membranes chronologically. At low concentrations, the SHS technology clearly exposed a multi-step transport process of MG on E. coli. After fitting the data to a multi-process kinematics model, it was revealed that MG transported through the outer membrane much faster than through the cytoplasmic membrane, which may reflect the efficient transitivity of the porin ion channels in the outer membrane. These observations demonstrate that SHS technology has the capability to be broadly applied for studying the interaction of small molecules with living cells.

In 2018, Dai et al. [35] studied azithromycin (AZM)-induced changes to E. coli membrane properties monitored in vitro by SHS (Fig. 5.13). AZM contains macrolides and is clinically used to treat infections caused by bacteria. Macrolides can bind to bacterial ribosome subsets, thereby inhibiting protein synthesis in bacteria, so AZM is widely used as antibiotic. Based on its pharmacological

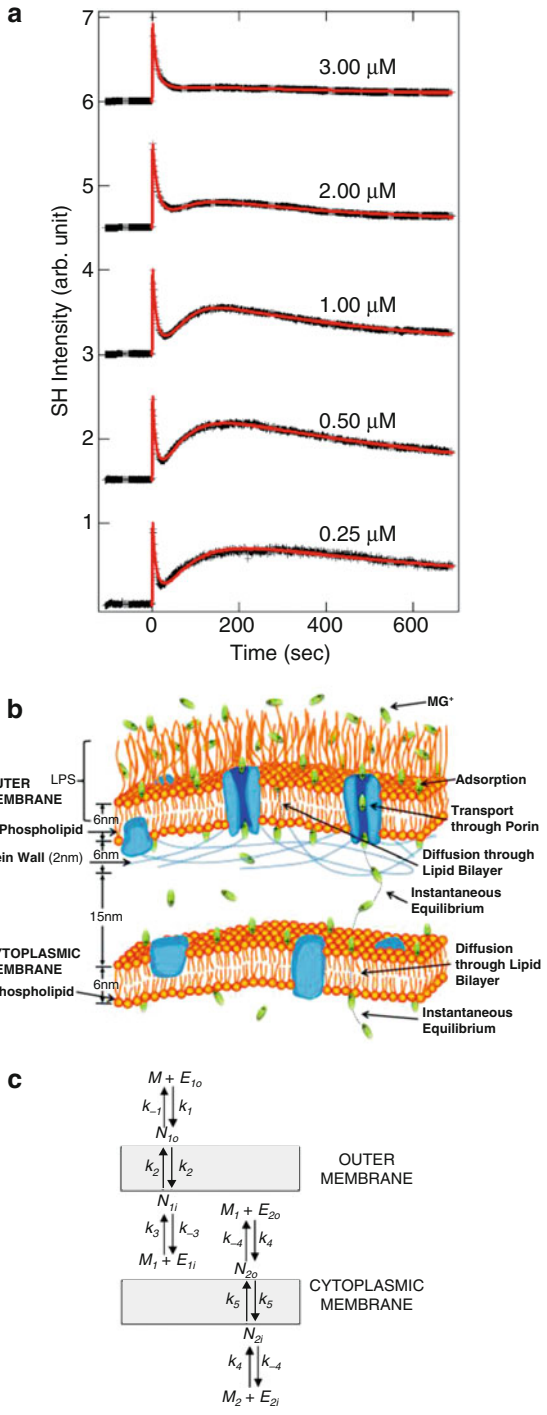

Fig. 5.12 (**a**) Adsorption isotherm expressed in SH intensity for MG^+ ion on the *E. coli* cell. (Solid line) Nonlinear least-square fit of a modified Langmuir model. (Error bars) Standard deviations. (**b**) Illustration of the two membranes of E. coli bacteria. Types of interactions of the molecular ion with the membranes are listed on the right side. (**c**) Schematic depiction of all adsorption, desorption, and transport processes and their associated rate constants which comprise the kinetic model. The values M, E, and N represent free MG^+, empty surface adsorption sites, and adsorbed MG^+, respectively. The values $k_{\pm 1, \pm 3, \pm 4}$ are adsorption/desorption rate constants and $k_{2,5}$ are transport rate constants [34]

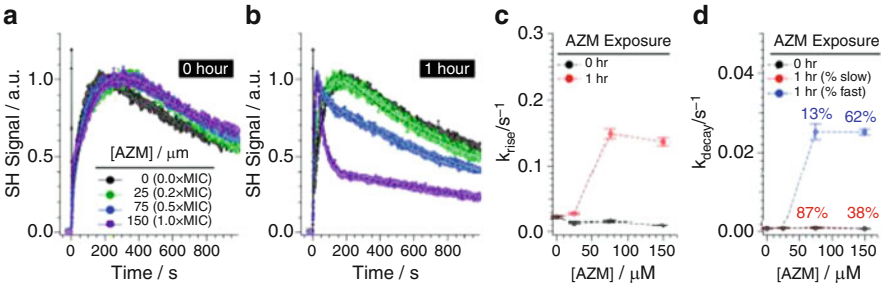

Fig. 5.13 Representative time-resolved SHS signal collected during bacterial uptake of MG following (**a**) 0 h or (**b**) 1 h exposure to 0 (black), 25 (green), 75 (blue), or 150 μM (purple) AZM. SHS intensities have been normalized to the CM (cytoplasmic membrane) transport peak. Dashed lines represent best fit results. Fit deduced rate constants corresponding to (**c**) adsorption onto the outer surface of the CM and (**d**) transport across the CM, as a function of AZM concentration. The relative fraction of fast (blue) and slow (red) transport are annotated above the corresponding markers in (**d**). Error bars depict standard deviation of the rates from minimally $n = 3$ trials for each AZM concentration [35]

properties, AZM must enter cells in order to function, so it is meaningful to study the interaction between macrolides and cell membranes. Existing studies have displayed that the size of AZM can not be passively transported through the bacterial outer membrane porin channel, but can rapidly enter cells through the so-called self-promoting pathway. This special pathway is accomplished by disrupting the lipo-polysaccharide on the outer membrane, resulting in enhanced permeability of the outer membrane. Previous studies have examined the interaction of AZM and model cell membranes, demonstrating that macrolides alter the structure of phospholipids and the fluidity of membranes. Dai et al. used real *E. coli* cells to quantitatively study the interaction of different concentrations of AZM with *E. coli* bilayer membranes. The enhanced membrane permeability allows the SHG-active molecules to transport faster through the membrane, which is a faster decay rate of the signal intensity reflected in the SHG spectrum, so SHS can be used to detect changes in membrane permeability. When *E. coli* cells were not pretreated with AZM for a certain period of time, the rate of adsorption and transport on the cytoplasmic membrane were almost the same regardless of the concentration of AZM added. When *E. coli* cells were pretreated with AZM for 1 h, the permeability of the outer membrane and the cytoplasmic membrane of *E. coli* changed greatly, especially at high concentrations, the rate of adsorption and transport on the cytoplasmic membrane became faster. The adsorption and transport rate constants were fitted by least squares method. It was found that when the bacteria were pretreated with high concentration of AZM, the decay of the SHG signal generated on the cytoplasmic membrane was divided into two rates. Moreover, as the concentration of AZM increased, the proportion of rapid decay accounted for more, indicating that AZM of high concentration induced a secondary efficient transport pathway across the cytoplasmic membrane. This study demonstrates that SHS is a new tool for monitoring changes in the properties of live bacterial membranes induced by antibacterial agents.

5.3 Sum Frequency Generation Spectroscopy

SFG is also a second-order nonlinear optical effect, which determines its nonsignaling for isotropic matter. Therefore, SFG has high sensitivity to the surface or interface and enables detection of submolecular level at interface. Compared with infrared spectroscopy, SFG is more sensitive to discriminate the secondary structure of peptides. It is an ideal technique for detecting and characterizing the polypeptide or protein structure at the solid–liquid interface in situ. It is a powerful experimental tool for studying vibrational spectroscopy and kinetic changes at interface [36].

5.3.1 History

Both SFG and SHG belong to the second-order nonlinear optical effect. Therefore, the discovery of SFG originated from the study of nonlinear optics. The discovery and development of nonlinear optics benefited from the advent of lasers in the 1960s. The exploration and application of laser technology has opened up many important technologies and research fields, among which nonlinear optics is one of the most representative fields. As mentioned in Sect. 5.2.1, the SHG effect was discovered in 1961, which marked the birth of nonlinear optics. In the second year, the formula derived by Bloembergen et al. laid the theoretical foundation for nonlinear optics including SFG and SHG [37–39], for which they won the Nobel Prize in 1981. In 1962, Bass et al. [40] first observed the SFG signal in triglycine sulfate crystal. Subsequently, discoveries and reports on the generation process of the sum frequency appeared one after another. The researchers found that in many nonlinear crystals, the output of coherent light can be obtained even under the illumination by two lasers of different wavelength. These works meant that the laser frequency obtained from the laser was not limited to the initial frequency emitted by the laser medium, but also the frequency-adjustable laser can be obtained by the sum frequency or difference frequency coherence process of the nonlinear crystal, undoubtedly promoting the vigorous development of the laser manufacturing industry and applied lasers.

The purpose of the initial research using the SFG and SHG was to reveal the mechanism of the generation of sum frequency, the nonlinear optical properties of the detected matter, and the influence of external environmental changes on the nonlinear optical properties of the material. Like 1985, Dick et al. [41] used SFG and SHG for surface film structure studies and second-order nonlinear optical coefficient measurements. In 1987, Shen et al. [42] used the near-vibration energy level enhancement phenomenon of the SFG signals to measure the vibration modes and spectral curves of adsorbed molecules on the surface of glass, metals and semiconductors, respectively, and obtained the SFG vibration spectrum (SFG-VS) of the interface molecules, which was the first time SFG had been used for interface research. Since then, SFG-VS had been widely used to study the structure, state

and kinetics of interface molecules. In recent decades, SFG-VS has been used for various interfaces, not only limited to gas/solid interface, but also extended to gas/liquid, liquid/liquid and liquid/solid interfaces. An important type of model system is single-layer or multi-layer molecular film, such as organic molecular layer on surface of metal or polymer, or Langmuir film and LB film. Because of the biofilm similarity of these systems and the potential significance in the application of materials and microelectronic devices, the SFG-VS studies on these systems have attracted the attention of many researchers. Researches on surface composition and structure of polymers are also critical for understanding the surface properties of polymeric materials. Others have also studied some liquid or solid interfaces, such as the interface of electrodes.

5.3.2 Theory

Both SFG and SHG are three-photon optical processes, but their principles are slightly different. The SHG method utilizes two photons with a frequency of ω to simultaneously interact with a nonlinear optical medium to obtain an emitted photon with a frequency of 2ω. Since the two photons have the same frequency, it is only necessary to use a laser with a sufficiently high intensity to generate SFG signal. The SFG method uses two beams of different frequencies ω_1 and ω_2 (usually one beam of visible light with a fixed wavelength and the other beam of infrared light with a tunable wavelength) to interact with a nonlinear medium to generate a sum frequency of $\omega_1 + \omega_2$. Since one of the incident lights of the SFG is infrared light with a tunable wavelength, the infrared light can be coupled with the vibrational energy level in the interface molecule, thereby obtaining near-resonance enhancement of the SFG signal during the vibration transition. The SFG spectrum thus obtained can be used as a powerful tool for obtaining molecular level information such as symmetry and orientation of interfacial molecules.

Through SFG spectrum, the orientation angle of the molecular groups at interface can be quantitatively analyzed. The specific method is as follows. Measure the SFG spectrum of different polarization combinations (ssp, ppp) at sample interface. For example, ssp means that the polarizations of the sum-frequency beam, visible beam and IR beam are s, s and p, respectively. The spectral intensity of the SFG is

$$I_\omega = \frac{8\pi^3\omega_s^2 \sec^2\theta_\omega}{c^3 n_1(\omega_1)n_1(\omega_2)n_1(\omega)}\left|\chi_{\text{eff}}^{(2)}\right|^2 I_1(\omega_1)I_2(\omega_2) \tag{5.5}$$

where $n_i(\omega_i)$ is the refractive index of the medium with optical frequency ω_i; ω and θ_ω are the frequency and exit angle of the sum-frequency beam; $I_1(\omega_1)$ and $I_2(\omega_2)$ are the intensity of the incident visible beam and IR beam, respectively; $\chi_{\text{eff}}^{(2)}$ is the effective second-order nonlinear polarizability tensor component. The measured ssp SFG spectra correspond to the effective second-order nonlinear polarizability $\chi_{\text{eff}}^{(2)}$.

According to the projection relationship of the polarization coordinates in the laboratory coordinate system and the Fresnel coefficient of the light reflected and transmitted at the interface, the second-order polarizability $\chi^{(2)}_{ijk}$ of the molecules can be obtained (i, j, k is the laboratory coordinate system, where ssp corresponds to $\chi^{(2)}_{yyz}$ of the isotropic XY interface). The second-order nonlinear polarizability $\chi^{(2)}_{ijk}$ of the molecule in laboratory coordinates (X, Y, Z) and the molecular hyperpolarizability $\beta^{(2)}_{\eta\xi\zeta}$ in molecular coordinates (η, ξ, ζ are molecular axes) can be converted to each other by Euler formula. The three Euler angles: the tilt angle θ is the angle between the major axis ζ of the molecular group and the Z axis (interface normal) in laboratory coordinates, the twist angle ψ is the rotation angle of the molecular group around the ζ axis, and azimuth angle φ is the angle between the projection of ζ axis on the XY plane and the X axis. SFG spectral analysis can obtain the orientation angle of molecular groups at the interface. The correspondence between the effective second-order nonlinear polarizability tensor $\chi^{(2)}_{\text{eff}}$ and all components of the molecular hyperpolarizability tensor $\beta^{(2)}_{\eta\xi\zeta}$ can be obtained through $\chi^{(2)}_{\text{eff}} \rightarrow \chi^{(2)}_{ijk} \rightarrow \beta^{(2)}_{\eta\xi\zeta}$. The value of θ, ψ, φ obtained by solving the equation is the orientation angle of the molecular group at the interface. Interfacial symmetry is applied to quantify molecular orientation angle. The tensor $\chi^{(2)}$ is simplified in molecular symmetry, and Raman tensor and Raman depolarization ratio of the molecular group are also utilized. The flow chart of Fig. 5.14 shows how the SFG spectra are analyzed to get molecular orientation angles.

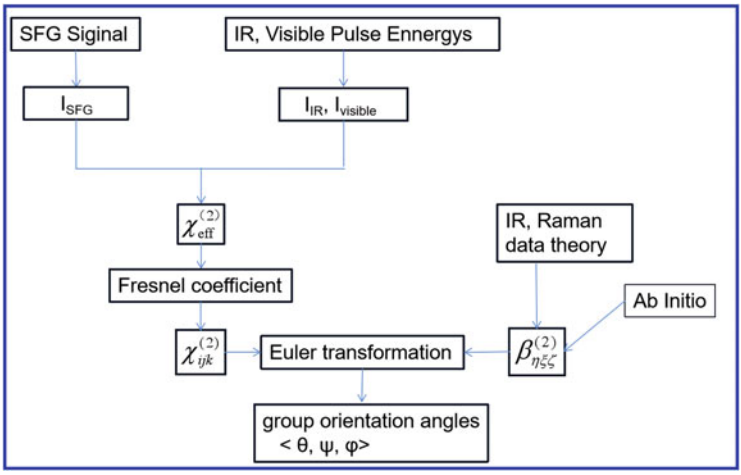

Fig. 5.14 Illustration of the steps to obtain molecular group orientation in SFG data analysis. Some of these steps could be avoided by using reference samples or spectral ratios acquired with different polarization combinations

5.3.3 Application

As a unique interface detection and analysis method, SFG-VS can be used to change the experimental configuration to fit for various interfaces or surfaces according to actual conditions. The three-photon transition process of SFG can be simplified into an infrared vibration excitation process and an anti-Stokes Raman emission process. If the incident infrared light resonates with the vibrational level transition of the molecule, the SFG signal could be enhanced. Through measuring SFG spectra of molecules at surface/interface and quantitatively analyzing the spectra, various information such as group orientation, alignment conformation, molecular density, molecular adsorption, intermolecular hydrogen bonding and reaction kinetics can be obtained, which is beneficial to understand the interface molecular properties. In the past two decades, the development and application of SFG-VS in interface research in the fields of physics, chemistry, biology, materials and catalysis have become more and more extensive and in-depth.

For the complexity and the low sensitivity detection of SFG-VS, early studies on SFG-VS focused on interfaces composed of simple molecules such as air/water interface, air/alcohol interface, and air/quart interface. In addition, there are 27 third-order tensors in the nonlinear optical process, and the SFG signal is also affected by the incident angle and the interface molecular density. In the face of complex and SFG-VS information, the lack of effective quantitative analysis was a major obstacle to the development of SFG-VS. Early Rao et al. [43] used model molecules to simplify the research system, thereby developing methods for meticulous measurement and analysis of interface and obtaining information about molecular structure, orientation, and kinetics. These experiences and formulas derived from simple molecular systems have laid the foundation for the study of various complex molecular systems. Through the developed methods using SFG-VS for interface research, the vibration peaks of each group can be assigned according to molecular symmetry, thereby characterizing the interface molecular structure and the changes of physicochemical properties of the molecule produced by external conditions. However, even in recent years, research on simple molecular interfaces is still one of the hot topics in interface science research. With the development of laser experimental technology and the improvement of theoretical methods, SFG-VS can get more comprehensive, accurate, and reliable molecular-level information.

Since the interface science itself was derived from the study of molecular membranes at the gas/liquid interface, initial researches from Langmuir film to LB film, self-assembled membrane, phospholipid bilayer membrane, and other molecular membranes composed of various molecules have high application value in the field of surface materials and semiconductor devices. Due to the ordered arrangement of interface molecules, the Langmuir film formed on the air/water interface is an excellent system for SFG to perform microscopic interface detection and analysis. Shen et al. [44] formed a Langmuir film on the air/water interface of liquid crystal molecules, and described the method of using SFG intensity under various polarization combinations to quantitatively analyze and obtain interface molecular

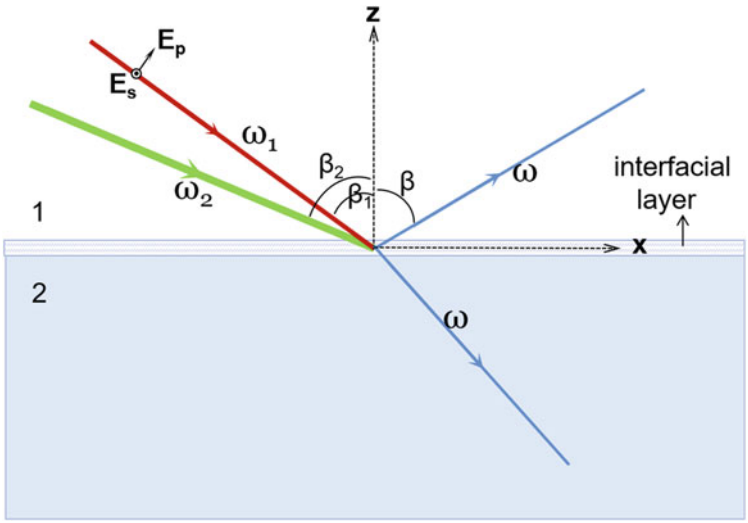

Fig. 5.15 Geometry for SHG and SFG from an interface in the reflection direction [44]

orientation and alignment structure, which laid a foundation for the study of complex molecular systems (Fig. 5.15). Based on this work, interface research using SFG-VS has rapidly expanded to the detection on LB film and other kinds of interface.

With the development of SFG-VS, researchers have carried out pioneering work in many fields such as electrochemistry and catalysis. Monitoring the surface molecular regulation process with SFG-VS is also one of the hot spots in recent years. The detection of the electrochemically controlled MHAE molecular layer conducted by Lahann et al. [45], and the detection of the azobenzene derivative self-assembled membrane of the gold nanolayer conducted by Wagner [46] et al. belonged to this type of research.

SFG-VS is also very extensive in the study of complex systems, such as polymers, peptides, proteins, and other macromolecules. These advances have also played an important role in understanding complex systems, such as polymer surfaces and cell membrane surfaces. The surface microstructure of polymer materials, especially the number and orientation of functional groups, directly determines the physical and chemical properties of the polymer surface. The accurate characterization of these molecular layer properties is conductive to understanding the molecular mechanism of the special functions and properties of polymers, and provides strong technical support for the development and application of polymer materials. Chen et al. [47, 48] carried out a series of work on the polymer interface. They used SFG-VS to clearly monitor and analyze the conformational transformation, rearrangement, and copolymerization of polymer molecules, and had strong use value from the perspective of new material development. The polymer system affected by temperature or pH is also one of the research hotspots in recent years. These molecules can be used not only to design various material interfaces but also

to simulate the folding process of long-chain proteins. The SFG-VS method can be used to obtain the understanding of their properties on the interface at molecular level, and can also provide new ideas for the structural design and performance regulation of these polymers.

The interaction of biomolecules at interfaces is very important in many processes. With the promotion of SFG, the application of SFG-VS in biomedical systems has also been greatly expanded. Phospholipid bilayer membrane is a model system for studying biomacromolecules. As a kind of biomimetic membrane, the phospholipid bilayer can simulate the structure of real cell membrane and be used to explore the microstructure of cell membrane. Studies on phospholipid membranes have initially focused on Langmuir monolayers formed by phospholipid molecules at gas/liquid interface. Roke et al. [49] used SFG-VS to study the orientation change of the side chain of the Langmuir phospholipid membrane during the phase transition caused by increasing membrane pressure. On the basis of the development of the Langmuir-Schaefer method, Chen et al. [50–57] studied and discussed the phase transition process of symmetric lipid bilayer membrane composed of various phospholipid molecules and the Flip-Flop characteristics of asymmetric lipid bilayer membrane. The interaction between the lipid bilayer membrane and polypeptide molecules and the structural properties of the proteins on the bilayer membrane were also quantitatively analyzed [58, 59]. Although SFG and SHG can not analyze the whole structure and overall morphology of biomacromolecules, the interaction characteristics and kinetic processes of biomacromolecules at the interface can be analyzed and characterized by dipole moment group labeling and characteristic peak tracking. This has important guiding significance for molecular layer interpretation of protein catalytic properties, development of biochips, and molecular kinetics simulation of cell membrane surface.

As a vibrational spectroscopy, SFG has the capacity of identifying secondary structure of peptides/proteins under different interfacial conditions [60–62]. SFG signal intensity is determined by the ordering of relative molecular groups. Compared with α-helix and β-sheet structures, the ordering of random coil is very low, which leads to the easy assignment of the peaks in the SFG spectra. As shown in Fig. 5.16, from the SFG spectra, we can clearly distinguish different secondary structural peaks.

Zhan Chen's lab developed systematic methods to analyze the SFG spectra of amide I band to determine the orientation of the peptides/proteins at interfaces. They developed methodology and calculated hyperpolarizability using a bond additivity model, the tilt angle of a α-helical structure can be deduced from SFG polarization measurements, as shown in Fig. 5.17 [57]. Similarly, the tilt and twist angles of an antiparallel β-sheet can also be determined [63]. For complex protein orientation determination, the tilt and twist angles are also needed to accurately define. Chen's group improved the methodology by combining the complementary measurements of SFG and ATR-FTIR spectroscopies, which could precisely determine the orientation of complex proteins [63].

Owing to its molecular surface/interface specificity, SFG-VS has become a versatile and powerful tool to investigate multiple interfaces. However, most SFG

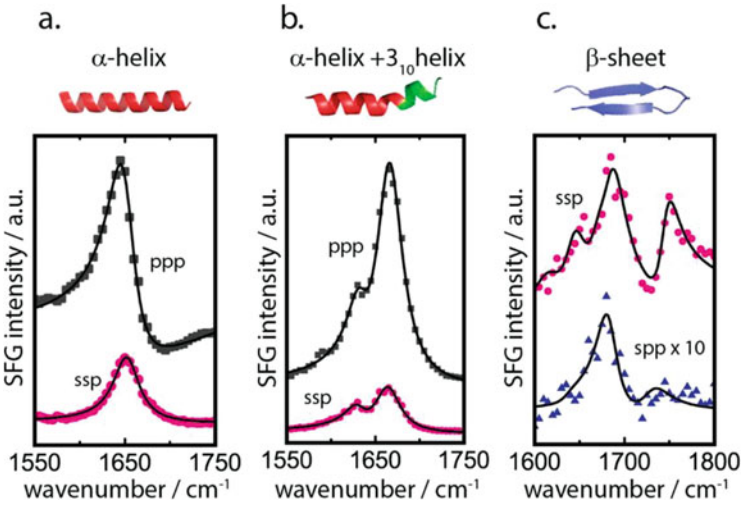

Fig. 5.16 SFG spectra collected from membrane associated peptides: (**a**) α-helical MSI-78; (**b**) alamethicin with α-helical and 3_{10}-helical segments; (**c**) β-sheet tachyplesin I [60–62]

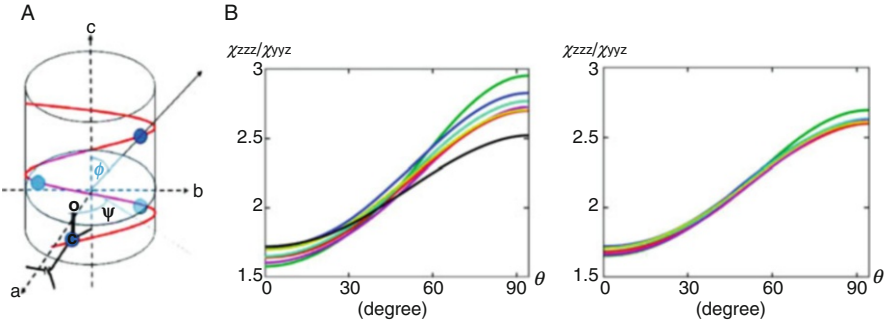

Fig. 5.17 (**a**) Correlation between the direction of the amide I transition dipole moment in one peptide unit and the molecular axis of an α-helix. The first peptide unit in Pauling's α-helix is also illustrated. (**b**) Relationship between the χ_{zzz}/χ_{yyz} ratio and θ for α-helices with different chain lengths; (left) blue: 10; green: 12; red: 13; cyan: 15; purple: 16; yellow: 17; and black: 18 residues; (right) blue: 28; green: 30; red: 31; cyan: 33; purple: 33; and yellow: 35 residues [57]

experiments were carried out to study the planar surface/interface. Expanding the application scope of SFG-VS to study the interface of submicron particles in suspension is an important development direction. Sylvie Roke et al. [64–66] deduced the formula for obtaining the SFG signal of spherical particles by the spherical scattering method. Through analyzing the results using a Rayleigh-Gans-Debye approximation, they could get information about the local molecular order and density of these chains at surface of the particle, which provides a new method

for measuring and characterizing colloidal particles in solution systems. Sylvie Roke's team also applied SFG scattering (SFS) to study the phospholipid vesicles [67]. As shown in Fig. 5.18, they found that charge and hydration transmembrane asymmetry occurred in liposomes in aqueous solution. In some cases, transmembrane asymmetry could happen, and then the PO_2^- vibrational stretching mode could be detected by SFS. The average orientation angle with respect to the surface normal of the phosphate group was quantified by analyzing the SFS spectra.

5.4 Summary and Outlook

How to obtain quantitative information from SFG spectrum is the key to characterizing interface molecules and gaining understanding at molecular level. Polarization analysis of SFG-VS is one of the most important methods of quantitative analysis. Changing the experimental configuration is also one of the most significant experimental techniques in SFG-VS. For a long time, researchers have only used the parameters of the experimental configuration as the basis for calculating the parameters in the interface molecular orientation angle function. In fact, the changing the experimental configuration can also adjust the contribution ratio of the macro second-order polarizability in the SFG spectrum, thereby changing the spectral shape, which can be another powerful tool for the quantitative analysis of the SFG-VS. The absolute phase of the second-order polarizability in SFG-VS is the key to determining the orientation of the interface molecules. The general approach is to obtain the relative phase by spectral fitting, but the simulated method is not accurate enough when multiple peaks are coherent. Morita et al. obtained the potential function of the interface molecule by theoretical simulation to get the absolute phase. The SFG phase-sensitive measurement method developed by Shen et al. [67–72] can accurately obtain the real and imaginary parts of the effective second-order polarizability in the SFG signal, which was also one of the analytical methods for the absolute phases of the second-order polarizability.

Since SFG technology relies on laser technology, the latter's advancement will also drive the development of the former. The application of dual resonance SFG based on ultraviolet and visible segment optical parametric amplifiers is becoming more and more widely used. The dual resonance sum frequency process can simultaneously resonate with the electron energy level and the vibration energy level of the interface molecules, which greatly enhances the generated SFG signal. More importantly, it can be used to study the coupling effect between the electron energy level and the vibration energy level of the molecules, and to understand the intramolecular detailed interaction and to correct the approximation and deviation in the quantitative calculation. The dual resonance experiment was used for the detection of chiral molecules, and the chiral response could be enhanced by 10 or even 100 times.

Since the molecular vibration relaxation process is about picoseconds, a short femtosecond laser must be used to detect and analyze the relaxation process after

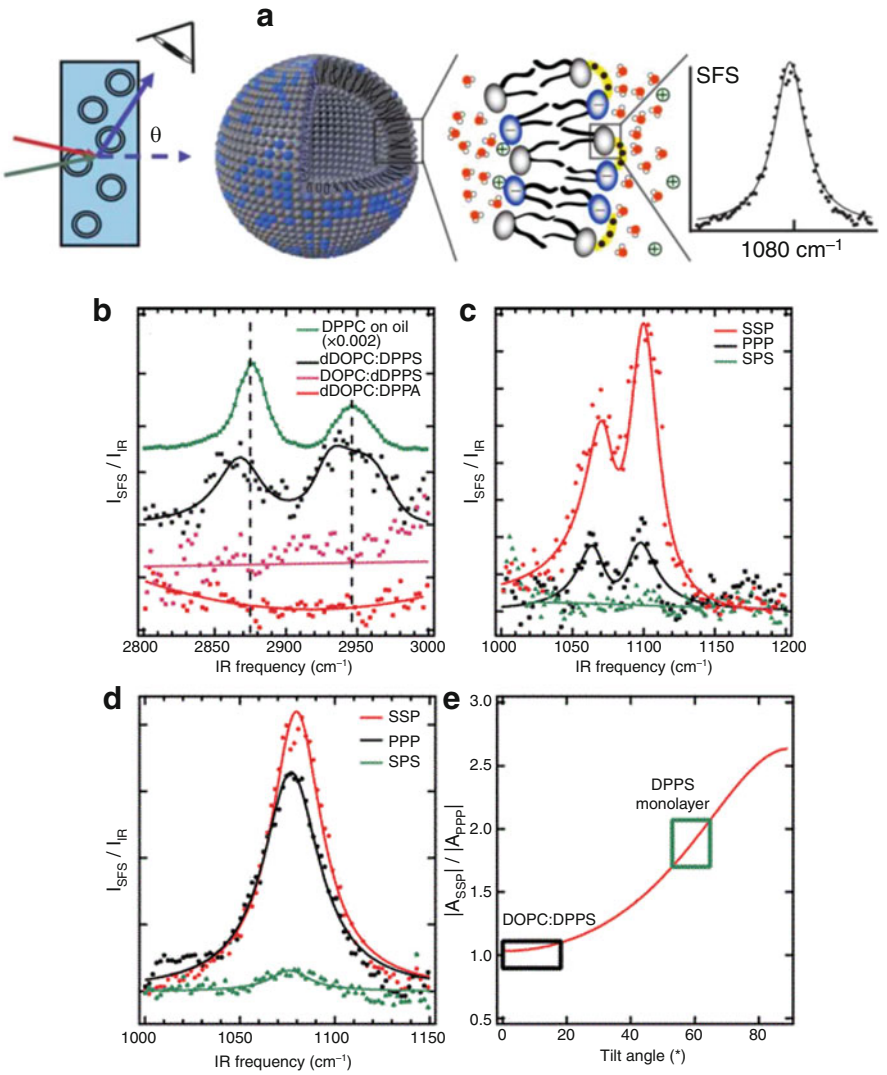

Fig. 5.18 (**a**) scehemtic of SFS measurement lipid veci 18 Quantifying transmembrane asymmetry. (**b**) SFS (SSP) spectra taken in the C-H stretch region of ~100 nm diameter liposomes in pure water composed of 1:1 mixtures of d_{66}-DOPC–DPPS (black), DOPC–d_{62}-DPPS (purple), and d_{66}-DOPC: DPPA (red) and the spectrum of the DPPC monolayer on oil droplets (green). The solid lines represent fits to the data. The SFS data are offset vertically for clarity. (**c**) SFS spectra of a DPPC monolayer on oil droplets, recorded in SSP (red), PPP (black), and SPS (green) polarization combinations. (**d**) SFS spectra of DOPC–DPPS liposomes in SSP (red), PPP (black), and SPS (green) polarization combinations. (**e**) Dependence of the amplitude ratio of the SSP and PPP polarization combinations of the s-PO_2^- stretch mode on the tilt angle. The boxes indicate the measured ratios obtained from the spectra in Panels (**c**) and (**d**)

molecular vibration excitation and the kinetics of interface molecular interaction. With the widespread use of femtosecond lasers, broadband SFG technology and pump-probe technology have also evolved. Broadband SFG technology utilized the excitation of broadband lasers, and then simultaneously detects the SFG signal at different wavelengths using optical multiplier and CCD, which can greatly improve the speed of data acquisition. Bonn et al. [73–76] developed time-resolved sum frequency generation and two dimensional-infrared SFG (IR-SFG) by using femtosecond SFG equipment and pump-probe technology, and combined with high vacuum reactor for detecting ultra-fast reaction kinetics of molecular vibration relaxation and phonon vibration relaxation and electron energy transfer at surface of different metal catalysis.

These new experimental techniques have opened up new directions for the widespread use of nonlinear optical detection methods. Additionally, the various nonlinear optical detection technologies developed in recent years include not only SFG and SHG technologies but also many optical imaging technologies that integrate multiple functions, such as SHG + TPF (two photon fluorescence), CARS (coherent anti-stokes Raman spectroscopy) + SFG. Many of the technologies described above can not only obtain multiple dimensional images with spectral resolution and spatial resolution but also gradually develop into effective in situ. Imaging techniques that do not require molecular markers have broad application prospects in the fields of biomedicine and materials.

References

1. Franken PA, Weinreich G, Peters CW, et al. Generation of optical harmonics. Phys Rev Lett. 1961;7(4):118–9.
2. Terhune RW, Maker PD, Savage CM. Optical harmonic generation in calcite. Phys Rev Lett. 1962;8(10):404–6.
3. Wang CC. Second-harmonic generation of light at the boundary of an isotropic medium. Phys Rev B. 1969;178(3):1457–60.
4. Brown F, Matsuoka M. Effect of adsorbed surface layers on second-harmonic light from silver. Phys Rev. 1969;185(3):985–7.
5. Rudnick J, Stern EA. Second-harmonic radiation from metal surfaces. Phys Rev B. 1971;4 (12):4274–90.
6. Chen CK, Heinz TF, Ricard D, et al. Detection of molecular monolayers by optical second-harmonic generation. Phys Rev Lett. 2014;46(15):1010–2.
7. Fleischmann M, Hendra PJ, Mcquillan AJ. Raman spectra of pyridine adsorbed at a silver electrode. Chem Phys Lett. 1974;26(2):163–6.
8. Heinz TF, Chen CK, Ricard D, et al. Spectroscopy of molecular monolayers by resonant Second-harmonic generation. Phys Rev Lett. 1982;48(7):478–81.
9. Tom HWK, Heinz TF, Shen YR. Second-harmonic reflection from silicon surfaces and its relation to structural symmetry. Phys Rev Lett. 1983;51(21):1983–6.
10. Guyotsionnest P, Chen W, Shen YR. General considerations on optical second-harmonic generation from surfaces and interfaces. Phys Rev B. 1986;33(12):8254–63.
11. Guyotsionnest P, Shen YR. Local and nonlocal surface nonlinearities for surface optical second-harmonic generation. Phys Rev B. 1987;35(9):4420–6.

12. Guyotsionnest P, Shen YR. Bulk contribution in surface second-harmonic generation. Phys Rev B. 1988;38(12):7985–9.
13. Shen YR. Optical second harmonic generation at interfaces. Annu Rev Phys Chem. 1989;40 (1):327–50.
14. Freund I, Deutsch M, Sprecher A. Connective tissue polarity. Optical second-harmonic microscopy, crossed-beam summation, and small-angle scattering in rat-tail tendon. Biophys J. 1986;50(4):693–712.
15. Freund I, Deutsch M. Macroscopic polarity of connective tissue is due to discrete polar structures. Biopolymers. 1986;25:601.
16. Freund M. Deutsch, Second-harmonic microscopy of biological tissue. Opt Lett. 1986;11(2):94.
17. Han M, Zickler L, Giese G, et al. Second-harmonic imaging of cornea after intrastromal femtosecond laser ablation. J Biomed Opt. 2004;9(4):760–6.
18. Cox G, Kable E, Jones A, et al. 3-dimensional imaging of collagen using second harmonic generation. J Struct Biol. 2003;141(1):53–62.
19. Campagnola PJ, Millard AC, Terasaki M, et al. Three-dimensional high-resolution second-harmonic generation imaging of endogenous structural proteins in biological tissues. Biophys J. 2002;82(1):493–508.
20. Theodossiou T, Rapti GS, Hovhannisyan V, et al. Thermally induced irreversible conformational changes in collagen probed by optical second harmonic generation and laser-induced fluorescence. Lasers Med Sci. 2002;17(1):34–41.
21. Tai DC, Tan N, Xu S, et al. Fibro-C-Index: comprehensive, morphology-based quantification of liver fibrosis using second harmonic generation and two-photon microscopy. J Biomed Opt. 2009;14(4):044013.
22. Sun W, Chang S, Tai D, et al. Nonlinear optical microscopy: use of second harmonic generation and two-photon microscopy for automated quantitative liver fibrosis studies. J Biomed Opt. 2008;13(6):064010.
23. Strupler M, Pena AM, Hernest M, et al. Second harmonic imaging and scoring of collagen in fibrotic tissues. Opt Express. 2007;15(7):4054–65.
24. Wu X, Zhuo S, Chen J, et al. Real-time in vivo imaging collagen in lymphedematous skin using multiphoton microscopy. Scanning. 2011;33(6):463–7.
25. Pena M, Fabre A, Débarre D, et al. Three-dimensional investigation and scoring of extracellular matrix remodeling during lung fibrosis using multiphoton microscopy. Microsc Res Tech. 2007;70(2):162–70.
26. Zhuo S, Chen J, Xie S, et al. Extracting diagnostic stromal organization features based on intrinsic two-photon excited fluorescence and second-harmonic generation signals. J Biomed Opt. 2009;14(2):020503.
27. Bouevitch O, Lewis A, Pinevsky I, et al. Probing membrane potential with nonlinear optics. Biophys J. 1993;65(2):672–9.
28. Campagnola PJ, Wei MD, et al. High-resolution nonlinear optical imaging of live cells by second harmonic generation. Biophys J. 1999;77(6):3341–9.
29. Millard C, Jin L, Lewis A, et al. High sensitivity of second harmonic generation from styryl dyes to cell membrane potential. Biophys J. 2003;86(2):1169–76.
30. Millard C, Jin L, Wei M, et al. Sensitivity of second harmonic generation from styryl dyes to transmembrane potential. Biophys J. 2004;86(2):1169–76.
31. Eckenrode MH, Jen SH, Han J, et al. Adsorption of a cationic dye molecule on polystyrene microspheres in colloids: effect of surface charge and composition probed by second harmonic generation. J Phys Chem B. 2005;109(10):4646–53.
32. Gonella G, Dai HL. Determination of adsorption geometry on spherical particles from nonlinear Mie theory analysis of surface second harmonic generation. Phys Rev B. 2011;84(12):121402.
33. Kumal RR, Nguyenhuu H, Winter JE, et al. Impacts of salt, buffer, and lipid nature on molecular adsorption and transport in liposomes as observed by second harmonic generation. J Phys Chem C. 2017;121(29):15851.

34. Zeng J, Eckenrode HM, Dounce SM, et al. Time-resolved molecular transport across living cell membranes. Biophys J. 2013;104(1):139–45.
35. Gh MS, Wilhelm MJ, Dai HL. Azithromycin-induced changes to bacterial membrane properties monitored in vitro by second-harmonic light scattering. ACS Med Chem Lett. 2018;9 (6):569–74.
36. Ding B, Chen Z. Sum frequency generation vibrational spectroscopy. Berlin: Springer; 2013.
37. Armstrong JA, Bloembergen N, Ducuing J, et al. Interactions between light waves in nonlinear dielectric. Phys Rev. 1962;127(6):1918–39.
38. Bloembergen N, Pershan PS. Light waves at the boundary of nonlinear media. Phys Rev. 1962;128(2):606–22.
39. Ducuing J, Bloembergen N. Observation of reflected light harmonics at the boundary of piezoelectric crystals. Phys Rev Lett. 1963;10(11):474–6.
40. Bass M, Franken PA, Hill AE, et al. Optical mixing. Phys Rev Lett. 1962;8(1):18.
41. Dick B, Gierulski A, Marowsky G, et al. Determination of the nonlinear optical susceptibility $\chi^{(2)}$, of surface layers by sum and difference frequency generation in reflection and transmission. Appl Phys B Lasers Opt. 1985;38(2):107–16.
42. Zhu XD, Suhr H, Shen YR. Surface vibrational spectroscopy by infrared-visible sum frequency generation. Phys Rev B. 1987;35(6):3047–50.
43. Rao Y, Comstock M, Eisenthal KB. Absolute orientation of molecules at interfaces. J Phys Chem B. 2006;110(4):1727–32.
44. Zhuang X, Kim D, Miranda P, et al. Mapping molecular orientation and conformation at interfaces by nonlinear optics. Phys Rev B. 1999;59(19):12632–40.
45. Lahann J, Mitragotri S, Tran TN, et al. A reversibly switching surface. Science. 2003;299 (5605):371–4.
46. Wagner S, Leyssner F, Kördel C, et al. Reversible photoisomerization of an azobenzene-functionalized self-assembled monolayer probed by sum-frequency generation vibrational spectroscopy. Phys Chem Chem Phys. 2009;11(29):6242–8.
47. Chen Z, Shen YR, Somorjai GA. Studies of polymer surfaces by sum frequency generation vibrational spectroscopy. Annu Rev Phys Chem. 2002;53(1):437–65.
48. Chen Z, Ward R, Tian Y, et al. Surface composition of biopolymer blends Biospan-SP/Phenoxy and Biospan-F/Phenoxy observed with SFG, XPS, and contact angle goniometry. J Phys Chem B. 1999;103(15):2935–42.
49. Roke S, Schins J, Müller M, et al. Vibrational spectroscopic investigation of the phase diagram of a biomimetic lipid monolayer. Phys Rev Lett. 2003;90(12):128101.
50. Chen X, Wang JC, Chen Z. Real-time structural investigation of a lipid bilayer during its interaction with melittin using sum frequency generation vibrational spectroscopy. Biophys J. 2007;93(3):866–75.
51. Chen X, Boughton AP, Tesmer JJ, et al. In situ investigation of heterotrimeric G protein betagamma subunit binding and orientation on membrane bilayers. J Am Chem Soc. 2007;129(42):12658–9.
52. Wang J, Lee SH, Chen Z. Quantifying the ordering of adsorbed proteins in situ. J Phys Chem B. 2008;112(7):2281–90.
53. Even MA, Wang J, Chen Z. Structural information of mussel adhesive protein Mefp-3 acquired at various polymer/Mefp-3 solution interfaces. Langmuir. 2008;24(11):5795–801.
54. Clair SVL, Nguyen K, Chen Z. Sum frequency generation studies on bioadhesion: elucidating the molecular structure of proteins at interfaces. J Adhes. 2009;85(8):484–511.
55. Ye S, Nguyen KT, Le CS, et al. In situ molecular level studies on membrane related peptides and proteins in real time using sum frequency generation vibrational spectroscopy. J Struct Biol. 2009;168(1):61–77.
56. Nguyen KT, Clair SVL, Ye S, et al. Orientation determination of protein helical secondary structure using linear and nonlinear vibrational spectroscopy. J Phys Chem B. 2009;113 (36):12169–80.

57. Avery W, Som A, Xu Y, et al. Dependence of antimicrobial selectivity and potency on oligomer structure investigated using substrate supported lipid bilayers and sum frequency generation vibrational spectroscopy. Anal Chem. 2009;81(20):8365–72.
58. Zoltán P, Wang J, Clarke ML, et al. Sum frequency generation vibrational spectroscopy studies of protein adsorption on oxide-covered Ti surfaces. J Phys Chem B. 2004;108(23):7779–87.
59. Wang J, Clarke ML, Chen X, et al. Molecular studies on protein conformations at polymer/liquid interfaces using sum frequency generation vibrational spectroscopy. Surf Sci. 2005;587(1):1–11.
60. Yang P, Ramamoorthy A, Chen Z. Membrane orientation of MSI-78 measured by sum frequency generation vibrational spectroscopy. Langmuir. 2011;27(12):7760–7.
61. Ye S, Nguyen KT, Chen Z. Interactions of alamethicin with model cell membranes investigated using sum frequency generation vibrational spectroscopy in real time in situ. J Phys Chem B. 2010;114:3334–40.
62. Nguyen KT, King JT, Chen Z. Orientation determination of interfacial beta-sheet structures in situ. J Phys Chem B. 2010;114(25):8291–300.
63. Boughton P, Yang P, Tesmer VM, et al. Heterotrimeric G protein beta1gamma2 subunits change orientation upon complex formation with G protein-coupled receptor kinase 2 (GRK2) on a model membrane. Proc Natl Acad Sci U S A. 2011;108(37):15019–20.
64. Roke S, Bonn M, Petukhov AV. Nonlinear optical scattering: the concept of effective susceptibility. Phys Rev B. 2004;70(11):2516–28.
65. Roke S, Roeterdink WG, Wijnhoven JEGJ, et al. Vibrational sum frequency scattering from a submicron suspension. Phys Rev Lett. 2003;91(25):258302.
66. Strader ML, Aguiar HBD, Beer AGFD, et al. Label-free spectroscopic detection of vesicles in water using vibrational sum frequency scattering. Soft Matter. 2011;7:4959–63.
67. Ostroverkhov V, Waychunas GA, Shen YR. New information on water interfacial structure revealed by phase-sensitive surface spectroscopy. Phys Rev Lett. 2005;94(4):046102.
68. Du Q, Freysz E, Shen YR. Sum-frequency vibrational spectroscopy of water interfaces. Am Inst Phys. 1993;290:157–61.
69. Ji N, Ostroverkhov V, Chen CY, et al. Phase-sensitive sum-frequency vibrational spectroscopy and its application to studies of interfacial alkyl chains. J Am Chem Soc. 2007;129(33):10056–7.
70. Tian C, Ji N, Waychunas GA, et al. Interfacial structures of acidic and basic aqueous solutions. J Am Chem Soc. 2008;130(39):13033–9.
71. Ji N, Ostroverkhov V, Tian CS, et al. Characterization of vibrational resonances of water-vapor interfaces by phase-sensitive sum-frequency spectroscopy. Phys Rev Lett. 2008;100(9):204–7.
72. Tian CS, Shen YR. Isotopic dilution study of the water/vapor interface by phase-sensitive sum-frequency vibrational spectroscopy. J Am Chem Soc. 2009;131(8):2790–1.
73. Hess C, Bonn M, Funk S, et al. Hot-band excitation of CO chemisorbed on Ru(001) studied with broadband-IR sum-frequency generation. Chem Phys Lett. 2000;325(1):139–45.
74. Bonn M, Ueba H, Wolf M. Theory of sum-frequency generation spectroscopy of adsorbed molecules using the density matrix method—broadband vibrational sum-frequency generation and applications. J Phys. 2005;17(8):S201.
75. Ghosh A, Smits M, Bredenbeck J, et al. Femtosecond time-resolved and two-dimensional vibrational sum frequency spectroscopic instrumentation to study structural dynamics at interfaces. Rev Sci Instrum. 2008;79(9):093907.
76. Bredenbeck J, Ghosh A, Smits M, et al. Ultrafast two dimensional-infrared spectroscopy of a molecular monolayer. J Am Chem Soc. 2008;130(7):2152–3.

Chapter 6
Chemiluminescence and Its Biomedical Applications

Chunsun Zhang, Yan Su, Yi Liang, Wei Lai, Jun Jiang, Hongyang Wu, Xinyuan Mao, Lin Zheng, and Ruoyuan Zhang

Abstract Chemiluminescence (CL) is an important detection method, and has been widely used in the field of biomedical analysis. The generalized CL comprises electrochemiluminescence (ECL) and light-initiated chemiluminescence (LiC). ECL contains two processes of electrochemical reaction and CL reaction, and can be applied to detection of nucleic acids, proteins, cells, and some small molecules. In recent years, a growing number of ECL luminescent substances have been reported, and many technologies have been developed for integrating with ECL. This indicates that ECL has great potential in biomedical applications. LiC is an immunoassay method that combines labeling and luminescence techniques. It has a simple principle and some distinct features and advantages compared with other immunoassay technologies. With the advance of the LiC, many related instruments and reagents have been developed, which promotes the application of LiC in biomedicine. CL is widely used in biological detection and can be used for in vitro diagnosis of many diseases, such as diabetes and thyroid disease. The development of biochips, especially microfluidic biochips, enrich the application of CL in in vitro detection. The chip development for enzyme substrate, nucleic acid, protein, cell, and others make it possible to complete large-scale biomedical detection rapidly and efficiently. For in vivo detection, CL can also be applied in many areas. With the development of advanced CL technologies, some researchers try to apply the in vivo CL technologies to cells, tissues, and individuals, and some satisfactory results have been achieved. In short, CL technologies have been recognized by more and more scholars, and their applications have a great significance in the development of biomedicine.

C. Zhang (✉) · Y. Su · Y. Liang · W. Lai · J. Jiang · H. Wu · X. Mao · L. Zheng · R. Zhang
MOE Key Laboratory of Laser Life Science, College of Biophotonics, South China Normal University, Guangzhou, China

Guangdong Provincial Key Laboratory of Laser Life Science, College of Biophotonics, South China Normal University, Guangzhou, China
e-mail: zhangcs@scnu.edu.cn

X. Zhao, M. Lu (eds.), *Nanophotonics in Biomedical Engineering*,
https://doi.org/10.1007/978-981-15-6137-5_6

Keywords Chemiluminescence · Electrochemiluminescence · Light-initiated chemiluminescence · Biochips · Biomedical applications

6.1 Introduction of Chemiluminescence

6.1.1 Concept

Chemiluminescence (CL) is an optical radiation phenomenon that occurs in the course of a chemical reaction. It is based on the principle that some molecules absorb the energy released by the reaction and then transfer to the excited state, when the excited state returns to the ground state, the energy is released in the form of light radiation. It can be seen that any CL reaction requires two critical steps with excitation and radiation, and three conditions are met. Firstly, the reaction must provide sufficient excitation energy. Secondly, the reaction requires that at least one substance absorbs energy from a chemical reaction and becomes to an excited state. Thirdly, the generated excited state molecules can radiate the photons and go back to the ground state, or make another molecule receive its energy to become the excited state and then radiate the photons.

In a chemical reaction, the excited state of a substance capable of emitting visible light has at least 168–294 kJ/mol of energy, and the normal redox reactions can provide such energy. Thus, most of the chemiluminescent reactions are redox reactions. CL analysis is also a process of the determination of redox energy transfer that is one of the important features different from other assays.

CL analysis has many advantages, such as high sensitivity, wide linear range, and simple detection instrument. In the CL reaction, the luminous intensity is related to the reaction rate, therefore all the factors that affect the reaction rate can be used as the basis for the establishment of the determination method. At present, CL analysis has been widely used in medicine [1], biology [2], food [3], environment [4] and other fields.

6.1.2 Classification of CL

6.1.2.1 General Classification

The generalized CL comprises electrochemiluminescence (ECL) and light-initiated chemiluminescence (LiC).

ECL is a kind of light radiation produced by chemical reaction between electrode reaction products or between electrode products and certain components in the system. It is a combination of CL and electrochemistry, which integrates the advantages of high sensitivity of CL and controllable potential of electrochemistry. Compared with CL, ECL can not only obtain luminous signal but also acquire the

corresponding electrochemical information. Consequently, ECL provides a very favorable research method for the study of reaction process, reaction rate, and diffusion coefficient on the electrode.

Light-initiated chemiluminescent assay (LiCA) is also one of the CL techniques, which is used for homogeneous immunodetection. This technique for detecting the substance relies on the chemical energy transition that the two particles are close to each other. In the reaction system, the concentrations of the two particles are not high, which leads to a low probability of random collision, and causes a small background of this reaction system. At present, various biomolecules can be detected with this technology.

6.1.2.2 Classification by Reaction Media

CL can be divided into gas phase and liquid phase categories according to its reaction medium. For example, the determination of reactive oxygen species [5], SO_2 [6] belongs to the gas phase CL system. Liquid phase CL is the reaction in solution. A large number of liquid phase CL reactions have been reported using different luminescent materials, such as luminol [7], quantum dots [8], oxalate peroxide [9], potassium permanganate [10], and ruthenium (II) pyridine complex [11], which are all important compounds in CL reaction.

Luminol is one of the popularly used liquid-phase chemiluminescent reagents. Luminol emits blue light in the chemiluminescent reaction with a maximum light emission wavelength of 425 nm when it is oxidized to an excited state substance in an alkaline aqueous solution. Within a certain concentration range, the luminous intensity is directly proportional to the concentration of luminol, H_2O_2, and catalyst. Many CL reactions can produce H_2O_2 by the reaction of oxidases with the appropriate substrate, and then the H_2O_2 is determined by the luminol CL method. Currently, most of the luminol systems with the actual application value are treated with H_2O_2 as the oxidant.

The CL system of oxalate peroxide is composed of aromatic oxalate, hydrogen peroxide, and fluorescent agent, which can be used for the determination of amines [12] and fluorescent substances [13]. In principle, the oxyoxalate system is different from others, because the system must use a fluorescent substance, and when the fluorescent substance changes, the color of the light can also change.

Potassium permanganate is an important oxidant, which can react with some alkaloids directly and can be used to detect inorganic substances such as Fe^{2+} [14] and organic substances like morphine [15]. Although many substances can be oxidized by the potassium permanganate, the luminous intensity is extremely weak, hence the analysis data are often difficult to obtain by a conventional photoelectric conversion device. From the application of the potassium permanganate reaction system, the principle and method of the recent research results are basically not much different from the earlier examples [16].

$Ru(bpy)_3^{2+}$ is a composition formed by the Ru^{2+} and the three 2,2′-pyridine, which has an octahedral space configuration and six coordination numbers of center ions [17]. $Ru(bpy)_3^{2+}$ has unique chemical stability, oxidation-reduction quality, and

strong fluorescence characteristics. The excited state of $Ru(bpy)_3^{2+}$ can emit orange light with a maximum wavelength of 620 nm. $Ru(bpy)_3^{2+}$ can be reduced by a plurality of organic substances or a reaction intermediate, where luminous intensity is linearly related to the concentration of organic compounds. $Ru(bpy)_3^{2+}$ can also be used as a marker for immunoassays [18] or a marker for DNA quantitative detection [19].

6.1.3 Application of CL in Biomedicine

Early CL was mainly used for the determination of metal elements. At the end of 1970s, Velan and Halmann [20] first established a CL enzyme immunoassay method. Nowadays, CL has become an important analytical approach in life science research, and been widely applicated in biomedical fields, including cytological analysis [21], molecular biological analysis [22], biosensor analysis [23], and luminous imaging analysis [24]. Cytological examination is mainly aimed at the detection of intracellular ATP and the determination of cell activity [25]. The applications in the field of molecular biology mainly include the detection of small molecules such as glucose, uric acid, and biological macromolecules such as genes and proteins. The biosensors based on CL mainly include enzyme sensors, nucleic acid sensors, protein sensors, cell sensors, and others. With the deepening of CL analysis, more and more superior luminous reagents will be developed, detection instruments will be constantly updated, and the application field will also be expanded.

6.2 Electrochemiluminescence (ECL)

6.2.1 Introduction

ECL is an analytical detection technology combining CL with electrochemistry [26, 27]. It retains the advantages of high sensitivity, wide linear range, and simple instrumentation [28], and has been developed into a highly sensitive analytical method [29, 30]. At the same time, there are many benefits unmatched against CL methods [31], such as good reproducibility, stable reagents, and being easy to control, which has attracted wide attention [32].

The ECL phenomenon was first discovered by Dufford et al. in 1927, and they found that the luminescence would be generated when the Green reagent was applied at a voltage of 500–1500 V in anhydrous diethyl ether solution [33]. Subsequently, Harvey found that when alkaline luminol solution was electrolyzed at 2.8 V voltage, luminescence occurred in both cathode and anode [34]. Thus, the scientists opened the way to explore ECL.

In the middle of 1960s, the rapid development of electronic technology and the emergence of highly sensitive photoelectric sensors provided the strong technical support for detailed research of ECL. Kuwana with his partners [35] were the first to

investigate the ECL behavior and luminescence mechanism of luminol on platinum electrodes. Subsequently, the ECL phenomenon of tripyridine ruthenium was one of the most important discoveries in the 1980s. After the 1990s, the ECL equipment, electrode materials and luminescent materials had been greatly developed. At the same time, ECL has being also developed towards miniaturization and point of care testing (POCT).

6.2.1.1 Conception of ECL

ECL refers to a luminescence phenomenon that occurs when a certain voltage or current is applied to a system containing luminescent substances. The luminescent substances undergo electrochemical and chemical reactions on the electrode surface, then become the excited state though electron transfer, finally returns to the ground state from the excited state [36]. The occurrence of the ECL phenomenon generally undergoes two processes of electrochemical reaction and chemiluminescence.

6.2.1.2 Types of ECL

According to the potential control method of the luminescence process and the types of substances involved in the luminescence reaction, ECL can be divided into the following two types: quenching ECL and co-reactant triggered ECL. The former is produced by a single illuminant, and the latter involves illuminants and a suitable co-reactant.

Luminescent materials are the source of ECL detection technology, and their response signals directly affect the sensitivity and accuracy of detection. Typical ECL luminescent materials are mainly luminol and its derivatives, trisruthenium and its derivatives, and quantum dot systems represented by semiconductor quantum dots [8].

Luminol ECL

Luminol is a synthetic organic compound, also known as luminescent ammonia. In 1929, Harvey discovered its luminescence phenomenon [34]. There have been many studies on the luminescence behavior of luminol, and the mechanism of oxidative luminescence and reduction luminescence have been proposed [37]. Luminol itself can be irreversibly oxidized by electrooxidation on the electrode, and the oxidized state and reduced state are not involved in the luminescent system. Luminol usually uses H_2O_2 as a co-reactant to enhance its luminous efficiency. Luminol-H_2O_2 system is widely used in the bioanalysis field because of its advantages such as high quantum yield and stable chemical properties [38, 39].

Tridipyridine ruthenium ECL

Hercules and Lytle discovered the ECL phenomenon of Tridipyridine ruthenium ($Ru(bpy)_3^{2+}$) in 1966 [40]. $Ru(bpy)_3^{2+}$ has high luminous efficiency, good water solubility, strong chemical stability, long-life time excited state, and other advantages. In addition, $Ru(bpy)_3^{2+}$ is reversible on the surface of the electrode and can be recycled, so it is the most widely used luminescent substance in the field of ECL.

6.2.2 New Technique of ECL

Since the new century, ECL testing has been continuously integrated with other technologies, and has made great progress in the research of new technologies and new methods. In terms of new technologies, solid-state ECL has become a hot topic of research and has obtained more and more attention. At the same time, it is also an eternal topic to explore more ECL systems, such as quantum dots, carbon and nitrogen compounds as well as others.

6.2.2.1 Solid-State ECL

At present, relevant researches on solid-state ECL have aroused great interest. Among them, $Ru(bpy)_3^{2+}$ has the advantages of good water solubility, stable chemical properties and recyclability [41], Therefore, $Ru(bpy)_3^{2+}$ can be fixed to the electrode surface for constructing a reagent-free ECL sensor. After years of exploration and development, people have tried a variety of methods to directly fix $Ru(bpy)_3^{2+}$ on the electrode surface, such as single layer membrane method [42], polymer membrane method [43], organic-inorganic hybrid composite membrane method [44] and others.

6.2.2.2 New Luminescent Materials of ECL

In recent years, with the in-depth study of people, more and more new types of luminescent materials have been greatly developed. In addition to the classic systems of $Ru(bpy)_3^{2+}$ and luminol, new luminescent materials such as quantum dots have become more and more popular. After continuous research and exploration, these new materials with good luminescent properties and physicochemical properties will have great application value in light-emitting diodes, display devices, and bioluminescent markings.

Quantum Dots-Based ECL

With the gradual development of people's cognitive field from the macro world to the micro world, nanoscale science and technology have developed rapidly. Understanding and transforming nature in the nanometer range reflect a new scientific exploration. Quantum dots are made up of a small number of atoms, all of which are below 100 nm in size and look like tiny dots. With the further penetration of nanotechnology and various disciplines, the application of quantum dots has developed into a cross-disciplinary field involving multiple disciplines [45, 46].

Ding et al. found that semiconductor nanocrystals would undergo redox reactions at a certain potential [47], which could produce corresponding ECL processes. This discovery combines ECL technology with nanotechnology to open up a new technology and method for the application of quantum dot ECL.

Carbohydrates and Nitrogenous Compounds-Based ECL

With the development of graphene and its oxides, two-dimensional nanomaterials have received special attention from researchers. As a two-dimensional sheet structure, a metal-free semiconductor material-graphite phase carbon nitride material (g-C_3N_4) [48] has been widely used in recent years, and it has relatively stable physical and chemical properties. The optical properties and good biocompatibility, as well as the characteristics of their own ECL, are favored by researchers. In addition, g-C_3N_4 has good dispersibility in water after acid treatment, and has a large number of carboxyl groups and amino groups on the surface, which makes it widely used in sensors.

6.2.3 Integration of ECL with Other Technologies

ECL technology has the advantages of high sensitivity, wide monitoring range, and simple equipment. The ECL technology can be combined with other technologies, which can not only improve its selectivity but also achieve simultaneous detection of multiple components.

Solution chemical analysis is the most basic and classical analytical method in analytical chemistry and has a long history. However, its operation is complicated, time-consuming, laborious, and the analysis results are affected by uncertainly subjective factors. After continuous research, a series of automatic analysis methods and equipment have been developed. The most commonly used methods are flow injection (FI) analysis and microfluidic technology. ECL combined with these technologies not only has high sensitivity and wide range of application, but also can analyze and detect quickly [49].

High-performance liquid chromatography (HPLC) is a fast and efficient method for analysis and separation, and it can be used in combination with ECL technology

to form a trace and ultra-trace analysis method. In recent years, the application of HPLC-ECL technology has become more and more widespread [50, 51].

Capillary electrophoresis (CE) has higher resolution than HPLC, and has the characteristics of simple operation, small sample size, fast analysis speed, and low cost. At the same time, CE-ECL technology has the advantages of high sensitivity, good detectability, low detection limit, wide linear range, and simplicity of instrument [52].

6.2.4 Application of ECL Detection

In recent years, with the advancement and development of ECL technology, the research and application range of ECL is more extensive, and it has penetrated into the detection and analysis of nucleic acids, proteins, cells, biological small molecules, drugs, ions, and so on. ECL technology has become a very active research hotspot, and the application fields are becoming more and more extensive.

6.2.4.1 Detection of Nucleic Acids

Nucleic acid is an important biological macromolecule and one of the most basic substances in life. It can be used as a genetic material, has the function of storing and transmitting information and controling protein synthesis, and plays an important role in living organisms. It is researched that many genetic diseases in humans are associated with variations in base sequences in nucleic acid molecules. Therefore, the detection of disease-related mutations has far-reaching implications for gene screening, early diagnosis, and treatment of genetic diseases [53].

Conventional nucleic acid hybridization uses a radiolabeling detection method, but the development of the method is affected by the inherent disadvantages of the radioisotope itself and the limitations of the instrument used. It has received widespread attention to use the ECL technology for nucleic acid detection. ECL nucleic acid detection can be mainly classified into a label type [54], an embedded type [55], and a solid-state ECL method [56] depending on the mode of action between the luminescent substance and the nucleic acid. The label type mainly forms a signal probe for generating ECL by bonding a luminescent substance and a single-stranded nucleic acid molecule. The embedded type is that the luminescent substance is embedded in the groove region of the double-stranded structure of the double-stranded nucleic acid molecule. The solid-state ECL method fixes the luminescent substance on the surface of the electrode and does not directly interact with the nucleic acid. For example, Zhang's group reported a cloth-based ECL gene sensor (shown in Fig. 6.1) that uses an embedded proximity hybridization method to detect K-ras gene fragments [55].

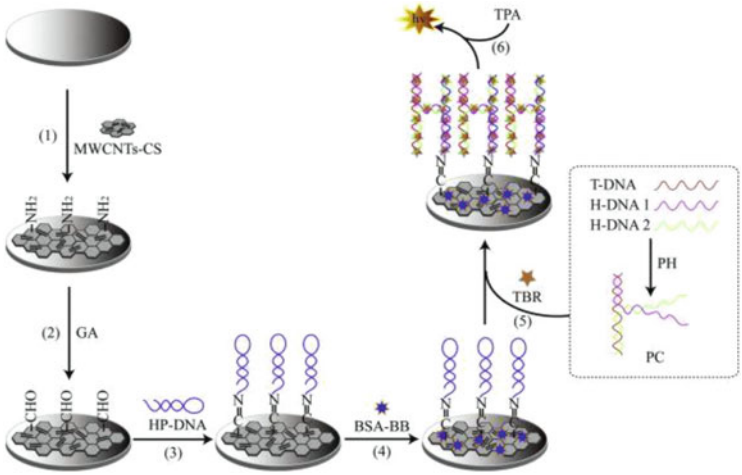

Fig. 6.1 Schematic illustration of the preparation of DNA biosensor and PH-ECL strategy for K-ras gene detection [55] (CS—chitosan, MWCNTs—multiwalled carbon nanotubes, GA—glutaraldehyde, T-DNA—target DNA, HP-DNA—amino-modified capture hairpin DNA, BSA-BB—bovine serum albumin blocking buffer, H-DNA1—help DNA 1, H-DNA2—help DNA 2, TBR—$Ru(bpy)_3^{2+}$, TPA—tripropylamine, PH—proximity hybridization, PC—proximity complexes)

6.2.4.2 Detection of Proteins

Protein is the bearer of life activities. Especially in the occurrence and development of some major diseases, there are often some related proteins. Therefore, early detection and diagnosis are particularly important [57]. At present, the use of ECL technology combined with immunoassay technology to detect protein has become a very popular research content.

ECL immunoassay combines the characteristics of ECL technology and immunoassay technology, using luminescent substances to label antigens or antibodies, and the detection of the substance is achieved by the specific binding of the antigen–antibody and the change of the ECL signal before and after the reaction. Gao et al. [58] developed an ECL solid-state sensor (shown in Fig. 6.2). This work adopted $Ru(bpy)_3^{2+}$/AuNPs/Nafion modified glassy carbon electrode, and ferrocene was used as an ECL quencher to achieve the detection of the AFP protein.

6.2.4.3 Detection of Cells

Cells are the basic units that constitute an organism. Therefore, it is of great significance to study ECL cell sensors to better explore some important phenomena of life activities. Wu et al. reported a paper-based ECL cell sensor that used porous

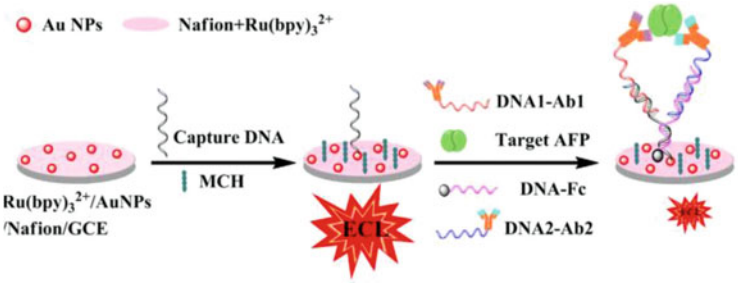

Fig. 6.2 Schematic diagram of the fabrication and the bioassay processes for the determination of AFP [58]

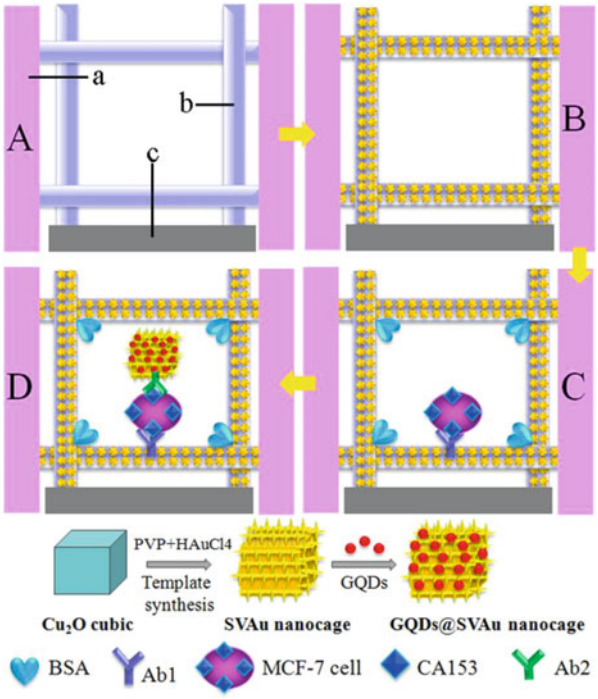

Fig. 6.3 Schematic representation of the fabrication procedures for this cell sensor [8]. Bare PCE: (**a**) wax-penetrated paper, (**b**) cellulose fibers in the paper cell zone (unprinted macroporous paper), (**c**) screen-printed carbon working electrode (**A**); Growth of Au nanoflowers layer on cellulose fiber surfaces (**B**); Immobilization of Ab1, blocking with BSA, and capture of MCF-7 cell (**C**); Immobilization of Ab2/GQDs@SVAu bioconjugates (**D**)

silver-palladium alloys as nanoprobes for the detection of multiple cancer cells [59]. Liu et al. developed a similar microfluidic paper chip cell device (shown in Fig. 6.3) that achieved the detection of the in situ MCF-7 cells by labeling antibodies with nanoluminescent materials and specifically binding to the cell surface antigen CA153 using a double sandwich method [8].

6.2.4.4 Detection of Biological Small Molecules

Biological small molecule active substances are an important part of living organisms and can be detected by using trace ECL analysis technology, such as the detection of hydrogen sulfide and hypochlorous acid. Hypochlorous acid is one of the important active oxygen species in the body and can resist the invasion of external bacteria and pathogens. However, it can cause tissue damage and a series of diseases if its concentration is too high in the body. Therefore, it is important to carry out the detection of hypochlorous acid in biological samples [60]. Hydrogen sulfide can participate in a variety of physiological and biochemical processes in the body and perform specific functions. In animals, hydrogen sulfide regulates blood vessel and nervous system functions. Yue et al. used a novel ruthenium compound as a recognition unit to establish an ECL sensor (shown in Fig. 6.4) that selectively detected extracellular H_2S content in mouse brain [61].

6.2.4.5 Detection of Drugs

In recent years, ECL has been widely used to detect different kinds of substances due to its low background signal, high sensitivity, and controllable reaction. In biomedical applications, quantitative detection of pharmaceutical ingredients is of great importance. For example, matrine is a quinolicilin alkaloid extracted from Brassica plants and can be used to treat cancer and inflammation [62, 63]. Miao et al. reported a method for the quantitative detection of matrine based on a solid-state ECL sensor modifying by $Ru(bpy)_3^{2+}/mSiO_2$/Nafion on a glassy carbon electrode (Fig. 6.5). And, the developed ECL sensor exhibits high sensitivity, low detection limit, and good luminescence stability [64].

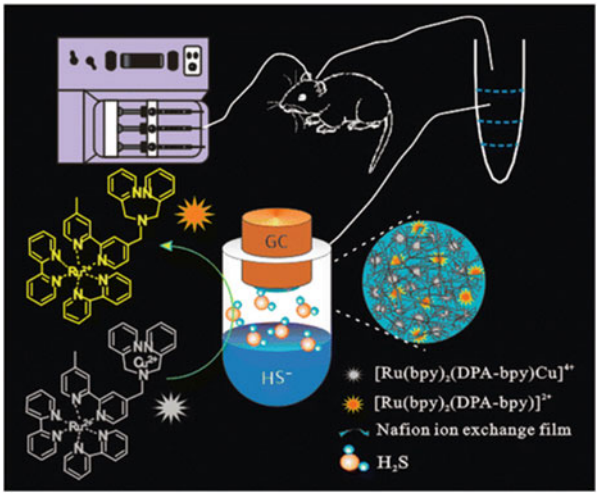

Fig. 6.4 Turn-on electrochemiluminescent sensor with a ruthenium (II) complex for sensing extracellular H_2S in rat brain, coupled with in vivo microdialysis

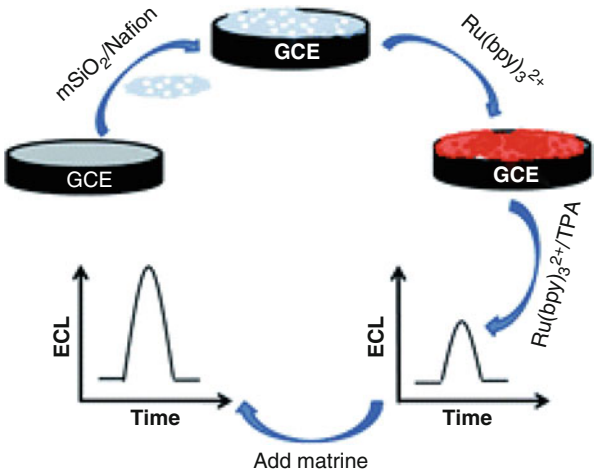

Fig. 6.5 ECL sensor based on $Ru(bpy)_3^{2+}/mSiO_2$/Nafion modified electrodes for the detection of matrine

6.2.4.6 Ion Detection

Along with the rapid development of the economy and society, the ecosystem on which human beings depend has tremendous pressure. Food and environmental pollution problems have become more and more prominent. Among them, metal pollution is particularly obvious. Metal ions can enter the human body through various food chains, which is extremely harmful to human health. For example, mercury is a highly toxic heavy metal, and mercury contamination can have a major impact on human health and the environment, even at low levels. Therefore, it is a very meaningful work to carry out highly sensitive detection of mercury ions. Zhai et al. developed a new method for ECL detection of mercury ions using Au-Ag bimetallic nanoclusters (shown in Fig. 6.6). This study shows that ECL signals are reduced when mercury ions are present [65].

6.3 Light-Initiated Chemiluminescence (LiC)

6.3.1 Preface

6.3.1.1 Background

LiC is a new generation of CL technology based on traditional CL and ECL. This technology was first reported by Ullman et al. in 1994 [66], and then successfully developed by DADE BEHRING INC of the United States. After continuous development, PerkinElmer produced related reagents (Alpha LISA), and later Siemens introduced immunodiagnostic reagent LOCI (luminescent oxygen channeling

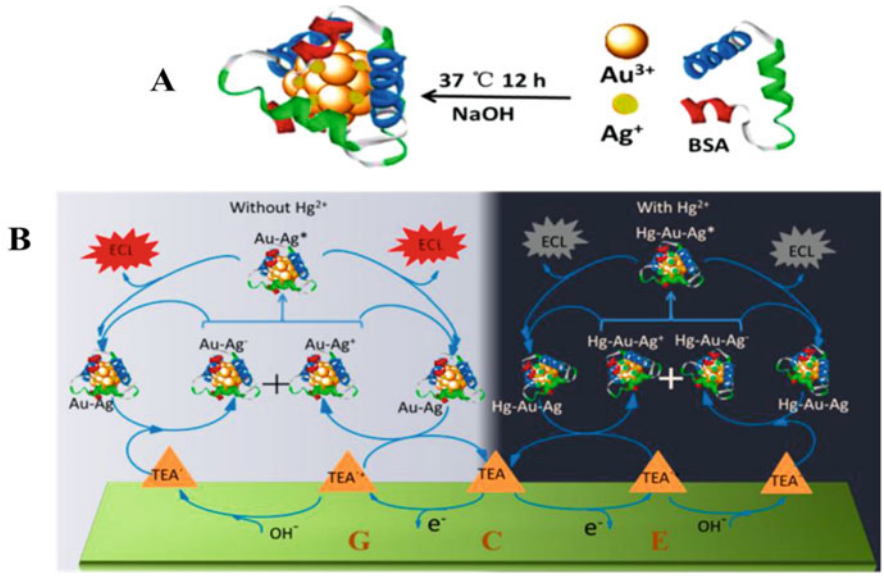

Fig. 6.6 (**a**) Preparation process of Au–Ag bimetallic NCs; (**b**) ECL mechanisms of Au–Ag bimetallic NCs and the proposed ECL sensor for Hg^{2+} detection

immunoassay). In recent years, China has gradually introduced related reagents and instruments [67].

LiCA is a novel homogeneous immunoassay technology that uses novel labeling techniques and luminescence techniques. Compared with traditional radioimmunoassay, ECL immunoassay and heterogeneous immunoassay, LiCA has the advantages of simple operation, high sensitivity, low cost, homogeneous no-wash, and so on. It can be widely applied to the study of biomolecular interactions.

6.3.1.2 Principle

Core Principle

The core principle of LiCA technology is the generation and transmission of high-energy oxygen, which is a process of light energy conversion from light energy to chemical energy. After being excited by red light (680 nm), the photosensitive donor bead can convert oxygen in the surrounding environment into high-energy oxygen, and the survival time of high-energy oxygen is only 4 μs. The short survival time determines that the propagation diameter of high-energy oxygen is small (about 200 nm). Therefore, when the luminescent acceptor beads are within the range of 200 nm, the chemical energy can be received and the high-energy light (610 nm) is emitted. Conversely, if no acceptor beads are present in the 200 nm diameter range,

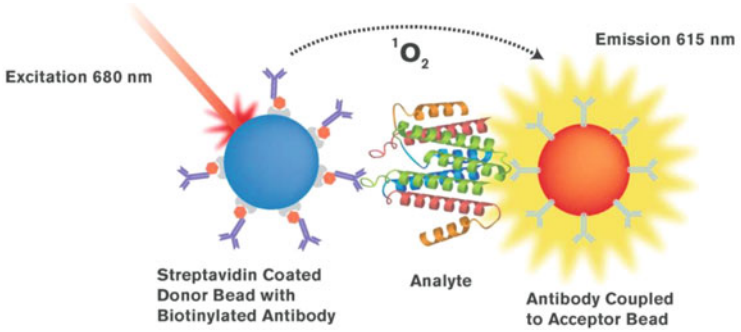

Fig. 6.7 Principle of light-initiated chemiluminescence reaction [68]

the high energy level will fall back to the ground-state oxygen without signal generation. This chemical energy transmission, which relies on the close proximity of the two particles, is the basis for the homogeneous reaction of LiCA (As shown in Fig. 6.7).

Other Principles

The double antibody sandwich method is a commonly used binding method in the LiCA technology. Firstly, the known antibodies are fixed on the donor beads, and then the tested antigen is added. Then, the luminescent particles that are specific to the tested antigen are added to form the structure of antibody–antigen–antibody sandwich. This structure can bring the distance between the two beads to within 200 nm, and finally generate a signal.

The competitive binding method detects small molecules such as haptens that cannot simultaneously bind two antibodies. Taking the testosterone quantitative analysis as an example, based on the LiCA platform, the testosterone-coated donor beads and biotin-labeled testosterone antibodies are selected. The testosterone and the surface testosterone molecules on the donor beads compete for a limited testosterone antibody (balanced competition mode) to form a complex, respectively. When a universal solution is added, the streptavidin binds to the biotin, but only two kinds of microspheres are close to each other to be laser-induced to generate an optical signal. As with other chemiluminescent competition methods, the competitive-LiCA method also obtains an inverse proportional function. The principle of competitive immune analysis is shown in Fig. 6.8.

6.3.1.3 System Composition

LiC technique is composed of donor bead, acceptor bead and intermediate carriers, each of which has its function. The donor beads contain a photosensitive compound

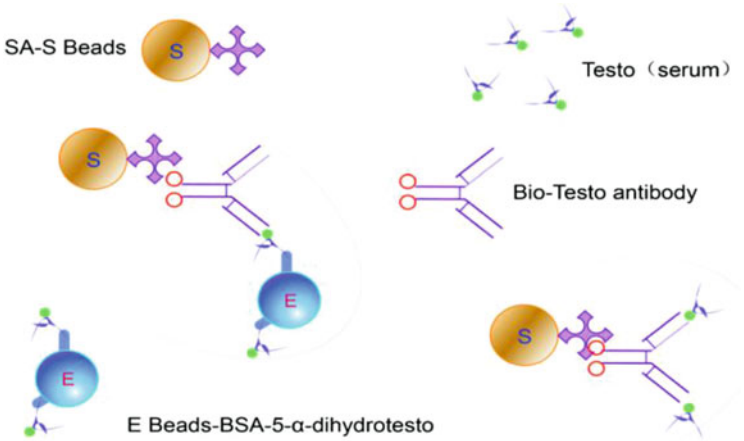

Fig. 6.8 Schematic diagram of competitive immune analysis [69]

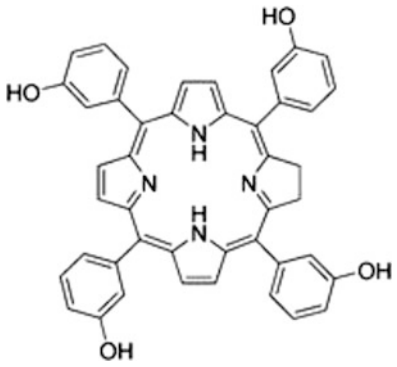

Fig. 6.9 Phthalocyanine molecular structure [70]

that can be excited by a 680 nm laser. The singlet oxygen generated by the donor bead transmits chemical energy to the acceptor bead, and the acceptor bead receives chemical energy to finally produce a CL signal of about 610 nm. Generally, and glucan treatment of microparticles is used to prevent nonspecific aggregation.

Donor Bead

The donor beads are approximately 200 nm in diameter, which are typically made of polystyrene. The photosensitive compound is generally a phthalocyanine substance, and the parent ring of the phthalocyanine substance is a benzene ring formed on the four pyrrole rings of the porphyrin, and the bridged methylene group is replaced with

an imine group (Fig. 6.9). Due to the existence of this conjugated system, the absorption band is expanded to 675–700 nm and has a good quantum yield. The complex of phthalocyanine and silicon has a long-lived triplet state, which can effectively sensitize the generation of singlet oxygen, and is a very nice photosensitive compound material. It is worth noting that the introduction of silicon ions can not only significantly increase the stability of phthalocyanine due to the large conjugated system but also improve the water solubility of phthalocyanines and reduce their association in water, and ultimately result in the increase in the efficiency of singlet oxygen production [71].

Acceptor Bead

The acceptor bead has a diameter of about 200 nm like the donor bead and is made of polystyrene. The luminescent compound is prepared by incorporating a thiophene derivative and a Europium (Eu) complex into the polystyrene microspheres (as shown in Fig. 6.10). In the luminescent microspheres, the dimethyl phthalate derivative and Eu are distributed. The former functions to receive the energy of the singlet oxygen and induce the continuous chemical reaction to generate the ultraviolet light (370–390 nm). And the latter is a fluorescent substance and is excited by ultraviolet light, and then the energy level transitions to the excited state, finally, the energy is released in the form of fluorescence (612 nm) in the process of returning to the ground state (as shown in Fig. 6.11).

Singlet Oxygen

Singlet oxygen ($^1O_2$) is the lowest excited state of molecular dioxygen and is well known as reactive oxygen species (ROS), which plays an important role in many reactions in the chemical, biological, and medical fields. In the field of chemistry, singlet oxygen is usually produced by photosensitivity (as shown in Fig. 6.12). The photosensitizer first absorbs the energy of the photon from the ground state (S_0) to the first excited state (S_1). In addition to the radiant/nonradiative transition back to the ground state, S_1 can also be converted to the triplet excited state (T1) by intersystem crossing (ISC), thereby activating the ground-state triplet oxygen

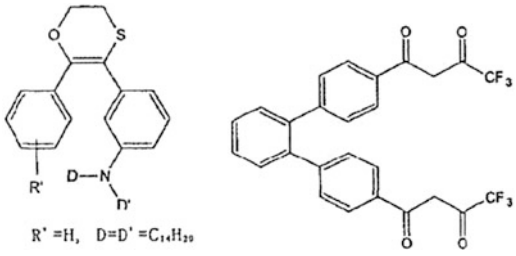

Fig. 6.10 Complex of dimethylthiophene derivative (left) and hydrazine (right) [72]

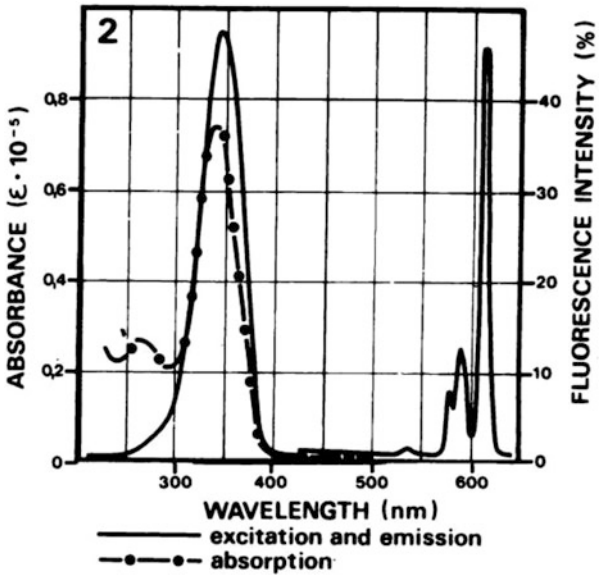

Fig. 6.11 Fluorescence excitation and fluorescence emission spectra of ruthenium [73]

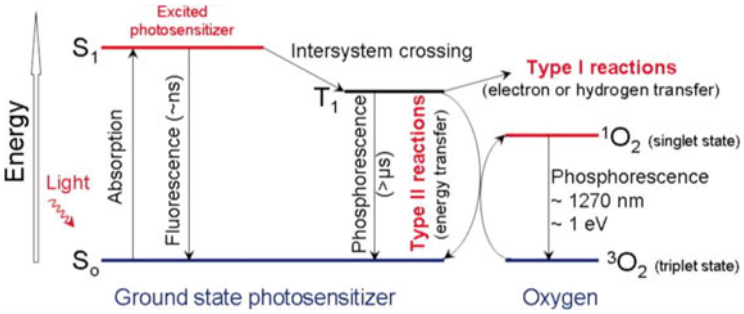

Fig. 6.12 Excited state of photosensitizer and generation of singlet oxygen [74]

molecule ($^3O_2$) to singlet state oxygen ($^1O_2$) by energy transfer. The singlet oxygen half-life is very short, only about 4 μs, so it can only be passed to a nearby location of about 200 nm. Therefore, it is also determined that the diameter of the photosensitive particles and the luminescent particles is about 200 nm [75].

6.3.1.4 Features and Advantages

LiC technology has high sensitivity. This technology uses nano-scale particles to increase the surface area of the reaction, and also completes the step-by-step

amplification of the optical signal. On the one hand, after the donor beads are excited by the excitation light, about 60,000 singlet oxygen is generated per second, and the first amplification of the signal is completed [76]. On the other hand, the singlet oxygen reacts with the thiophene derivative on the surface of the acceptor bead to generate ultraviolet light, which excites the lanthanide element, and then releases the light energy from the lanthanide element to complete the secondary and tertiary amplification. Consequently, sensitivity is greatly improved compared to conventional enzyme-linked immunosorbent assay (ELISA) [77].

LiC has a low background. Since LiC depends on the proximity of two kinds of particles, usually in the reaction system, the concentration of the particles is very low and the probability of collision between two particles is very low, resulting in the very weak background of the reaction system is very weak. This method reduces the background and improves the signal-to-noise ratio when combined with proper fluorescence wavelength and time-resolved counting mode. It is an ideal choice for complex sample detection. Moreover, it is difficult for general biological samples to produce the fluorescence at 680 nm. This technique uses 680 nm red light to reduce interference. The naturally occurring fluorescence time is typically less than 100 ns, and the technique uses a delayed 150 ms count mode to reduce interference.

Compared with traditional heterogeneous immunoassay, LiC technology has the characteristics of homogeneity and no-wash, avoiding washing error and cross-contamination, and improving the precision and accuracy of detection. The homogeneous environment facilitates the full contact of the particles and the full occurrence of the reaction. The glycosylation treatment on the surface of the microspheres avoids the aggregation of the particles to ensure the progress of the experiment.

LiC detection has the advantages of being fast, high-throughput, and sample-saving. Since the technology uses nanoparticles as a carrier, the reaction surface area is several tens of times higher than that of micropores, so the reaction time can be controlled from 10 min to half an hour. The fast and high-throughput testing can be done with common 96-well plates. Depending on the experiment, the amount of sample can be reduced to 10 μL, 5 μL, or even 2 μL [78].

LiC is extremely stable. The amplification process of the energy transfer signal is completed by organic molecules and dissolved oxygen. The small organic molecules are very stable by the protection of the particles. The dissolved oxygen concentration in the solution is a constant. Based on above advantages, the reaction process is a very stable reaction process, and not susceptible to the environments such as pH, temperature, and ionic strength [79].

LiC detection has the characteristics of target diversity. Because the technology relies on the interaction of two substances, generally speaking, the biomaterials that can be combined can be detected by this method, including some common DNA, RNA, and enzymes.

6.3.2 *Application and Current Status of Light-Initiated Chemiluminescence Technology*

LiC technology is widely used, covering receptors and ligands, proteins and proteins, and interactions between proteins and nucleic acids. Research results are of great significance for disease detection and drug development research.

6.3.2.1 Ligand–Receptor Interaction

Tumor necrosis factor (TNF-α) is a cytokine with multiple biological activities. On the one hand, it participates in the body's immune defense, resisting various pathogenic factors. On the other hand, it is involved in the induction of apoptosis. Abnormal secretion of TNF-α may lead to inflammation, tissue necrosis, and other consequences. The tumor necrosis factor receptor recognizes and specifically binds to the tumor necrosis factor ligand. We can combine the biotinylated antibody, the test sample, and the antibody-coated acceptor bead that are mixed and incubated, then add the streptavidin-coated donor bead to form the complex, and the amount of luminescence is related to the concentration of the complex. This result is tested to be consistent with traditional ELISA results [80].

6.3.2.2 Protein–Protein Interaction

In-depth study of protein interactions and construction of protein interaction networks are the basis for understanding biological activities under physiological or pathological conditions. Taking p53 as an example, it is the most relevant gene in human tumors, and p53 protein has a complete network of interactions. The rapid detection of p53-his fusion protein in cell lysates based on LiC has been successfully performed, which successfully detects the interaction of p53 with MDM2 and MDM4 (Fig. 6.13).

6.3.2.3 Protein–Nucleic Acid Interaction

Human tyrosine-DNA phosphodiesterase I (Tdp1) is an enzyme involved in the repair of DNA damage by human topoisomerase I (Top1). Tdp1 is ubiquitous in eukaryotes and has important physiological significance, because its homozygous mutation H493R in the catalyzed vesicle can cause spinal cord cerebellar ataxia with axonal neuropathy. Therefore, it is reasonable to develop a Tdp1 inhibitor in combination with camptothecin and deaminoisoquinoline for the treatment of cancer. Marchand et al. [82] reported the identification and preliminary characteristics of four Tdp1 inhibitors. The principle of the reaction is Tdp1 catalytic hydrolysis. The

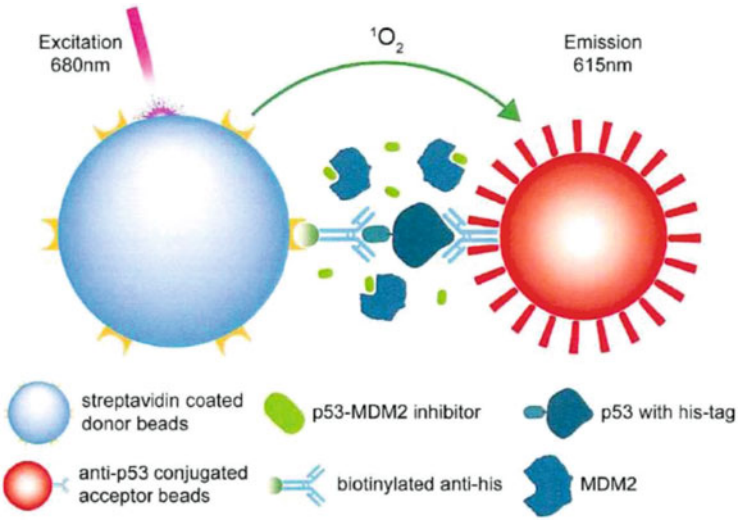

Fig. 6.13 Schematic diagram of photoluminescence screening for p53-MDM2 inhibitors [81]

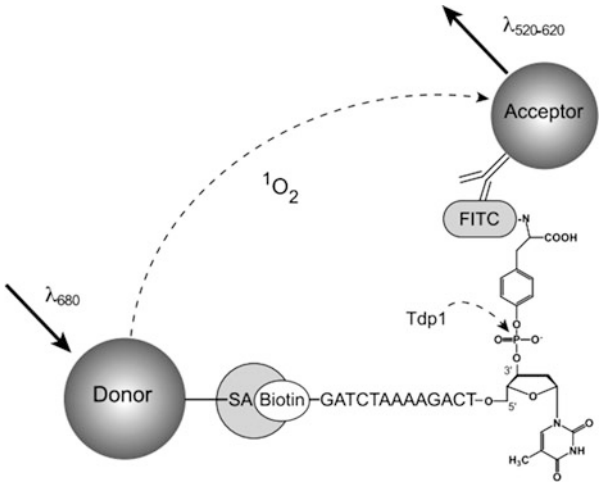

Fig. 6.14 Tdp1 catalytic hydrolysis, acceptor beads trigger blue-emitting emission [82]

red light shift excitation of the donor beads produces singlet oxygen, which triggers the blue shift light emission when the singlet oxygen encounters the recipient beads in its moving range (Fig. 6.14).

6.3.2.4 Other

Protein Kinase

Protein kinases are directly involved in many human diseases, because protein phosphorylation is an important link in many signal transduction pathways, and protein kinases are important substances that mediate these pathways. Guenat et al. used this technique to characterize the mechanism of peptide inhibitors by measuring the binding affinity of JNK inhibitors. This cell-based JNK kinase assay can be applied to other kinases [83] (Fig. 6.15).

Single Nucleotide Polymorphism

Single nucleotide polymorphisms (SNPs) are the cause of most genetic variations in humans. Due to their high density, SNPs are considered to be valuable tools for mapping genetic maps involving complex human diseases, drug reactions, and drug metabolism. The exploration of SNPs around the world is being carried out simultaneously with the development of SNP genotyping platforms. This technology has been successfully applied to high-throughput genotyping [84] (Fig. 6.16).

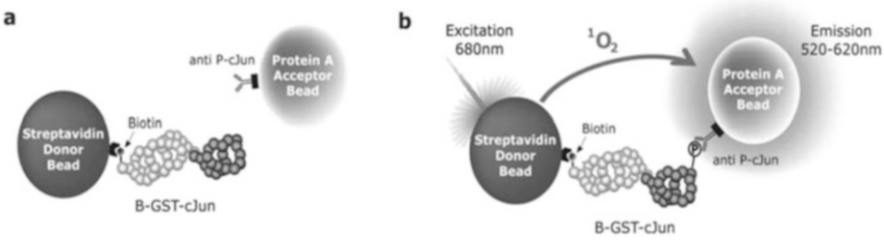

Fig. 6.15 Principles of AlphaScreen Kinase Assay [83]

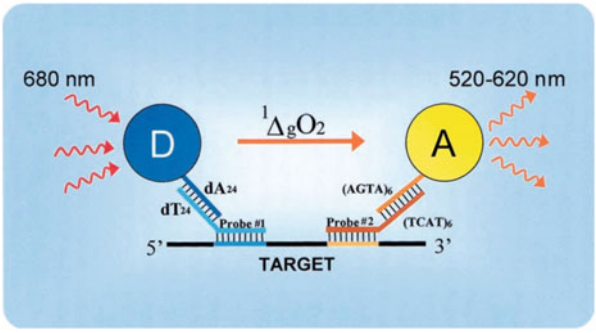

Fig. 6.16 Schematic diagram of AlphaScreen detection of nucleic acids [84]

6.3.3 Light-Initiated Chemiluminescence Instruments and Reagents

Clinical testing of immunology has gone through three phases: from radioimmunoassay to enzyme-linked immunoassay and then to CL immunoassays. The markers have undergone changes from radioisotopes to various enzyme makers and then to various CL substances.

CL is currently the mainstream of clinical immunoassays. Traditional CL detection reagents, mostly in heterogeneous systems, are excited by chemical reactions, and the reaction process requires repeated cleaning and separation. The reaction takes a long time and the automation design is complicated. Therefore, it is urgent to develop an automatic product with high accuracy, high sensitivity, easy operation and easy-to-use in clinical use. LiC assay emerges as the times require. LiC technology is the most advanced CL detection technology by introducing the laser technology and nano-microsphere technology to raise CL to a new level. The reaction system is carried out in a homogeneous reaction, which not only speeds up the reaction, but also avoids repeated separation and washing steps. Furthermore, the reaction system can effectively reduce the detection background, reduce the reaction time, and achieve more efficient automation.

At present, PerkinElmer has produced a variety of related reagents (Alpha Screen^{TM}) and has undergone several innovations in technology. This technique is an example of proximity assay based on nanobeads and is developed from a diagnostic assay technique called LOCI (Luminescent Oxygen Channeling Assay). Alpha LISA technology extends the basic Alpha Screen technology, which modifies the chemical structure of the acceptor beads to make the emitted light stronger and clearer, thus significantly reducing the interference from biological fluid matrices. Moreover, it provides an alternative technology for traditional ELISA assay (Fig. 6.17), and is suitable for high-throughput automated dosing and detection systems.

The technique also shows good results in applications such as the screening of Sendai virus [85] and the detection of aflatoxin [86].

At the same time, the LiCA photochemical CL detector and related reagents of Boyang Biotechnology (Shanghai) Co., Ltd. have also made rapid progress. The company has developed hepatitis B detection kit, thyroid function test kit, tumor detection kits, and so on. A series of LiCA products have begun clinical evaluation and promotion in Guangzhou, Shanghai, Yangzhou, and other places. LiCA is a homogeneous immunoassay that avoids the cumbersome separation and washing steps in ELISA, radioimmunoassay (RIA) and other detection methods, and increases the sensitivity of detection due to the increase in the surface area of the particles.

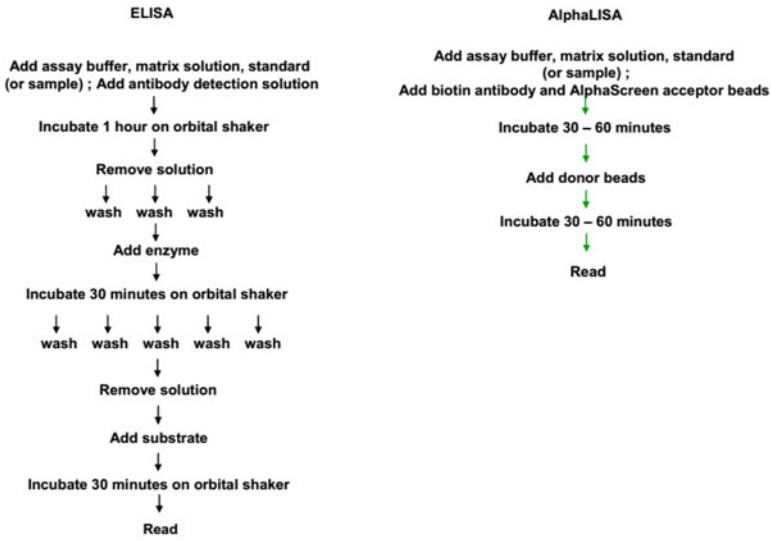

	ELISA	AlphaLISA
Selectivity	High	High
Sensitivity	Sensitive (pM range)	Sensitive (sub-pM)
Assay Format	Heterogeneous	Homogenous
Antibody req.	Requires matched antibody pairs	Used with antibody pairs
Assay vol.	large (25-50 µl)	small (≥ 5 µl)
Dynamic range	limited (~2 orders of mag.)	large (~4 orders of mag.)
Instrumentation	any luminescent reader	requires high energy laser

Fig. 6.17 Comparison of ELISA and AlphaLISA methods [68]

The instrument and related reagents also have excellent performance in applications [87] such as detection of chloramphenicol in eggs and milk [88] and detection of serum prolactin [89].

6.3.4 Expectation

LiCA achieves homogeneous and no-clean detection with its unique detection principle. It has the advantages of high sensitivity, good uniformity, and wide detection range. This technology effectively avoids the fluorescence interference of samples and has the characteristics of simple and convenient operation, low sample demand, easy detection, and easy optimization of the detection system. Although LiCA is a promising test method, like many technologies, there are many problems with this technology, such as the cost of reagent instruments is high, research and application are not deep enough, and the types of kits that can be

used for clinical tests are still very few [90]. The research and development of biomarkers for various diseases requires a sensitive, high-throughput, easy-to-use, and simple detection platform, which can help medical workers or researchers to detect the occurrence of diagnostic interventions in the early stages of the disease. With the continuous improvement of the manufacturing process in the future, the products based on this technology can be gradually miniaturized, and the requirements for the use environment are gradually reduced, so that the application range of the technology is continuously expanded.

6.4 Application of CL in Biological Detection and In Vitro Diagnosis

6.4.1 Introduction

CL analysis is a trace analysis method developed in the past 30 years, which has significant advantages such as high sensitivity, convenient operation, rapid analysis, needlessness of external light source, and easy automation [91–93]. In recent years, while improving and perfecting the original luminescent reagents and system, the synthesis of new luminescent reagent, the development of new systems and the co-application of other technologies have further broadened the application range of CL. Now it has been widely used in biological detection, such as detection of nucleic acid, protein, small biological molecules, drugs, and ions, as well as in vitro diagnostics, such of diagnostics of diabetes, thyroid disease, and tumor markers.

6.4.2 Application of CL in Biological Detection

6.4.2.1 Detection of Nucleic Acids

Nucleic acid hybridization is one of the most widely applied techniques in biochemistry and molecular biology. It is an effective method for qualitative and quantitative detection of specific DNA or RNA sequences. For its simple operation, no marks, no radioactive pollution, etc., CL is greatly concerned [94]. It has been widely used in nucleic acid detection. And it generally uses CL markers such as acridine ester, horseradish peroxidase (HRP), and analog enzyme for detection [95, 96].

HRP is a common CL marker, which can catalyze luminol–H_2O_2 system to generate strong CL signals. This enzyme catalyzed CL reaction has high detection sensitivity, stable signal, and long signal duration. Zhang's group [97] introduced a new type of paper-based microfluidic DNA sensor, which used a typical sandwich structure consisting of covalent bond fixed capture probe-DNA amplification product-biotin labeled signal probe and HRP-streptavidin (SA) complex to catalyze CL reaction to detect DNA amplification products (Fig. 6.18).

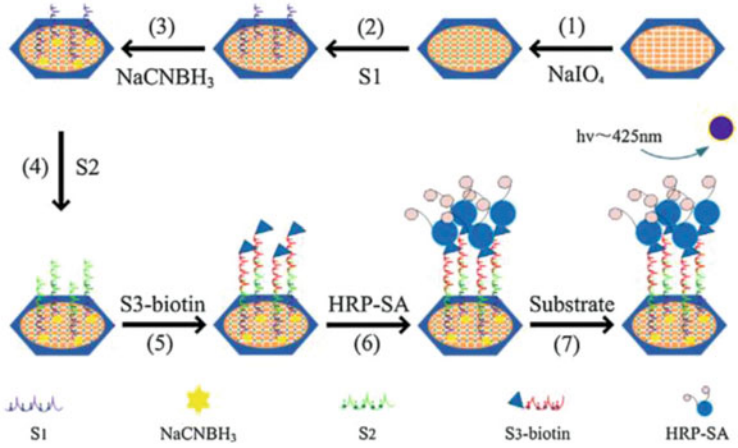

Fig. 6.18 A new type of paper-based microfluidic DNA sensor [97]

6.4.2.2 Detection of Proteins

Determination of protein is of great significance in scientific research and clinical practice. CL determination of protein samples has been realized by using heme, natural enzymes or metalloporphyrin compounds to catalyze CL. Li et al. [98, 99] used CL based on manganese porphyrin compounds to quantitatively detect vascular endothelial growth factor (VEGF). However, single CL analysis has some limitations in anti-interference performance, specificity and sensitivity of detection, and multiple analysis of complex samples. CL analysis combined with other technologies can improve the function and expand the application range significantly.

Zhang et al. [100] combined CL with ELISA in China initially, and this method was applied to the determination of hepatitis B surface antigen and antibody, alpha-fetoprotein, and ferritin successfully. Jiang et al. [101] used gold nanoparticles to improve the CL intensity of luminol-H_2O_2 (Fig. 6.19), and detected carcinoembryonic antigen in human serum by using CL-capillary electrophoresis (CE).

6.4.2.3 Detection of Small Biological Molecules

Small biological molecules are those with a relative molecular mass less than 500, including water, monosaccharides, amino acids, vitamins, lipids, and nucleotides. Among them, glucose, uric acid, and glutathione will generate H_2O_2 by the corresponding enzymes, and luminol will generate CL with the H_2O_2 and $K_3Fe(CN)_6$, and then the concentration of them can be obtained.

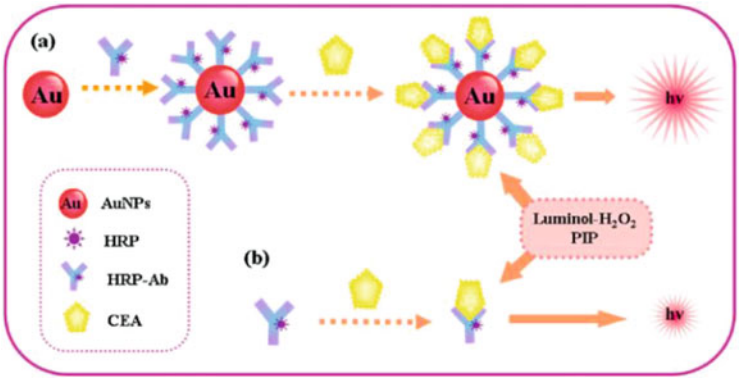

Fig. 6.19 (**a**, **b**) Sensitization of gold nanoparticles to luminol-H_2O_2 chemiluminescence [101]

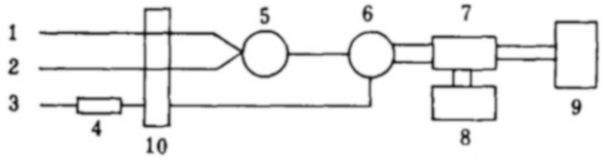

Fig. 6.20 Schematic of flow injection system [102]. (1) luminol; (2) $K_3Fe(CN)_6$; (3) fluid under test; (4) immobilized enzyme column; (5) mixing tube; (6) six-way valve; (7) photomultiplier; (8) negative high voltage; (9) recorder; (10) peristaltic pump

Yuan et al. [102] proposed a glucose sensor based on sol-gel to fix glucose oxidase. This sensor was used in the flow injection system with CL analysis (Fig. 6.20) to achieve the rapid detection of glucose.

In addition, CL can be used in conjunction with other reaction principles such as resonance energy transfer (RET). Freeman et al. [22] applied CL resonance energy transfer (CRET) based on DNA enzyme catalysis to detect ATP. They designed two DNA sequences containing anti-ATP aptamer and DNA enzyme sequences, when ATP is present, these DNA sequences can form into stable G-quadruplet structures that catalyze the production of CL signals. In addition, the combination of CdSe/ZnS quantum dots and CRET can reduce background interference significantly [103–105].

6.4.2.4 Detection of Drugs

Drug testing is a discipline that studies chemical testing, drug stability, bioavailability and clinical testing of drugs. Its purpose is to ensure the quality and safety of drugs. Commonly used methods for the determination of drugs include volumetric titration, fluorescence, atomic absorption, gas chromatography, high-performance liquid chromatography, thin-layer scanning, infrared spectroscopy, and mass

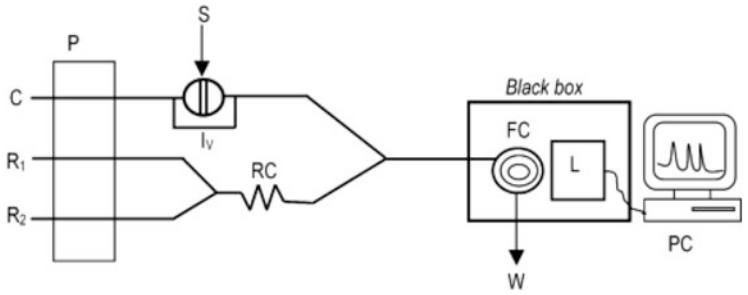

Fig. 6.21 Schematic diagram of the flow-injection system for dopamine determination [107]. P: peristaltic pump; C: water carrier stream; R1: potassium hexacyanoferrate(III) solution; R2: luminol and potassium hexacyanoferrate(II) in sodium hydroxide solution; RC: mixing coil; S: sample; I_V: injection valve; L: luminometer; FC: flow cell; PC: computer; W: waste

spectrometry. With the development of pharmaceutical analysis, the analytical method is required to be sensitive, rapid, accurate, and automatic. Some of the original low-sensitive, operating-fiddly analysis methods could be phased out, and some of the large equipments are too expensive and difficult to promote. However, CL becomes the hot topics in the current study of analytical chemistry because of its advantages such as high sensitivity, fast analysis speed, and being easy to realize automation. At present, it has been used in the analysis of antibiotics, alkaloids, vitamins, and anti-tuberculosis and antihypertensive drugs.

Lian et al. [106] established a rapid flow injection CL for the determination of the commonly used antibiotic—ciprofloxacin (CPLX). Based on CPLX-sensitized Ce (IV)-SO_3^{2-}, this method was well applied to the analysis of CPLX in human serum and urine samples.

Nalewajko et al. [107] established a method for the determination of dopamine by flow injection CL inhibition method based on the strong inhibition phenomenon of dopamine on luminol-hexacyanoferrate(III) system (Fig. 6.21). This method is not very selective to other drugs containing polyphenolic groups, but does not interfere with the determination of dopamine in commercial samples containing only the measured drug.

6.4.2.5 Detection of Ions

Many ions can be determined by CL. Some ions can be directly determined because they can enhance or inhibit the reaction and some ions can be indirectly determined by displacement coupling reaction. Li and Zhang [108] used Hg(II) displacement Fe (II)-EDTA complexes of Fe(II) and Fe(II)-luminol-dissolved oxygen to produce CL, and established a new method for determination of mercury ion. And this method was used for the determination of mercury in industrial wastewater successfully. Gao [109] combined the reaction of oxidation from $K_4Fe(CN)_6$ to $K_3Fe(CN)_6$ by nitrite

Table 6.1 Chemical analysis of inorganic ions and compounds

Analyte	Reaction system	Detection limit	Linear range	Reference
La(III)	Luminol-H_2O_2-Cr(III)	4×10^{-8} mol/L	1×10^{-7}–1×10^{-4} mol/L	Yue et al. [110]
Cd(II)	Luminol-8-Hydroxyquinoline-5-sulfonic acid-Cd(II)-H_2O_2	1.0×10^{-8} g/mL	2×10^{-8}–1.0×10^{-6} g/mL	Zhu et al. [111]
Eu(III)	Luminol-H_2O_2-Cr(III)	2×10^{-8} mol/L	1×10^{-7}–1×10^{-4} mol/L	Zhu and He [112]
Cu(II)	Dichlorofluorescein-H_2O_2	0.2 ng	0.5–7.5 ng	Safavi and Baezzat [113]
NO	Luminol-H_2O_2	1.7×10^{-13} mol/L	1.7×10^{-12}–1.7×10^{-9} mol/L	Zhou et al. [114]
H_2O_2	H_2O_2-Br_2	3.5×10^{-7} mol/L	1.0×10^{-6}–4.0×10^{-3} mol/L	Zheng et al. [115]
I_2	$KMnO_4$-HCHO-I_2	1.8×10^{-8} g/mL	1.0×10^{-7}–8.0×10^{-6} g/mL	He and Wan [116]
SO_2	Mn(III)-SO_2	8.0×10^{-8} mol/L	3.0×10^{-7}–1.0×10^{-4} mol/L	Zheng and Zhang [117]

with uric acid-$K_3Fe(CN)_6$-luminol CL reaction, and established a new indirect method for the determination of nitrite in environmental water samples and food. More ion measurements are shown in Table 6.1.

6.4.3 Application of CL in In Vitro Diagnosis

In vitro diagnosis (IVD) refers to products and services that obtain clinical diagnosis information through in vitro detection of human samples such as blood, body fluids, and tissues to judge diseases or body functions. Eighty percent of clinical diagnostic information comes from IVD. IVD has become an important part of human disease prevention, diagnosis, and treatment increasingly. It is also a significant part of ensuring human health and building a harmonious society.

6.4.3.1 Diabetes Diagnosis

In patients with diabetes, NADPH oxidase on the membranes of polymorphonuclear leukocyte (PMN) is activated by soluble or granular factors to produce superoxide anion radicals, which are then converted to hydrogen peroxide and light radicals.

The CL-based blood glucose concentration of patients is significantly higher than that of normal people. However, when NADPH oxidase is inhibited or hexose phosphate bypass is blocked, the blood glucose concentration of the diabetic group and the normal group are inhibited to different degrees. Blood glucose concentration in diabetic patients can also reflect the level of circulating immune complex. Patients with high circulating immune complexes also have high blood glucose concentration.

6.4.3.2 Diagnosis of Thyroid Disease

The thyroid is an endocrine gland that secretes bioactive thyroid hormones. Thyroid hormone plays an important role in metabolism, growth and development, nervous system, cardiovascular system, and digestive system. The increase or decrease of thyroid hormone levels can lead to thyroid dysfunction, endocrine disorders. Therefore, the correct detection of thyroid-related hormones is of great significance for the diagnosis and treatment of thyroid diseases. Hu et al. [118] used CL immunoassay (CLIA) to detect the serum thyroid hormone level of pregnant women and found that there were significant differences between different pregnancies and nonpregnancies, which can be used as indicators for screening during pregnancy. CLIA has lots of advantages in detecting thyroid hormone, such as high sensitivity, simple instruments, and wide linear range. It provides an important reference for early diagnosis of thyroid diseases, and has a broad application prospect.

6.4.3.3 Reproductive Hormone Testing

Reproductive endocrine hormones play an important role in regulating the development of sexual characteristics and the reproduction of race, and their content and concentration play a decisive role in the realization of their functions. The early detection methods of reproductive hormone level mainly include biological analysis, chemical analysis, and immunological analysis. The operation of biological analysis is more complicated and the accuracy needs to be improved. Chemical analysis can improve the accuracy of detection in some extent, but it is difficult to detect the trace of reproductive hormone in serum. Immunological analysis uses radioimmunoassay for hormone detection. Although the reagent cost is low and the operation is simple, the radioactivity of the marker has certain pollution to the environment, so it is phased out. Chemical immunoassay not only has advantages in accuracy and operation but also controls the cost of detection effectively, so it has become one of the most commonly used method for the detection of reproductive hormone.

6.4.3.4 Tumor Marker Diagnosis

Tumor marker is a kind of marker that reflects the presence or absence of tumor, and its type and content can be used as the basis of tumor diagnosis. This substance can be produced by tumor tissue, and present in tumor tissue itself or be secreted into body fluids. It can also be stimulated by tumor tissue and produced by host cells. The detection of tumor markers has certain application value for the early discovery of the disease, the development of the disease, the evaluation after treatment, the monitoring of recurrence and metastasis, etc., which can fight for the treatment time and prolong the life of patients.

6.4.3.5 Other Tests

Other disease detection items include chlamydia antigen associated with infectious diseases, creatine kinase and myoglobin related to cardiovascular diseases, total IgE and specific IgE related to allergic diseases, and some viral markers such as HIVl/2Ab. Most of the clinical detection projects combine the immune technology based on the specific binding of antigen and antibody with the CL with high sensitivity and high throughput to develop an automated detection system.

6.4.3.6 Summary and Prospect

In general, CL has been well applied and developed in the field of biological detection and in vitro diagnosis. The detection performance and process have been improved and simplified after combining CL with many other technologies or principles. The combination of CE, flow injection system and CL has realized the fluid controllability of sample detection and greatly promoted the development of CL. But the used equipment usually is complex and varied. The fusion of microarray chip concept and CL analysis improves the integration of detection system, and promotes the transformation of the detection system towards miniaturization and portability. In terms of detection methods, CL is coupled with RET, specific immune reaction, and other principles, which extends the application of CL and provides a new idea for the application of CL analysis in the field of biological detection and in vitro diagnosis. The combination of CL imaging technology with the analysis and separation technologies can further improve the selectivity, sensitivity, speed, and flux of detection and analysis.

6.5 Application of CL in Biochips

6.5.1 Introduction

In the 1990s, with the launch of the Human Genome Project, the biochip was developed rapidly as a high-technology. It is very different from the bio-computer chip that was reported previously. Bio-computer chip is a novel computer chip which uses biomolecules as components, stores the data through organic compounds, and uses biological operation as an information processing tool [119]. The biochip described in this chapter is a micro-biochemical analysis instrument, which is developed on the basis of mutual penetration of biotechnology, microelectronics as well as chemistry. Its emergence will have a major impact on the fields of molecular biology, disease diagnosis and treatment, new drug development, crop breeding and improvement, judicial signing, and so on.

6.5.1.1 Traditional Biochip

The traditional biochip is based on glass, quartz, or polymer materials, designed with theories of molecular biology, analytical chemistry, material physics, medical detection, etc., and manufactured by various processing methods. These advantages enable researchers to complete various life science experiments on a chip of varying sizes. The biochip is like a small lab that can perform a variety of complex operations and calculations, and has the advantages of high detection speed and accuracy, and low energy consumption. According to the biological components fixed on the chip, the traditional biochip can be divided into three categories: nucleic acid chip, protein chip and chip lab. They modify different biomolecules (oligonucleotides, cDNA, genomic DNA, polypeptides, antigens, antibodies, etc.) in the form of large-scale arrays to shape a solid-phase surface that interacts with the target and reacts in parallel. Chemical reactions (e.g., hybridization, immune reactions) are carried out between the chip and fluorescent-labeled target molecules; different markers will present different fluorescence spectra after being irradiated by excitation light. Then signals will be collected by laser confocal microscanner or CCD camera (charge couple device). Datas are analyzed by the computer to obtain relevant biological information at last [120].

6.5.1.2 Microfluidic Biochip

Microfluidic biochip is a hot field in the development of current miniaturized total analysis systems. The microfluidic biochip uses the chip as the experimental platform, uses material physics, analytical chemistry, biomedicine, and other disciplines as the theoretical basis, relies on microelectromechanical processing technology, and takes the microchannel network system as the main structure and the life science as

the main application object, which is the hot direction of current biochip technology. Its goal is to integrate the entire experimental processes on a single chip, including sampling, dilution, reagent addition, reaction, separation, and detection.

Features and Advantages

The microfluidic biochip has characteristics of controllable liquid fluidity, minimal consumption of samples and reagents, and fast analysis. It can perform simultaneous analysis of hundreds of samples in a few minutes or even less time, as well as realize the sample online preprocessing and analysis.

Substrate Material

The commonly used materials for the microfluidic biochips can be classified into rigid materials and elastic materials. Among them, rigid materials include single crystal silicon [121], glass [38, 39], quartz [122], and rigid organic polymer materials such as polymethyl methacrylate [123]; and elastic materials have polydimethylsiloxane (PDMS) [124] and others. In addition, some research groups have proposed some new materials in recent years, such as paper [125], cloth [103–105], and thread [126].

Processing Technology

Recently, the researches on microfluidic biochip processing technology have attracted the attention of many researchers. At present, the etching technology [127] is widely used in silicon wafers, glass, and quartz chips; the laser etching [128] and hot pressing [129] technologies are mainly used in polymer chips; and the processing methods for fiber chips have plasma processing [130], photolithography [131], and wax screen printing [132].

6.5.2 Typical Applications

6.5.2.1 Enzyme Substrate Biochip

In the CL enzyme substrate biochips, there are mainly two types of luminescent substances. One is 1,2-dioxane derivative (AMPPD), it can be catalyzed and hydrolyzed by alkaline phosphoric enzyme (ALP) and emits the blue light at 470 nm under alkaline conditions. AMPPD takes about 15 min to reach the maximum luminescence intensity, and the price of AMPPD is expensive, these have led to its infrequent use in CL. The other type is luminol. In biological systems, horse radish

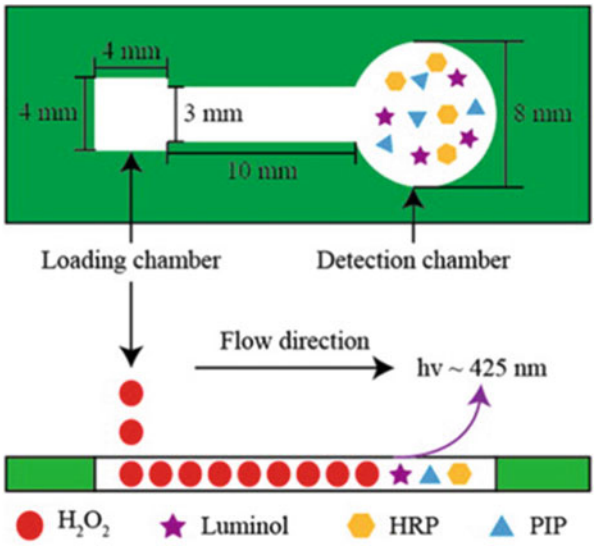

Fig. 6.22 Schematic diagram of the detection of H_2O_2 by a cloth-based chemiluminescence biochip [133]

peroxidase (HRP) is commonly used to decompose H_2O_2 into water and monooxygen, in which monooxygen can react with luminol. Luminol and corresponding enzyme sources are convenient and inexpensive, and the luminescence response time of luminol takes only a few seconds, so the luminol is widely used in biochips. For example, Zhang's group [133] developed a cloth-based CL biochip for the determination of residual H_2O_2 in meat products (Fig. 6.22).

Later, this research group developed a cloth-based CL glucose biochip [134]. Glucose was catalyzed by glucose oxidase (GOD) to produce gluconic acid and H_2O_2; then H_2O_2 could be decomposed by HRP to obtain monooxygen; in the end, CL signal could be produced by reaction of luminol and monooxygen (Fig. 6.23). Finally, it was proved that the biochip could be used for the detection of glucose in clinical urine and serum samples.

6.5.2.2 Nucleic Acid Biochip

Most of the current common CL nucleic acid biochips use nucleic acid probe technology. Nucleic acid probe is a kind of DNA or RNA labeled with the marker, which can hybridize with complementary nucleic acid sequence, and the nucleic acid sample to be detected is determined by whether the two have hybridized. Commonly used nucleic acid probe labels include radioisotopes, enzymes, fluorescein, etc. Markers of CL nucleic acid biochip are usually selected a substance which can be detected directly or indirectly by CL, such as biotin, peroxidation enzyme and ALP, and these markers can be attached to the nucleic acid probe by chemical modification or enzymatic reaction. For example, a research team has developed a new paper-based microfluidic biochip that used biotin as the marker for the detection of *Listeria monocytogenes* DNA [97]. Another research group proposed a chemical biochip that

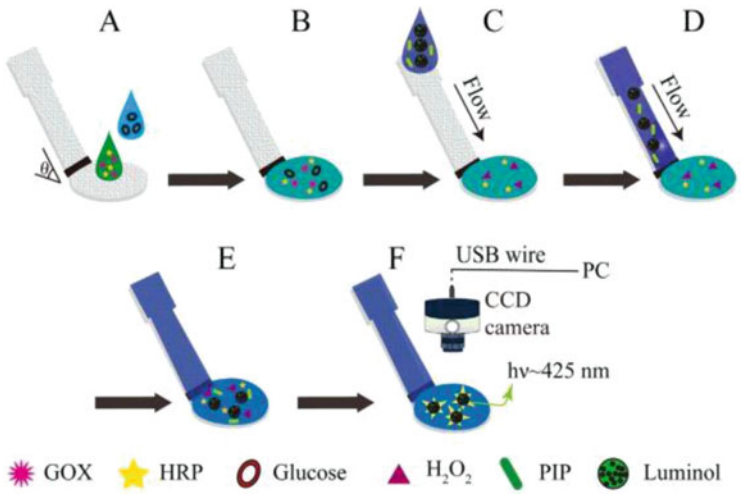

Fig. 6.23 (**a–f**) Detection process and schematic diagram of the cloth-based chemiluminescence glucose biochip

could be used for multiple amplification and detection of viral and bacterial DNA. The recombinase polymerase amplification (RPA) method was used to isolate the two viruses. It could realized the automation of multiple isothermal amplification on the chip, and amplify and detect the DNA of three microorganisms simultaneously [135]. Figure 6.24 shows the schematic and flow diagram of RPA automation on the chip.

6.5.2.3 Protein Biochip

At present, protein biochips are widely used in clinical fields, including gene expression screening, specific antigen–antibody detection, protein interaction research, new drug research and development, and disease research. The antibody labeled with luminescent substances can be fixed on the chip, when the protein to be tested can specifically bind to it, the marker will be stimulated to produce CL. The detection results are obtained through the signal collection and analysis system finally. For example, Zong et al. [136] developed a protein array chip combined with heme, G-quadruplex and gold nanoparticles to detect four different proteins simultaneously (Fig. 6.25).

In addition, the method of DNA microarray technology combined with neighboring hybridization chain reaction (HCR) could detect a group of protein biomarkers sensitively [137] (Fig. 6.26).

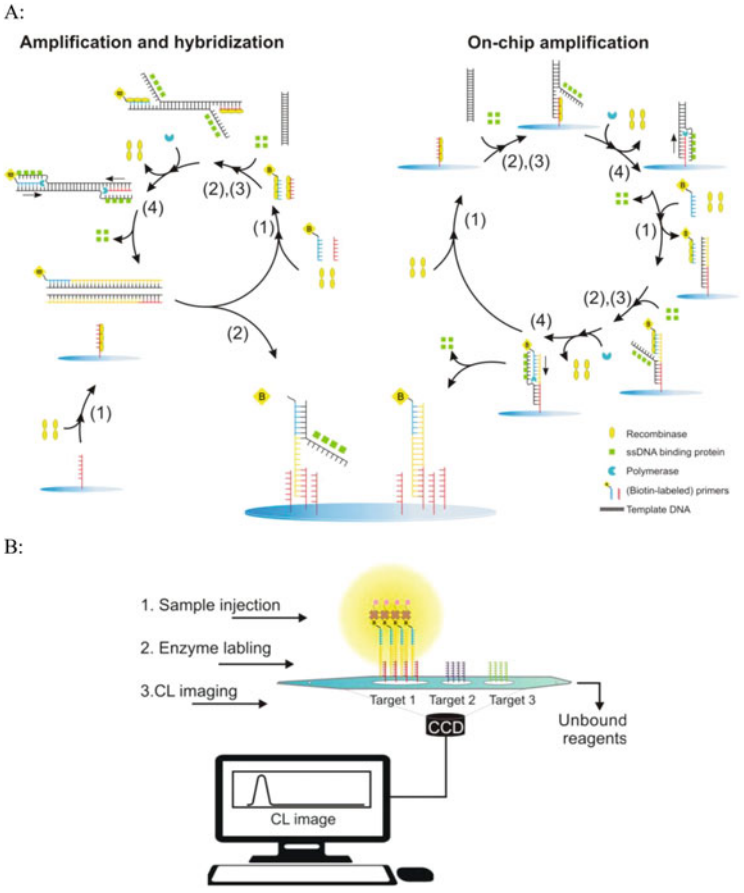

Fig. 6.24 Schematic (**a**) and flow diagram (**b**) of RPA automation on the chip [135]

6.5.2.4 Cell Biochip

Cells are the basic units of living organisms, and the cell research plays an important role in life sciences and clinical medicine. At present, the cell analysis commonly uses the cell analyer, which has the disadvantages of single function, poor operability, long analysis time, low efficiency, and high sample consumption. The combination of CL and cell biochips shows great advantages. First, the size of the biochip can be matched to the single cell size, which makes it easy to operate. Second, the multidimensional network structure of the biochip is close to the physiological environment where the cell lives, so that the cell can grow and reproduce in the chip. Third, the high-throughput characteristic of the biochip can be used for multivariate detection, which enables a large amount of information to be obtained on a biochip. Fourth, the biochip can be flexibly designed and combined, so that the processes of cell culture, sorting, and lysis can be integrated on the chip directly. For

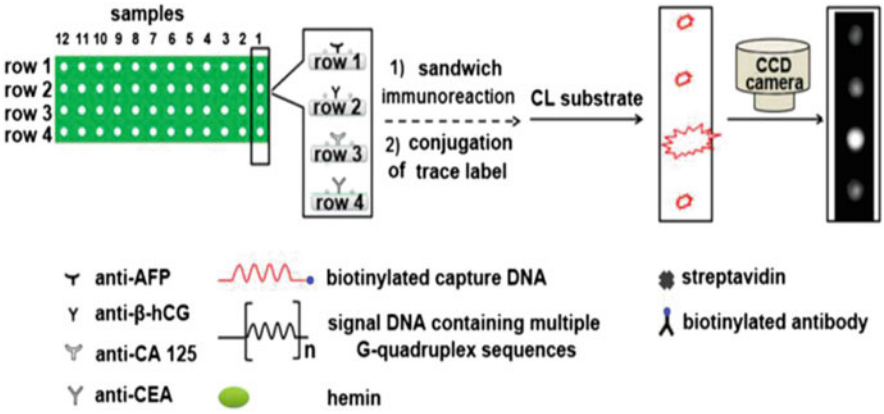

Fig. 6.25 Schematic diagram of CL detection of tumor markers by protein array chip [136]

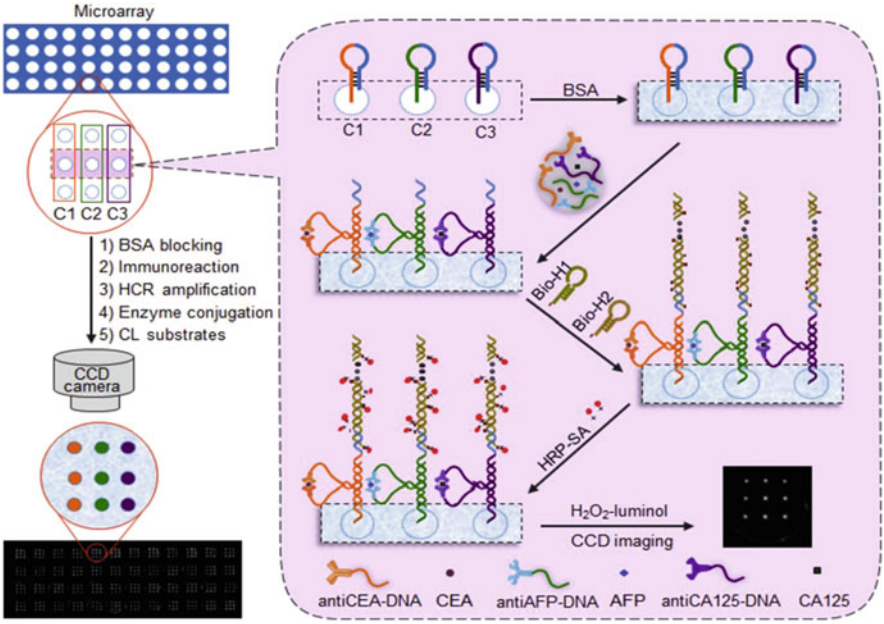

Fig. 6.26 Principle of detection and process for imaging analysis [137]

example, Chen et al. [138] developed a platform with large specific surface, which integrated the poly-dimethylsiloxane (PDMS) and microfiltration membrane (PMM). With the combination of PMM, functionalized microbeads and antibodies against specific cell surface proteins, and CL technology, the chip could be used to separate immune cell subsets in blood samples quickly, efficiently, and with the high throughput (Fig. 6.27).

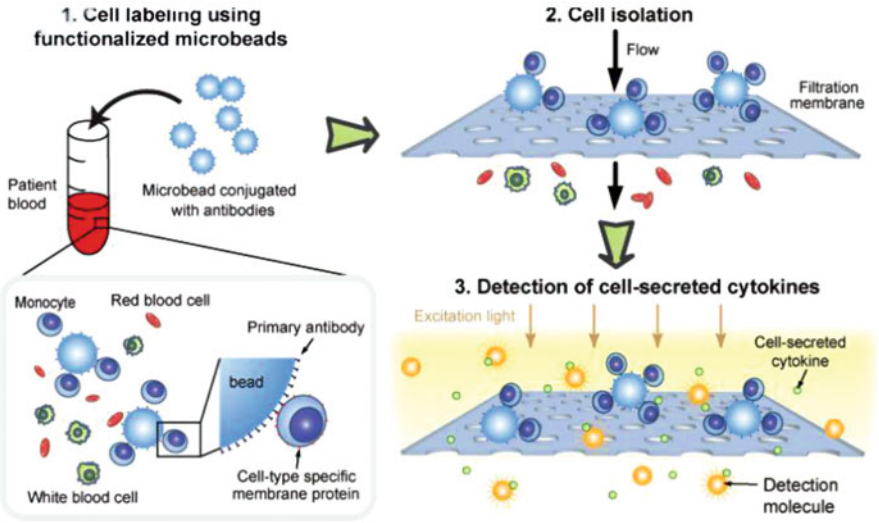

Fig. 6.27 Isolation and immunophenotyping of immune cell subsets in blood samples [138]

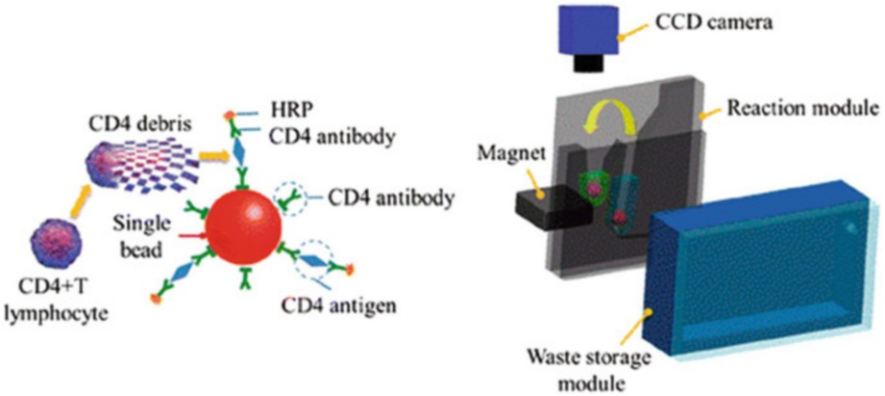

Fig. 6.28 Point-of-care CD4 + T lymphocyte count system [139]

In addition, Qiu et al. [139] developed a cell biochip consisting of three chambers: reaction chamber, detection chamber, and waste storage chamber, which could count CD4 + T lymphocytes (Fig. 6.28). The CL reaction should be carried out in a separate chamber in order to reduce the nonspecific binding of the enzyme. And the waste liquid could be released into the waste storage chamber simply by opening the vent.

6.5.2.5 Other Chips

CL biochips can be used to detect small biological molecules, such as glutathione (GSH). GSH is a major endogenous antioxidant that plays an important role in cell defense against toxins and free radicals. Shi et al. [140] developed a biochip that combined microfluidic electrophoresis with CL to quantitatively detect GSH in rat liver single cell by using the enhanced effect of sulfhydryl compounds on the lumino-H_2O_2 system (Fig. 6.29).

CL biochips can also be applied to drug screening. For example, beekeepers often use antibiotics and chemotherapy to treat or prevent bacteria or other bee's diseases, these antibiotics may contaminate honey. In order to protect human health, it is crucial to detect drug residues in food. Currently, multiple analyses of antibiotics in honey can be performed selectively using the CL biochip technology [141].

In addition, the CL biochips usually are used in ion detection. Wu et al. [142] designed a CL biochip induced by peroxynitrite for the detection of nitrite in water and beverages samples (Fig. 6.30).

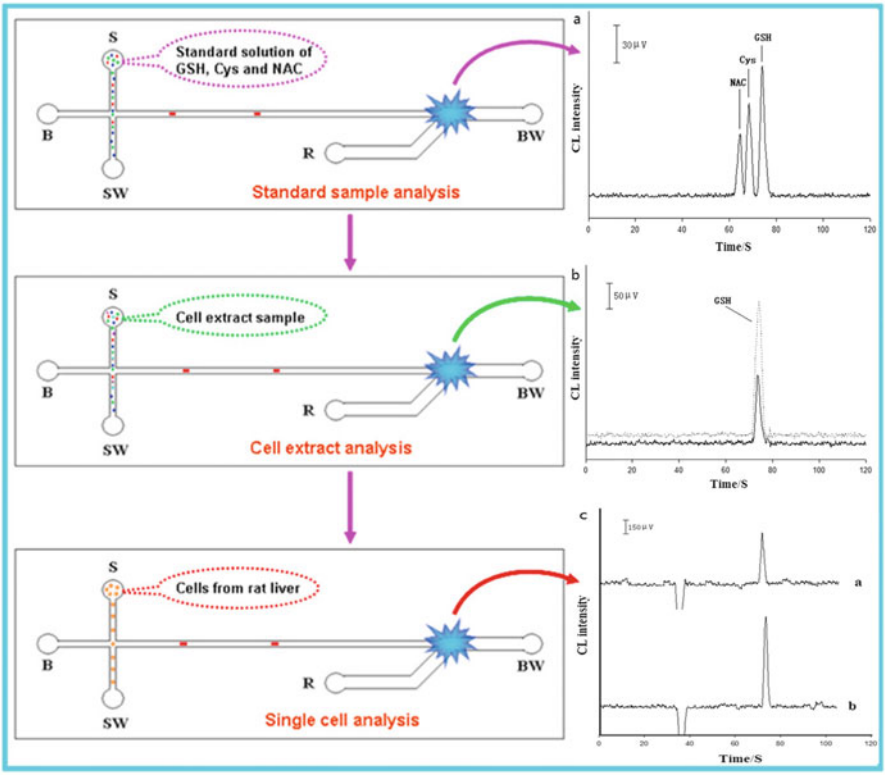

Fig. 6.29 Schematic diagram of GSH assay in rat liver single cells [140]

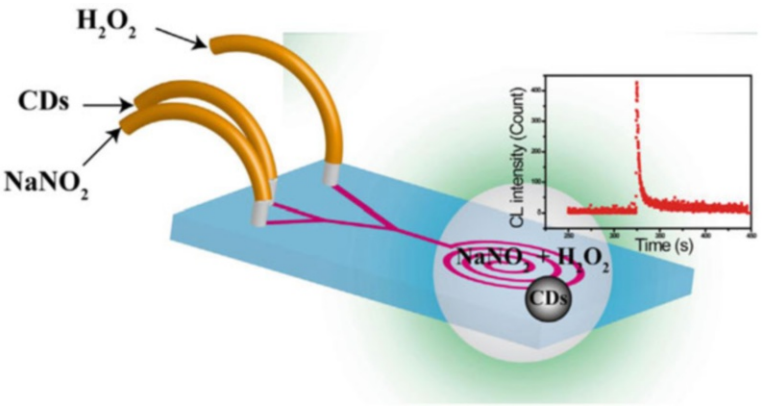

Fig. 6.30 Schematic diagram of the detection of nitrite by carbon dots (CDs)-$NaNO_2$-acidified H_2O_2 system [142]

6.5.3 Development Trend of CL Biological Chip

The CL biochip has many advantages, such as small size, high efficiency, good sensitivity, easy operation, and rapid detection, and is widely used in biomedical and clinical detection, environmental protection, and other fields. With the advancement of technology and the improvement of scientific requirements, there are several development trends in CL biochips: (1) developing or integrating of new materials, such as introducing nanomaterials [143], to improve the detection sensitivity; using fiber materials [103–105] to reduce chip cost; and developing flexible materials [144] to expand the application range. (2) Applying or combining new technologies, e.g., smart phone can be used to control the flow of droplets on the chip and as signal receiver [145]; 3D printing technology can be used to manufacture biochips, which can save production time, make chips more diversified, and also can be used for personalized customization [146]; and combined with high-performance liquid chromatography technology, biological applications are more extensive [147]. (3) The sensing devices are gradually developed towards integration, portability and industrialization; as a common technology in the field of point-of-care testing (POCT), the CL biochip is expected to realize the commercialization of the product; and at present, such portable automatic analytical instrument has become a research hotspot [148]. To sum up, in combination with the current development, the CL biochip has made breakthroughs in processing technologies, detection methods, and many other aspects, and has gradually matured. In the future, it will enter a deeper level of research, and how to speed up the process of product integration and commercialization has become an important topic of this technology. It is believed that, CL biochips can replace the current many large biochemical testing equipment, and promote the development of life science, environmental science, and other fields in the near future.

6.6 Chemiluminescence In Vivo Application

6.6.1 Introduction

6.6.1.1 Conceptual Framework

In recent years, the CL detection technology has received extensive attention due to its high sensitivity. Numerous chemicals have been discovered, which has enhanced or suppressed CL reactions to CL detection. It has promoted the application of CL detection technology, especially the application of CL technology in vivo detection.

The application of CL in living cells is based on the principle that free radicals generated by cell activation impart energy to the luminescent group, causing the luminescent group to change from the ground state to the excited state. The luminescent group will produce a strong CL phenomenon when it changes from the unstable excited state to the ground state. Cells that can be activated in vivo can be divided into phagocytic cells and nonphagocytic cells. The former includes neutrophils, monocytes, and macrophages, and the latter includes various lymphocytes, erythrocyte, and eosinophils.

The application of CL in tissues is based on the fact of enzymatic reaction. The CL tissue sensor is made by placing animal or plant tissue section on the electrodes as a catalyst for the enzymatic reaction. According to the different tissue materials used, it can be divided into plant tissue and animal tissue. According to the analysis method, it is classified into static type and circulation type [149].

6.6.1.2 Development Status

Since the 1990s, the CL detection technology has been widely used in clinical diagnosis, biomedical research, environmental protection, and other fields. The combination of CL and other detection technologies is also constantly evolving. The current conventional method that combines CL detection and chromatographic techniques uses a luminescent agent or an enzyme that catalyzes a luminescent reaction as a label in an enzyme-linked reaction. This method has been applied to living cells, tissues, and individuals.

Neutrophils, macrophages, erythrocyte, and lymphocytes are the commonly used cells in the application of CL to living cells. Neutrophils located in the bone marrow are closely related to the phagocytic and digestive functions of cells, and they are often used as clinical indicators of inflammation [150]; in addition, the application of CL in macrophages possesses a good prospect for in vivo luminescence detection; erythrocytes are closely related to oxygen transport in human body, and the application of CL technology in erythrocyte has realized the determination of hemoglobin content. The method has high accuracy, simple operation, and strong practicability, and has broad application prospects in biomedical research; lymphocyte chemiluminescence (LY-CL) induced by T-lymphocytes will be a sensitive method for

studying lymphocyte activation, interaction of lymphocytes with macrophages, and rapid determination of lymphocyte activity [151].

More than 10 years after the introduction of the enzyme electrode, a tissue sensor based on an enzymatic reaction has gradually emerged as a derivative electrode of an enzyme electrode. Initially, in static CL tissue sensor, the analytes are uniformly mixed with the luminescent reagent by stirring or injection, and then the whole process of the CL reaction is detected. However, the static CL tissue sensor has some defects, such as slow sample loading rate and poor reproducibility, and debased sensitivity and stability resulting from the long-term contact between the luminescent reagent and the tissue material. The emergence of flow-through CL tissue sensors solves the above problems [152]. Since luminescent reagents and analytes flow on the sensor surface, the retention volume and time of the reagents can be precisely controlled. Thus, the sensitivity and precision of the sensor has been improved, which make it easier to achieve fast and accurate detection than static one.

At present, the application of CL in individuals has achieved the use of CL analysis for detecting serum C-peptide concentrations in the same individuals with an oral glucose tolerance test, where the volunteer is tested before and after serving sugar at different time points; its clinical feasibility remains to be further proved [153].

6.6.2 Application of Chemiluminescence in Cells

6.6.2.1 Application of CL in Neutrophils

Neutrophils are colorless and extremely light red cells derived from bone marrow, the cytoplasm of them contains a large number of lysosomes that contain lysozyme, alkaline phosphatase and acid hydrolase. Neutrophils have phagocytic and bactericidal effects and are involved in the phagocytosis and digestion of cells.

In 1972, Allen et al. [150] first discovered that human peripheral blood neutrophils were accompanied by CL during phagocytic bacteria, and the phenomenon associated with the chain oxidation of free radicals. Bacteria, immune complexes, and other substances in the serum contact with neutrophil surface receptors after IgG, IgM, and complement conditioning, thereby being phagocytosed to form phagosomes, while neutrophils generate oxidative phagocytosis. In the above process, free radicals such as $_1O^2$, H_2O_2, OCl^-, $OH^\bullet$ release photons from the excited state back to the ground state, producing CL. However, this natural light of neutrophils is very weak, so it is necessary to add a luminescent agent such as luminol or luster to generate strong CL so as to make it detected by a highly sensitive photometer. In 1982, Horan et al. [154] found that the oxidative activity of neutrophils was closely related to the rate of bacteriolysis, and the bactericidal ability was directly proportional to the luminescence intensity. It is worth noting that neutrophil/lymphocyte ratio (NLCR) can be detected by neutrophil CL [155], which is a blood routine commonly used for clinical inflammation analysis [156]. The NLCR will

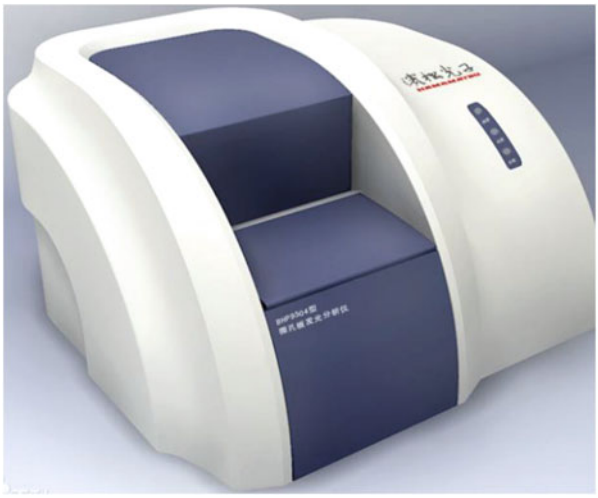

Fig. 6.31 Beijing Furui chemiluminescence analyzer

increase significantly in just a few hours when the body develops bacterial infection. The NLCR has more value than the detection of neutrophil or lymphocyte alone, and can use the CL immunoassay analyzer (such as Fig. 6.31) to detect the percentage of neutrophils and lymphocytes to analyze the inflammatory response.

6.6.2.2 Application of CL in Macrophages

Macrophages are phagocytic cells located in phagocytic cells that digest cell debris and pathogens in the form of fixed or free cells, activating lymphocytes or other immune cells.

In 1999, Cui et al. [157] used the CL method to observe the changes of phagocytic function of mouse spleen macrophages and the changes of C3b receptors related to spleen macrophage function in spleen macrophages. The purpose was to investigate the effect of holmium laser on the function of spleen macrophages. In 2013, Zhang [158] used a multifunction microplate reader to detect the CL of $O_2^{\bullet -}$ in mouse macrophages. In addition, combined with confocal imaging technology to image the living body, the fluorescence detection of $O_2^{\bullet -}$ in mice was achieved, which has a good prospect of in vivo application.

6.6.2.3 Application of CL in Erythrocytes

Erythrocytes are the most abundant blood cells in the blood and have the function of immunization. Erythrocytes have no mitochondria, so they release energy by breaking down glucose. Erythrocytes are also the most important medium for transporting

oxygen, they are bright red when transporting oxygen, but dark purple when transporting carbon dioxide.

In 2006, Zhang et al. [159] used erythrocytes to replace horseradish peroxidase as the marker of the second antibody in double antibody sandwich immunoassay, and established a new immunochemiluminescence method for the determination of hepatitis B virus surface antigen. After the immune response is completed, sensitized erythrocytes that bind to the antigen–antibody immune complex are hemolyzed in the hypotonic solution, releasing the hemoglobin. Then, based on the principle that hemoglobin has catalytic effect on the luminol-H_2O_2 CL system, the content of hemoglobin is determined by the CL method, and the measured luminous intensity was linearly related to the concentration of antigen to be measured. In 2015, Li et al. [99] used a dedicated single-cell analysis glass microfluidic chip (Fig. 6.32) and luminol-H_2O_2 chemiluminescence system to establish a new method for the determination of hemoglobin content in individual human erythrocytes.

6.6.2.4 Application of CL in Lymphocytes

Lymphocytes are the smallest leukocytes, they produced by the lymphatic organs and found mainly in the lymphatic vessels. They are important cellular components of the body's immune response function and are the main performers of almost all immune functions of the lymphatic system. According to the migration pathway, surface molecules and functions, they can be divided into T-lymphocytes (also known as T cells), B-lymphocytes (also known as B cells), and natural killer (NK) cells.

In 1978, Wrogemann et al. [160] first reported that mouse T cells were stimulated by ConA or calcium ionophore A23187 to produce a lymphocyte

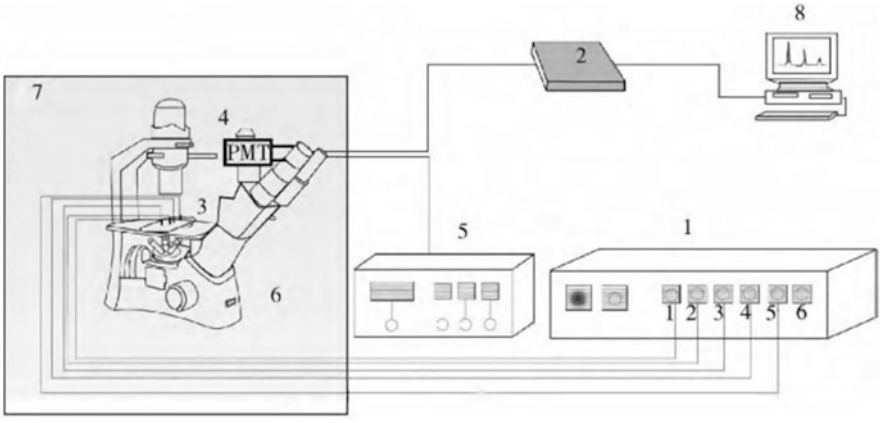

Fig. 6.32 Microfluidic chip chemiluminescence detection device [99]. (1) multichannel high-voltage power supply; (2) signal collector; (3) glass microfluidic chip; (4) photomultiplier tube; (5) DC power supply; (6) inverted microscope; (7) black box; (8) computer

chemiluminescence (LY-CL). In 1984, Mookerjee et al. [161] studied the relationship between mouse lymphocyte proliferation and LY-CL in detail. The results showed that LY-CL was related to lymphocyte maturation, and lymphocytes acquired the ability to produce CL during differentiation and maturation in the presence of macrophages.

6.6.3 Application of CL in Tissue

Arnold and Rechnitz first proposed the concept of tissue sensor, which was based on the principle of enzyme-catalyzed reaction, using animal and plant tissues as molecular recognition systems [162].

In recent years, the enzyme extraction technology as a traditional technology has some inherent disadvantages such as low enzyme activity and high price. The emergence of a group of catalytically active new biological materials has solved these problems, and the animal and plant organization is a large class of these new biomaterials. Compared with the traditional enzyme sensor, the tissue sensors are not only easy to take but also easy to manufacture, and the synergistic action of various enzymes in the animal and plant tissues can maintain the high activity of the enzyme, which helps to improve the stability and sensitivity of the sensor.

The animal tissue sensors can be classified into the kidney tissue sensor, liver tissue sensor, intestinal tissue sensor, muscle tissue sensor, thymus tissue sensor, and so on, depending on the tissue material used for the sensor electrode. Since the porcine kidney tissue is rich in glutaminase, a tissue sensor constructed with a section of the fresh porcine kidney cortex as a catalytic material is capable of detecting glutamine [163]. The concentration of glutamine in human cerebrospinal fluid is associated with hepatic coma and Reyes syndrome, so the sensor can be used for the diagnosis of hepatic coma and meningitis. For the same reason, sensors constructed from liver tissue which is rich in catalase can be used to detect H_2O_2 and other peroxides.

6.6.3.1 Application of CL in Plant Tissue

Roots, stems, leaves, flowers, fruits, and seeds are widely used as raw materials for plant tissue sensors based on the enzyme-catalyzed reaction. Most of the plant tissue sensors that have been reported so far are detected by electrochemical methods. The tissue substrate is detected by attaching the tissue section to the electrode or by thoroughly mixing the tissue section with the electrode material to construct the tissue electrode. This method has some disadvantages, such as little fixed biological material and low electrode catalytic activity, which limit the detection performance of the sensor.

Based on the shortcomings of the above methods, Huang [164] developed a chemiluminescent plant tissue sensor by introducing a CL transducer into a tissue sensor and using mushroom tissue as a molecular recognition component. When ethanol passes through the homemade mushroom tissue column, it is converted into H_2O_2 by the ethanol oxidase in the mushroom tissue, and then the ethanol is measured by the CL transduction reaction using the basic luminol-potassium ferricyanide.

In the above static analysis process, the substrate needs to be diffused to the biocatalyst layer for the reaction, and the response time is long and the sensitivity is low. This inherent drawback shortens the life of the sensor, so the concept of the flow-through CL sensor is introduced into the biosensor. Peng [165] fixed Luminol and Co^{2+} in an anion and cation exchange resin column as transducers for the reaction of H_2O_2 produced by the enzymatic reaction. Oxalate also can be detected using oxalate oxidase in spinach tissue in combination with flow injection techniques. In this type of sensor, the combination of high-capacity immobilization technology and flow analysis technology improves the sensitivity of the sensor and shortens the response time, meeting the requirements of real-time analysis and in vivo analysis.

6.6.4 Application of CL in Individuals

In the systemic circulation, the concentration of C-peptide can be used as the basic information reflecting insulin secretion and insulin resistance, especially in the case of treatment with exogenous insulin, it can be used to judge the secretion of endogenous insulin and the evaluation of the remaining β-cell mass and function of the pancreas [166]. In clinical medicine, it is important to determine the concentration of C-peptide. Among the clinical test methods, whether it is the classical radioimmunoassay technique [167], the enzyme immunoassay technique [168] or the CL immunoassay technique which has been widely used nowadays, its essence belongs to the category of immunodetection technology. However, current clinical laboratories and reagent manufacturers have not been able to establish standardized reference systems for C-peptide detection.

In 2010, Zhang et al. from Wangjing Hospital of China Academy of Chinese Medical Sciences [153] used three kinds of the CL analysis, which was commonly used in clinical laboratories, to test the concentration of C-peptide in serum at different time points of fasting and sugar during oral glucose tolerance test in the same individual. The experimental results show that there are significant differences between the results of different methods. Even the chemiluminescence enzyme immunoassay (CLIA) and electrochemiluminescence immunoassay (ECLIA), which are automated detection systems, have significant differences in measured values. It is mentioned that the concentration of C-peptide has certain limitations in the selection of clinical specimens and detection methodologies. Therefore, the conclusions obtained and the feasibility of the mutual recognition indicators

proposed are still to be further verified. However, with the in-depth study of the standardization system for the serum C-peptide detection and the establishment and improvement of high-specificity reference systems, the results of high conformity and comparability will bring more clear and unified conclusions to clinical application.

References

1. Wei GL, Dang GH, Li H. Ultrasensitive assay of clindamycin in medicine and bio-fluids with chemiluminescence detection. Luminescence. 2007;22(6):534–9.
2. Antje JB, Nicole AS, Naomi SS, Joseph R, Eun ML, Richard AM. Biosensor for dengue virus detection: sensitive, rapid, and serotype specific. Anal Chem. 2002;74:1442–8.
3. Wong AWK, Grundig B, Hu J, Renneberg R. Comparative study of hydrogel-immobilized 1-glutamate oxidases for a novel thick-film biosensor and its application in food samples. Biotechnol Lett. 2002;22:267–72.
4. Freire RS, Thongnagamadee S, Duran N, Wang J, Kubota LT. Mixed enzyme (laccase/tyrosinase)-based remote electrochemical biosensor for monitoring phenolic compounds. Analyst. 2002;127:258–61.
5. Wu XZ, Min LY, Akiyama K. Chemiluminescence study of active oxygen species produced by TiO_2 photocatalytic reaction. Luminescence. 2005;20:36–40.
6. Wu FW, He ZK, Meng H, Zeng Y. Determination of sulfite in sugar and sulfur dioxide in air by chemiluminescence using the $Ru(bipy)_3^{2+}$-$KBrO_3$ system. Analyst. 1998;123 (123):2109–12.
7. Liu Z, Qi W, Xu G. Recent advances in electrochemiluminescence. Chem Soc Rev. 2015a;44 (10):3117–42.
8. Liu F, Ge S, Su M, Song X, Yan M, Yu J. Electrochemiluminescence device for in-situ and accurate determination of CA153 at the MCF-7 cell surface based on graphene quantum dots loaded surface villous Au nanocage. Biosens Bioelectron. 2015b;71:286–93.
9. Jonsson T, Emteborg M, Irgum K. Heterocyclic compounds as catalysts in the peroxyoxalate chemiluminescence reaction of bis(2,4,6-trichlorophenyl)oxalate. Anal Chim Acta. 1998;361:205–15.
10. Mitsana-Papazoglou A, Fragaki A, Chamosfakidi P, Calokerinos AC. Chemiluminometric behaviour of erythromycin and related compounds. Anal Chim Acta. 2000;410:153–7.
11. Chen Y, Xu J, Su J, Xiang Y, Yuan R, Chai YQ. In situ hybridization chain reaction amplification for universal and highly sensitive electrochemiluminescent detection of DNA. Anal Chem. 2012;84:7750–5.
12. Nozaki O, Waeda T, Kato Y. Amines for detection of dopamine by generation of hydrogen peroxide and peroxyoxalate chemiluminesce. J Biolumin Chemilumin. 1996;11:309–13.
13. Cepas J, Silva M, Perez-Bendito D. Sensitive peroxyoxalate chemiluminescence determination of psychotropic indole derivatives. Analyst. 1996;121:49–54.
14. He YH, Lu JR. Chemiluminescence reaction of potassium permanganate-formaldehyde-inorganic reductant system. Chin J Anal Chem. 2002;30(5):598–600.
15. Amiott E, Andrews ARJ. Morphine determination by HPLC with improved chemiluminescence detection using a conventional silica based column. J Liq Chromatogr Relat Technol. 1997;20:311–25.
16. Lin JM. Basic theory and application of chemiluminescence. Beijing: Chemical Industry Press Co., Ltd.; 2004.
17. Chen GN, Lin RE, Xie ZH, Duan JP, Zhang L. A study on electrochemilumicescence of [Ru $(bpy)_2$(*L*-Trp)]ClO_4 complex in water solution. Acta Chim Sin. 1998;56(5):433–8.

18. Afsharan H, Navaeipour F, Khalilzadeh B, Tajalli H, Mollabashi M, Ahar MJ, Rashidi MR. Highly sensitive electrochemiluminescence detection of p53 protein using functionalized Ru-silica nanoporous@gold nanocomposite. Biosens Bioelectron. 2016;80:146–53.
19. Wu MS, Qian GS, Xu JJ, Chen HY. Sensitive electrochemiluminescence detection of c-Myc mRNA in breast cancer cells on a wireless bipolar electrode. Anal Chem. 2012;84:5407–14.
20. Velan B, Halmann M. Chemiluminescence immunoassay; a new sensitive method for determination of antigens. Immunochemistry. 1978;15:331–3.
21. Melucci D, Roda B, Zattoni A, Casolari S, Reschiglian P, Roda A. Field-flow fractionation of cells with chemiluminescence detection. J Chronatogr A. 2004;1056:229–36.
22. Freeman R, Liu XQ, Willner I. Chemiluminescent and chemiluminescence resonance energy transfer (CRET) detection of DNA, metal ions, and aptamer-substrate complexes using Hemin/G-Quadruplexes and CdSe/ZnS quantum dots. J Am Chem Soc. 2011;133 (30):11597–604.
23. Wu BL, Zhang GM, Gao CG, Shang SM. Application and development of biosensors. Chin Biotechnol. 2004;24(7):65–9.
24. Pasini P, Musiani M, Russo C, Valenti P, Aicardi G, Crabtree JE, Baraldini M, Roda A. Chemiluminescence imaging in bioanalysis. J Pharm Biomed Anal. 1998;18:555–64.
25. Roda A, Pasini P, Mirasoli M, Michelini E, Guardigli M. Biotechnological applications of bioluminescence and chemiluminescence. Trends Biotechnol. 2004;22(6):295–303.
26. Tokel NE, Bard AJ. Electrogenerated chemiluminescence. IX. Electrochemistry and emission from systems containing tris (2, 2′-bipyridine) ruthenium (II) dichloride. J Am Chem Soc. 1972;94(8):2862–3.
27. Liu J, Xing D, Shen X, Zhu D. Electrochemiluminescence polymerase chain reaction detection of genetically modified organisms. Anal Chim Acta. 2005;537(2):119–23.
28. Hu YF, Li JP, Liu R, Hao ZB. Recent progress of application of CE-ECL. Phys Test Chem Anal B Che Anal. 2011;5:50.
29. Miao W. Electrogenerated chemiluminescence and its biorelated applications. Chem Rev. 2008;108(7):2506–53.
30. Fähnrich KA, Pravda M, Guilbault GG. Recent applications of electrogenerated chemiluminescence in chemical analysis. Talanta. 2001;54(4):531–59.
31. Deaver DR. A new non-isotopic detection system for immunoassays. Nature. 1995;377 (6551):758–60.
32. Xu GB, Dong SJ. Electrochemiluminescence and its application. Chin J Anal Chem. 2001;29 (1):103–8.
33. Dufford RT, Nightingale D, Gaddum LW. Luminescence of Grignard compounds in electric and magnetic fields, and related electrical phenomena. J Am Chem Soc. 1927;49(8):1858–64.
34. Harvey N. Luminescence during electrolysis. J Phys Chem. 1929;33(10):1456–9.
35. Kuwana T, Epstein B, Seo ET. Electrochemical generation of solution luminescence. J Phys Chem. 1963;67(10):2243–4.
36. Richter MM. Electrochemiluminescence (ECL). Chem Rev. 2004;104(6):3003–36.
37. Haapakka KE, Kankare JJ. The mechanism of the electrogenerated chemiluminescence of luminol in aqueous alkaline solution. Anal Chim Acta. 1982;138:263–75.
38. Wang ZY, Guo WY, Di JW TYF. The study on electrochemiluminescence of luminol on ITO glass. Spectrosc Spectr Anal. 2005a;25(10):1564–7.
39. Wang H, Huang HQ, Dai ZP, Gao Y, Ma B, Wang L, Bai JL, Lin BC. Investigation of self-made glass microfluidic chips and their basic properties. Chem Res Chin Univ. 2005b;11:69–71. 11.
40. Hercules DM, Lytle FE. Chemiluminescence from reduction reactions. J Am Chem Soc. 1966;88(20):4745–6.
41. Ding SN, Xu JJ, Chen HY. Some progresses in the electrogenerated chemiluminescence techniques of $Ru(bpy)_3^{2+}$. Sci Pap Online. 2007;2(8):595–606.
42. Miller CJ, McCord P, Bard AJ. Study of Langmuir monolayers of ruthenium complexes and their aggregation by electrogenerated chemiluminescence. Langmuir. 1991;7(11):2781–7.

43. Zhuang YF, Ju H. Study on electrochemiluminesce of Ru $(bpy_3)^{2+}$ immobilized in a titania sol-gel membrane. Electroanalysis. 2004;16(17):1401–5.
44. Choi HN, Cho SH, Lee WY. Electrogenerated chemiluminescence from Tris (2,2′-bipyridyl) ruthenium (II) immobilized in titania–perfluorosulfonated ionomer composite films. Anal Chem. 2003;75(16):4250–6.
45. Ritter KA, Lyding JW. The influence of edge structure on the electronic properties of graphene quantum dots and nanoribbons. Nat Mater. 2009;8(3):235.
46. Zhu SJ, Zhang JH, Tang SJ, Qiao CY, Wang L, Wang HY, Liu X, Li B, Li YF, Yu WL, Wang XF, Sun HC, Yang B. Surface chemistry routes to modulate the photoluminescence of graphene quantum dots: from fluorescence mechanism to up-conversion bioimaging applications. Adv Funct Mater. 2012;22(22):4732–40.
47. Ding Z, Quinn BM, Haram SK, Pell LE, Korgel BA, Bard AJ. Electrochemistry and electrogenerated chemiluminescence from silicon nanocrystal quantum dots. Science. 2002;296(5571):1293–7.
48. Cheng C, Huang Y, Wang J, Zheng B, Yuan H, Xiao D. Anodic electrogenerated chemiluminescence behavior of graphite-like carbon nitride and its sensing for rutin. Anal Chem. 2013;85(5):2601–5.
49. An JR, Chen X, Chen H. Investagation of electrochemiluminescence of luminol in aqueous alkaline solution. Chin J Anal Chem. 1988;2:37–42.
50. Chen X, Li MJ, Yi CQ, Tao Y, Wang XR. Electrochemiluminescence determination of nitro polycyclic-aromatic hydrocarbons using HPLC separation. Chromatographia. 2003;58 (9):571–7.
51. Skotty DR, Lee WY, Nieman TA. Determination of Dansyl amino acids and oxalate by HPLC with electrogenerated chemiluminescence detection using tris (2,2′-bipyridyl) ruthenium (II) in the mobile phase. Anal Chem. 1996;68(9):1530–5.
52. Yin XB, Yang XR, Wang EK. Some aspects in capillary electrophoresis-electrochemical electrochemiluminescence with microchip technique. Progre Chem. 2005;17(02):181–5.
53. Wu HM. Chemical biology: a rapidly rising frontier. Progr Chem. 2000;12(04):423.
54. He YP, Zhang F, Zhang B, Zou GZ. Dichroic mirror-assisted electrochemiluminescent assay for simultaneously detecting wild-type and mutant p53 with photomultiplier tubes. Anal Chem. 2018;90(8):5474–80.
55. Su Y, Liang Y, Wu HY, Jiang JJ, Lai W, Zhang CS. A three-dimensional cloth-based microfluidic label-free proximity hybridization-electrochemiluminescence biosensor for ultrasensitive detection of K-ras gene. Sensor Actuat B Chem. 2019;296:126654.
56. Liu Z, Zhang X, Ge X, Hu L, Hu Y. Electrochemiluminescence sensing platform for ultrasensitive DNA analysis based on resonance energy transfer between graphitic carbon nitride quantum dots and gold nanoparticles. Sensor Actuat B Chem. 2019;297:126790.
57. Wang QJ, Liao MY. The application of proteomics in drug toxicology. Fore Med Sci Sect Pharm. 2003;30(4):238–41.
58. Gao HF, Wang XF, Li M, Qi HL, Gao Q, Zhang CX. Proximity hybridization-regulated electrogenerated chemiluminescence bioassay of α-fetoprotein via target-induced quenching mechanism. Biosens Bioelectron. 2017;98:62–7.
59. Wu L, Ma C, Ge L, Kong Q, Yan M, Ge S, Yu J. Based electrochemiluminescence origami cyto-device for multiple cancer cells detection using porous AuPd alloy as catalytically promoted nanolabels. Biosens Bioelectron. 2015;63:450–7.
60. Cao LY, Zhang R, Zhang WZ, Du ZB, Liu CJ, Ye ZQ, Song B, Yuan JL. A ruthenium (II) complex-based lysosome-targetable multisignal chemosensor for in vivo detection of hypochlorous acid. Biomaterials. 2015;68:21–31.
61. Yue X, Zhu Z, Zhang M, Ye Z. Reaction-based turn-on electrochemiluminescent sensor with a ruthenium (II) complex for selective detection of extracellular hydrogen sulfide in rat brain. Anal Chem. 2015;87(3):1839–45.
62. Kavalali G, Akcasu A. Isolation of choline ascorbate from Apium graveolens. J Nat Prod. 1985;48(3):495.

63. Zhang L, Wang T, Wen X, Wei Y, Peng X, Li H, Wei L. Effect of matrine on HeLa cell adhesion and migration. Eur J Pharmacol. 2007;563(1):69–76.
64. Miao C, Wu B, Cao H, Jia N. Sensitive electrochemiluminescence detection of matrine based on Ru $(bpy)_3^{2+}$ and mesoporous silica nanosphere modified electrodes. Anal Methods. 2014;6 (21):8592–7.
65. Zhai Q, Xing H, Zhang X, Li J, Wang E. Enhanced electrochemiluminescence behavior of Gold–Silver bimetallic nanoclusters and its sensing application for Mercury (II). Anal Chem. 2017;89(14):7788–94.
66. Ullman EF, Kirakossian H, Singh S, Wu ZP, Irvin BR, Pease JS, Switchenko AC, Irvine JD, Dafforn A, Skold CN. Luminescent oxygen channeling immunoassay: measurement of particle binding kinetics by chemiluminescence. Proc Natl Acad Sci U S A. 1994;91(12):5426–30.
67. Gao YC. Research progress and application of photoexcited chemiluminescence technology. Chin J Lab Med. 2009;32(4):474–6.
68. Eglen RM, Reisine T, Roby P, Rouleau N, Illy C, Bosse R, Bielefeld M. The use of AlphaScreen technology in HTS: current status. Curr Chem Genom. 2008;1:2–10.
69. Cui YQ, She TT, Zhao H, Li JZ, Li LX, Gao WZ, Li HQ. Competitive light-initiated chemiluminescent assay: using 5-dihydrotestosterone-BSA as competitive antigen for quantitation of total testosterone in human sera. Anal Bioanal Chem. 2019;411(3):745–54.
70. Couleaud P, Morosini V, Frochot C, Richeter S, Raehm L, Durand JO. Silica-based nanoparticles for photodynamic therapy applications. Nanoscale. 2010;2(7):1083–95.
71. Fan MG, Yao JN, Dong ZH. Molecular photochemistry and photonic materials science. 1st ed. Beijing: Science Press; 2009. p. 335–47.
72. Dong ZN. Development of photosensitive chemiluminescence immunoassay for hepatitis B virus surface antigen and time-resolved fluorescence immunoassay for human immunodeficiency virus. Southern Medical University; 2012.
73. Soini E, Kojola H. Time-resolved fluorometer for lanthanide chelates-a new generation of nonisotopic immunoassays. Clin Chem. 1983;29(1):65–8.
74. Agostinis P, Berg K, Cengel KA, Foster TH, Girotti AW, Gollnick SO, Hahn SM, Hamblin MR, Juzeniene A, Kessel D, Korbelik M, Moan J, Mroz P, Nowis D, Piette J, Wilson BC, Golab J. Photodynamic therapy of cancer: an update. Cancer J Clin. 2011;61(4):250–81.
75. Ding LL, Luan LQ, Shi JW, Liu W. Application of phthalocyanine in photodynamic therapy. Chinese J Inorg Chem. 2013;29(08):1591–8.
76. Bielefeld-Sevigny M. AlphaLISA immunoassay platform-the "No-Wash" high-throughput alternative to ELISA. Assay Drug Dev Technol. 2009;7(1):90–2.
77. Liu TC, Huang H, Dong ZN, He A, Li M, Wu YS, Xu WW. Development of an amplified luminescent proximity homogeneous assay for quantitative determination of hepatitis B surface antigen in human serum. Clin Chim Acta. 2013;426:139–44.
78. Howland S, Eglen R. AlphaLISA™ in biomarker detection for drug discovery. Technology & Services; 2007.
79. Dudal S, Baltrukonis D, Crisino R, Goyal MJ, Joyce A, Osterlund K, Smeraglia J, Taniguchi Y, Yang JH. Assay formats: recommendation for best practices and harmonization from the global bioanalysis consortium harmonization team. AAPS J. 2014;16:194–205.
80. Wang K, Zhang Y, Zhang W, Zhou B, Ma ZH, Zhu W, Huang B. Establishment and evaluation of mouse tumor necrosis factor ELISA, TRFIA and ALPHAScreen detection methods. Immunol J. 2010;26(02):152–5. 166.
81. Xiong YF, Wu YS, Luo SH, Gao Y, Xiong YJ, Chen DX, Deng H, Hao WB, Liu TC, Li M. Development of a novel immunoassay to detect interactions with the transactivation domain of p53: application to screening of new drugs. Sci Report. 2017;7(1):9185.
82. Marchand C, Lea WA, Jadhav A, Dexheimer TS, Austin CP, Inglese J, Pommier Y, Simeonov A. Identification of phosphotyrosine mimetic inhibitors of human tyrosyl-DNA phosphodiesterase I by a novel AlphaScreen high-throughput assay. Mol Cancer Ther. 2009;8(1):240–8.
83. Guenat S, Rouleau N, Bielmann C, Bedard J, Maurer F, Allaman-Pillet N, Nicod P, Bielefeld-Sevigny M, Beckmann JS, Bonny C, Bosse R, Roduit R. Homogeneous and nonradioactive

high throughput screening platform for the characterization of kinase inhibitors in cell lysates. J Biomol Screen. 2006;11(8):1015–26.
84. Beaudet L, Bedard J, Breton B, Mercuri RJ, Budarf ML. Homogeneous assays for single-nucleotide polymorphism typing using AlphaScreen. Genome Res. 2001;11(4):600–8.
85. Chang H, Gao W, Zhang JY, Xiang ZG, Wei Q. Application of photoexcited chemiluminescence immunoassay in the detection of Sendai virus. Chin J Comparat Med. 2015;25 (05):58–61.
86. Wu Z, Zong Y, Li CX, Chen WL, Xu KX. Study on the detection method of aflatoxin based on photochemical chemiluminescence homogeneous immunoassay. Opt Tech. 2019;45 (01):117–23.
87. Han WM. Application evaluation of LiCA photoexcited chemiluminescence detector. Guide Chin Med. 2011;9(30):40–1.
88. Zhang Y, Huang B, Zhang J, Wang K, Jin J. Development of a homogeneous immunoassay based on the AlphaLISA method for the detection of chloramphenicol in milk, honey and eggs. J Sci Food Agric. 2012;92(9):1944–7.
89. Ren J, Liu SL, Li HQ. Establishment and performance evaluation of serum prolactin photoexcited chemiluminescence method. J Clin Lab Med. 2019;37(07):495–8.
90. Yan L, Zhao XH, Xu Y. Research progress in homogeneous photochemiluminescence immunoassay technology. Life Sci. 2016;28(09):1083–8.
91. Roda A, Pasini P, Guardigli M, Baraldini M, Musiani M, Mirasoli M. Bio-and chemiluminescence in bioanalysis. Anal Chem. 2000;366:752–9.
92. Soper SA, Warner IM, McGown LB. Molecular fluorescence, phosphorescence, and chemiluminescence spectrometry. Anal Chem. 1998;70(12):477R.
93. Gerardi RD, Barnett NW, Lewis SW. Analytical applications of tris(2,2′-bipyridyl)ruthenium (III) as a chemiluminescent reagent. Anal Chim Acta. 1999;378(1-3):1–41.
94. Roda A, Pasini P, Baraldini M, Musiaani M, Gentilomi G, Robert C. Chemiluminescent imaging of enzyme-labeled probes using an optical microscope-videocamera luminograph. Anal Biochem. 1998;257:53.
95. Zheng LC, Liu XH, Zhou M, Ma YJ, Wu GF, Lu XQ. Ultrasensitive determination of DNA sequences by flow injection chemiluminescence using silver ions as labels. Anal Chim Acta. 2014;848:67–73.
96. El-Mahdy AFM, Shibata T, Kabashima T, Kai M. Dendrimer-like polymeric DNAs as chemiluminescence probes for amplified detection of telomere DNA on a solid-phase membrane. Chem Commun. 2014;50(7):859–61.
97. Liu FF, Zhang CS. A novel paper-based microfluidic enhanced chemiluminescence biosensor for facile, reliable and highly-sensitive gene detection of *Listeria monocytogenes*. Sensors Actuators B Chem. 2015;209:399–406.
98. Li WY, Zhang QF, Zhou HP, Chen J, Li YX, Zhang CY, Yu C. Chemiluminescence detection of a protein through the aptamer-controlled catalysis of a porphyrin probe. Anal Chem. 2015a;87(16):8336–41.
99. Li XT, Zhang LC, Zhao SL. Determination of hemoglobin content in human red blood cells based on microfluidic chip electrophoresis chemiluminescence. J Anal Test. 2015b;34 (03):308–13.
100. Zhang ZJ, Bai MQ, Zhang XR. Chemiluminescence enzyme immunoasay with coupling reaction I. Determination of HRP and labeled HRP by chemiluminescence analysis. Acta Chim Sin. 1991;04:389–93.
101. Jiang J, Zhao SL, Huang Y, Qin GX, Ye FG. Highly sensitive immunoassay of carcinoembryonic antigen by capillary electrophoresis with gold nanoparticles amplified chemiluminescence detection. J Chromatogr A. 2013;1282:161–6.
102. Yuan DQ, Shu YL, Zhang HL. A chemiluminescence glucose sensor based on GOD immobilized by Sol-Gel. Fujian Anal Test. 2000;01:1169–72.
103. Liu M, Wang ZY, Zhang CY. Recent advance in chemiluminescence assay and its biochemical applications. Chin J Anal Chem. 2016a;12:1934.

104. Liu M, Liu R, Wang D, Liu CL, Zhang CS. A low-cost, ultraflexible cloth-based microfluidic device for wireless electrochemiluminescence application. Lab Chip. 2016b;16(15):2860–70.
105. Liu R, Zhang P, Li HJ, Zhang CS. Lab-on-cloth integrated with gravity/capillary flow chemiluminescence (GCF-CL): towards simple, inexpensive, portable, flow system for measuring trivalent chromium in water. Sensors Actuat B Chem. 2016c;236:35–43.
106. Lian N, Zhao HC, Sun CY, Chen SL, Lu Y, Jin LP. A study on terbium sensitized chemiluminescence of ciprofloxacin and its application. Microchem J. 2003;74(3):223–30.
107. Nalewajko E, Ramirez RB, Kojlo A. Determination of dopamine by flow-injection analysis coupled with luminol-hexacyanoferrate(III) chemiluminescence detection. J Pharm Biomed Anal. 2004;36(1):219–23.
108. Li WH, Zhang ZJ. FI-determination of mercury by flow injection coupled chemiluminesence reaction. Phys Test Chem Anal B Chem Anal. 1999;10:457–62.
109. Gao Q. Uric acid-hexacyanoferrate (III)-luminol chemiluminescence system for the determination of trace nitrite. Chin J Anal Chem. 2002;07:812–4.
110. Yue ZG, Zhan G, Wei W, Lv PP, Yue H, Wang LY, Su ZG, Ma GH. Surface charge affects cellular uptake and intracellular trafficking of chitosan-based nanoparticles. Biomacromolecules. 2011;12(7):2440–6.
111. Zhu CQ, Wang L, Li YX. Determination of trace copper(II) by catalytic kinetic spectrophotometry. Anal Lab. 1999;18(6):31–3.
112. Zhu ZJ, He SM. Quenching-chemiluminescence determination of europium with luminol. Phys Test Chem Anal B Che Anal. 1999;12:538–9.
113. Safavi A, Baezzat MR. Chemiluminescence flow injection determination of copper (II). Anal Lett. 2000;33(4):667–75.
114. Zhou YK, Zhu YF, Bai ZW, Sun YL. Study on the determination of nitric oxide using luminol-H_2O_2 chemiluminescent method. J Anal Sci. 1999;6:476–9.
115. Zheng XW, Yang M, Zhang ZJ. Flow injection chemiluminescence determination of hydrogen peroxide with in-situ electrogenerated Br_2 as the oxidant. Anal Lett. 2008;32(15):3013–28.
116. He YH, Wan ZY. Study on chemiluminescence reaction of potassium permanganate-formaldehyde-Γ system. Anal Lab. 2001;01:70–2.
117. Zheng XW, Zhang ZJ. Flow-injection chemiluminescence detecting sulfite with in situ electrogenerated Mn^{3+} as the oxidant. Sensors Actuat B Chem. 2002;84(2-3):142–7.
118. Hu LL, Xu YJ, Luo XH, Peng J, Wang XJ, Jia LT, Yang PF. The reference range of thyroid hormones levels in normal pregnant women in Henan Province. Chin J Clin Res. 2014;27 (04):388–90.
119. Liu CC, Wen ML. Biochips. Anal Instrum. 2001;03:37–9.
120. Shi R, Sun K, Wang XR, Chen WD. Application of biochip in disease diagnosis. J Anim Husband Veterin Med. 2005;03:23–4.
121. Ye MY, Yin XF, Fang YL. Processing of microfluidic chip silicon positive mold. Microfabric Technol. 2004;03:59–64.
122. Dai ZP, Liu X, Lin BC. A glass/quartz microfluidic chip and its sealing method. China. 200510046834.7. 2007.
123. Zhou XM, Dai ZP, Luo Y. Hydrophilic polymethyl methacrylate microfluidic chip material, chip and preparation method thereof. China. 200310105076.2. 2005.
124. Duffy DC, McDonald JC, Schueller OJA, Whitesides GM. Rapid prototyping of microfluidic systems in poly(dimethylsiloxane). Anal Chem. 1998;47:4974–84.
125. Chen L, Zhang CS, Xing D. Paper-based bipolar electrode-electrochemiluminescence (BPE-ECL) device with battery energy supply and smartphone read-out: a handheld ECL system for biochemical analysis at the point-of-care level. Sensors Actuat B Chem. 2016;237:308–17.
126. Liu R, Liu CL, Li HJ, Liu M, Wang D, Zhang CS. Bipolar electrochemiluminescence on thread: a new class of electroanalytical sensors. Biosens Bioelectron. 2017;94:335–43.
127. Zheng XL, Yan JW, Hu N, Yang J, Yang J. Research progress in materials and processing methods of microfluidic chips. Sensors Microsyst. 2011;30(06):1–4. 7.

128. Roberts MA, Rossier JS, Bercier P, Girault H. UV laser machined polymer substrates for the development of microdiagnostic systems. Anal Chem. 1997;69:2035–42.
129. Martynova L, Locascio LE, Gaitan M, Kramer GW, Christensen RG, MacCrehan WA. Fabrication of plastic microfluid channels by imprinting methods. Anal Chem. 1997;69:4783–9.
130. Li X, Tian JF, Nguyen T, Shen W. Paper-based microfluidic devices by plasma treatment. Anal Chem. 2008;80:9131–4.
131. Martinez AW, Phillips ST, Wiley BJ, Gupta M, Whitesides GM. FLASH:A rapid method for prototyping paper-based microfluidic devices. Lab Chip. 2008;8:2146–50.
132. Lu Y, Shi WW, Jiang L, Qin JH, Lin BC. Rapid prototyping of paper-based microfluidics with wax for low-cost, portable bioassay. Electrophoresis. 2009;30:1497–500.
133. Guan WR, Zhang CS, Liu FF, Liu M. Chemiluminescence detection for microfluidic cloth-based analytical devices (μCADs). Biosens Bioelectron. 2015;72:114–20.
134. Li HJ, Liu CL, Wang D, Zhang CS. Chemiluminescence cloth-based glucose test sensors (CCGTSs): a new class of chemiluminescence glucose sensors. Biosens Bioelectron. 2017;91:268–75.
135. Kunze A, Dilcher M, Abd El Wahed A, Hufert F, Niessner R, Seidel M. On-chip isothermal nucleic acid amplification on flow-based chemiluminescence microarray analysis platform for the detection of viruses and bacteria. Anal Chem. 2016;88(1):898–905.
136. Zong C, Wu J, Xu J, Ju HX, Yan F. Multi layer hemin/G-quadruplex wrapped gold nanoparticles as tag for ultrasensitive multiplex immunoassay by chemiluminescence imaging. Biosens Bioelectron. 2013;43:372–8.
137. Xiao Q, Wu J, Dang PY, Ju HX. Multiplexed chemiluminescence imaging assay of protein biomarkers using DNA microarray with proximity binding-induced hybridization chain reaction amplification. Anal Chim Acta. 2018;1032:130–7.
138. Chen WQ, Huang NT, Oh B II, Timothy T, Shanley TP, Kurabayashi K, Fu JP. Surface-micromachined microfiltration membranes for efficient isolation and functional immunophenotyping of subpopulations of immune cells. Adv Healthcare Mater. 2013;2 (7):965–75.
139. Qiu XB, Yang S, Wu D, Wang D, Qiao S, Ge SX, Xia NS, Yu DL, Qian SZ. Rapid enumeration of CD4+T lymphocytes using an integrated microfluidic system based on Chemiluminescence image detection at point-of-care testing. Biomed Microdevices. 2018;20(1):15.
140. Shi M, Huang Y, Zhao JJ, Li ST, Liu RJ, Zhao SL. Quantification of glutathione in single cells from rat liver by microchip electrophoresis with chemiluminescence detection. Talanta. 2018;179:466–71.
141. Popa ID, Schiriac EC, Cuciureanu R. Multi-analytic detection of antibiotic residues in honey using a multiplexing biochip assay. Rev Med Chir Soc Med Nat Iasi. 2012;116(1):324–9.
142. Wu J, Wang X, Lin YT, Zheng YZ, Lin JM. Peroxynitrous-acid-induced chemiluminescence detection of nitrite based on Microfluidic chip. Talanta. 2016;154:73–9.
143. Zong C, Zhang DD, Yang H, Wang SM, Chu M, Li P. Chemiluminescence immunoassay for cardiac troponin T by using silver nanoparticles functionalized with hemin/G-quadruplex DNAzyme on a glass chip array. Microchim Acta. 2017;184(9):3197–204.
144. Lin CC, Sun DS, Lin YL, Tsai TT, Cheng C, Sun WH, Ko FH. A flexible and miniaturized hair dye based photodetector via chemiluminescence pathway. Biosens Bioelectron. 2017;90:349–55.
145. Zeng Z, Zhang KD, Wang W, Xu WJ, Zhou J. Portable electrowetting digital microfluidics analysis platform for chemiluminescence sensing. IEEE Sensors J. 2016;16(11):4531–6.
146. Zhang Y, Ge SG, Yu JH. Chemical and biochemical analysis on lab-on-a-chip devices fabricated using three-dimensional printing. Trends Anal Chem. 2016;85:166–80.
147. He YY, Xu SJ, Deng M, Yang DQ, Chen FN. Determination of propyl gallate in edible oil by high-performance liquid chromatography with chemiluminescence detection. Instrum Sci Technol. 2017;45(4):404–11.

148. Hu BF, Li JJ, Mou L, Liu Y, Deng JQ, Qian W, Sun JS, Cha RT, Jiang XY. An automated and portable microfluidic chemiluminescence immunoassay for quantitative detection of biomarkers. Lab Chip. 2017;17(13):2225–34.
149. Aboul-Enein HY, Stefan RI, Staden JF, Zhang XR, Garcia-Campana AM, Baeyens WRG. Recent developments and applications of chemiluminescence sensors. Crit Rev Anal Chem. 2000;30(4):271–89.
150. Allen RC, Stjernholm RL, Steele RH. Evidence for the generation of electronic excitation state (s) in human polymorphonuclear leukocytes and its participation in bactericidal activity. Biochem Biophys Res Commun. 1972;47(2):679.
151. Guo RM, Shao ZJ, Sun YN, Han M. In emergency department chest pain in patients with acute inflammation index and immediate admission hs-cTN I correlation analysis. J Clin Emerg Call. 2019;20(01):45–51.
152. Nakamura MM, Coichev N, Lin JM, Yamada M. Flow-injection investigation of the chemiluminescent reaction of bis(2,4,6-(trichlorophenyl)oxalate) with free chlorine. Anal Chim Acta. 2003;484(1):101–9.
153. Zhang RX, Lin HL, Tan YG. Comparative analysis of clinical results of different chemiluminescence methods for detection of serum c-peptide. J China Jpn Friend Hosp. 2010;24 (04):236–8.
154. Horan TD, Dennis E, Mcpherson TA. Association of neutrophil chemiluminescence with microbicidal activity. Clin Immunol Immunopathol. 1982;22(2):259.
155. Chen D, Niu X, Liu Y. Value of PCT il-1 and NLCR combined detection for early differential diagnosis of pathogenic bacteria in patients with bloodstream infection. Hebei Med. 2019;02:226–9.
156. Saeed DF, Wilson MJ, Tyagi MA. Neutrophil LymphocyteCount Raitio (NLCR) in predicting the histological grade of paediatric CNS tumours. Neuro-Oncology. 2017;19:10–5.
157. Cui F, Ren YS, Chen TR. Effects of he-ne laser irradiation on chemiluminescence and C-3b receptor in mouse spleen macrophages. Chin J Phys Ther. 1999;03:38–9.
158. Zhang WH. Design and synthesis of new chemiluminescence/fluorescent probe and its application in detection of bioactive species. Shandong Normal University; 2013.
159. Zhang WY, Wei JY, Guo J, Chen GQ. Chemiluminescence immunoassay of erythrocyte labeled antibody. Acta Chem Sin. 2006;08:1435–8.
160. Wrogemann K, Weidemann M, Peskar B. Chemiluminescence and immune cell activation I. Early activation of rat thymocytes can be monitored by chemiluminescence measurements. Eur J Immunol. 1978;8(10):749–52.
161. Mookerjee BK, Wakerle H, Sharon N, Fischer H. Chemiluminescence and lymphocyte proliferation: parallelism in collaboration between subpopulations of thymus cells for both types of responses. J Leukoc Biol. 1984;35:427–38.
162. Arnold MA, Rechnitz GA. Tissue-based membrane electrode with high biocatalytic activity for measurement of adenosine 5′-monophosphate. Anal Chem. 1981;131:91–6.
163. Arnold MA, Rechnitz GA. Comparison of bacterial, mitochondrial, tissue, and enzyme biocatalysts for glutamine selective-membrane electrodes. Anal Chem. 1980;52:1170–4.
164. Huang YM. Chemiluminescent plant tissue sensors determine ethanol. In: The eighth national luminescence analysis and kinetic analysis conference; 2005.
165. Peng Y. Flow injection chemiluminescent plant tissue sensor for determination of oxalate. J Adv Biochem. 2001;22(2):215–7.
166. Palmer JP, Fleming GA, Greenbaum CJ, Herold KC, Jansa LD, Kolb H, Lachin JM, Polonsky KS, Pozzilli P, Skyler JS, Steffes MW. C-peptide is the appropriate outcome measure for type I diabetes clinical trials to preserve b-cell function: report of an ADA workshop. Diabetes. 2004;53:250–64.
167. Wang DQ. Development status and prospect of radioimmunoassay. Mark Immunoass Clin. 2012;19(04):249–51.
168. Hao FY, Wang CY. Progress and automation of enzyme immunoassay. Chin J Misdiagn. 2007;1:23–6.

Chapter 7
Luminescent Conjugated Polymer Dots for Biomedical Applications

Guo Li, Tianshe Yang, Weiwei Zhao, Shujuan Liu, Wei Huang, and Qiang Zhao

Abstract Luminescent conjugated polymer dots (CP-dots) have achieved significant progress in biomedical fields due to their excellent properties, such as excellent photophysical properties, good biocompatibility, tunable optical properties, and easy surface functionalization. In this chapter, recent advances on luminescent CP-dots for biomedical applications have been summarized, including their design strategy, preparation method, chemical structure, optical property, functionalization strategy, and biological applications. Importantly, their applications in biosensing, bioimaging, and disease therapy have been highlighted. Finally, the challenges and perspectives existing in the future development of luminescent CP-dots are also discussed.

Keywords Luminescent conjugated polymer dots · Biological detection · Biosensing · Bioimaging · Disease therapy

7.1 Introduction

Nanomaterials, as a class of important functional materials with one or more dimensions at the nanometer sizes of 0.1–100 nm, have attracted growing research interest in recent years. In comparison with their bulk counterparts [1–3], the nanoscale materials possess unique size-dependent optical and electronic properties [4, 5], due to their quantum size effect [6], surface effect [7], and macroscopic quantum tunneling effect [8], etc. These superior properties have endowed them potential applications in various fields including catalysis [9], chemical sensors [10],

G. Li · T. Yang · W. Zhao · S. Liu · W. Huang · Q. Zhao (✉)
Key Laboratory for Organic Electronics and Information Displays and Jiangsu Key Laboratory for Biosensors, Institute of Advanced Materials (IAM), Nanjing University of Posts and Telecommunications (NUPT), Nanjing, Jiangsu, P. R. China
e-mail: iamqzhao@njupt.edu.cn

X. Zhao, M. Lu (eds.), *Nanophotonics in Biomedical Engineering*,
https://doi.org/10.1007/978-981-15-6137-5_7

bioimaging [11], nonlinear optics [12], information storage [13], etc. In particular, luminescent nanomaterials have been widely studied since the beginning of research in nanomaterials. Recently, significant advances have been achieved for luminescent nanomaterials in the biomedical applications. There are mainly two types of luminescent nanomaterials, namely inorganic nanomaterials and organic nanomaterials, which are named after their compositions. Inorganic luminescent nanomaterials, including noble metal nanoclusters [14], carbon- or silicon-based nanomaterials [15, 16], and rare-earth-based nanophosphors [17], have been widely used in biomedical fields. Organic luminescent nanomaterials, especially those based on luminescent conjugated polymers (CPs) with π-delocalized backbones and fast electron transfer, have also enabled them wide applications in various biomedical fields, such as imaging, sensor, diagnosis, phototherapy, and photo-triggered drug delivery or release [18–21].

CPs, which are with the unique characteristics of delocalized electronic structures and organic π-conjugated backbones, show efficient coupling interactions among various optoelectronic segments [18, 20, 21]. Excitons can be effectively migrated to lower-energy electron/energy acceptor sites over long distances to quench the luminescence of CPs or to achieve the signal amplification of acceptors [18, 22–24]. Luminescent CP-dots have been widely applied in biomedical fields due to their unique properties, including excellent photophysical properties, good biocompatibility, tunable optical properties, and easy surface functionalization [18, 21]. These works focused on highly sensitive detection of disease-related biomarkers and diagnosis of pathogenic microorganisms [19]. Beyond sensing, optical imaging based on CP-dots, including near-infrared (NIR) luminescence imaging, time-resolved luminescence imaging (TRLI), and photoacoustic imaging (PAI) have also been successfully reported [25–28]. In addition, these nanomaterials have been applied in phototherapy, including photodynamic therapy (PDT) and photothermal therapy (PTT) [19, 28]. Moreover, anticancer therapy, gene delivery, multimodal therapy, drug delivery, and release are also included [19].

In this chapter, we summarize recent advances in luminescent CP-dots for biomedical applications, including their design strategy, preparation method, chemical structure, optical property, functionalization strategy, and biological applications. Especially, their applications in biosensing, bioimaging, and disease therapy have been highlighted. Finally, the challenges and perspectives existing in the future development of luminescent CP-dots are also discussed.

7.2 Advantages of Conjugated Polymer Dots for Biomedical Applications

CP-dots have been widely applied in the biomedical fields due to their unique properties, such as high brightness, superior photostability, excellent biocompatibility, tunable spectral property, and versatile surface modification. [18, 19]. Firstly, the

backbone structures of CP-dots can be properly regulated by introducing various components into the backbones and modifying the pendant chains with diverse recognition elements. Secondly, the fundamental photophysical property of CP-dots is easy to be tuned by changing their backbone structures. Thirdly, CP-dots can also offer stable hydrophobic backbones for the encapsulation and delivery of drugs, which can be monitored by the optical property of CP-dots. They also have the ability to be used as effective, protective, self-tracking, and stable carriers to transfer genes with decreased cytotoxicity in comparison with available transfection commercial reagents and no immune reaction compared to viral carriers [19, 29]. In addition, multifunctional CP-dots can be acquired through modifying various functional groups in order to achieve the integration of both detection and therapy [29].

7.3 Design, Synthesis, and Functionalization of Conjugated Polymer Dots

7.3.1 Structure and Category of CPs

The design strategies for CPs focus on two main components, i.e., π-conjugated backbones and side chains, which constitute the major structures of the CPs. Firstly, the π-conjugated backbones have significant influence on the fundamental photophysical properties of CPs, such as the energy levels, charge transport properties, and luminescence quantum yields. The charged side chains, including carboxyl, sulfonic, phosphate groups and cationic quaternary ammonium groups, endow CPs the improved dispersibility in aqueous solution. Although numerous CPs have been developed during the past few decades, the basic backbone structures show no significant changes. According to the types of basic backbone structures, CPs can be divided into several categories, including poly(fluorene) (PF), poly(*p*-phenyleneethynylene) (PPE), poly(fluorene-co-phenylene) (PFP), poly(thiophene) (PT), poly(*p*-phenylenevinylene) (PPV), and their derivatives. The conventionally reported typical reactions for the preparations of CPs are shown in Scheme 7.1. All these backbones can be synthesized by classic organic reactions, such as Heck coupling reaction [30], Sonogashira coupling reaction [31], Suzuki coupling reaction [32], Wessling reaction [33], and $FeCl_3$ oxidative polymerization [34].

7.3.2 Preparation of CP-Dots

In general, three typical methods are employed to prepare CP-dots, including miniemulsion, nanoprecipitation, and self-assembly methods (Scheme 7.2).

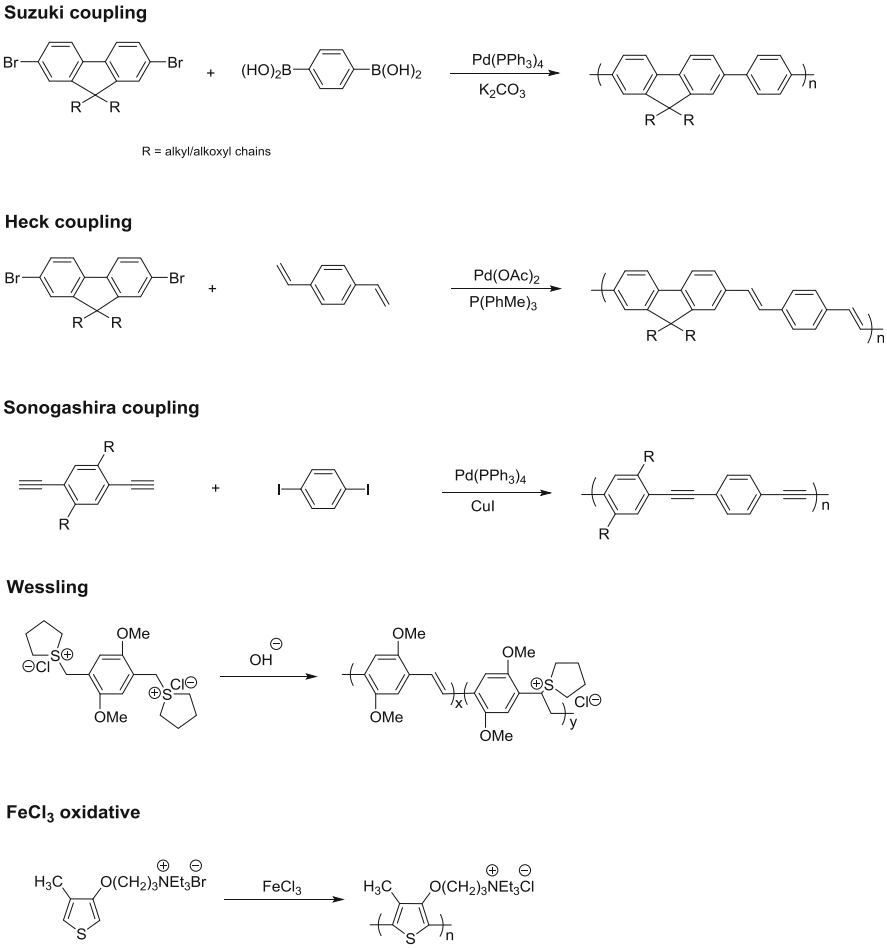

Scheme 7.1 Typical polymerization methods for the preparation of CPs

7.3.2.1 Nanoprecipitation Method

In the nanoprecipitation approach, CPs are firstly dissolved in miscible solvents, such as acetonitrile and tetrahydrofuran (THF). Then, the as-prepared organic solution is quickly injected into a large amount of excess water under ultrasonication. The aggregation of CPs leads to the formation of CP-dots due to the improved hydrophobic interaction. Water-dispersible CP-dots can be obtained through removing the organic solvents by evaporation. Many reports have indicated that the particle diameters are highly determined by the starting CPs concentrations in organic solvent [35, 36]. As the concentration increases, the diameters of the CPs-dots become larger. In addition, the mixture of a polymer acceptor and a polymer donor is another route to prepare CP-dots with small sizes. Chiu et al.

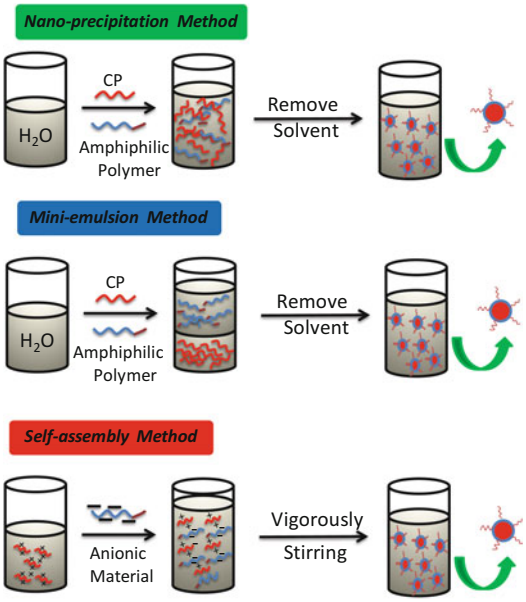

Scheme 7.2 Schematic representation of three preparation methods of CP-dots

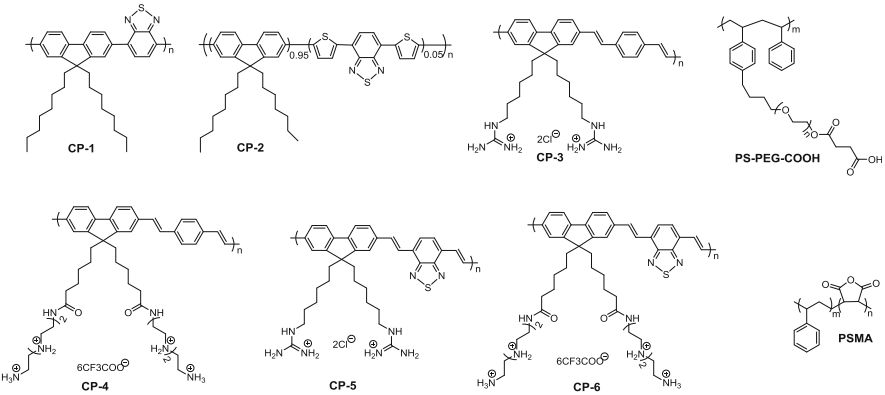

Scheme 7.3 Chemical structures of **CP-1**, **CP-2**, **CP-3**, **CP-4**, **CP-5**, **CP-6**, PS-PEG-COOH, and PSMA

adopted amphiphilic poly(styrene-co-maleic anhydride) (PSMA) (Scheme 7.3) as carbonyl donors, **CP-1** or **CP-2** (Scheme 7.3) as polymer acceptor, and polymer matrices poly(styrene-g-ethylene oxide) (PS-PEG-COOH) (Scheme 7.3) as nano-encapsulated reagents to fabricate CP-dots through nanoprecipitation methods [37]. Dynamic light scattering measurement revealed that the acquired CP-dots exhibited an average diameter of ~15 nm in aqueous solution.

7.3.2.2 Miniemulsion Method

In the miniemulsion approach, CPs or prepolymerized monomers are firstly dispersed in a nonpolar solvent. Then, the obtained solution is transferred into an aqueous solution containing surfactants to prevent the unwelcome coalescence of emulsion droplets. Under ultrasonication, the organic solution is mixed with the aqueous solution to further form a stable miniemulsion. After removing the organic solvents via evaporation, a stable dispersion of CP-dots can be obtained in aqueous solution. Employing the method, Mecking et al. synthesized poly-(arylene diethynylene) CP-dots through a step-by-step polymerization of the monomers under Glaser coupling condition [38]. By covalently bonding fluorene and perylene dyes, the CP-dots with tunable emission colors can be obtained by controlling intramolecular energy transfer. In comparison with CPs in a good solution, the absorption spectra of CP-dots exhibited blue-shift through the nanoprecipitation and miniemulsion methods, which was ascribed to the reduced conjugation length and constrictively collapsed and unordered conformation [39].

7.3.2.3 Self-Assembly Method

In the self-assembly method, the oppositely charged CPs and co-assembling reagents are, respectively, dissolved in water. Then, the as-obtained dispersions are mixed together at a specific ratio under stirring. Finally, the functionalized CP-dots are precipitated through a high-speed centrifugation. For example, Wang et al. synthesized multifunctional CP-dots through the interaction of cationic CPs and anionic functional molecules (Scheme 7.4). The antibacterial CP-dots were fabricated through electrostatic interactions between a cationic porphyrin (TPPN, Scheme 7.4) and a water-dispersible polythiophene (**CP-9**, Scheme 7.4) [40]. To enhance the antitumor performance of CP-dots, they developed a self-assembly method by an integration of anionic chlorambucil and cationic pentathiophene (5T) (Scheme 7.4) [41]. In addition, Wang et al. synthesized bifunctional CP-dots for applications in imaging and drug delivery through assembling cationic **CP-7** and poly(L-glutamic acid) modified antitumor drug doxorubicin (PG-Dox) (Scheme 7.4). They have developed and demonstrated multifunctional CP-dots through applying electrostatic interaction between the positive **CP-8** and the negative disodium salt 3,3′-dithiodipropionic acid (SDPA) (Scheme 7.4) [42].

7.3.3 Functionalization of CP-Dots

In order to achieve the desirable application of CP-dots in biomedical field, a variety of multifunctional CPs have been synthesized and the corresponding functional strategies have been explored. In 1986, Lowe et al. firstly utilized CPs as an

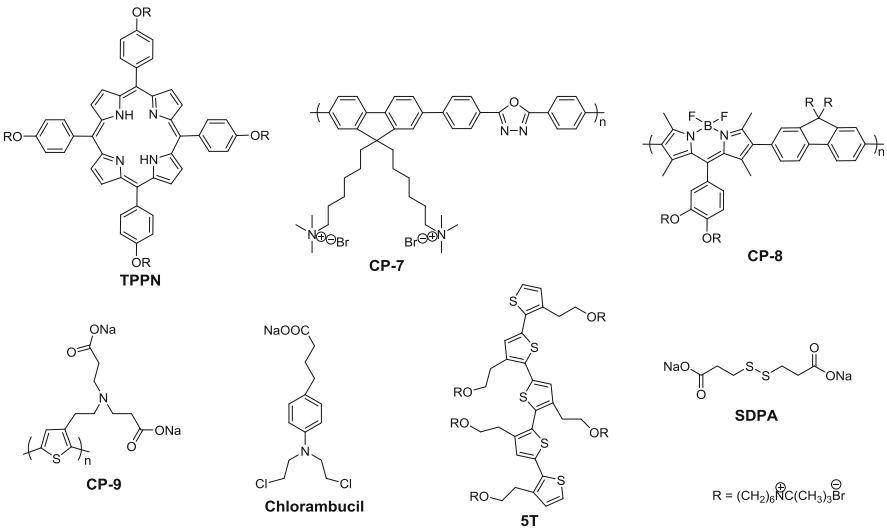

Scheme 7.4 Chemical structures of TPPN, **CP-7**, **CP-8**, **CP-9**, chlorambucil, 5T, and SDPA

enzymatic responsive sensor [43]. After that, various functionalization strategies of CPs have been provided for biomedical applications. Herein, two versatile strategies are introduced.

7.3.3.1 Functionalization on CPs Backbone

In the first strategy, highly efficient Förster resonance energy transfer (FRET) pairs, intramolecular donor–acceptor units and the extended π conjugated monomers can be introduced into the backbone, which can greatly change the photophysical property of the polymer and provide effective method for achieving excellent CP-dots. In addition, the specific functional groups, such as amino groups, alkoxyl chains, carboxyl groups, and targeted moiety, can also be introduced into the backbones of CPs (Scheme 7.5). To achieve functionalization of CP-dots, the monomers are covalently attached to functional groups followed by polymerization to acquire various functionalized CP-dots. To achieve the desired functionality, energy acceptor or targeted group have been introduced into CPs backbones. Through modifying the side chains, Wang et al. developed various emissive CP-dots (**CP-3**, **CP-4**, **CP-5,** and **CP-6**) (Scheme 7.3) through a nanoprecipitation method. From the point of structure, **CP-5** and **CP-6** have the same hydrophobic basic framework but various pendant chains. The absorption and emission spectra of **CP-4** and **CP-6** showed more red-shift than those of **CP-3** and **CP-5** for the reasons that the inter-chain aggregated and energy transfer of CPs happened among the backbones [44].

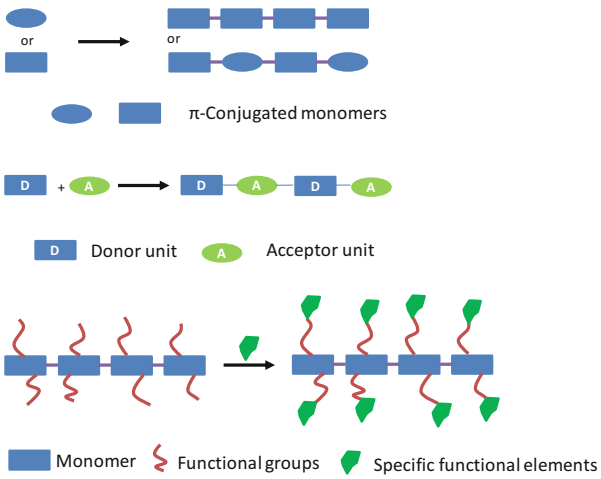

Scheme 7.5 The modes and functionalization on CPs backbone

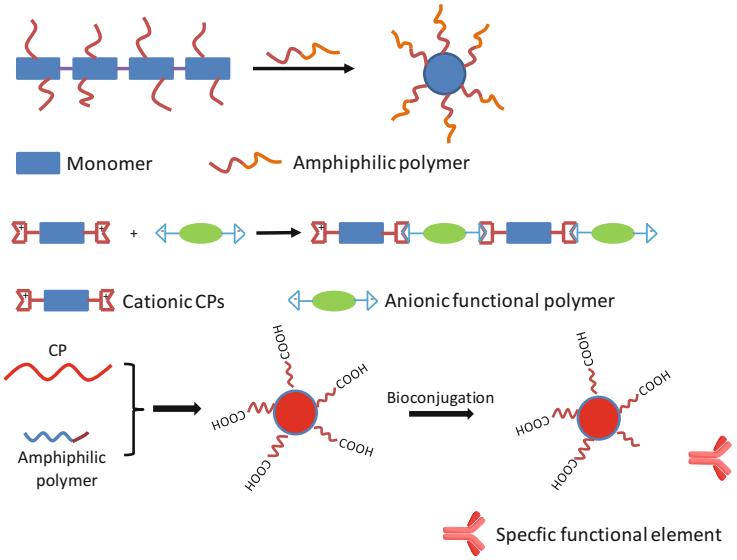

Scheme 7.6 The modes and functionalization of CPs by self-assembly

7.3.3.2 Self-Assembly

In the self-assembly strategy, CPs themselves are functionalized through embedding recognition groups based on electrostatic or hydrophobic interactions (Scheme 7.6). Wang et al. synthesized multifunctional CP-dots through the self-assembly of cationic CPs and anionic functional molecules (Scheme 7.5). The functionalized

CP-dots were synthesized through electrostatic interactions between a water-dispersible cationic porphyrin (TPPN, Scheme 7.4) and anionic polythiophene (**CP-9**) (Scheme 7.4) [40]. They have synthesized four CPs with red, yellow, green, and blue emissions, and applied them as carboxyl functionalized CP-dots by a nanoprecipitation approach based on hydrophobic interactions between the CPs and poly(styrene-co-maleicanhydride) (PSMA) [25]. Another strategy is surface functionalization, which serves as an extension of the second method. The surface carboxyl or amino groups are firstly generated on the CP-dots using an amphiphilic polymer. Then, the functional elements (sugar protein) are grafted to the specific surface functional groups (-NH_2 or -COOH) by condensation reaction (Scheme 7.6). Based on the surface bioconjugation approach, Chiu et al. developed a universal strategy to prepare CP-dots and demonstrated their application in specific cellular targeting and biorthogonal labeling [37].

7.4 Biological Detection

Luminescent CP-dots are an important class of sensing materials for biological detection, which possess characteristic features of signal amplification and distinctive light-harvesting ability [18, 22]. Compared with the sensing materials based on small molecules, luminescent CP-dots show outstanding advantages of wide detection range, high sensitivity, and tunable spectral response characteristics [18, 21]. To date, a great number of CP-dots-based luminescent sensing materials used in biological detection adopt the typical fluorescence quenching response by electron-deficient analyte systems and photo-triggered electron transfer mechanism [19, 20].

The energy transfer inside the CP-dots or intra-particle energy transfer of CP-dots from the polymer donor to the dye acceptor can be influenced by the compact stacking structure and high content of fluorescence polymers. The efficient energy transfer can enhance the fluorescence brightness, adjust the emission color, and improve the photostability [29, 45–48, 51–53]. These advantages endow them important applications in sensing of analytes or external environment.

7.4.1 Ion Detection

Ion detection plays an important role in the biomedical field. Many conventional fluorescent probes show turn off response through using the CPs emission quenching via electro-deficient analytes by photoinduced electron transfer (PET) mechanism [21, 29]. However, a turn-on fluorescent response of probes upon interacting with analytes is more desirable from the point of practical. In the case, the fluorescence of CPs-dots firstly decreases with the reversible coordination interaction between a quenching analyte and the organic π-conjugated polymer backbone. And then, a balance of the analyte-quencher complex is established.

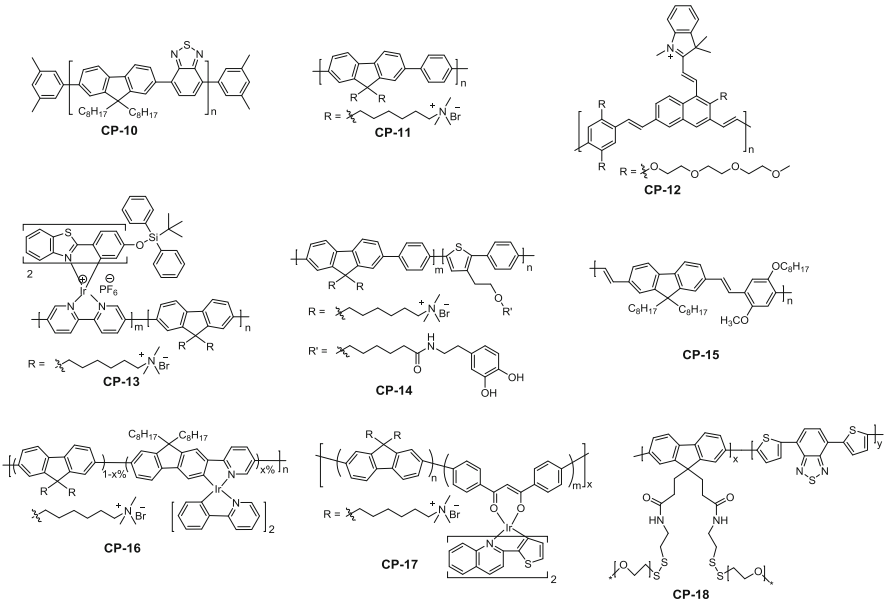

Scheme 7.7 Conjugated polymers (**CP-10 ~ CP-18**) for biological detection

Finally, the emission of CP-dots recovers by a selective linkage of a target analyte with the quenching unit, which changes the balance toward the analyte-quencher complex [18, 21]. Moreover, a large number of nonfluorescent CP-dots are used as fluorescent probes for ion detection. They can display fluorescence nature after interacting with different analytes. Herein, the fluorescent detection of CP-dots for mercury (Hg^{2+}), calmodulin (CaM), hydrosulfide anions (HS^{-}) and fluoride (F^{-}) as examples are highlighted.

Mercury is a global pollutant in living organisms and environment due to its extreme toxicity. Fluorescence detection of Hg^{2+} ions has become an important route to quantifying Hg^{2+} concentration through the changes of the fluorescence intensity of the probes [21]. CP-dots have been reported as important fluorescent probes with low detection limit, wide detection range and quantitative analysis, especially for ultra-low Hg^{2+} concentration. Harbron et al. synthesized fluorescent CP-dots through doping nonfluorescent rhodamine derivatives in **CP-10** (Scheme 7.7) and used them for the detection of Hg^{2+} ions [45]. The as-prepared CP-dots emitted green-yellow fluorescence when the rhodamine derivatives on the nanoparticle surface contact Hg^{2+} and then started to show orange-red fluorescence via FRET from the CP-dots to the rhodamine dyes. This signal amplification endowed the CP-dots to be responsive to Hg^{2+} with low concentrations, in particular, in the range of 0.7–10 parts/billion.

CaM can regulate a variety of Ca^{2+}-dependent signal transductions and mediate activities of many proteins [46]. After Ca^{2+}-binding, the conformation of CaM from the closed form to the open one is observed, transferring to a clavate dumbbell-

shaped biomacromolecule. Accurate detection of CaM is essential for cellular activities, such as motility, secretion, and cell division. Wang et al. developed a hybrid CP-dots based on **CP-11** (Scheme 7.7) and graphene oxide (GO) for the detection of Ca^{2+}-triggered conformation changes of CaM by FRET mechanism [47]. In this hybrid system, the CaM was able to label the green fluorescent protein (EGFP). Upon Ca^{2+}-coordination, the conformation of CaM changed from the closed form to the open one. The excellent recyclable change towards the concentrations of Ca^{2+} between 0 and 1.0×10^{-3} M suggested that the assembly of EGFP-CaM with GO could be controlled by Ca^{2+} reversibly and quantitatively. In addition, the transition of CaM is observed through the emission color changing under UV light excitation. This work revealed that hybrid CP-dots system showed excellent potential as diagnostic sensing materials for detecting Ca^{2+}-induced conformation changes in biological process.

Hydrosulfide anion is a key analyte, which attracts considerable attentions to develop various types of sensing materials due to the significance in industrial toxicity, pathology, human physiology, and biomedicine [48]. Fluorescent CP-dots-based sensing platform has the ability to monitor the low concentration of HS^- anions in physiological media [49]. Nesterov et al. developed an effective turn-on amplifying fluorescent sensor based on CP-dots through introducing cyanine (as an analyte-specific unit) into the π-conjugated backbone (including the naphthalene fragment) of **CP-12** (Scheme 7.7) for the detection of HS^- anions [50]. The specific reaction of HS^- and the cyanine unit in CP-dots generated an efficient electronic insulation of the conjugated unit from the naphthalene fragment, thus causing significant enhancement of energy gap at this local site. This higher bandgap site diminished exciton migration length and caused the improved sensing performance of about tenfold higher detection sensitivity and a wide analyte detection region from nanomolar to millimolar. The signal amplification strategy can be further applied for designing a large number of other fluorescent sensing materials.

Fluorine ion is closely related to environmental and human dental health concerns [51]. It is of considerable interest to develop a novel probe that can accurately, rapidly, sensitively, and selectively detect F^- ions in water and biomolecular process [51]. Zhao et al. developed ratiometric luminescence and lifetime probes based on CP-dots for the detection of F^- ions [52]. They introduced *tert*-butyldiphenylsilyl (as a F^--responsive unit) into red phosphorescent iridium(III) complex, which was linked to the main π-conjugated backbone of blue-emitting polyfluorene-based **CP-13** (Scheme 7.7). The fast response between CP-dots and F^- can be achieved within 2 min. The ratios (the fluorescence intensity at 600 nm to that at 400 nm) of the CP-dots showed an excellent linear relation within the F^- level from 5 to 13 μM. The CP-dots detection limit was measured to be 7.0 parts/billion, which was obviously lower than the recommended maximum limit of F^- in practical drinking water.

7.4.2 pH Detection

pH is a key parameter in cellular and tissue homeostasis [53]. Therefore, it is of big significance to develop pH-responsive probe [54]. A turn-on pH sensing CP-dots platform can be achieved through linking a pH-response moiety to a CP. This platform is not involved in an aggregation effect but related to the property of pH-response moiety. The combination of pH-dependent property of pH-response moiety and the signal amplification features of CPs are expected to achieve a quick, acid-responsive, and sensitive pH sensor. For example, Wang et al. have reported a CP-dots-based pH assay probe, in which dopamine was covalently grafted to the side chain of a water-soluble **CP-14** (Scheme 7.7) [55]. The dopamine has various redox states, which can reversibly change between hydroquinone as reduced state and quinone as oxidized state in aqueous solution with the change of pH. At low pH, dopamine in its hydroquinone form shows strong fluorescence due to the missing electron transfer from the CPs backbone to hydroquinone. As pH increasing, the proportion of quinone structure of dopamine increases due to its auto-oxidation, therefore effective electron transfer from the CPs backbone to quinone generates and the emission of the CP-dots is quenched. The significant fluorescent response of CP-dots can be used to detect various pH.

7.4.3 Temperature Detection

Temperature is an important physical parameter in chemical or biological systems, which has significant influences on the equilibrium constants and biochemical reaction kinetics [56]. In general, CPs containing the temperature-sensitive moiety have the ability of temperature determination in cellular and tissue. Chiu et al. developed temperature-sensitive dye-rhodamine B (RhB)-attached CP-dots through a two-step process, in which RhB was first attached to polystyrene polymer (PS-NH_2) for PS-RhB, and then, PS-RhB and **CP-15** (Scheme 7.7) experienced nanoprecipitation process for the preparation of CP-dots [56]. The emission intensity of the as-synthesized CP-dots decreased with increasing temperature. It showed excellent temperature sensitivity (the liner range was 10–60 °C, $R^2 = 0.998$). Moreover, owing to the temperature insensitivity of **CP-15**, the as-prepared CP-dots could be applied in ratiometric temperature sensing under the excitation of a single wavelength (~450 nm) and possessing a linear range ($R^2 = 0.996$) for the temperature sensing, which well matched the physiologically relevant temperatures.

7.4.4 Biomolecule Detection

Accurately, sensitive and selective detection of ultralow levels of unique biomolecules is vital in early clinical diagnoses and therapy of diseases [57]. CP-dots, with a signal fluorophore doping in CPs, have been demonstrated to detect different biomolecules [19]. FRET-based mechanism has been widely used for biomolecule detection. The signal amplification effect of the backbone endows an excellent sensing ability to biomolecule analytes. Based on the typical FRET-based mechanism, one-step FRET process and two-step FRET process are mainly demonstrated. Moreover, two typical interactions, that is, chemical and physical interaction, between CPs and biomolecules, are mainly highlighted.

The one-step FRET process is the direct energy transfer from a single donor to acceptor. In the process, the interactions between CP-dots and analytes are mainly hydrophobic and electrostatic [19, 21]. For example, Huang et al. reported donor–acceptor (polyfluorene as donor and iridium(III) complex as acceptor) architecture **CP-16** (Scheme 7.7), which showed weak FRET responses toward proteins [58]. The hydrophobic interaction between proteins and CP-dots was able to break self-formed CPs aggregates, minimizing the FRET process. The emission ratio of I_{430}/I_{605} of CP-dots showed good relationship in the region of 0–10 μM. The detection limit of the CP-dots was 0.006 μM. Furthermore, they synthesized water-soluble CP-dots containing iridium(III) complexes and polyfluorene and demonstrated their applications in time-resolved luminescent heparin detection [27]. The electrostatic interaction between **CP-17** (Scheme 7.7) and heparin triggers the CP-dots to be more compact, which was beneficial for improving the energy transfer from polyfluorene to iridium(III) complexes. The quantification range for heparin sensing was 0–70 μM in aqueous solution and 0–5 μM in serum, respectively. After addition of heparin, a 90-times maximum enhancement in the fluorescence ratio of I_{632}/I_{430} of CP-dots was achieved.

Chemical interaction is another typical interaction between CP-dots and biomolecular, which have been applied in biomolecule detection [22, 29]. Huang et al. have developed **CP-18** (Scheme 7.7) with side disulfide linking to PEG chains [59]. The high-performance ratiometric probe was used as solubility-fluorescence changes for detecting thiol. A 12 times maximum enhancement in the fluorescence ratio of I_{628}/I_{420} of CP-dots from 0.095 (without thiol) to 1.15 (with thiol) was found. According to the measurement results, the detection limit of the CP-dots was 0.021 mM. Owing to other cleavable-specific linkages can replace the disulfide, this design strategy can be extended as a versatile detection system for other analytes which can cleave the linkages.

Two-step FRET process affords many advantages, such as, higher-efficiency long-range energy transfer and more superior detection sensitivity for acceptor, than that of one-step FRET [60]. It is two parallel one-step energy transfers from a single donor to two different acceptors. Through the unique two-step FRET process, the detection sensitivity of CP-dots for adenosine deaminase (ADA) can be greatly improved. Guo et al. have developed this platform to monitor the enzymatic activity

of ADA [61]. In this system, an aptamer can be able to assemble into adenosine, causing ethidium bromide (EB) non-emissive, which was the final energy acceptor. The **CP-11** (Scheme 7.7) served as the energy donors, which could significantly enhance the emission of EB by a two-step FRET through adenosine transforming into inosine via ADA hydrolysis. At a region from 0 to 16 U/L of ADA, the enhancing ratio was linearly dependent on the level of ADA. The detection limit of ADA was measured to be 0.5 U/L. The ADA reaction time was 25 min, which was much more rapid and facile than that reported in literature [62, 63].

7.4.5 Hypoxia Detection

Hypoxia, defined as oxygen-deprived condition, is a distinct feature of multifarious disease including tumors [64], stroke [65], and retinal disease [66]. Accurate hypoxia detection is not only very important for disease diagnosis, but also can be applied to evaluate therapeutic effects [67]. Phosphorescent transition-metal complexes (PTMCs)-based probes can be applied in fully reversible real-time monitoring of O_2 concentrations in vitro by employing the energy transfer between the triplet excited state of the metal complex and the triplet ground state of O_2 [68]. The CP-dots fabricated by introducing PTMCs into fluorescent CPs possessed the amplified signal output of CPs and the long emission lifetime of PTMCs, which endowed them excellent bio-probes for O_2 sensing.

Platinum(II) porphyrin complexes as an excellent class of O_2 sensor can be covalently attached into CPs backbone, and then the obtained CPs are self-assembled to form CP-dots in aqueous solution for oxygen detection [69]. For example, Zhao et al. developed dual-emissive **CP-19** and **CP-20** (Scheme 7.8) for oxygen detection through combining oxygen-responsive phosphorescent platinum (II) porphyrin into oxygen-insensitive polyfluorene backbone [69, 70]. Oxygen sensing mechanism of CP-dots is shown in Fig. 7.1. When the O_2 level decreased, the blue-emission intensity showed negligible change, while the red-emission intensity remarkably enhanced, revealing the phosphorescence sensitivity of Pt (II) porphyrin to O_2. The quantitative oxygen detection result of the two CPs was demonstrated through a good linearity equation. The K_{sv} values were calculated to be 1.67×10^{-2} $mmHg^{-1}$ for **CP-19** and 1.63×10^{-2} $mmHg^{-1}$ for **CP-20**. The detection limit of the **CP-19** was 0.5 mmHg. Similarly, Papkovsky et al. adopted polyfluorene (**CP-21**) (Scheme 7.8) or poly(fluorene-alt-benzothiadiazole) as a FRET antenna and a fluorescent reference to covalently bond with metalloporphyrin and realized the quantitative O_2 imaging in a wide range of cell [71]. These CP-dots showed phosphorescence from Pt(II) porphyrin complex components with 5–10 times higher brightness and the improved two-photon cross section in comparison with the reported MM2 probes. In addition, the cell staining ability of these CP-dots could be adjusted with negatively and positively charged groups through grafting to the CPs. The zwitterionic CP-dots offered very high staining efficiency of live cells

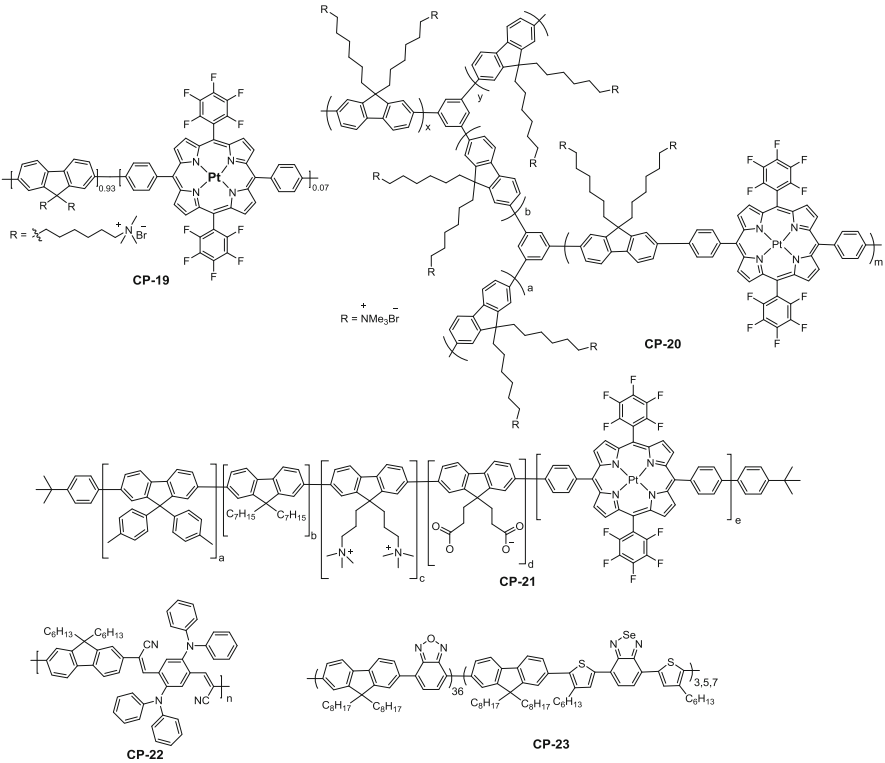

Scheme 7.8 Conjugated polymers (**CP-19 ~ CP-23**) for biological detection

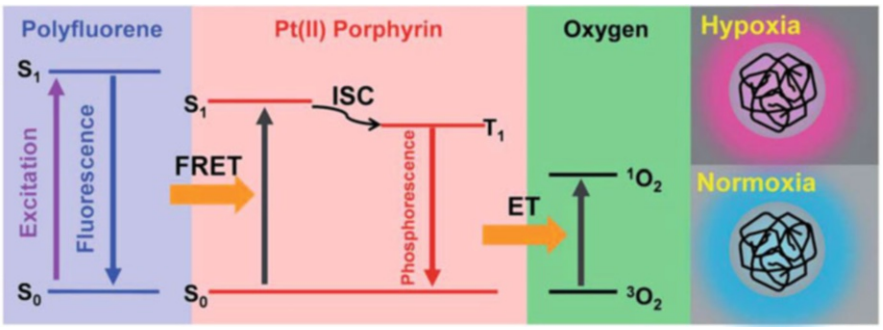

Fig. 7.1 Oxygen sensing mechanism of CP-dots and schematic illustrations of the energy level of the moieties in CP-dots. (Reprinted with permission from Ref. [69]. Copyright 2015 Royal Society of Chemistry)

and spheroid cell models and could be applied to quantitatively detect O_2 via photoluminescence lifetime imaging microscopy (PLIM).

7.4.6 ROS Detection

Reactive oxygen species (ROS) are considered as fundamental signaling members, which can regulate various biological species in a large number of physiological processes and associate with diverse pathophysiological processes, including autoimmunity, aging, and cancer diseases [72, 73]. Thus, developing probes to detect the generation of ROS is critical to both understanding the detailed effects of ROS in a large number of etiology-related diseases and well optimizing therapeutic interventions. Generally, CP-dots-based nanocomposites are designed by comprising a ROS-sensitive fluorophore unit (as the energy donor) and a ROS-inert core (as the energy acceptor), enabling the FRET from the donor to acceptor in the absence of ROS. The presence of ROS can decompose the energy fluorophore core of acceptor and subsequently disturb the FRET within the nanocomposites, ultimately causing an enhanced emission of the donor fluorophore unit.

One strategy is that a ROS-sensitive fluorophore unit is conjugated to the surface of CPs through nanoprecipitation methods. For example, Rao et al. have demonstrated a NIR CP-dots to detect reactive oxygen and nitrogen species (RONS) in inflammatory microenvironments in living mice [74]. The RONS-sensitive fluorophore unit (IR775COOH) was conjugated to the **CP-22** (Scheme 7.8) surface via a carbodiimide-activated coupling effect to generate CP-dots. The RONS could decompose the IR775COOH and then disturbing the FRET process within CP-dots, ultimately causing an increased fluorescence intensity of **CP-22**. The emission intensity ratio of F/F_0 (F and F_0 stand for the fluorescence intensities at 678 nm in the presence and absence of RONS, respectively) changes showed a good linear relation to the levels of RONS in the ranges of 0–0.4 μM. The detection limit for the RONS was 10 nM in solution.

Another method is to incorporate the ROS-sensitive and -inert fluorophores into an all-in-one CPs to generate the nanoprobe. For instance, Chiu et al. reported a homogeneous fluorescent probe, which could be used for the ratiometric detection of hypochlorous acid [75]. In **CP-23** (Scheme 7.8), benzoxadiazole (OBT) acted as an energy donor and a ClO^- sensitive unit, 4,7-bis(2-thienyl)-2,1,3-benzoselenadiazole (SeTBT) served as the energy acceptor, which enabled FRET from the OBT to the SeTBT without ClO^-. The CP-dots was prepared using PS-PEG-COOH and **CP-23** through a nanoprecipitation method. The ClO^- could oxidize the fluorophore SeTBT and then inhibit the FRET process within CP-dots, ultimately causing an increased fluorescence of OBT in green channel and a decreased emission of SeTBT in NIR channel. The emission intensity ratio shifts showed a good linear relationship with ClO^- levels in the ranges of 0–50 μM and 50–250 μM, respectively. The detection limit of the CP-dots for ClO^- was 0.5 μM. The prepared homogeneous

probe could solve some problems of leakage or differential photobleaching when ratiometric measurements were carried out.

7.5 Biological Imaging

Due to the excellent optical properties and easy functionalization, CP-dots have been successfully applied in various biological imaging, including fluorescence imaging, time-resolved luminescence imaging, photoacoustic imaging, and multimodal imaging [18, 19, 29].

7.5.1 Fluorescence Imaging

Fluorescence imaging technique has attracted growing attention due to their significant advantages of the availability of various biocompatible imaging agents, excellent temporal and spatial resolution and noninvasive nature [76]. Fluorescent CP-dots are developed as a desirable candidate in the fluorescence imaging application because of their excellent properties, such as excellent biocompatibility, superior photostability, high brightness, tunable spectral properties, and facile surface modification [18, 19, 29].

Conventional fluorescence imaging is considered as a kind of important optical imaging technique with the UV-vis emission region [77]. Many research results have demonstrated that CP-dots under the excitation of visible light display enhanced performance in the fluorescence imaging. Liu et al. have developed the integrated CP-dots nanocomposites through using gold nanoparticles (Au NPs) and CPs (**CP-24**, **CP-25**) (Scheme 7.9) by the miniemulsion approach [78, 79]. Au NPs acted as a powerful contrast agent in computed tomography and dark-field imaging due to the strong light scattering property from the localized surface plasma resonance. The fluorescence of CPs was well maintained in the nanocomposite due to the unique location of Au NPs. Therefore, the incorporation nanocomposite has been successfully used for fluorescence and dark-field dual-modal cellular imaging.

A multicolor CP-dots can be excited at various wavelengths, which well match with those available in commercial instruments used for fluorescence imaging [80]. Wang et al. firstly developed a new approach for constructing multicolor CP-dots-encoded (**CP-3 ~ CP-6**, Scheme 7.3) microparticles on the bases of noninvasive bacteria self-assembly [44]. A facile fabrication of multispectral microparticles has been achieved by bacteria-mediated assemblies of CP-dots for cell imaging. Furthermore, they developed four CPs (**CP-26 ~ CP-29**) (Scheme 7.9) with different emission colors and then applied them to synthesize carboxyl (-COOH) functionalized CP-dots through the nanoprecipitation approach with the hydrophobic interaction of the CPs and poly(styrene-co-maleicanhydride) (PSMA) [25]. The CP-dots functionalized with -COOH could also be developed through

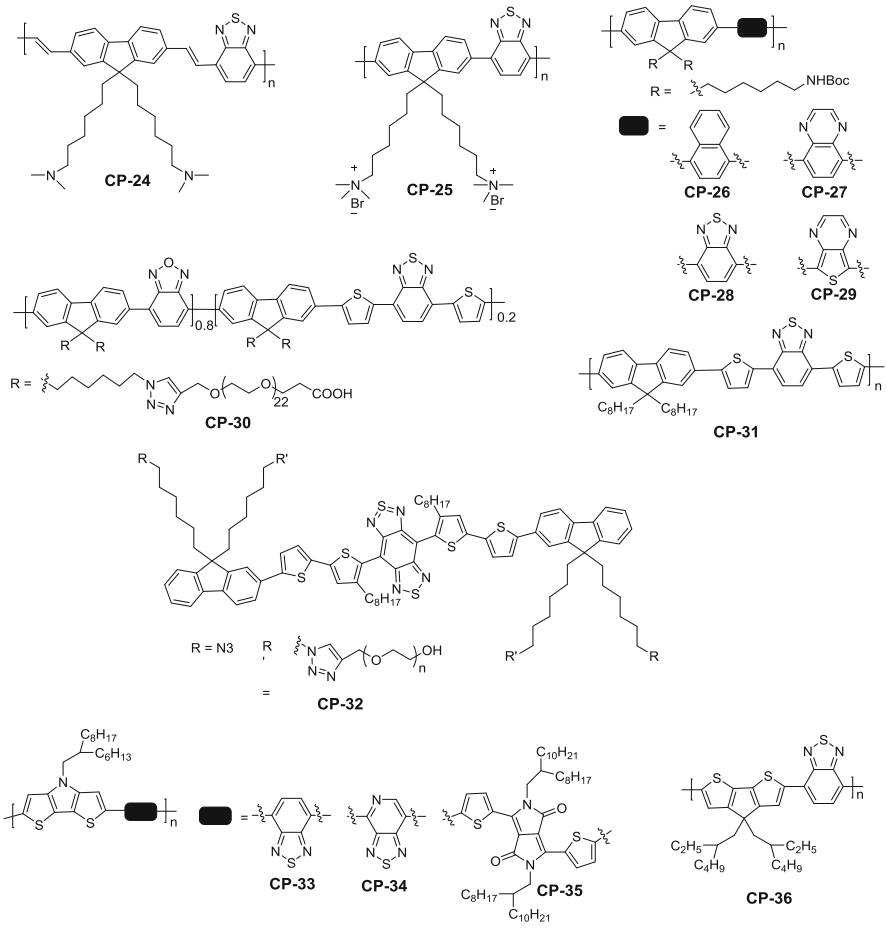

Scheme 7.9 Conjugated polymers (**CP-24 ~ CP-36**) for fluorescence imaging

nanoprecipitation of four CPs with PSMA. Then, the acquired CP-dots were further modified with fundamental antibody for CP-dots-antibody conjugates. **CP-26 ~ CP-29**/PSMA CP-dots were modified by the antibody anti-EpCAM and used for MCF-7 cell imaging (Fig. 7.2a). As exhibited in Fig. 7.2b, multicolor fluorescence images of CP-dots were found under excitation at various wavelengths (405, 488 and 559 nm). Thus, the CP-dots could be excited by various wavelengths (405, 488 and 559 nm) that matched well to those available in commercial laser scanning confocal microscope applied for biosensor and biological imaging. Through binding each tumor cell to two CP-dots attached with various antibodies, much better specificity for targeted imaging and sensing was accomplished in comparison with single-antibody recognition form to tumor cells. The new approach has endowed multicolor CP-dots the ability for targeted imaging and other biological applications.

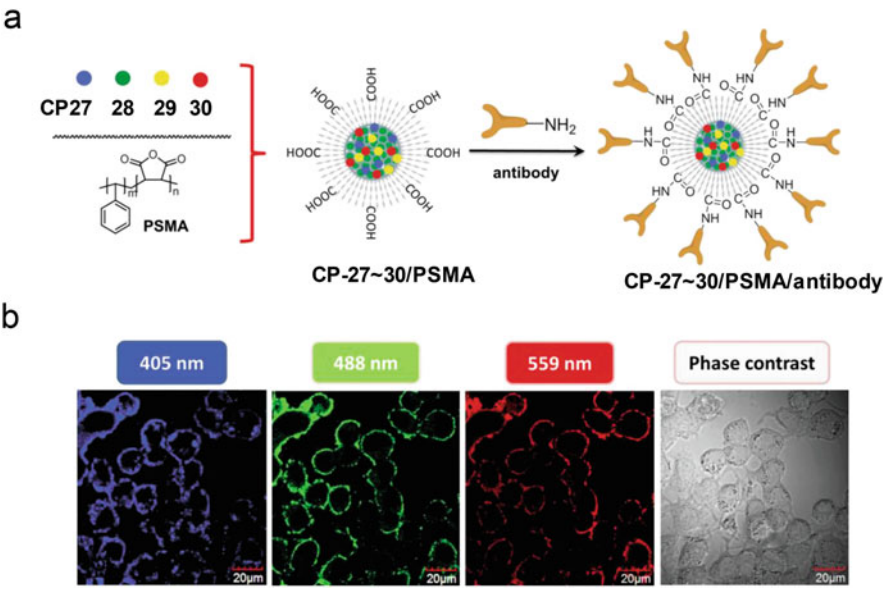

Fig. 7.2 (**a**) The preparation of multicolor CP-dots (**CP-26 ~ CP-29**/PSMA) and their modification with an antibody. (**b**) Multichannel fluorescence images of MCF-7 cells with **CP-26 ~ CP-29**/PSMA/anti-EpCAM CP-dots. The excitation wavelengths are 405, 488, and 559 nm. (Reprinted with permission from Ref. [25]. Copyright 2014 Wiley-VCH)

In comparison with conventional fluorescence imaging, NIR fluorescence imaging is more desirable because the NIR region affords a particular interrogation window for biological applications with minimal interferential absorption, the deep penetration depth and low degree of scattering [81]. CP-dots offer a convenient approach for achieving NIR fluorescence by introducing the extended π conjugated monomers or the engineered donor–acceptor units into the backbone to lower the energy level.

Liu et al. have developed a bright NIR fluorescent **CP-30** (Scheme 7.9) with a high quantum yield of 25% and a large stokes shift of approximately 200 nm, which is suitable for cell imaging [82]. Phosphorylcholine with a zwitterionic molecular part, which is abundant onto the extracellular surface of the cell membrane, has been applied to decorate the **CP-31** (Scheme 7.9) surface by nanoprecipitation method [83]. The phosphorylcholine coating produces effective and rapid endocytosis and endows these CP-dots to enter cells within 30 min, and be clearly observed at 0.5 cm tissue penetration depth. The CP-dots are tolerant to physiologically ubiquitous ROS, generating durable emission both in vitro and in vivo.

Most recently, the imaging in the second NIR window (NIR-II, 1000–1700 nm) has attracted more and more research interest, because excellent fluorescence imaging performance can be obtained in this region, such as deeper penetration depth, superior temporal and spatial resolution, and higher signal/noise ratio (S/N) compared to the visible (400–750 nm) and NIR-I window (750–1000 nm) imaging

[84]. Dai et al. explored the molecular engineering on the donor unit through a shielding unit-donor-acceptor-donor-shielding unit structure, where benzobisthiadiazole (BBDT) serves as acceptor, thiophene serves as the donor and 9,9′-dialkyl substituted fluorene was employed as the shielding units [85]. The oligomer displays the optimum activity with fluorescence peaks centered at 1048 nm and a high QY of 5.3% in water. The high fluorescent performance of **CP-32** (Scheme 7.9) offers ultrafast (>25 frames/s) fluorescence imaging in the NIR-II window with superior spatial resolution. The S/N of imaging is 4.9 ± 0.3.

7.5.2 Time-Resolved Luminescence Imaging

Time-resolved luminescence imaging is an effective way to distinguish the probe signals from background fluorescence or other luminophores with the similar emission wavelength [86]. TRLI technique mainly include time-gated luminescence imaging (TGL) and PLIM. In TGL method, the detector only collects the comparatively long-lived luminescence signals of the target probes and eliminates the unwanted short-lived background fluorescence through controlling the starting time for on-state of the detector, which considerably improves the detection accuracy and sensitivity [87, 88]. However, TGL method can only analyze the long-lived photon intensity over the gate time, which is usually used for the detection of analytes by long-lived probes. By contrast, PLIM can distinguish the lifetimes of every individual pixel and induce a significant alteration in the luminescence lifetime [89, 90]. The method can map lifetime spatial distribution in cells and tissues. To date, many CP-dots comprising of long-lived PTMCs and CPs with signal amplification nature have been reported as phosphorescent bioprobes for TRLI applications.

Zhao et al. have firstly reported a long-lived **CP-17**-based CP-dots (Scheme 7.7) containing polyfluorene units and phosphorescent Ir(III) complex and applied them for time-resolved luminescent heparin detection and photoluminescence lifetime imaging of KB cell membrane [27]. The phosphorescent turn-on **CP-17** probe for visual heparin sensor displayed high selectivity and quantification detection limit (0–70 μM and 0–5 μM in water and serum, respectively). The luminescence images suggested that the green emission was resulted from the short-lived background fluorescence, and the red emission was mainly assigned to the long-lived phosphorescence from CP-dots. TGL technique was adopted for heparin detection in complicated environment and in real patient blood samples, which clearly indicated the potential clinical application of the probe. The PLIM results indicated that the long-lived phosphorescent emission signals of **CP-17** CP-dots on the cell membrane could be differentiated from the short-lived background fluorescence. In a later work, a dual-emissive **CP-19** (Scheme 7.8) was synthesized by using polyfluorenes as an O_2-insensitive fluorophore and platinum(II) porphyrin as an O_2-sensitive phosphor, which could produce CP-dots in the aqueous solution owing to their amphiphilic structures [69]. Based on the sensitivity of long phosphorescence lifetime from Pt(II) porphyrins to oxygen, they used the CP-dots in TRLI of

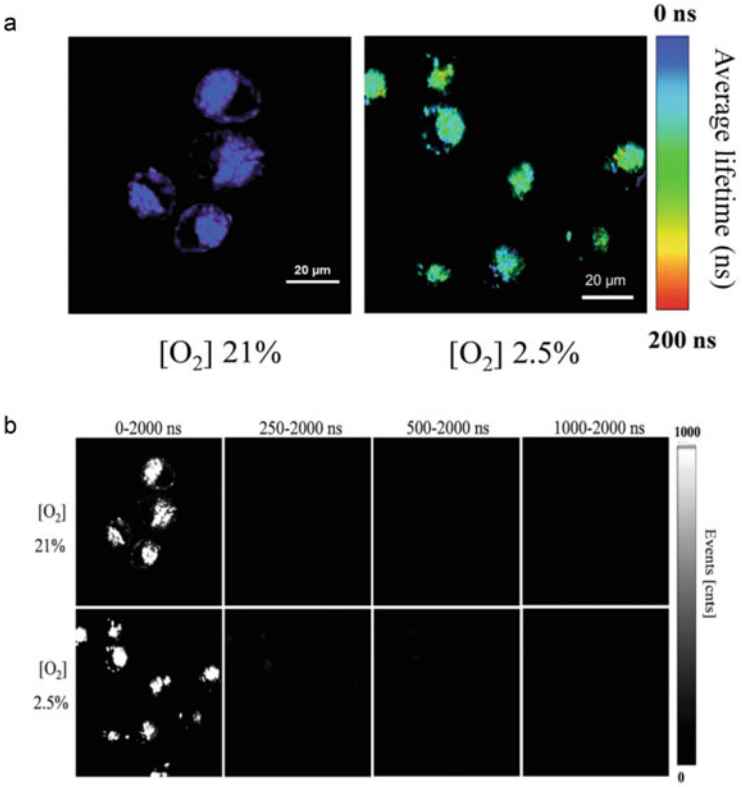

Fig. 7.3 (**a**) Photoluminescence lifetime images (λ_{ex} = 405 nm) of HepG2 cells incubated with 10 mg mL^{-1} CP-dots at 37 °C for 2 h at O_2 concentrations of 21% and 2.5%, respectively. The magnification of the objective lens is 40×. The luminescence signals were collected in the range of 420–680 nm. (**b**) Time-gated luminescence intensity images (λ_{ex} = 405 nm) of HepG2 cells incubated with the CP-dots (mg mL^{-1}) at 37 °C for 2 h at 21% or 2.5% O_2 with different time delays. The magnification of the objective lens is 40×. The luminescence signals were collected in the range of 420–680 nm. (Reprinted with permission from Ref. [69]. Copyright 2015 Royal Society of Chemistry)

intracellular oxygen concentrations. As shown in Fig. 7.3a, the emission lifetime was about 17 ns at 21% O_2 and enhanced to approximately 95 ns when the O_2 content decreased to 2.5%. The PLIM of intracellular O_2 concentration was achieved due to the relatively long average lifetime of CP-dots, in which the interference from short-lived background fluorescence was eliminated. TGLI technique accomplished highly sensitive O_2 sensing by collecting the signal at a long time range (250–2000 ns) (Fig. 7.3b). The research paved an avenue for the dual-emissive CP-dots to serve as TRLI bioprobes.

7.5.3 *Photoacoustic Imaging*

PAI detects phonon instead of photon under light irradiation and offers higher spatial resolution and deeper tissue penetration in comparison with the conventional optical spread range [91]. The PAI reagent should possess the characteristics of high photostability and large extinction coefficient at NIR range. CP-dots possessing strong NIR absorbance have been considered as a kind of promising candidates for PAI agent. They can be easily prepared by rational D-A structure control (intramolecular charge transfer) and systemically administrating organic nanoparticles (intra-particle molecular orbital engineering).

CP-dots with D-A structures have been widely applied in the fields of PAI. A higher D-A strength can lead to the stronger intramolecular charge transfer and lower band gap, which can further improve the photoacoustic signal [92]. Liu et al. synthesized three CP-dots comprising of CPs (**CP-33 ~ CP-35**) (Scheme 7.9) with D-A structures and DSPE-PEG_{2000} as a matrix through nanoprecipitation method and applied them in PAI [93]. The extinction coefficient of **CP-35**-dots at 808 nm was 57.7 L g^{-1} cm^{-1}, which was much larger than various reported PAI agents including $Cu_{2-x}Se$ NPs (8.5 L g^{-1} cm^{-1}), Bi_2Se_3 nanosheets (11.5 L g^{-1} cm^{-1}), PorCP (34.7 L g^{-1} cm^{-1}), PFTTQ (3.6 L g^{-1} cm^{-1}), and ICG (47.0 L g^{-1} cm^{-1}), which suggested the strongest light harvesting ability of the **CP-35**-dots. The increased D-A strength of the corresponding CP-dots contributed to red-shifted absorption (703 nm for **CP-33**, 748 nm for **CP-34**, and 858 nm for **CP-35**), and inhibited fluorescence emission at 866 nm, 865 nm, and 885 nm with fluorescence QY of 3.2‰, 0.74‰, and 0.22‰, higher extinction coefficients of 55.0 L g^{-1} cm^{-1}, 62.8 L g^{-1} cm^{-1}, and 95.7 L g^{-1} cm^{-1}, respectively, which caused improved photoacoustic signals. The photoacoustic measurement of **CP-35**-dots in tumor showed a high photoacoustic signal to background ratio of 47, which was superior to many reported photoacoustic contrast agents, such as ICG [94–97].

Intra-particle molecular orbital engineering strategy is another efficient route to prepare CP-dots for PAI. Pu et al. prepared CP-dots with amplified PAI brightness for new organic optical agents [28]. The doped CP-dots were synthesized by nanoprecipitation method using **CP-36** (Scheme 7.9) as the primary component and (6,6)-phenyl-C71-butyric acid methyl ester (PC70BM) as the secondary dopant. The molecular orbitals of the optical parts were aligned to endow the electron affinity and ionization potential of **CP-36**, which were higher than those of PC70BM. The energy level alignment favored PET within the confined system and caused quenched emission after light irradiation, which ultimately generated amplified PAI brightness (Fig. 7.4). The PAI brightness of the doped **CP-36**-dots was amplified 1.8-fold in the tumor in comparison with the nondoped CP-dots.

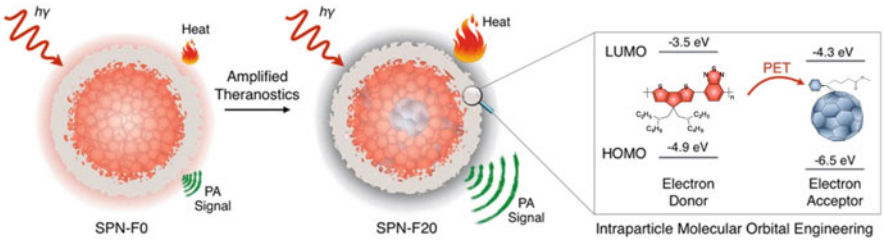

Fig. 7.4 Illustration of PET-induced amplified theranostic **CP-36**. The highest occupied molecular orbital (HOMO) and lowest unoccupied molecular orbital (LUMO) are −4.9 and −3.5 eV for **CP-36** and −6.5 and −4.3 eV for PC70BM. (Reprinted with permission from Ref. [28]. Copyright 2016 American Chemical Society)

7.5.4 Multimodal Imaging

Imaging modality generally contains optical imaging, TRLI, photoacoustic, computed tomography, magnetic resonance imaging (MRI), ultrasound, and positron emission tomography or single photon emission computed tomography [98]. Each imaging modality owns unique advantages along with intrinsic limitations, such as low spatial resolution, poor tissue penetration depth, high cost, and insufficient sensitivity. To achieve a better imaging performance, multimodal imaging, generally, dual modal or trimodal imaging, was developed. The combination of various imaging modalities is beneficial for overcoming obstacles existing in individual imaging, which can achieve higher spatial resolution, deeper penetration depth and more detailed biological information [99].

Liu et al. firstly reported the dual-modal imaging of iron oxides-based CP-dots including fluorescence imaging and MRI [100]. The CP-dots were prepared by encapsulating **CP-24** (as emission unit) (Scheme 7.9) and iron oxides (as magnetic domain) using a mixture of poly(lactic-co-glycolic-acid)-poly(ethylene glycol)-folate (PLGA-PEG-FOL) and PLGA through nanoprecipitation approach. They could serve as efficient bioprobes to accomplish targeting dual-modal imaging in vivo measurement. The signal intensity of MRI decreases with the increasing concentrations of **CP-24**, because **CP-24** could shorten the spin-spin relaxation time. The **CP-24**-dots containing iron oxides as bioprobes had superparamagnetic MRI with no reduced fluorescence intensity. The multimodal system based on CP-dots encapsulating different reagents with specific functionalities can provide great potential for in vivo bioimaging.

7.6 Therapy

Photo-induced tumor therapy usually contains two main types, such as PDT and PTT. In recent years, CP-dots have been reported as excellent therapeutic agents in phototherapy. They can be synthesized through grafting or encapsulating various photosensitizers and photothermal units into hydrophobic CPs backbone [19, 29].

7.6.1 Photodynamic Therapy

As an emerging therapeutic modality, PDT possesses many advantages of noninvasive performance and highly efficient decreased disfigurement in comparison with conventional methods, such as surgery, chemotherapy, and radiotherapy [101]. It is usually composed of three components, i.e., photosensitizer (PS), molecular oxygen (O_2), and light. In PDT process, under proper wavelength irradiation, photosensitizer is activated to convert O_2 into cytotoxic ROS, which eradicates cancer cells. However, hypoxia in solid tumor microenvironment leads to low efficiency of PDT treatment. Some typical strategies have been explored to overcome tumor hypoxia, including in situ O_2 generation from endogenous H_2O_2 of tumor catalyzed by catalase or metal oxides, and direct O_2 delivering with endoperoxide, hemoglobin, calcium peroxide [101]. To date, many CP-dots-based therapeutic platforms have been established in PDT.

Considering the easy modification and versatile functionalization of CPs, CP-dots agents can be designed by integrating CPs with PS, catalase and bioactive molecules to meet the needs of various bioapplications for diagnosis and therapy. For example, some bioactive molecules, such as folic acid and peptides, have been grafted on the surface of CPs to achieve targeting CP-dots [19, 25, 29]. Wang et al. demonstrated an multifunctional CP-dots-based therapeutic platform, in which folic acid was aminated onto the surface of **CP-37** (Scheme 7.10), horseradish peroxidase (HRP) as oxygen-delivering unit was conjugated on a amphiphilic Janus dendrimer surface, and *meta-tetra*(hydroxyphenyl)-chlorin (m-THPC) acted as photosensitizer [102]. The CP-dots-based therapeutic platform could simultaneously achieve imaging and targeted PDT in tumors.

Besides grafting PS into CPs, some PS units can be designed in CPs backbone. Wang et al. described the design of **CP-38** (Scheme 7.10) containing polythiophene-porphyrin dyads and endowed concurrently PDT and imaging functions [103]. In **CP-38**-dots, energy was transferred from the polythiophene backbone to the porphyrin units under photoexcitation, which led to the generation of toxic singlet oxygen ($^1O_2$). PTMCs units can be introduced to CPs backbone or side chain, which offered phosphorescent CPs-dots with functions of phosphorescence and PSs. Huang et al. introduced phosphorescent Ir(III) complexes as PS to fluorene-contained **CP-39** (Scheme 7.10) via Suzuki coupling reaction, in which an efficient energy transfer was achieved from the main chain of **CP-39** to the Ir(III) complex

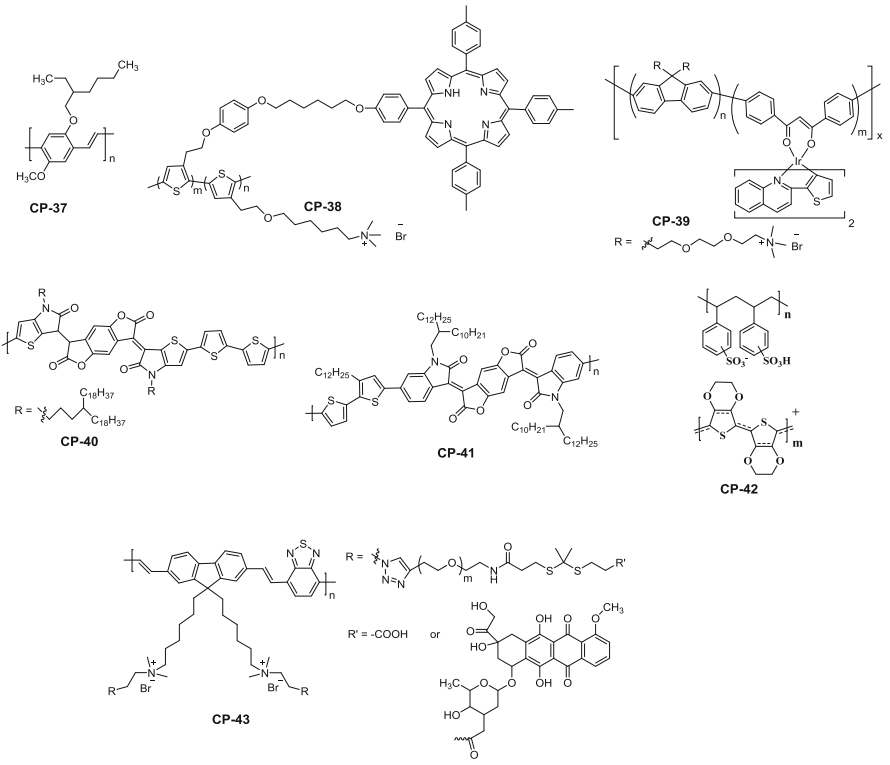

Scheme 7.10 Conjugated polymers (**CP-37 ~ CP-43**) for therapy

[104]. In the PDT process, triplet-state oxygen was transferred into the singlet oxygen, which caused cellular damage, leading to the apoptosis and cell death (Fig. 7.5). In addition, Zhao et al. have also developed CP-dots based on the hyperbranched **CP-20** (Scheme 7.8) containing platinum(II) porphyrin as PS for PDT [70].

7.6.2 Photothermal Therapy

PTT ablates tumor cells with localized heat, in which photothermal agents absorb NIR light and convert light energy into heat [105, 106]. It is highly selective and minimally invasive because PTT only happens at targeting sites and has good photothermal agent accumulations under concurrent NIR laser exposure [105, 107, 108]. In general, NIR organic dyes with strong NIR absorbance were adopted as photothermal agents; however, the photobleaching and hydrophobicity hinder their applications in PTT. In contrast, CP-dots with strong NIR absorption have unique

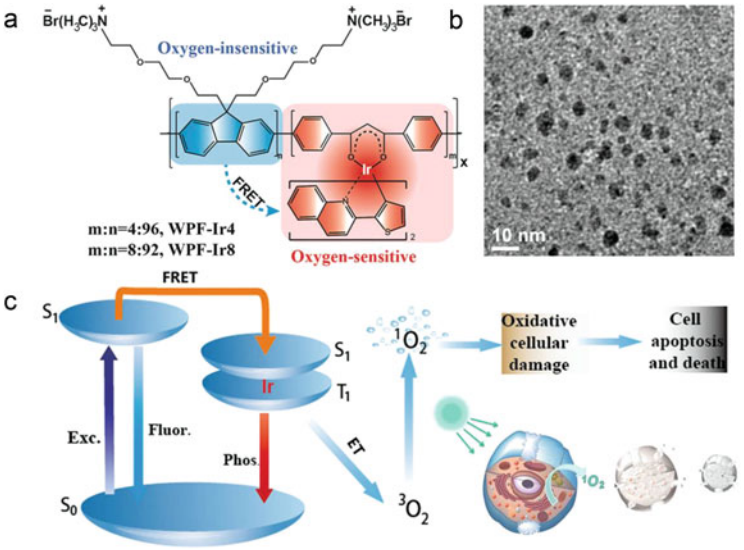

Fig. 7.5 (**a**) Chemical structures of phosphorescent **CP-39** with the Ir(III) complex. (**b**) TEM of WPF-Ir4 in water. (**c**) Mechanism illustrating the oxygen sensing and PDT. (Reprinted with permission from Ref. [104]. Copyright 2014 Wiley-VCH)

advantages of good photostability, outstanding biocompatibility, large extinction coefficient, and favorable nonradiative exciton decay pathway to efficiently produce photothermal energy, which make them efficient PTT agents. The strategies for the preparations of CP-dots with strong NIR absorbance can be divided into two types, i.e., rationally designing molecular structure and systemically administrating organic nanoparticles.

CP-dots with an increased D-A strength possess enhanced red-shifted absorption and higher extinction coefficients, which have a positive effect on the PTT. As shown in Fig. 7.6, the CP-dots was formed based on CPs (**CP-33 ~ CP-35**) (Scheme 7.9) with D-A structure through a nanoprecipitation method [93]. The CP-dots with higher D-A strength had larger red-shifted absorption, faster photothermal heating, and highly efficient PTT in vitro and in vivo. In addition, Pu et al. developed an intraparticle molecular orbital engineering strategy to construct efficient CP-dots-based (**CP-36**) (Scheme 7.9) nanotheranostics with amplified PTT efficiency [28]. The temperature increase of the doped **CP-36**-dots was amplified 1.3-fold in the tumor in comparison with the nondoped CP-dots.

Recently, photothermal conversion in the second NIR optical window (NIR-II) has attracted considerable attention because it provides deeper tissue penetration and higher spatial resolution in phototherapy treatment [84, 85]. **CP-40**-dots (Scheme 7.10) with a narrow band gap has been reported as NIR-II photothermal materials, which own a high absorption coefficient of 39.5 L g^{-1} cm^{-1} (1064 nm) [109]. When used as photothermal nanoagents, it shows a high photothermal conversion efficiency of 50% and excellent imaging-guided PTT tumor treatment.

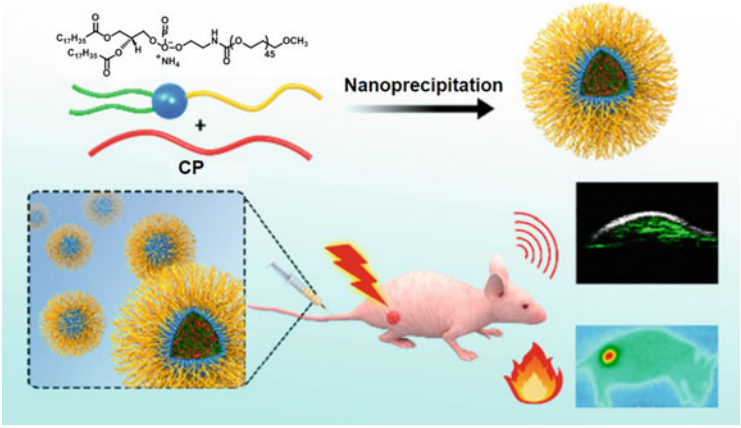

Fig. 7.6 Illustration of the formation of **CP-35**-dots and photothermal performance in cancer theranostics. (Reprinted with permission from Ref. [93]. Copyright 2017 American Chemical Society)

7.6.3 Combined Therapy

To achieve a better therapeutic performance, a combined therapy of PDT, PTT, chemotherapy, or radiotherapy has been reported [110, 112]. The combination of two or more therapeutic modalities facilitates combination of their advantages. The multifunctional CP-dots can be served as therapeutic agents for combined therapy. Their construction strategies are generally similar to the above-mentioned methods, including modifying the backbone or side chain of CPs, grafting or/and embedding specific functional units in CP-dots, and surface functional modification of CP-dots.

With D-A structures of a narrow band gap, CP-dots have been reported in the applications of PDT and PTT. Chen et al. first prepared D-A-type **CP-41** (Scheme 7.10) with 2,2-bithiophene as the donor and thiophene-fused benzodifurandione-based oligo(phenylenevinylene) as the acceptor [110]. The CP-dots were further fabricated from **CP-41** and poly(ethylene glycol)$_{114}$-*b*-poly(caprolactone)$_{60}$ (PEG-PCL) through a nanoprecipitation method. They realized highly efficient combined therapy of PDT and PTT because of the excellent photothermal conversion and singlet-to-triplet transition in the CPs with low bandgap.

In addition, CP-dots with the function of drug delivery can further improve the therapeutic efficacy of cancer. The drug carrier platform based on CP-dots can be established through loading multiple functional molecules including a water-soluble anti-cancer drug doxorubicin (DOX), a water-insoluble drug SN38 (a camptothecin derivative), or a photosensitizer chlorine 6 (Ce6) into PEDOT:PSS-PEG through π-π stacking and hydrophobic interaction. Liu et al. first synthesized PEDOT:PSS-PEG nanoparticles through the layer-by-layer assembly of commercial **CP-42** (Scheme 7.10) and PEGylation, and then loading them with three different therapeutic molecules (DOX, SN38, and Ce6) [111]. The CP-dots-based drug carriers can

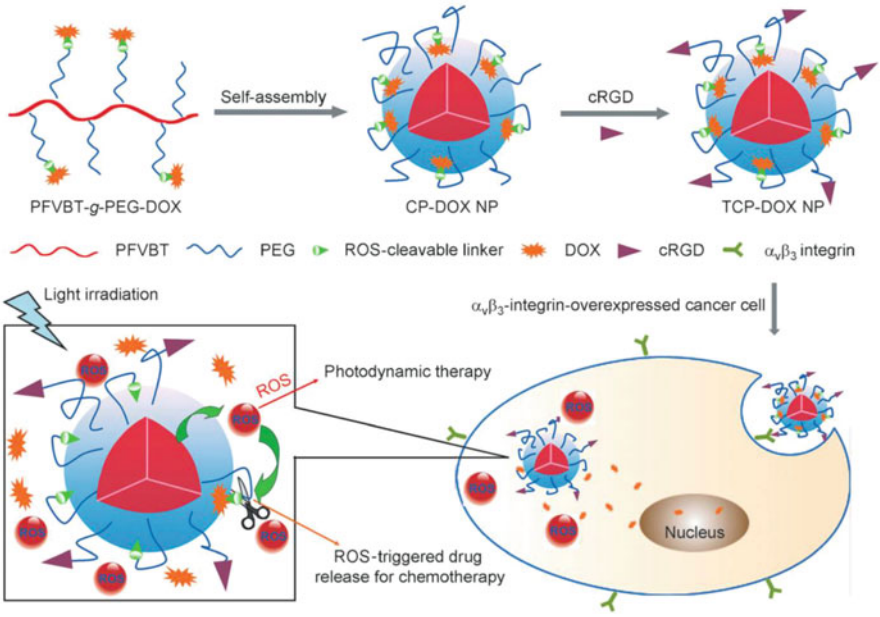

Fig. 7.7 Schematic illustration of the light-regulated ROS-activated on-demand drug release and the combined chemo-photodynamic therapy. *PEG* poly (ethylene glycol). (Reprinted with permission from Ref. [112]. Copyright 2014 Wiley-VCH)

achieve drug delivery and combined therapy of PDT, PTT, and chemotherapy of cancer.

Besides loading drugs and delivery, drug release is a key factor to enhance therapeutic efficacy of cancer therapy. Liu et al. developed PEGylated **CP-43** (Scheme 7.10) as cancer-targeted nanocarriers, which can be applied for the combined therapy of chemotherapy and PDT (Fig. 7.7) [112]. Under single-light irradiation, the **CP-43**-dots acted as a PDT agent to generate ROS. At the same time, ROS could further activate drug release for chemotherapy. As a result, the combined therapy showed an enhanced therapeutic activity than the PDT or chemotherapy alone. The work provided an alternative approach to deliver and release encapsulated drugs and explored versatile theranostics with PDT and chemotherapy for tumor treatment.

7.7 Conclusion and Outlook

Luminescent CP-dots play a key role in biomedical applications because they exhibit several unique advantages, such as excellent photophysical properties, good biocompatibility, tunable optical properties, and easy surface functionalization. This chapter mainly summarizes recent progress on luminescent CP-dots for biomedical

applications, including their design strategies, preparation methods, and applications in biosensing, bioimaging, and therapy.

These CP-dots show high brightness, excellent photostability, good biocompatibility, and outstanding ability for sensing, imaging, and therapy. However, there still exists some drawbacks that hinder these CP-dots for more efficient biomedical applications. Firstly, it is rather difficult to acquire CP-dots with the uniform size through the as-reported preparation methods. Besides, although the existing CP-dots have possessed specific target functions in vivo, the specificity is rather low and the accumulation of CP-dots cannot be avoided in other organs and tissues. Lastly, from the views of practical applications, the innate metabolic processes and pathways of CP-dots in vivo are unclear so far. Therefore, more efforts should be made to solve the existing problems and investigate more significant and desirable performance through the design of new CP-dots. We sincerely hope that this chapter can inform readers about the current advancements of CP-dots from preparation to biomedical applications.

References

1. Lu L, Shen Y, Chen X, et al. Ultrahigh strength and high electrical conductivity in copper. Science. 2004;304:422–6.
2. Alivisatos AP, Barbara PF, Castleman AW, et al. From molecules to materials: current trends and future directions. Adv Mater. 1998;10:1297–336.
3. Colvin VL. The potential environmental impact of engineered nanomaterials. Nat Biotechnol. 2003;21:1166–70.
4. Bruchez M Jr, Moronne M, Gin P, et al. Semiconductor nanocrystals as fluorescent biological labels. Science. 1998;281:2013–6.
5. Gu Y, Kuskovsky IL, Yin M, et al. Quantum confinement in ZnO nanorods. Appl Phys Lett. 2004;85:3833–5.
6. Goldstein AN, Echer CM, Alivisatos AP. Melting in semiconductor nanocrystals. Science. 1992;256:1425–7.
7. Ball P, Garwin L. Science at the atomic scale. Nature. 1992;355:761–6.
8. Reed MA, Frensley WR, Matyi RJ, et al. Realization of a threeterminal resonant tunneling device: the bipolar quantum resonant tunneling transistor. Appl Phys Lett. 1989;54:1034–6.
9. Corma A. From microporous to mesoporous molecular sieve materials and their use in catalysis. Chem Rev. 1997;97:2373–420.
10. Fan H, Lu Y, Stump A, et al. Rapid prototyping of patterned functional nanostructures. Nature. 2000;405:56–60.
11. Chan WCW, Nie S. Quantum dot bioconjugates for ultrasensitive nonisotopic detection. Science. 1998;281:2016–8.
12. Wang Y, Xie X, Goodson T. Enhanced third-order nonlinear optical properties in dendrimer-metal nanocomposites. Nano Lett. 2005;5:2379–84.
13. Service RF. Nanocrystals may give boost to data storage. Science. 2000;287:1902–3.
14. Chen LY, Wang CW, Zhi ZQ, et al. Fluorescent gold nanoclusters: recent advances in sensing and imaging. Anal Chem. 2015;87:216–29.
15. Zhu SJ, Tang SJ, Zhang JH, et al. Control the size and surface chemistry of graphene for the rising fluorescent materials. Chem Commun. 2012;48:4527–39.
16. Shen JH, Zhu YH, Yang XL, et al. Graphene quantum dots: emergent nanolights for bioimaging, sensors, catalysis and photovoltaic devices. Chem Commun. 2012;48:3686–99.

17. Peng JJ, Xu W, Teoh CL, et al. High-efficiency in vitro and in vivo detection of Zn^{2+} by dye assembled upconversion nanoparticles. J Am Chem Soc. 2015;137:2336–42.
18. Feng X, Liu L, Wang S, et al. Water-soluble fluorescent conjugated polymers and their interactions with biomacromolecules for sensitive biosensors. Chem Soc Rev. 2010;39:2411–9.
19. Feng LH, Zhu CL, Yuan HX, et al. Conjugated polymer nanoparticles: preparation, properties, functionalization and biological applications. Chem Soc Rev. 2013;42:6620–33.
20. McQuade DT, Pullen AE, Swager TM. Conjugated polymer-based chemical sensors. Chem Rev. 2000;100:2537–74.
21. Thomas SW, Joly GD, Swager TM. Chemical sensors based on amplifying fluorescent conjugated polymers. Chem Rev. 2007;107:1339–86.
22. Swager TM. The molecular wire approach to sensory signal amplification. Acc Chem Res. 1998;31:201–7.
23. Dwight SJ, Gaylord BS, Hong JW, et al. Perturbation of fluorescence by nonspecific interactions between anionic poly(phenylenevinylene)s and proteins: implications for biosensors. J Am Chem Soc. 2004;126:16850–9.
24. Jiang YF, McNeill J. Light-harvesting and amplified energy transfer in conjugated polymer nanoparticles. Chem Rev. 2017;117:838–59.
25. Feng L, Liu L, Lv F, et al. Preparation and biofunctionalization of multicolor conjugated polymer nanoparticles for imaging and detection of tumor cells. Adv Mater. 2014;26:3926–30.
26. Ke CS, Fang CC, Yan JY, et al. Molecular engineering and design of semiconducting polymer dots with narrow-band, near-infrared emission for in vivo biological imaging. ACS Nano. 2017;11:3166–77.
27. Shi HF, Sun HB, Yang HR, et al. Cationic polyfluorenes with phosphorescent iridium(III) complexes for time-resolved luminescent biosensing and fluorescence lifetime imaging. Adv Funct Mater. 2013;23:3268–76.
28. Lyu Y, Fang Y, Miao QQ, et al. Intraparticle molecular orbital engineering of semiconducting polymer nanoparticles as amplified theranostics for in vivo photoacoustic imaging and photothermal therapy. ACS Nano. 2016;10:4472–81.
29. Wu CF, Chiu DT. Highly fluorescent semiconducting polymers dots for biology and medicine. Angew Chem Int Ed. 2013;52:2–26.
30. Bao ZN, Chen YM, Cai RB, et al. Conjugated liquid crystalline polymers-soluble and fusible poly(phenyleneviny1ene) by the heck coupling reaction. Macromolecules. 1993;26:5281–6.
31. Jiang JX, Su F, Trewin A, et al. Synthetic control of the pore dimension and surface area in conjugated microporous polymer and copolymer networks. J Am Chem Soc. 2008;130:7710–20.
32. Blouin N, Michaud A, Gendron D, et al. Toward a rational design of poly(2,7-carbazole) derivatives for solar cells. J Am Chem Soc. 2008;130:732–42.
33. Gowri R, Mandal D, Shivkumar B, et al. Synthesis of novel poly[(2,5-dimethoxy-p-phenylene)vinylene] precursors having two eliminatable groups: an approach for the control of conjugation length. Macromolecules. 1998;31:1819–26.
34. Liu B, Yu WL, Lai YH, et al. Synthesis, characterization, and structure-property relationship of novel fluorene-thiophene-based conjugated copolymers. Macromolecules. 2000;33:8945–52.
35. Kurokawa N, Yoshikawa H, Hirota N, et al. Size-dependent spectroscopic properties and thermochromic behavior in poly(substituted thiophene) nanoparticles. ChemPhysChem. 2004;5:1609–15.
36. Szymanski C, Wu CF, Hooper J, et al. Single molecule nanoparticles of the conjugated polymer MEH-PPV, preparation and characterization by near-field scanning optical microscopy. J Phys Chem B. 2005;109:8543–6.
37. Wu CF, Hansen SJ, Hou QO, et al. Design of highly emissive polymer dot bioconjugates for in vivo tumor targeting. Angew Chem Int Ed. 2011;50:3430–4.

38. Baier MC, Huber J, Mecking S. Fluorescent conjugated polymer nanoparticles by polymerization in miniemulsion. J Am Chem Soc. 2009;131:14267.
39. Pecher J, Mecking S. Nanoparticles from step-growth coordination polymerization. Macromolecules. 2007;40:7733–5.
40. Xing CF, Xu QL, Tang HW, et al. Conjugated polymer/porphyrin complexes for efficient energy transfer and improving light-activated antibacterial activity. J Am Chem Soc. 2009;131:13117–24.
41. Yang GM, Liu LB, Yang Q, et al. A multifunctional cationic pentathiophene: synthesis, organelle-selective imaging, and anticancer activity. Adv Funct Mater. 2012;22:736–43.
42. Chong H, Nie CY, Zhu CL, et al. Conjugated polymer nanoparticles for light-activated anticancer and antibacterial activity with imaging capability. Langmuir. 2012;28:2091–8.
43. Foulds NC, Lowe CR. Enzyme entrapment in electrically conducting polymers. J Chem Soc Faraday Trans. 1986;82:1259–64.
44. Feng XL, Yang GM, Liu LB, et al. A convenient preparation of multi-spectral microparticles by bacteria-mediated assemblies of conjugated polymer nanoparticles for cell imaging and barcoding. Adv Mater. 2012;24:637–41.
45. Childress ES, Roberts CA, Sherwood DY, et al. Ratiometric fluorescence detection of mercury ions in water by conjugated polymer nanoparticles. Anal Chem. 2012;84:1235–9.
46. Issihiki M, Anderson RGW. Function of caveolae in Ca^{2+} entry and Ca^{2+}-dependent signal transduction. Traffic. 2003;4:717–23.
47. Yuan HB, Qi JJ, Xing CF, et al. Graphene-oxide-conjugated polymer hybrid materials for calmodulin sensing by using FRET strategy. Adv Funct Mater. 2015;25:4412–8.
48. Szabó C. Hydrogen sulphide and its therapeutic potential. Nat Rev Drug Discov. 2007;6:917–35.
49. Peng HJ, Cheng YF, Dai CF, et al. A fluorescent probe for fast and quantitative detection of hydrogen sulfide in blood. Angew Chem Int Ed. 2011;50:9672–5.
50. Chiang CH, Pangeni D, Nesterov EE. Higher energy gap control of fluorescence in conjugated polymers: turn-on amplifying chemosensor for hydrogen sulfide. Macromolecules. 2017;50:6961–6.
51. Kubik S. Anion recognition in water. Chem Soc Rev. 2010;39:3648–63.
52. Zhao Q, Zhang C, Liu S, et al. Dual-emissive polymer dots for rapid detection of fluoride in pure water and biological systems with improved reliability and accuracy. Sci Rep. 2015;5:16420.
53. Webb BA, Chimenti M, Jacobson MP, et al. Disregulated pH: a perfect storm for progression. Nat Rev Cancer. 2011;11:671–7.
54. Wang YG, Zhou KJ, Huang G, et al. A nanoparticle-based strategy for the imaging of a broad range of tumours by nonlinear amplification of microenvironment signals. Nat Mater. 2014;13:204–12.
55. Wen Q, Liu L, Yang Q, et al. Dopamine-modified cationic conjugated polymer as a new platform for pH sensing and autophagy imaging. Adv Funct Mater. 2013;23:764–9.
56. Ye FM, Wu CF, Jin YH, et al. Ratiometric temperature sensing with semiconducting polymer dots. J Am Chem Soc. 2011;133:8146–9.
57. Wang J. Nanomaterial-based amplified transduction of biomolecular interactions. Small. 2005;11:1036–43.
58. Sun P, Lu X, Fan Q, et al. Water-soluble iridium(III)-containing conjugated polyelectrolytes with weakened energy transfer properties for multicolor protein sensing applications. Macromolecules. 2011;44:8763–70.
59. Li J, Tian C, Yuan Y, et al. A water-soluble conjugated polymer with pendant disulfide linkages to PEG Chains: a highly efficient ratiometric probe with solubility-induced fluorescence conversion for thiol detection. Macromolecules. 2015;48:1017–25.
60. Watrob HM, Pan CP, Barkley MD. Two-step FRET as a structural tool. J Am Chem Soc. 2003;125:7336–43.

61. Wang C, Tang YL, Liu Y, et al. Water-soluble conjugated polymer as a platform for adenosine deaminase sensing based on fluorescence resonance energy transfer technique. Anal Chem. 2014;86:6433–8.
62. Zhang K, Yang QL, Zhang J, et al. An enzyme substrate binding aptamer complex based time-resolved fluorescence sensor for the adenosine deaminase detection. Biosens Bioelectron. 2013;42:87–92.
63. Zhang K, Wang K, Xie MH, et al. DNA-templated silver nanoclusters based label-free fluorescent molecular beacon for the detection of adenosine deaminase. Biosens Bioelectron. 2014;52:124–8.
64. Wilson WR, Hay MP. Targeting hypoxia in cancer therapy. Nat Rev Cancer. 2011;11:393–410.
65. Prass K, Scharff A, Ruscher K, et al. Hypoxia-induced stroke tolerance in the mouse is mediated by erythropoietin. Stroke. 2003;34:1981–6.
66. Frank RN. Diabetic retinopathy. N Engl J Med. 2004;350:48–58.
67. Zhang G, Palmer GM, Dewhirst MW, et al. A dual-emissive-materials design concept enables tumour hypoxia imaging. Nat Mater. 2009;8:747–51.
68. Papkovsky DB, Dmitriev RI. Biological detection by optical oxygen sensing. Chem Soc Rev. 2013;42:8700–32.
69. Zhao Q, Zhou X, Cao T, et al. Fluorescent/phosphorescent dual-emissive conjugated polymer dots for hypoxia bioimaging. Chem Sci. 2015;6:1825–31.
70. Zhou XB, Liang H, Jiang PF, et al. Multifunctional phosphorescent conjugated polymer dots for hypoxia imaging and photodynamic therapy of cancer cells. Adv Sci. 2016;3:1500155.
71. Dmitriev RI, Borisov SM, Duessmann H, et al. Versatile conjugated polymer nanoparticles for high-resolution O_2 imaging in cells and 3D tissue models. ACS Nano. 2015;9:5275–88.
72. Diehn M, Cho RW, Lobo NA, et al. Association of reactive oxygen species levels and radioresistance in cancer stem cells. Nature. 2009;458:780–3.
73. Dröge W. Free radicals in the physiological control of cell function. Physiol Rev. 2002;82:47–95.
74. Pu KY, Shuhendler AJ, Rao JH. Semiconducting polymer nanoprobe for in vivo imaging of reactive oxygen and nitrogen species. Angew Chem Int Ed. 2013;52:1–6.
75. Wu L, Wu IC, DuFort CC, et al. Photostable ratiometric pdot probe for in vitro and in vivo imaging of hypochlorous. J Am Chem Soc. 2017;139:6911–8.
76. Ntziachristos V, Bremer C, Weissleder R. Fluorescence imaging with near-infrared light: new technological advances that enable in vivo molecular imaging. Eur Radiol. 2003;13:195–208.
77. Grobe E, Calatayud A. Applications of chlorophyll fluorescence imaging technique in horticultural research. Sci Hortic. 2012;138:24–35.
78. Geng JL, Li K, Pu KY, et al. Conjugated polymer and gold nanoparticle co-loaded PLGA nanocomposites with eccentric internal nanostructure for dual-modal targeted cellular imaging. Small. 2012;8:2421–9.
79. Yuan YY, Ding D, Li K, et al. Tumor-responsive fluorescent light-up probe based on a gold nanoparticle/conjugated polyelectrolyte hybrid. Small. 2014;10:1967–75.
80. Bates M, Huang B, Dempsey GT, et al. Multicolor super-resolution imaging with photo-switchable fluorescent probes. Science. 2007;317:1749.
81. Frangioni JV. In vivo near-infrared fluorescence imaging. Curr Opin Chem Biol. 2003;7:626–34.
82. Liu J, Geng JL, Liu B. A bright far-red and near-infrared fluorescent conjugated polyelectrolyte with quantum yield reaching 25%. Chem Commun. 2013;49:1491–3.
83. Pu KY, Shuhendler AJ, Valta MP, et al. Phosphorylcholine-coated semiconducting polymer nanoparticles as rapid and efficient labeling agents for in vivo cell tracking. Adv Healthcare Mater. 2014;3:1292–129.
84. Hong GS, Zou YP, Antaris AL, et al. Ultrafast fluorescence imaging in vivo with conjugated polymer fluorophores in the second near-infrared window. Nat Commun. 2014;5:4206.

85. Yang QL, Hu ZB, Zhu SJ, et al. Donor engineering for NIR-II molecular fluorophores with enhanced fluorescent performance. J Am Chem Soc. 2018;140:1715–24.
86. Sun H, Liu S, Lin W, et al. Smart responsive phosphorescent materials for data recording and security protection. Nat Commun. 2014;5:3601.
87. Dai Z, Tian L, Song B, et al. Development of a novel lysosome-targetable timegated luminescence probe for ratiometric and luminescence lifetime detection of nitric oxide in vivo. Chem Sci. 2017;8:1969–76.
88. Connally RE, Piper JA. Time-gated luminescence microscopy. Ann N Y Acad Sci. 2008;1130:106–16.
89. Liu C, Wang XW, Zhou Y, et al. Timing and operating mode design for time-gated fluorescence lifetime imaging microscopy. Sci World J. 2013;2013:1–5.
90. Howard SS, Straub A, Horton NG, et al. Frequency-multiplexed in vivo multiphoton phosphorescence lifetime microscopy. Nat Photonics. 2013;7:33–7.
91. Wang LV. Multiscale photoacoustic microscopy and computed tomography. Nat Photonics. 2009;3:503–9.
92. Vezie MS, Few S, Meager I, et al. Exploring the origin of high optical absorption in conjugated polymers. Nat Mater. 2016;15:746–53.
93. Guo B, Sheng Z, Hu D, et al. Molecular engineering of conjugated polymers for biocompatible organic nanoparticles with highly efficient photoacoustic and photothermal performance in cancer theranostics. ACS Nano. 2017;11:10124–34.
94. Zhang SH, Sun CX, Zeng JF, et al. Ambient aqueous synthesis of ultrasmall PEGylated $Cu_{2-x}Se$ nanoparticles as a multifunctional theranostic agent for multimodal imaging guided photothermal therapy of cancer. Adv Mater. 2016;28:8927–36.
95. Qin H, Zhou T, Yang SH, et al. Fluorescence quenching nanoprobes dedicated to in vivo photoacoustic imaging and high-efficient tumor therapy in deep-seated tissue. Small. 2015;11:2675–86.
96. Xie HH, Li ZB, Sun ZB, et al. Metabolizable ultrathin Bi_2Se_3 nanosheets in imaging-guided photothermal therapy. Small. 2016;12:4136–45.
97. Pu KY, Mei JG, Jokerst JV, et al. Diketopyrrolopyrrole-based semiconducting polymer nanoparticles for in vivo photoacoustic imaging. Adv Mater. 2015;27:5184–90.
98. Lee DE, Koo H, Sun IC, et al. Multifunctional nanoparticles for multimodal imaging and theragnosis. Chem Soc Rev. 2012;41:2656–72.
99. Kim JY, Piao YZ, Hyeon T. Multifunctional nanostructured materials for multimodal imaging, and simultaneous imaging and therapy. Chem Soc Rev. 2009;38:372–90.
100. Li K, Ding D, Huo D, et al. Conjugated polymer based nanoparticles as dual-modal probes for targeted in vivo fluorescence and magnetic resonance imaging. Adv Funct Mater. 2012;22:3107–15.
101. Fan WP, Huang P, Chen XY. Overcoming the achilles' heel of photodynamic therapy. Chem Soc Rev. 2016;45:6488–519.
102. Zhang YR, Pang L, Ma C, et al. Small molecule-initiated light-activated semiconducting polymer dots: an integrated nanoplatform for targeted photodynamic therapy and imaging of cancer cells. Anal Chem. 2014;86:3092–9.
103. Xing CF, Liu LB, Tang HW, et al. Design guidelines for conjugated polymers with light-activated anticancer activity. Adv Funct Mater. 2011;21:4058–67.
104. Shi HF, Ma X, Zhao Q, et al. Ultrasmall phosphorescent polymer dots for ratiometric oxygen sensing and photodynamic cancer therapy. Adv Funct Mater. 2014;24:4823–30.
105. Lovell JF, Liu TW, Chen J, et al. Activatable photosensitizers for imaging and therapy. Chem Rev. 2010;110:2839–57.
106. Lovell JF, Jin CS, Huynh E, et al. Porphysome nanovesicles generated by porphyrin bilayers for use as multimodal biophotonic contrast agents. Nat Mater. 2011;10:324–32.
107. Jaque D, Maestro LM, Rosal B, et al. Nanoparticles for photothermal therapies. Nanoscale. 2014;6:9494–530.

108. Lyu Y, Zeng JF, Jiang YY, et al. Enhancing both biodegradability and efficacy of semiconducting polymer nanoparticles for photoacoustic imaging and photothermal therapy. ACS Nano. 2018;12:1801–10.
109. Sun TT, Dou JH, Liu S, et al. Second near-infrared conjugated polymer nanoparticles for photoacoustic imaging and photothermal therapy. ACS Appl Mater Interfaces. 2018;10:7919–26.
110. Yang T, Liu L, Deng Y, et al. Ultrastable near-infrared conjugated-polymer nanoparticles for dually photoactive tumor inhibition. Adv Mater. 2017;29:1700487–95.
111. Gong H, Cheng L, Xiang J, et al. Near-infrared absorbing polymeric nanoparticles as a versatile drug carrier for cancer combination therapy. Adv Funct Mater. 2013;23:6059–67.
112. Yuan YY, Liu J, Liu B. Conjugated-polyelectrolyte-based polyprodrug: targeted and image-guided photodynamic and chemotherapy with on-demand drug release upon irradiation with a single light source. Angew Chem Int Ed. 2014;53:7163–8.

Chapter 8
Dark-Field Hyperspectral Imaging (DF-HSI) Modalities for Characterization of Single Molecule and Cellular Processes

Nishir Mehta, Sushant Sahu, Shahensha Shaik, Ram Devireddy, and Manas Ranjan Gartia

Abstract Hyperspectral dark-field spectroscopy is achieved by combing a dark-field optical microscope with a hyperspectral detector. Due to recent advancements in optics, detection systems, image reconstruction, and computational capacity, the optical resolution of hyperspectral imaging (HSI) can now be translated down to micrometer and nanometer dimensions. Thus, making it possible to exquisitely detect and analyze single nanostructures to heterogeneous biological systems. HSI can now be used to validate, assist, and replace traditional imaging and spectroscopic technologies used to study plasmonic nanoparticles. Plasmonic nanostructures are of tremendous importance to study DNA coupling mechanisms in biosensors, virus–host interactions in the infected cells, live cell imaging coupled with motion detection of nano-objects, cancer detection, immunotherapies, toxicity and transport mechanisms, and targeted drug delivery. Many biological problems can be solved by capturing and understanding electromagnetic radiation–matter interactions in the form of scattering, transmission, and absorption by a high-throughput and robust imaging modality. Another active area of research where HSI has been used as a low-cost, label-free technique is to investigate single cellular processes, single molecule interactions, and un-mix information of tissue-level structures in the surgical procedures. This book chapter provides a brief description attributed to working principle of dark-field hyperspectral imaging. Further, advanced applications of HSI in detecting single and ensemble plasmonic nanostructures, single molecule events, environmental sensing, single cell imaging, biological analysis, and surgical vision are described.

Nishir Mehta and Sushant Sahu contributed equally to this work.

N. Mehta · S. Sahu · S. Shaik · R. Devireddy · M. R. Gartia (✉)
Department of Mechanical and Industrial Engineering, Louisiana State University, Baton Rouge, LA, USA
e-mail: mgartia@lsu.edu

X. Zhao, M. Lu (eds.), *Nanophotonics in Biomedical Engineering*,
https://doi.org/10.1007/978-981-15-6137-5_8

Keywords Hyperspectral · Spectroscopy · Nanoparticles · Plasmon resonance · Spectral mapping · Bioimaging · Single cell · Dark-field · Microscopy · Label-free · High-throughput

8.1 Introduction

Intrinsic interactions between light and physical matter such as scattering, absorption and transmission have long been used to study and characterize chemical, biological, and inorganic substances. The underlying principle of these studies is related to the observation that the radiative properties of the substance being studied is related to its physiochemical state. For example, the intracellular organelles present in biological systems refract, scatter, absorb, and transmit light in different ways. Techniques that utilize these differences in light–matter interactions to characterize the substances are commonly denoted as spectral imaging methods. Spectral imaging requires optical imaging methodologies as well as extensive data storage and analysis [1]. Successive improvements in imaging modalities, optical devices, and software analysis have now enabled trained engineers and scientists to collect and analyze data down to the nanoscale with radiative spectral data ranging over the full electro-magnetic spectrum or commonly termed as hyper-spectral-imaging (HSI).

HSI enables precise quantitative and qualitative information obtained from disparate surfaces and morphologies to be stored in the form of optical images, akin to but more sophisticated version of a moving picture. Significant technological improvements enabled capture and storage of high contrast and low signal-to-noise ratio images. These improvements allow the operator to focus light at oblique angles with high collimation and with extremely fine detection and collection settings [2–4]. Given the large amount of optical data being obtained, the resulting optical images consists of tens to hundreds of pixels with each pixel being stores as a three-dimensional data set. The pixel data or the three-dimensional hypercube data set includes information on two spatial dimensions and one spectral dimension, i.e., it generates spectral image over a two-dimensional surface [5, 6]. By generating hypercube data at various spatial locations within the sample it is now possible to generate a fully three-dimensional spectral data over the entire volume of the sample being investigated. The spectral data, thus obtained, is then cross-referenced and cross-checked using highly complex algorithms and associated software to analyze precisely and quickly the state of the micro- to nanomaterials. Integration of HSI with correlative imaging technique has recently enabled scientists and engineers to produce complimentary and previously unobtainable data. For example, integrating fluorescence microscopy with HSI it is now possible to obtain information on chemical variations within a sample, or alternatively using light imaging techniques alone it is now possible to develop minimally invasive (or even noninvasive) diagnostic methodologies for human health and disease [5].

8.2 Dark-Field Hyperspectral Imaging (DF-HSI): Operating Principles, Hardware, Software, and Limitations

As stated earlier, imaging techniques have long been used for sample analysis and characterization. These imaging techniques are typically classified as monochrome, RGB, spectroscopy, multispectral, and hyperspectral imaging. Briefly, monochromatic techniques collect information on light interacting with a sample at a single wavelength; hence, the monochromatic. The RGB or the red, green, blue technique collects information on light interacting with a sample at these three wavelengths and also additionally collects information on the spatial location from which the light is collected. Spectroscopy allows the full spectra of the light to be collected but does not allow for spatial information. Multispectral and hyperspectral are similar to spectroscopy in that the information is collected over the full range of wavelengths, but in addition they also obtain spatial or location information [5]. Hyperspectral imaging provides better spectral resolution (<5 nm) compared to multispectral imaging (>10 nm). In addition, the number of spectral bands that can be obtained with a multispectral system is limited to less than 10 while the spectral bands in a HSI system can vary from 10 to 100 in a continuous range. Thus, HSI methods generate a more complete set of data to analyze and correlate to the state of the sample being studied, and unlike other spectral imaging methods, collects and processes information from across the entire electromagnetic spectrum [1–4, 7–10]. This extra spectral information obtained using continuous hyperspectral imaging will generate an accurate and finer understanding of the micro- and nano-states of the sample from visible to near-infrared spectrum (350–2500 nm); an understanding that is not feasible using discrete imaging techniques or datasets [5].

The various hardware components of a typical HSI system are as follows (Fig. 8.1):

1. a light emitting diode or a halogen bulb or a tunable laser to act as a light source to illuminate the sample.
2. A high-resolution light collimator or adapter.
3. A visible and hyperspectral spectrometer or detector array situated at the focal point that receives and converts the electromagnetic energy into electrical signals for HSI [5].
4. An optical microscope.
5. An optical dual mode fluorescence module coupled with an optical imaging camera and other lens/slit combinations for bright-field and dark-field analysis.
6. Several light dispersive elements such as prism-grating, monochromatic lens, or optical filters.
7. Different HSI image capture schemes are implemented in commercial microscopy systems. These HSI image capture schemes are classified as whiskbroom (spatial or point scan), pushbroom (line scanning), staring (spectral scan), and snapshot (no scan), shown in Fig. 8.2. A more detailed description of these approaches can be found in the following excellent references [11–14].

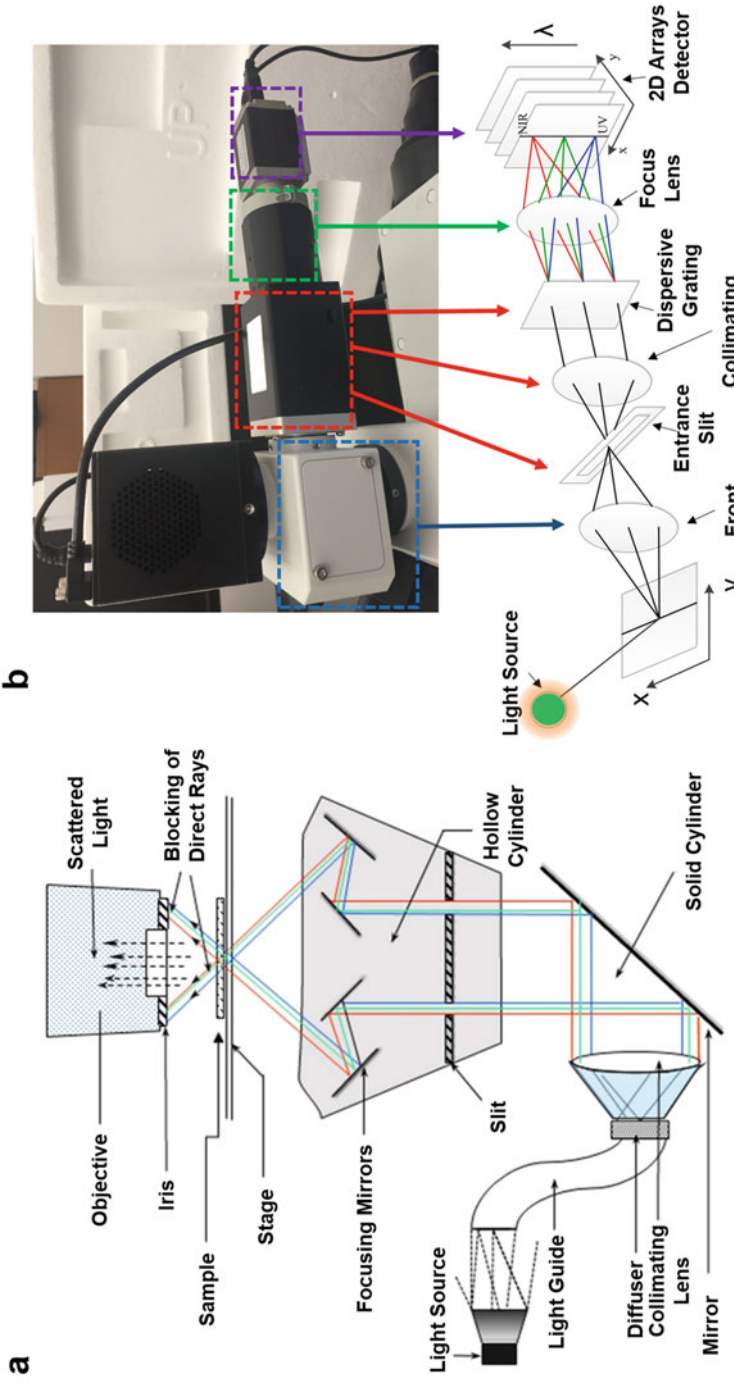

Fig. 8.1 (**a**) A labeled schematic of the condenser optics in CytoViva hyperspectral imaging system. Reproduced or redrawn with permission from [4]. (**b**) Hyperspectral imaging system spectrograph light path and optics [5]

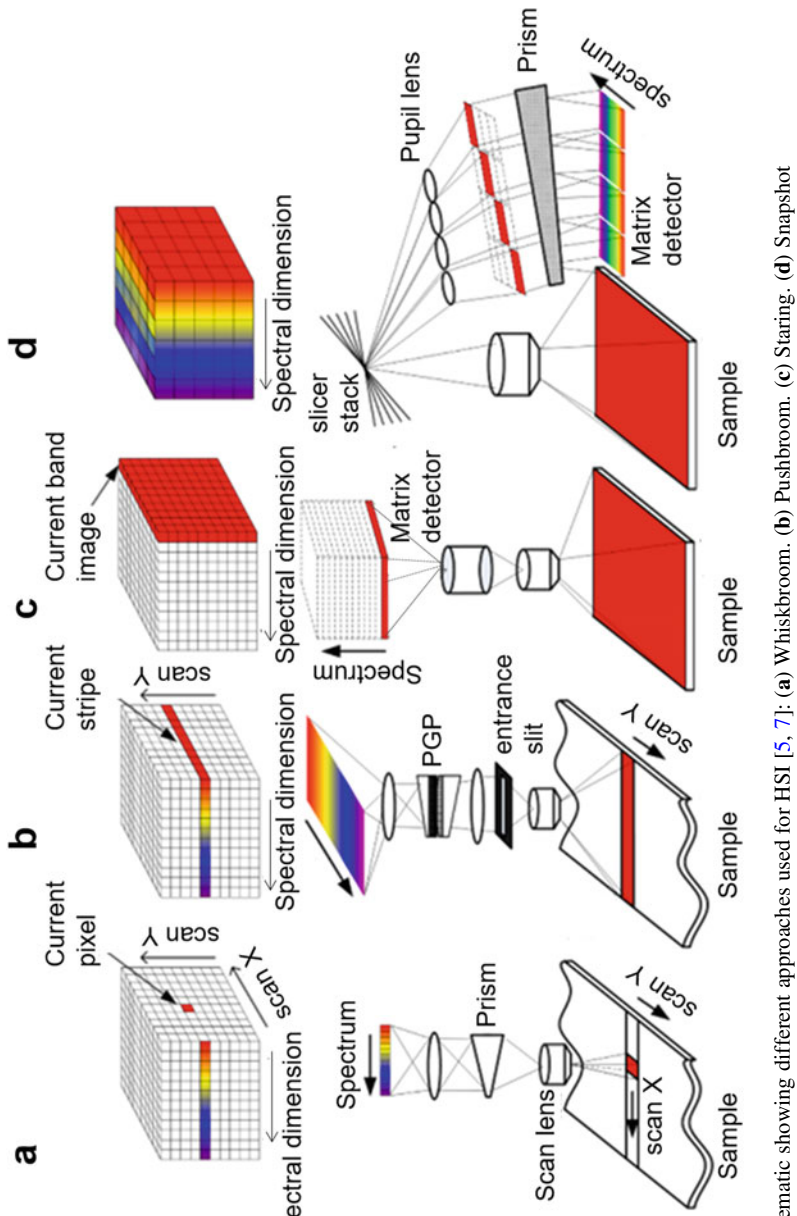

Fig. 8.2 Schematic showing different approaches used for HSI [5, 7]: (**a**) Whiskbroom. (**b**) Pushbroom. (**c**) Staring. (**d**) Snapshot

8. Highly specialized software for the hyperspectral imaging analysis. Commercially available custom written imaging codes and software allows the user to easily enhance images as well as to reduce the signal-to-noise ratio by appropriate filtering and reducing end wavelengths. The software stores the spectral data obtained from each pixel and subsequently from the entire two-dimensional surface. These data can be used for further analysis. The imaging software is also capable of eliminating spectral irregularities, errors due to fiber optics cables, and vibration in the camera and the spectrograph. Fundamentally, the operating principle is simple: it analyzes the collected data and compares it with similar data from different samples to deduce or identify similarities and differences among the samples. Alternatively, if baseline (reference) libraries are available, precise and quantitative analysis of the samples can also be performed with the purpose of finding objects, identifying materials, or detecting processes.

8.3 Advanced Analytical Applications of DF-HSI

8.3.1 Plasmonic Nanostructures

Nanostructured materials are generally referred as materials having one of their dimensions of the order of 1–100 nm. Because of nanoscale quantum confinement effects, they exhibit unique optical properties different from those of their bulk analogs. Noble metal nanoparticles such as silver (Ag) and gold (Au) have been known to display beautiful colors as a consequence of their interaction with visible electromagnetic light radiation by generating, localized surface plasmon resonance (LSPR) (Fig. 8.3). LSPR happens when the frequency of electromagnetic radiation matches the natural frequency of collective excitation of electron oscillation in metal nanoparticles that are much smaller than the incident wavelength of light. When the size of gold, silver, and copper particles is reduced to less than the wavelength of

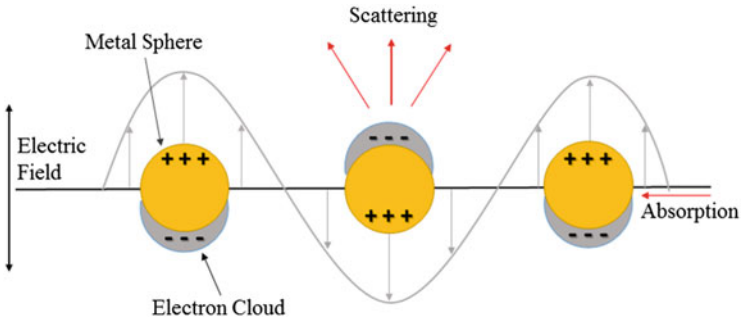

Fig. 8.3 Schematic illustration of LSPR phenomenon

light, incident light couples to localized surface plasmon resonance (LSPR) modes in nanoparticles and they exhibit intense absorption and scattering spectra at the resonant wavelength. This phenomenon allows the nanoparticles to serve as extremely intense nonbleaching labels for immunoassays [15, 16], biochemical sensors [17–23], and optoelectronic device components [24].

Silver (Ag) and gold (Au) nanoparticles have long been employed to stain glasses to produce colorful glasses. The ancient cup of Lycurgus is a well-known fourth century Roman relic placed in the British Museum and is formed of dichroic glass comprising gold (Au) and silver (Ag) colloidal nanoparticles. This famous cup changes color, based on direction of light illumination in which it is viewed, appearing red by transmitted light and green by reflected or scattered light. This effect is now known to originate from unique LSPR characteristics of Ag and Au metal nanoparticles embedded in the glass material.

The LSPR wavelength of metal nanoparticles depends on nanoparticle size, shape, orientation, and refractive index of the medium [25]. In accordance with the Mie theory, the extinction spectrum which is the sum of absorption and scattering of metal nanoparticles can be calculated as follows [26, 27]

$$E(\lambda) = \frac{24\pi^2 N a^3 {\varepsilon_{\text{out}}}^{3/2}}{\lambda \ln(10)} \left[\frac{\varepsilon_{\text{i}}(\lambda)}{\left(\varepsilon_{\text{r}}(\lambda) + \chi\varepsilon_{\text{out}}\right)^2 + \varepsilon_{\text{i}}(\lambda)^2} \right]$$

where a is the radius of the metal nanoparticle under the condition $a \ll \lambda$; ε_{out} is the dielectric constant of the medium surrounding the nanoparticle; ε_{i} and ε_{r} represent the imaginary and real portion of the dielectric function of the metal nanoparticle, respectively; χ describes the polarization factor that related with the aspect ratio of the nanoparticle, which equals 2 for a sphere. The values of χ can be up to 20 depending on the high aspect ratio of metal nanostructures. The particle of interest is represented as N finite polarizable elements, each of which can interact with the applied electromagnetic field. Compared to the incident field, the electromagnetic field of the metal nanoparticle is amplified when the dielectric constant of metal nanoparticles is roughly equal to $\varepsilon_{\text{r}} = -2\varepsilon_{\text{out}}$ [28, 29]. Also, in the extinction spectrum, the scattering cross-section of metal nanoparticles increases with increasing size of metal nanoparticles.

8.3.2 DF-HSI for Monitoring Single Molecule Events

In order to probe and visualize plasmonic nanomaterials dark field optical microscopy is a viable option. Amongst all light microscopy techniques, dark-field optical microscopy is relatively simple, fast, inexpensive, and noninvasive. In recent years, it has been widely used for observing chemical reactions [17, 18], for biosensing [20], and for detecting single molecules [17, 18, 30]. The imaging contrast in

dark-field microscopy arises from the elastic scattering of light by metal nanoparticles. The use of dark-field condenser ensures oblique angle illumination such that only light from test sample is collected by the microscope objective, while keeping the incident light out from entering into the microscope objective, resulting in a dark background. By integrating a spectrometer to the dark-field microscopy setup, the individual characteristic spectrum of nanoparticles can be characterized. When nanoparticles are characterized using ensemble methods, average behavior is measured and reported. Ensemble spectroscopic measurements is unable to detect small or rare differences between apparently identical molecules. Because an ultra-small quantity of analytes is sufficient to change the scattering spectrum of an individual nanoparticle, measurements based on a single nanoparticle scattering spectrum with DF-HSI significantly improve the sensitivity, compared with bulk spectroscopic measurements. In addition, improved sensitivity comes from narrow spectral linewidth from single nanoparticles as it is relatively easier to measure the shift of a spectrum with a narrower spectral linewidth.

Dark-field hyperspectral microscopy can concurrently acquire multiple parameters including the position, spectrum, and intensity kinetics from number of plasmonic nanoparticles in a single measurement. Thus, giving us useful multidimensional data that can be analyzed and linked to the target under study. The spectral changes of the plasmonic nanoparticles offers highly selective measurement of the LSPR signal changes associated with the molecular process under investigation. While constantly capturing the optical images of single nanoparticles upon interaction with analytes of interest, each nanoparticle performs as a nanosensor to report the molecular interactions that are happening on the nanoparticle surfaces. Moreover, similar to quantification using bulk spectroscopic measurements, the scattering intensity profile at the LSPR wavelength of metal nanostructures in single molecule measurements can be translated for quantification purposes in dark-field microscopy.

For example, a scattering recovery-based plasmon resonance energy transfer (SR-PRET) strategy is demonstrated for sensing fluoride ions (F^-) [31] using dark-field microscopy. Because of plasmonic resonance energy transfer (PRET) from gold nanoparticles (Au NPs) to adsorbed RdBS molecules assembled on the Au NP surface, the scattering from Au NPs is quenched. In the presence of fluoride (F^-) ions, the fluoride-driven breaking of Si-O bond results in the release of a rhodamine moiety of RdBS molecules, which obstructs the plasmon resonance energy transfer from the Au NPs to the RdBS molecules. Hence, the scattered light from Au NPs can be recovered leading to increased scattering intensity from Au NPs in presence of fluoride ions (Fig. 8.4). This method was applied for fluoride ion sensing with high sensitivity and selectivity in an aqueous solution and also in live HeLa cells [31]. Based on the difference in scattered intensity between aggregated and nonaggregated Au NPs, dark-field microscopy was used to observe and enumerate the number of complementary DNA-induced gold nanoparticle aggregates at the single molecule level. Detection limit of 100 fM DNA was achieved with this method, which enabled the ultrasensitive detection of single nucleotide polymorphisms [32]. Further, dark-field microscopy was used to achieve colorimetric

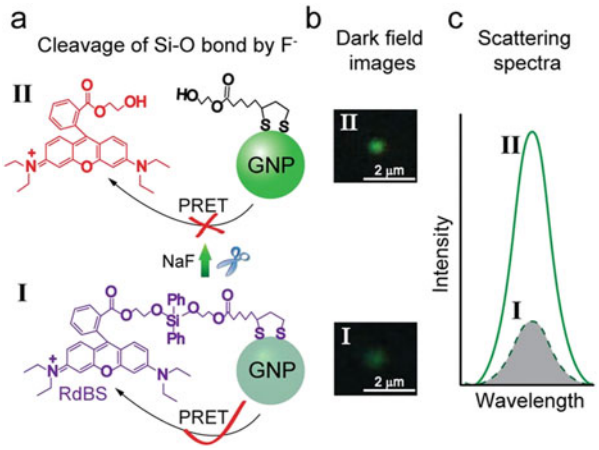

Fig. 8.4 (**a**) Schematic depiction of the process of scattering recovery-based plasmonic resonance energy transfer (SR-PRET). (**b**) The colored optical images of a typical gold nanoparticles (GNP) before (I) and after (II) addition of F^- ions, showing the recovery of the scattering intensity. (**c**) Scattering spectra before (I) and after (II) the addition of F^- ions, the notable resonance enhancement on the Rayleigh scattering spectrum is clearly seen [31]

sensing of cocaine. The cocaine associated aggregation of Au NPs resulted in a green-to-red color change of scattering spectra in the dark-field image, offering a pseudo-quantitative method to identify cocaine loadings in latent fingerprints (LFPs) [33]. Poon et al. demonstrated a single molecule scattering intensity measurement approach for the quantification of cancer-related biomarkers based on the plasmonic coupling between two different kind of plasmonic metal nanoparticles [34]. In the presence of antigen, a sandwiched immunocomplex was formed between the gold (Au NPs) and silver (Ag NPs), because of strong plasmonic coupling between metal nanoprobes leading to substantial enhancement in scattering intensity as opposed to that of individual metal nanoparticles. The intensity of Au nanoparticles is greatly enhanced by plasmon coupling with Ag NPs and target antigen (with up to sub-picomolar level limit of detection) can be easily obtained by statistically measuring and quantifying scattering signal intensity changes from individual nanoparticles in a dark-field microscopy images [34].

The LSPR frequency of plasmonic NPs is highly affected by the refractive index of the neighboring medium and the associated peak shift can be used to sense the molecular interaction taking place on the surface of NPs [17, 18, 20]. By employing asymmetrically functionalized, ~48.5 nm Au NPs as the plasmonic switch, Guo et al. [35] demonstrated that Au dimers generation showed on average 68 nm spectral peak shift upon DNA target-regulated alteration in their inter-particle distances. This large spectral shift results in a notable change in color and enables visualization of a target biomolecular binding event using dark-field microscopy. The limit of detection of target molecules achieved are $\sim 10^{-13}$ M in phosphate buffer saline (PBS) solution and $\sim 10^{-10}$ M in human serum [35]. The Au NPs dimer formation approach

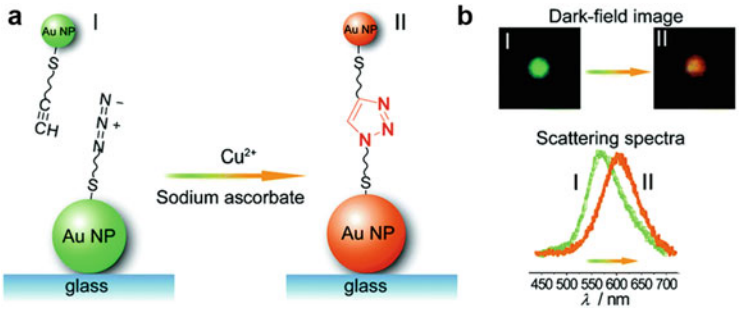

Fig. 8.5 (**a**) Gold (Au) nanoparticles are functionalized with azide and alkyne groups, respectively. The presence of Cu^{+} triggers the click-chemistry reactions and conjugates these nanoparticles to form a five-membered ring structure. (**b**) The click reaction results in a color change from green to orange under dark-field microscope (DFM), which is accompanied by a shift in the plasmonic band [30]

monitored through dark-field hyperspectral image analysis has also been used to detect and quantify detect mRNA splice variants in single cells [36]. Plasmon coupling induced spectral red-shift is also shown to monitor the Cu^{+}-catalyzed click chemistry reaction at the single particle level that couples an azide group and alkyne group to form a five-membered heteroatom ring structure [30]. In their study Long and coworkers functionalized 60 nm and 14 nm Au nanoparticles with azide and alkyne groups, respectively (Fig. 8.5). Through the Cu^{+}-catalyzed click reaction, a 14 nm Au NP is reacted with the 60 nm Au NP deposited on an ITO glass slide. This reaction leads to a color change from green to orange in a dark-field microscope along with a large red-shift of up to 43 nm in the plasmonic resonance Rayleigh scattering (PRRS) spectra [30]. This kind of system design enabled the sensing of copper ions with high selectivity and sensitivity.

Apart from pure plasmonic nanostructures, hybrid core-shell type plasmonic nanoprobes have also been used for single-nanoparticle-based spectral resonance peak shift characterizations, as the resonance coupling between the core-shell structure is also highly sensitive to the surface dielectric properties or morphology variations [37–39]. For instance, by employing Au@Ag core-shell nanorods, Xiong et al. reported ultrasensitive sulfide mapping in living cells via single particle spectroscopy [37]. The idea is based on the time-dependent scattering shifts of gold nanorods associated with Ag_2S generation on the nanorods. It turned out to be highly selective towards sulfide ions detections while showing a linear logarithmic relationship on sulfide ion concentrations in the range from 0.01 nM to 10 μM [37]. Likewise, Hao et al. synthesized ~50 nm Au@Ag core-shell nanoparticles for H_2S detection based on Ag_2S formation-driven color change of the individual plasmonic nanoprobes by using dark-field microscopy [38]. Core-shell Au@Ag nanostructures have also been found to exhibit high sensitivity towards the superoxide radical ion ($O_2^{\bullet -}$) concentration [39]. Using core-shell Au@Ag nanoprobe, Chen et al. [39] reported a plasmon resonance scattering (PRS) spectroscopy approach for monitoring the intracellular $O_2^{\bullet -}$ level in real time. The Au@Ag

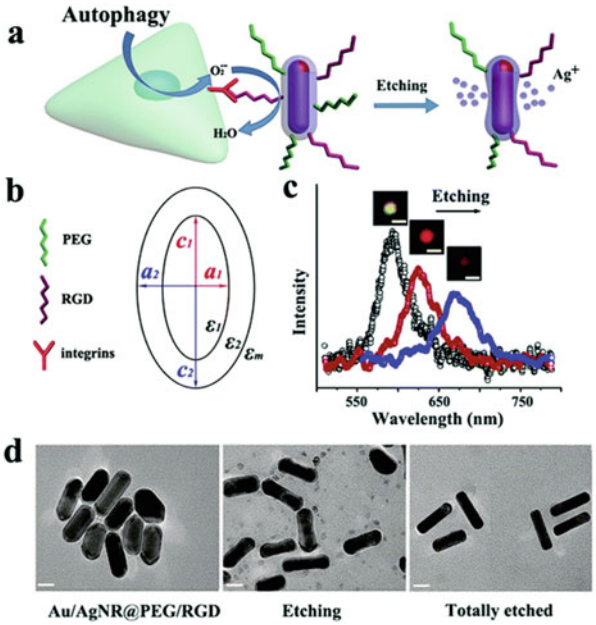

Fig. 8.6 (**a**) Illustration of the core-shell structure of Au@AgNRs [39]. (**b**) The model controlling the plasmon resonance scattering (PRS) spectrum of Au@AgNRs, where the prolate spheroidal dielectric (ε_1) core, with semi-axes $a_1 < c_1$, is coated with another confocal spheroidal dielectric (ε_2) shell with semi-axes $a_2 < c_2$. ε_m is the dielectric functions of the adjacent medium. (**c**) PRS spectra of a single probe etched by $O_2^{\bullet-}$ for 0, 30, and 60 min. The insets show the scattering images of the probe in each status. Scale bar is 500 nm. (**d**) HRTEM micrograph shows the transitions of nanoprobes during the etching process. Scale bar is 20 nm

nanoprobes are etched by superoxide anions ($O_2^{\bullet-}$), resulting in a noteworthy change in the plasmon resonance light-scattering spectrum upon etching of the silver shell by the superoxide $O_2^{\bullet-}$ produced. The Au@Ag nanostructures showed excellent sensitivity to $O_2^{\bullet-}$ concentration by visible red-shift in the plasmon resonance light-scattering spectrum (Fig. 8.6). This study allows the utility for real-time in situ monitoring and quantification of superoxide ions ($O_2^{\bullet-}$) during the process of autophagy [39].

LSPR spectral shifts has been utilized to study galvanic exchange reactions [40, 41]. Galvanic exchange reaction is an electrochemical process and it happens when the reduction of metal ions by an oxidizing metal with lower oxidation potentials come together leading to the metal atoms on the nanoparticles surface oxidize to ions and concurrent reduction of metal ions possessing higher oxidation potentials. The galvanic exchange reaction has a range of applications in catalysis [42], sensing [43], and material science [44]. The LSPR scattering spectra of single plasmonic nanoparticles have been used to monitor the galvanic exchange reaction mechanisms [40, 41]. The critical intermediates were found from scattering intensity and peak profile using surface plasmon resonance spectroscopy. The subtle

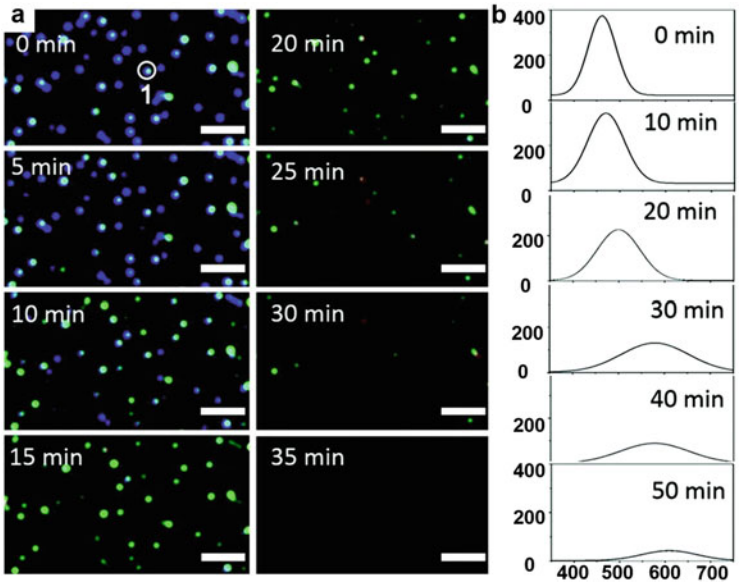

Fig. 8.7 (**a**) Schematic illustration of the time-dependent monitoring of the galvanic exchange (GE) reaction using a dark-field light scattering microscopy. The scale bar is 100 nm for all images [40]. (**b**) DFM images and spectra of spherical AgNPs during GE. The scale bar is 2 μm for all images

structural dynamics, characterized from single-nanoparticle trajectories, would be hidden in ensemble studies owing to heterogeneity in the spectroscopic features from different individual nanoparticles. Analyzing the scattering spectrum of single silver nanoparticles established the existence of nanosized voids in the intermediate step, and also found heterogeneous and fast transition kinetics [41]. Zhou et al. [40] visualized a galvanic exchange reaction by monitoring of the reaction between silver nanoparticles (Ag NPs) and Au^{3+} in real time using dynamic dark-field imaging of Ag NPs and LSPR scattering spectral shifts of Ag NPs. As shown in Fig. 8.7, upon addition of $HAuCl_4$ solution to the medium, Au^{3+} ions were reduced to metallic Au atoms, which were then deposited on the surface of Ag NPs. In the meantime, the Ag atoms of Ag NPs were oxidized to Ag^+ ions and get dissolved in the solution. These two processes lead to the creation of Ag/Au alloys on the surface of the Ag NPs. At last, hollow Ag/Au nanostructures were produced due to constant oxidative dissolution of Ag nanoparticles. The original scattering color of Ag NPs was blue, which shifted to the color comprising of blue-green (Fig. 8.7) and the measured changes in the blue and green ratio suggested the progress of the galvanic exchange process at the single molecule level [40].

Dark-field microscopy was utilized to understand the time-dependent optical properties of Ag nanoparticles in the presence of $[PtCl_6]^{2-}$. It captured the dynamic structural transformations leading to the understanding of the multidomain

Ag/AgCl/Pt nanostructures resulting from galvanic exchange process [45]. The single particle trajectory analysis further showed that surface ligands of Ag nanoparticles played a critical role in regulating the galvanic replacement kinetics [46]. Similarly, dark-field scattering microscopy was employed to study growth mechanism of single Ag@Hg nano alloy, through direct amalgamation of Ag nanoparticles with elemental mercury [47]. The scattered spectrum from Ag nanoparticles of different shapes, in the presence of the growth solution containing mercury, displayed a notable blue-shift followed by a red-shift in the spectrum, indicating the growth mechanism of Ag@Hg nano-alloys [47].

The scattering spectral band of a metal nanoparticle is highly sensitive to its electron density, which is subjected to change upon electron injection or electron extraction during nano-catalysis. It has been suggested that the electron density of metal nanoparticles could also impact the localized surface plasmon scattering spectra in addition to the quantification of electron exchange in nano-catalysis by using localized surface plasmon resonance spectroscopy [17, 48]. For example, the photo-induced reduction of *p*-aminothiophenol (p-ATP) on individual silver nanoparticles was investigated with a localized surface plasmon resonance (LSPR) spectroscopy technique [49]. The electron-transfer delay of *p*-aminothiophenol lead to the scattering light of silver nanoparticles show a bidirectional movement. The bidirectional scattering spectra shifted first bathochromically and hypsochromically thereafter, as a result of the electron transfer delay of p-ATP that revealed the photoinduced electron transfer path from *p*-aminothiophenol to O_2 through silver nanoparticles in the course of reaction, and enabled them to digitalize the connected electron transfer processes on the surface of silver nanoparticles at various time periods [49]. Xu et al. demonstrated the electron transfer between gold nanoparticles and methyl ammonium lead iodide as perovskite absorber $CH_3NH_3PbI_3$ at single molecule level by dark field microscopy along with plasmon resonance Rayleigh scattering spectroscopy [50]. The electron transfer process caused color change in dark-field microscopy images coupled with a huge red-shift of the scattering spectra [50] (Fig. 8.8). The degree of red-shift was found to be dependent on $CH_3NH_3PbI_3$ precursor of various concentrations that produces different formation of crystal grains [50]. Bi-directional electron transfer in a schottky junction was determined in real time with surface plasmon resonance microscopy (SPRM) by introducing semiconducting nanoparticles onto a planar gold film [51]. On excitation of the interface with blue light, light-driven electron injection from CdS nanoparticles to the gold film resulted in accumulation of holes in CdS, which oxidizes S^{2-} in the solution to deposit sulfur at the surface of nanoparticles (Fig. 8.9 Scheme I). While in a reverse process, propagating surface plasmon polaritons (SPPs) were formed in the gold film by a red beam excitation, energetic hot electrons are donated from Au to the CdS nanoparticle to reduce and dissolve the previously deposited sulfur to sulfide ions (Fig. 8.9 Scheme II). The time-dependent deposition and dissolution of sulfur on single CdS nanoparticles were observed in real time by surface plasmon resonance microscopy (SPRM), with an optical contrast in SPRM reflecting quantity of sulfur deposition (Fig. 8.9) [51]. More recently, Pereira et al. using dark-field hyperspectral microscopy technique showed the RGO@AuNPs species interacted

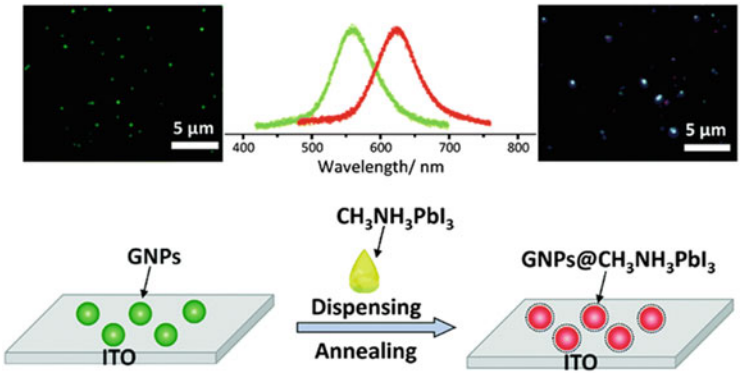

Fig. 8.8 Schematic representation of the interaction between gold nanoparticles (GNPs) and $CH_3NH_3PbI_3$ analysis revealed by conventional dark-field microscopy and plasmon resonance Rayleigh scattering spectroscopy [50]

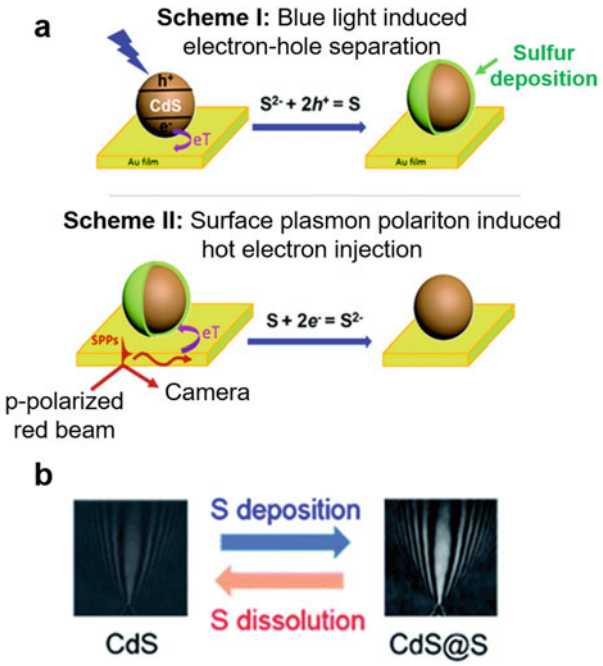

Fig. 8.9 (**a**) Bidirectional electron transfer at a Schottky junction consisted of a single CdS nanoparticle and planar gold film showing either deposition (Scheme I) or dissolution of sulfur (Scheme II). (**b**) Surface plasmon resonance microscopy (SPRM) to monitor the deposition and dissolution of sulfur at the surface of a single CdS nanoparticle [51]

with asphaltene, resulting in notable changes in plasmonic extinction spectra, mainly in the plasmon bandwidth indicating the charge transfer occurrence between the two species [52]. Li et al. showed that nano-bubbles can be used to study the gas-generating catalytic reaction, namely H_2 generation from formic acid dehydrogenation on a single Pd-Ag nanoplate, with a high temporal resolution (50 ms) via

dark-field microscopy by monitoring the scattering intensity on a single Pd-Ag nanoplate [53].

Long et al. observed the shift in scattering spectrum of a single gold nanorods when it catalyzed the electrochemical oxidation of H_2O_2 [54, 55]. They ascribed the observed red-shift in the spectrum to the formation of a hydroxide/oxide intermediates [54, 55]. More recently, the combination of electrochemistry with dark-field microscopy and hyperspectral imaging has been introduced as a tool for real-time monitoring of spectro-electrochemistry of individual nanoparticle reactions [56].

8.3.3 Environmental Applications

Engineered nanoparticles are largely used in consumer products, and one of the major routes of them getting disposed into our environment is through wastewater streams. Badireddy et al. demonstrated the use of hyperspectral dark-field microscopy for sensing, characterization, and analysis of various types of engineered nanoparticles in pure and complex water samples, such as simulated-wetland ecosystem water and wastewater [57]. Using enhanced dark field-based hyperspectral imaging technique, a dozen different nanoparticles were characterized under wet conditions across visible and near-infrared wavelengths. Additionally, the potential of this method was evaluated for detecting, differentiating, and assessing the relative abundance of mixture of variety of nanoparticles in ultrapure water [57]. The Fig. 8.10 depicts zoomed-in hyperspectral images and spectral signatures collected from various nanoparticles such as quantum dots (QD_{655nm}), Au NPs, and various types of Ag NPs. Their findings suggested that enhanced dark field microscopy-based hyperspectral image analysis could be a useful tool for detection and characterization of various engineered metal nanostructures in environmental systems enabling studies on the fate and transformation of engineered nanoparticles in complex water matrices [57]. Recently, Wilkinson and coworkers used HSI-DFM for visualizing Ag nanoparticles in wastewater effluents and biosolids [58]. Their study showed that the adsorption of natural organic matter was accountable for a large observed red-shift to their plasmonic resonance (450–570 nm) of the citrate stabilized Ag nanoparticles [58]. Mortimer et al. [59] employed hyperspectral microscopy for the detection, characterization, and subcellular mapping of silver (Ag), gold (Au), titanium dioxide (TiO_2), and copper oxide (CuO) NPs and quantum dots (QDs) in a unicellular freshwater organism—ciliated protozoan *Tetrahymena thermophila*—as a model aquatic organism. DF-HSI has also been used to investigate the bio-nano interactions between silver nanoparticles and the algae [60]. The results showed that majority of Ag NPs or their dissolution products were localized around the algal cell walls. More recently, DH-HSI has been employed to study the mechanisms and transport of Au nanoparticles uptake in plants [61].

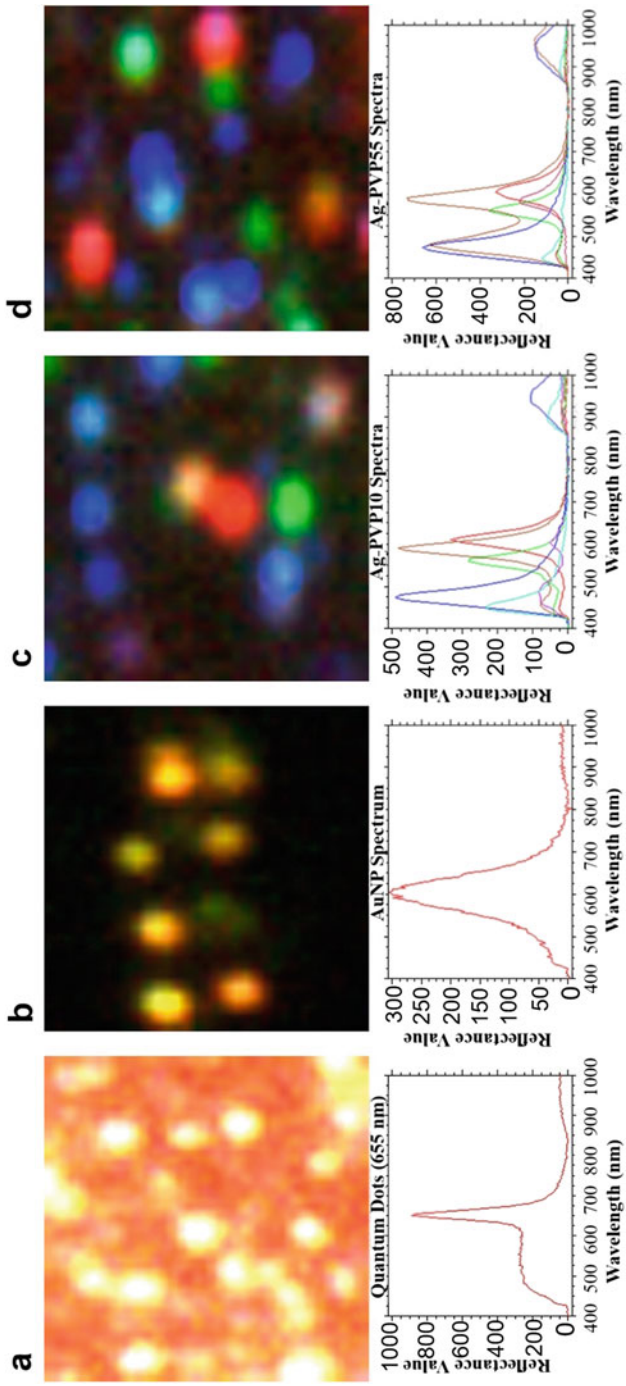

Fig. 8.10 Hyperspectral images and the spectral characteristics of various nanoparticles (quantum dots, Au NPs, Ag NPs) in visible and near-IR wavelengths (VNIR: 400–1000 nm) are shown here. All images were acquired using 100× objective/1.3 oil iris with a zoom in of 6×. The spectra were collected using 512 scans at a spectral resolution of 1.5 nm. Bilinear curve fitting was applied to all the above images to obtain smooth spherical objects (**a**–**d**). Scale: 3 cm = 50 μm [57]

8.4 DF-HSI in Bio-applications

There exist an identical morphology and genetic nature of individual cells in a specific bodily tissue, organs, or cultured cells, yet they are vastly heterogenic in way they interact with incoming radiation. Probing singular biological entities will enhance the understanding of cell-to-cell variations in a given heterogeneous population. Various imaging and surgery guidance systems are based on principle of propagation and interaction of light within biological environments. When a precisely channeled light beam impinges or enters a heterogeneous biological structure or cells, many different electromagnetic radiation–matter interactions in the form of light scattering, transmission, and absorption occurs because of intrinsic radiative nature of the sample and/or surface. Significant problems in medical field and diagnostics methods can be solved by understanding interaction mechanisms of electromagnetic waves and cellular structures, optical systems, and phenomena governing hyperspectral imaging, and the method to extract useful information by recording the light interaction. Important information like drug delivery pathways, disease initiation and propagation, cellular differentiation rate and yield, embryo development, understanding interaction of biological entities with their environment, and intercellular interactions study can be achieved by quantifying the heterogeneity of cells. The basic concept of spectral imaging systems (for example, HSI), hence, is straightforward: By calibrating and quantifying spectral reflectance inhomogeneity (electromagnetic radiation interactions) of a biological specimen being probed in the subwavelength regime, information of bio-mechanisms of the specimen being analyzed can be assessed. Significant scattering and absorbed radiation can be recorded for a given biological sample at sub-wavelength level particularly subcellular organelles with sizes ranging from less than 100 nm to 10 μm. As mentioned in the introduction, data collected from the sample is stored in three-dimensional data cube with two spatial and one spectral dimensions [5]. This section is organized to provide aforementioned general review of the optical characteristics of the single-cellular level and tissue-level biological structures along with the overview of the current hyperspectral imaging techniques for medical diagnostics/bioimaging and surgical applications.

8.4.1 Single Cellular Processes

Dark field hyperspectral imaging techniques represent a promising tool to analytically investigate nanostructures in biological environments. Capability of HSI to integrate dual modality of imaging and spectroscopy allows for the robust identification of the distribution and spatial location of unknown nanoparticles ex vivo as well as in vivo from their spectral features. Added advantages of using such integrated system instead of traditional imaging/spectroscopy methods include non-invasive, nondestructive, and minimalistic sample preparation, quick image

acquisition, rapid data analysis, comparatively cheaper and cost-effective system, and capability to precisely locate spatial distribution and identify materials in complex matrices (with user-built or known reference libraries). Biomarker information of biological sample in real time and analysis of cellular pathophysiology due to spectral resonance quality of relevant bio-entities can be successfully probed via HSI. Hence, the applications of hyperspectral imaging modality within the realm of image-guided surgeries and medical diagnostics is on an upward slope [62].

Hyperspectral imaging modality has been applied for the biomedical diagnosis of peripheral artery disease, the assessment of hemorrhagic shock, detection of laryngeal disorders, early classification and analysis of dental decay/cavities, and prompt recognition of kidney stones. Hyperspectral imaging modality has been validated for the early detection of ex vivo Aβ aggregates in the retina and the brain of mouse as well as in vitro analysis of chemicals for amyloid genesis modulating activities [4]. Based on these findings, extensive efforts are being carried out currently to employ HSI imaging in vivo to study live human/mice retina [63, 64]. Surface plasmon resonance characteristics of the plasmonic nano-probes has been used to enhance the spectral detection capability of dark-field HSI to quantify and map multiple epigenetic marks in single cells at singular modification resolution [2] as shown in Fig. 8.11. Traditional fluorescence microscopy is limited by spatial diffraction and low (S-N) signal-to-noise ratio. The S-N ratio was greatly improved and diffraction limit broken by dark-field hyperspectral imaging coupled with fluorescence microscopy tricks such as on/off mechanism and photoswitching to quantify cytosine modifications; one of the majorly utilized optical imaging modality to visualize in situ biomolecules at the molecular and single-cellular levels. Errors due to photobleaching, phototoxicity, and auto-fluorescence observed during traditional fluorescence microscopy can be minimized via dark-field HSI [2].

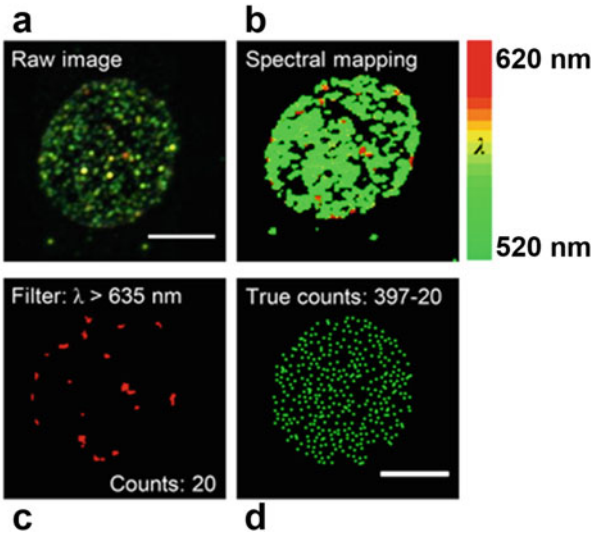

Fig. 8.11 Dark-field hyperspectral imaging using plasmonic nanoparticles and quantum dots to study modification of DNA in cells by quantifying 5-carboxylcytosine (**a**) Unmapped cell image (**b**) Mapped spectral image in the threshold 520–620 nm range, (**c**) Cell imaged at wavelength >635 nm, and (**d**) Pseudo-colored mapped parts of the single cell with Au nanoparticles (shown in figure via green dots) [2]

Cancer deaths amongst women in America are found to be due to cervical cancer. Current tests available in market are optical technique based. HSI is capable of capturing spectral data to identify genomic alterations and protein biochemical markers of single tumor cells in vitro. HSI also possesses the ability to examine the surface of tissue to examine malignant and precancerous cells as well as classify cancer grades based on morphological and structural changes. Tumor angiogenesis and tumor metabolism can be identified by measuring volume of blood and blood oxygenation. Sorg et al. [65] implemented HSI to procure multiple spatial maps of blood oxygenation in terms of hemoglobin saturation on the carcinoma cells of mouse at microvascular level. Sub 30 nm nanostructures stabilized with phospholipids without fluorophore were imaged and quantified by Misra et al. [66] using HSI imaging modality as shown in Fig. 8.12. HSI imaging was also utilized to investigate and quantify drug delivery pathways from the nanostructures inside the three-dimensional MCF-7 breast cancer cells. HSI combined with a multispectral wide-field fluorescence microscopy and advanced novel image processing techniques was used by Gosnell et al. [67] to monitor CD90 expression in order to detect genetic mutations in cancer.

HSI has been implemented to explore heart and circulatory pathology. Chin et al. [68] developed a protocol to test patients with and without peripheral arterial disease with a visible-near infrared hyperspectral imaging system by acquiring concentration maps of oxyhemoglobin and deoxyhemoglobin. Dark-field hyperspectral imaging

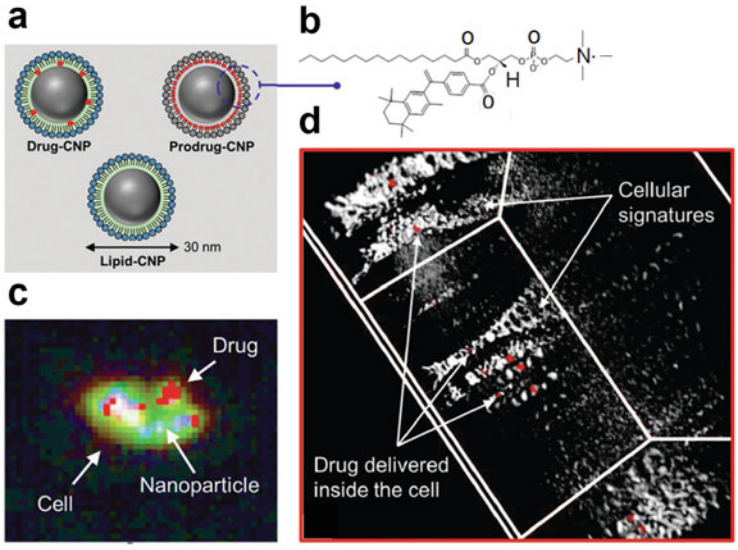

Fig. 8.12 (**a**) Three different conjugated carbon nanoparticles (CNP) mapped using hyperspectral imaging. (**b**) Molecular bond diagram of prodrug-CNP (**c**) Different color pixels exhibiting different materials in a spectrally mapped image displaying information of the drug delivery pathway in MCF-7 breast cancer cells (**d**) Localization of drug-CNP (red pixel, white arrow) in breast cancer with CNP for 4 h as studied by Misra et al. [66]

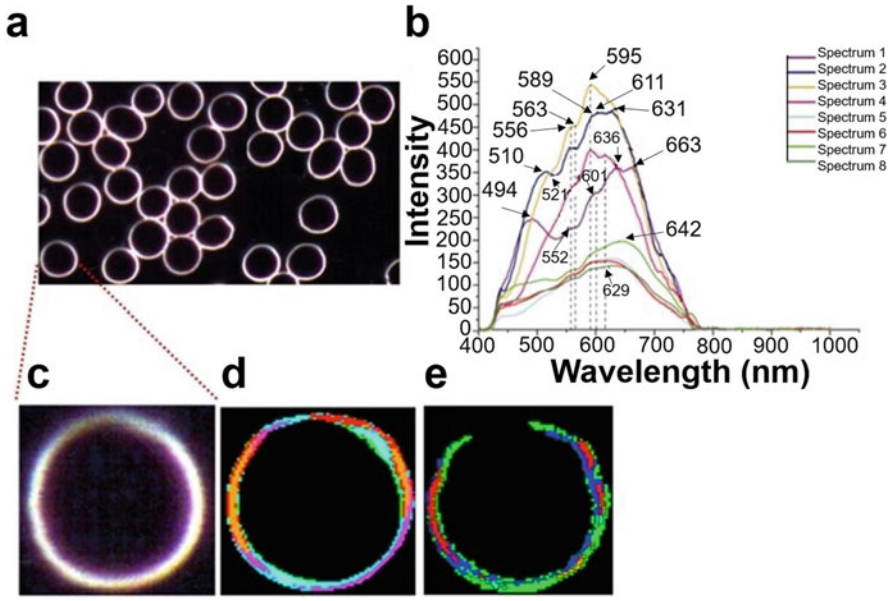

Fig. 8.13 Label-free HSI of human erythrocytes studied by Conti et al. [3]: (**a**) Dark-field image of the human RBC sample (**b**) User-defined spectral library consisting of different endmember spectra with arbitrary color coding (**c**) Magnified image of single-erythrocyte (**d**) Colored pixels with a match in spectra of the defined spectral library (**e**) Spectral mapping of five main components of red blood cells namely phospholipid, cholesterol, hemoglobin, spectrin and protoporphyrin

protocol to analyze human erythrocytes spectrally was developed and implemented by Conti et al. [3] which included user-built spectral library to study the composition of RBCs. Membrane of the RBCs and intercellular sub-membrane endmembers were sufficiently characterized by Conti et al. [3] as shown in Fig. 8.13. Precise mapping of the cellular entities is promising for the future application of HSI to detect large and small protein molecules, analysis of single molecular structure, and assembly of the membrane phospholipids [66]. Larsen et al. [69] acquired HSI fluorescence and reflectance data from excised aorta samples in vitro, using ultraviolet and white light illumination. Verebes et al. [8] collected distinct spectral signals of red blood cells (erythrocytes).

HSI study has also been applied for the identification and classification of the stem cell subpopulations [62], diagnostics of diabetic tissue [70], and analysis of the preimplantation embryos [71]. 3-D rotational dynamics of Au nanorods inside the live HEK293 cells was studied by Chaudhari and Pradeep [72] using polarized HSI. The study demonstrated data for the understanding of the state of an anisotropic nanostructure in complex environments. Relationship between development of Parkinson's disease and the physiological importance of iron in substantia nigra (SN) was analyzed visually by Oh et al. [7] and the molecular distribution of iron in cells was efficiently quantified via internal hyperspectral fluorescence signal as

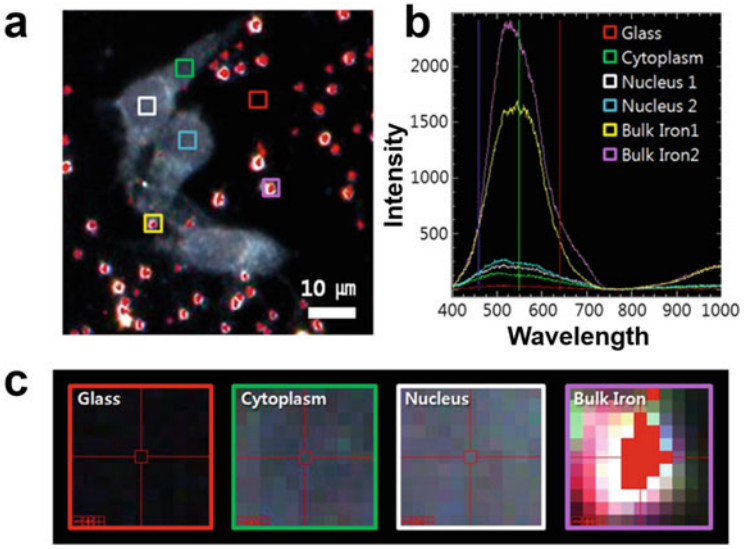

Fig. 8.14 HSI of SHSY5Y cells with iron compounds reprinted from Oh et al. [7]. (**a**) SHSY5Y cells continuously incubated with ferric ammonium nitrate for 1 h (**b**) Intensity count plotted against VNIR wavelengths for the marked regions in (**a**). Significant spectral peaks are seen between 450 and 650 nm (**c**) 17-times magnified HSI images containing data from glass-substrate, bulk-iron, nuclei, and cytoplasm

shown in Fig. 8.14. A dark field hyperspectral fluorescence imaging system in the visible to near infrared spectral wavelength range was used to study iron ions by Oh et al. [7]. Uptake of various metal-based nanostructures as well as quantum dots in the ciliated protozoan Tetrahymena thermophile at the concentration below sub-toxic level was investigated by Mortimer et al. [59].

Cellular differentiation (for example, adipogenic and osteogenic differentiation) analysis can be potentially carried out noninvasively and rapidly by applying HSI technique and spectroscopic mapping methods. RNA/cDNA analysis of the biological structures can be directly correlated with the mineralization data obtained using spectroscopy-based modality; significantly improving the robustness of the cell differentiation studies. The study was able to track adipose stem cells undergoing differentiation in a label-free manner. Integrating spectroscopy-based techniques like HSI with microfluidic devices and micro-scale technologies, the system can achieve high-throughput sorting-based assays along with the precision screening. Readily available commercial HSI software and image-analysis algorithms to process HSI images has significantly augmented the access of HSI systems with ease and exponentially improved the number and diversity of biological issues that can be addressed. Summary can be given in the following Table 8.1.

Table 8.1 Summary of applications of hyperspectral imaging system in medical regime

Biomedical application	Tissue/cell study	Marker	Spectral range	Resolution	Ref.
Retinal	Chromophores in optic disk/vascular structure	None	450–700 nm	1 nm	[73]
Dental	Teeth (molars, premolars, incisors)	None	900–1700 nm	–	[74]
Nerve fibers	Rabbit nerve sections	Comparison; No label and acetylthiocholine iodide	550–100 nm	2 nm	[75]
Cervical cancer	Cervical intraepithelial neoplasia (CIN)	Fluorescence markers—exalite and flavin adenine dinucleotide	330–480 nm	5 nm	[76]
Skin cancer	Tumor formation via tracheal carcinoma cells	Fluorescence	440–640 nm	10 nm	[77]
Breast cancer	DMBA-induced rat breast tumor	Oxyhemoglobin and deoxyhemoglobin	450–700 nm	5 nm	[78]
Gastric cancer	Mucosal surface of tumor from stomach	None	1000–2500 nm	6.29 nm	[79]
Prostate cancer	CWR22 cancer cells injected in mice	None	450–950 nm	2 nm	[80]
Ovarian cancer	Ovaries with attached fallopian tubes	None	400–640 nm	5 nm	[81]
Burn wounds	Depth imaging burn wounds	None	400–1100 nm	–	[82]
Amyloidopathic disorders	Aggregates of amyloid	External-none Internal-N-terminal fluorescein isothiocyanate	400–1000 nm	2.5 nm	[4]
Differentiate cancerous, normal, and precancerous cells	Cervical and squamous cell carcinoma (SCC)	Hematoxylin and eosin	470–690 nm	2.5 nm	[83]
Parkinson's disease	SHSY5Y (neuroblastoma dopaminergic cells)	None	400–1000 nm	2.5 nm	[7]
Epigenetic modifications on DNA	Cytosine quantification via 5-carboxylcytosine (5caC)	Gold and silver nanoparticles functionalized with anti-body	350–900 nm	0.5 nm	[2]
Erythrocytes (RBC)	Distribution of constituents	None	400–1700 nm	2.5 nm	[3]
White blood cells	Active and inactive WBC	None	400–1000 nm	2.5 nm	[8]

(continued)

Table 8.1 (continued)

Biomedical application	Tissue/cell study	Marker	Spectral range	Resolution	Ref.
Pigment localization and distribution	Cyanobacterial cells	Phycobilins and carotenoids	500–800 nm	1 and 3 nm	[9]
Toxicity and uptake assessment of Au nanoparticles	Bronchial epithelial cell line BEAS-2B, Chinese hamster ovary CHO, HEK 293 human embryonic kidney cell line	Citrate stabilized Au nanoparticles	400–1000 nm	2.5 nm	[84]
Antifungal activity of nanoparticles	*Candida albicans* ATCC 90028 and hyphae	13 metal nanoparticles	400–1000 nm	2.5 nm	[85]
Uptake of nanostructures in biological entity	Protozoan *Tetrahymena thermophila*	Metal nanoparticles and quantum dots	400–1000 nm	2.5 nm	[59]

8.4.2 Surgical Applications

Outcome of successful surgery is highly dependent on the sensory skills and intraoperative decision-making of a surgeon to detect malignant regions and correct them. Success-rate can be further improved by augmenting detection/diagnostic procedures with robust scientific evidence-based imaging combined with advance image processing such as HSI at macro and micro-cellular level. This offers noncontact real-time imaging facility. Various research studies have indicated successful application of HSI as complementing visual tool for surgical guidance. Using HSI, chemical maps can be overlaid on optical images by combining high-resolution spatial imaging and chemical specificity detection of light-resolved spectroscopy. This property of HSI can accelerate the process of tumor detection and assist in postoperative care. Surgical treatment and radiation therapy account for more than half of cancer cure procedures. It is extremely important to minimize loss of normal tissue and organelles during surgical operation. Difference in reflectance and absorbance spectra of real-time malignant tumor cells and benign tissue cells can be identified and separated by surgeon during intraoperative stage which otherwise is difficult to see and feel with naked senses. One-third of the cancer patients undergoing surgical treatment have chances of recurrence. Therefore, identification of postoperative residual tumor detection with the help of HSI can help suppress the mortality from reoccurring tumor cells. Panasyuk et al. [78] concluded that residual small tumor fragments 0.5–1 mm in size could be detected intraoperatively using HSI imaging. Sensitivity of 89% and a specificity of 94% was demonstrated by Panasyuk et al. on experimental DMBA-induced rat breast tumor model as shown in Fig. 8.15 which was closely comparable to histopathological examination. HSI can aid in identification of residual malignant tissue cells in tumor resection bed and help

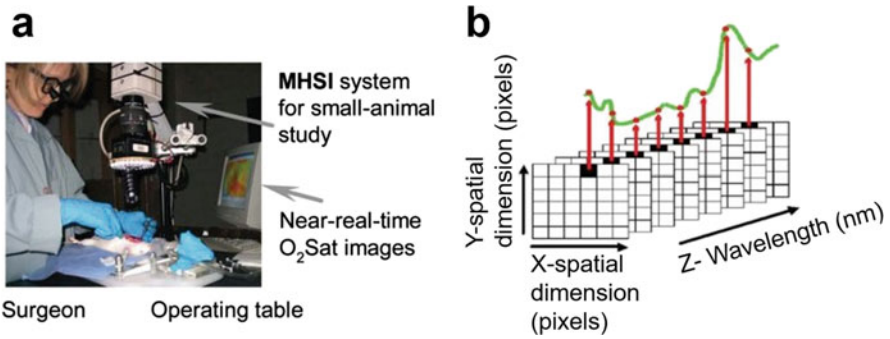

Fig. 8.15 (**a**) In vivo multispectral imaging/optical microscopy setup to investigate small animals (**b**) Representation of three-dimensional data cube. Oxygenated hemoglobin is represented by green-colored curve subject to the recording pixel [78]

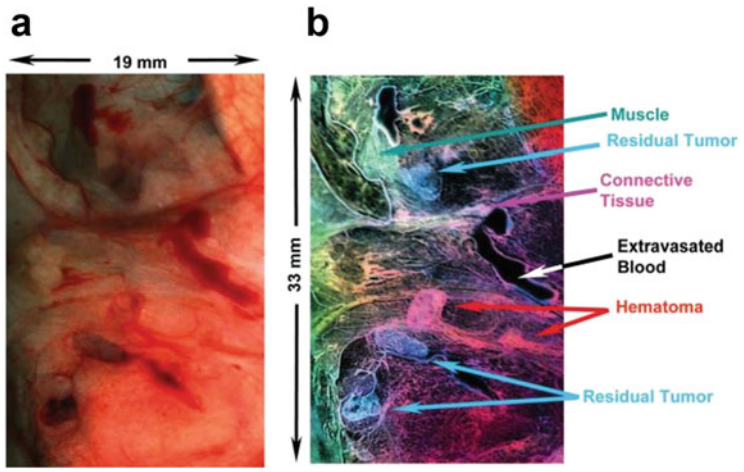

Fig. 8.16 Afromowitz et al. [82] studied wounds by analyzing depth of burn wound using principles of diffused reflection of light from tissue sample. Significant information is extracted from identification of hematoma (**a**) Optical image (**b**) Hyperspectral image exhibiting multiple entities due to pseudo-coloring of pixels with different spectral dataset

recognize effective biopsy sites within surgery. This in turn offers qualitative treatment, preservation of benign tissue margins, and effective patient care [78].

Blood coagulation, blood spilling, progressive fibrinolysis, and blood clot provide inevitable visual obstacles in the doctor's surgical field of view. Combining HSI and calibrating spectral difference due to change in optical depth, can immensely aid surgeons in successfully visualizing the operative surfaces which otherwise would be covered under blood and invisible to naked eye. This kind of depth-based inspection is critical in micro-level surgical treatments. Objects can be pseudo colored within real-time imaging on the basis of all-optical depth extraction as shown in Fig. 8.16.

During complex tissue operation such as laparoscopic surgery [86, 87] or gastrointestinal surgery [88], HSI can be used to examine hemoglobin concentration, water concentration, and tissue oxygen saturation in the tissue tract. Information regarding chemical composition with and without contrast agent can help determine viability of the tissue for new connections as well as resections of benign and malignant tumors. Radiation- and ion-free technique can help prevent adverse side effects of imaging. There is increase in cerebral blood flow after neuronal activity thereby increasing oxygen concentration to active neurons. Use of HSI for brain surgery and brain research can significantly improve treatment outcomes. Dynamic changes in the blood flow can be captured by fast frame rate camera. Akbari et al. [89, 90] used HSI to detect ischemic regions of the intestine as shown in Fig. 8.17.

Surgical outcomes can be improved largely by accurate, real-time recognition, and display of important anatomic structures, for example organs, nerves, and vascular structures [5]. Results of this application are well explained by Cha et al. [91], wherein they have demonstrated noninvasive hyperspectral analysis in comparison with fluorescence imaging to identify vein, nerve, artery imaging ex vivo porcine tissue, small bowel vascular imaging, simultaneous imaging of vessels and femoral nerve in a mice model, as well as hepatic artery visualization in a pig model as shown in Fig. 8.18.

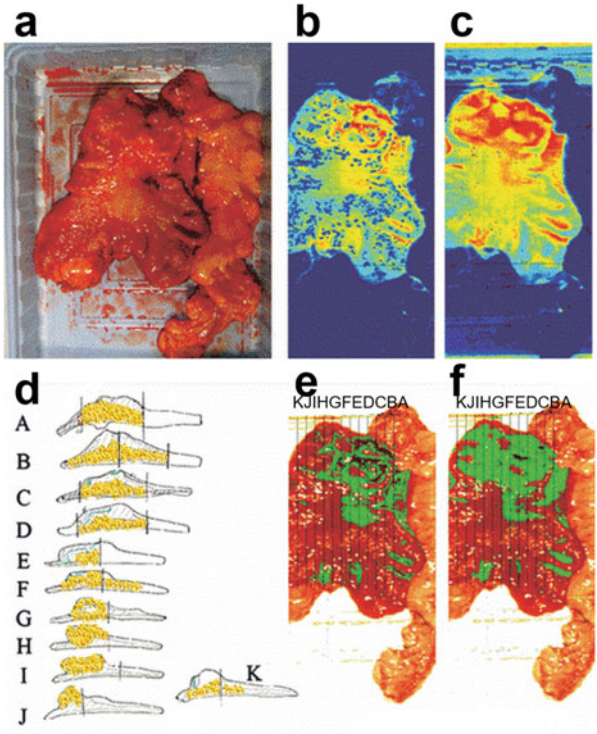

Fig. 8.17 Normalized cancer index (NDCI) and wavelength filtering is evaluated to detect tumor [88]. (**a**) the optical image of tissue; (**b**) spectral filter in the 1057–2440 nm range is used to enhance visualization of cancer regions in the hyperspectral image; red represents tumor cells (**c**) tumor cells with enhanced visualization due to application of NDCI method (**d**) results from pathology study (**e**) tumor detection via spectral filter (**f**) tumor detection via NDCI

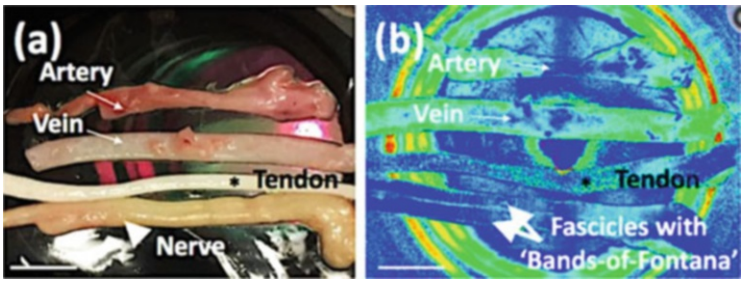

Fig. 8.18 Polarimetric image analysis of blood vessels [91] (**a**) Optical image clicked with color camera (**b**) Pseudo-colored representation of differentiated image to identify artery, vein, tendon, "bands of fontana"; based on spectral signatures collected from birefringence imaging method

8.5 Conclusions, Challenges, and Perspectives

The recent studies highlighted in this book chapter, demonstrated capability of DF-HSI as versatile tool for characterization of plasmonic nanomaterials and in subsequent, understanding and probing of the bio-nano interactions at single particle level. DF-HSI platform provides a low-cost, label-free technique that is minimally invasive and does not suffer from photobleaching and photoblinking issues. It requires a smaller sample volume making this technology a viable choice for routine quantitative analyses. Hyperspectral microscopy also provides intrinsic imaging contrast due to the variations in refractive index and cell thickness, which impact the absorption, reflection, and scattering of light from the single cells being investigated. However, the DF-HSI technique is limited in characterization of plasmonic nanoparticles below 20 nm in diameter because of poor scattering cross-sections exhibited from these small nanoparticles leading to a low signal-to-noise ratio. The applications are also limited as the sample needs to be immobilized on the transparent glass substrate to facilitate optical imaging by eliminating Brownian diffusion.

Moreover, in spite of recent accomplishments in probing and analyzing single particle processes to understand the structural–functional relationships, more examples are needed to show that microscopic studies lead to improved ensemble performances. Many studies use DF-HSI to show spectral similarities or differences but missing both a linkage between physicochemical properties and a profound interpretation of the results. Furthermore, large amounts of the generated data forming the hypercube require extensive data processing and careful statistical analysis from hundreds to thousands of individual molecules to deliver a reliable structural–functional relationship. In terms of applying DF-HSI to emerging biological systems such as stem cell analysis and cancer diagnostics are still in its nascent stage. Despite the progress made in cellular analysis, practical implementation of a system to probe the differentiation of stem cell in a label-free manner and maintaining the purity of the isolated cells remains a challenge. DF-HSI will be an important tool to achieve this feat in near future.

Furthermore, large amounts of the generated data forming the hypercube require extensive data processing and careful statistical analysis from hundreds to thousands of individual molecules is required to deliver a reliable structure–function relationship. Significantly there are two major challenges in order to develop fully compliant diagnostic support system based on hyperspectral imaging to rapidly detect cancer. Firstly, during live surgery there are motion artifacts present in the field of view (FOV) of the image capturing modality. Hence intraoperative imaging is challenging to due distortion in radiative properties, glare from mirrored-reflections, change in focal depth due to variation in curved boundaries. It requires in-depth and rigorous image-processing procedures to create analytical results. Secondly, data storage files of hyperspectral imaging are high volume, high velocity, and of high variety. It requires large computational power and is time-consuming. While it is important to note that real-time surgeries are limited by time to prevent negative effects in patient health. Therefore is extremely important to extract correct and only relevant information during intraoperative procedures in order to decrease dimensionality of the dataset and at the same time maintain precision of results.

Clearly, significant effort is still needed to improve the accuracy, reproducibility, and the adaptability of plasmonic particle-coupled DF-HSI analysis for single cell applications. Such efforts may target to improve the signal-to-noise ratio by improved experimental design and detection methods as well as by controlling the size, shape, and composition of the plasmonic nanostructures. Thus, there is a need to develop multimodal imaging modalities, which can simultaneously provide functional, morphological, and biochemical information of cells, scaffolds as well as extracellular matrix components. Efforts are being made to combine hyperspectral microscopy with other modalities like Fourier-transformed infrared and Raman spectroscopy to enhance the chemical specificity from the imaging data. Other areas of interest include enhancing the resolution and penetration depth of the hyperspectral microscopy to better understand spatial variations within heterogeneous tissues.

Acknowledgements MRG thanks the support from Louisiana Board of Regents RCS grant (Contract Number: LEQSF (2017-20)-RD-A-04), National Science Foundation (Award Number: 1660233), and Louisiana State University start-up funds.

References

1. Schultz RA, Nielsen T, Zavaleta JR, Ruch R, Wyatt R, Garner HR. Hyperspectral imaging: a novel approach for microscopic analysis. Cytometry. 2001;43:239–47.
2. Wang X, Cui Y, Irudayaraj J. Single-cell quantification of cytosine modifications by hyperspectral dark-field imaging. ACS Nano. 2015;9:11924–32.
3. Conti M, Scanferlato R, Louka M, Sansone A, Marzetti C, Ferreri C. Building up spectral libraries for mapping erythrocytes by hyperspectral dark field microscopy. Biomed Spectrosc Imag. 2016;5:175–84.

4. More SS, Vince R. Hyperspectral imaging signatures detect amyloidopathy in Alzheimer's mouse retina well before onset of cognitive decline. ACS Chem Neurosci. 2014;6:306–15.
5. Lu G, Fei B. Medical hyperspectral imaging: a review. J Biomed Opt. 2014;19:010901.
6. Vo-Dinh T. A hyperspectral imaging system for in vivo optical diagnostics. IEEE Eng Med Biol Mag. 2004;23:40–9.
7. Oh ES, Heo C, Kim JS, Suh M, Lee YH, Kim J-M. Hyperspectral fluorescence imaging for cellular iron mapping in the in vitro model of Parkinson's disease. J Biomed Opt. 2013;19:051207.
8. Verebes GS, Melchiorre M, Garcia-Leis A, Ferreri C, Marzetti C, Torreggiani A. Hyperspectral enhanced dark field microscopy for imaging blood cells. J Biophotonics. 2013;6:960–7.
9. Vermaas WF, Timlin JA, Jones HD, Sinclair MB, Nieman LT, Hamad SW, Melgaard DK, Haaland DM. In vivo hyperspectral confocal fluorescence imaging to determine pigment localization and distribution in cyanobacterial cells. Proc Natl Acad Sci. 2008;105:4050–5.
10. Boldrini B, Kessler W, Rebner K, Kessler RW. Hyperspectral imaging: a review of best practice, performance and pitfalls for in-line and on-line applications. J Near Infrared Spectrosc. 2012;20:483–508.
11. Schnarr K, Mooney R, Weng Y, Zhao D, Garcia E, Armstrong B, Annala AJ, Kim SU, Aboody KS, Berlin JM. Gold nanoparticle-loaded neural stem cells for photothermal ablation of cancer. Adv Healthcare Mater. 2013;2:976–82.
12. Gupta N. Development of staring hyperspectral imagers. In: Applied Imagery Pattern Recognition Workshop (AIPR), 2011 IEEE. Washington, DC: IEEE; 2011. p. 1–8.
13. Weitzel L, Krabbe A, Kroker H, Thatte N, Tacconi-Garman L, Cameron M, Genzel R. 3D: the next generation near-infrared imaging spectrometer. Astron Astrophys Suppl Ser. 1996;119:531–46.
14. Owen DM, Manning HB, de Beule P, Talbot C, Requejo-Isidro J, Dunsby C, McGinty J, Benninger RK, Elson DS, Munro I. Development of a hyperspectral fluorescence lifetime imaging microscope and its application to tissue imaging. In: Imaging, manipulation, and analysis of biomolecules, cells, and tissues V. Bellingham, WA: International Society for Optics and Photonics; 2007. 64411K.
15. Schultz S, Smith DR, Mock JJ, Schultz DA. Single-target molecule detection with nonbleaching multicolor optical immunolabels. Proc Natl Acad Sci. 2000;97:996–1001.
16. Yguerabide J, Yguerabide EE. Light-scattering submicroscopic particles as highly fluorescent analogs and their use as tracer labels in clinical and biological applications: II. Experimental characterization. Anal Biochem. 1998;262:157–76.
17. Wang W. Imaging the chemical activity of single nanoparticles with optical microscopy. Chem Soc Rev. 2018;47:2485–508.
18. Li T, Wu X, Liu F, Li N. Analytical methods based on the light-scattering of plasmonic nanoparticles at the single particle level with dark-field microscopy imaging. Analyst. 2017;142:248–56.
19. Yonzon CR, Jeoung E, Zou S, Schatz GC, Mrksich M, Van Duyne RP. A comparative analysis of localized and propagating surface plasmon resonance sensors: the binding of concanavalin A to a monosaccharide functionalized self-assembled monolayer. J Am Chem Soc. 2004;126:12669–76.
20. Anker JN, Hall WP, Lyandres O, Shah NC, Zhao J, Van Duyne RP. Biosensing with plasmonic nanosensors, nanoscience and technology: a collection of reviews from Nature Journals. Singapore: World Scientific; 2010. p. 308–19.
21. Haes AJ, Chang L, Klein WL, Van Duyne RP. Detection of a biomarker for Alzheimer's disease from synthetic and clinical samples using a nanoscale optical biosensor. J Am Chem Soc. 2005;127:2264–71.
22. Dahlin AB, Tegenfeldt JO, Höök F. Improving the instrumental resolution of sensors based on localized surface plasmon resonance. Anal Chem. 2006;78:4416–23.
23. McFarland AD, Van Duyne RP. Single silver nanoparticles as real-time optical sensors with zeptomole sensitivity. Nano Lett. 2003;3:1057–62.

24. Ozbay E. Plasmonics: merging photonics and electronics at nanoscale dimensions. Science. 2006;311:189–93.
25. Bohren C, Huffman D. Absorption and scattering of light by small particles. New York, NY: Wiley; 1983.
26. Willets KA, Van Duyne RP. Localized surface plasmon resonance spectroscopy and sensing. Annu Rev Phys Chem. 2007;58:267–97.
27. Haes AJ, Van Duyne RP. A unified view of propagating and localized surface plasmon resonance biosensors. Anal Bioanal Chem. 2004;379:920–30.
28. Petryayeva E, Krull UJ. Localized surface plasmon resonance: nanostructures, bioassays and biosensing—a review. Anal Chim Acta. 2011;706:8–24.
29. Jain PK, Lee KS, El-Sayed IH, El-Sayed MA. Calculated absorption and scattering properties of gold nanoparticles of different size, shape, and composition: applications in biological imaging and biomedicine. J Phys Chem B. 2006;110:7238–48.
30. Shi L, Jing C, Ma W, Li DW, Halls JE, Marken F, Long YT. Plasmon resonance scattering spectroscopy at the single-nanoparticle level: real-time monitoring of a click reaction. Angew Chem Int Ed. 2013;52:6011–4.
31. Shi L, Jing C, Gu Z, Long Y-T. Brightening gold nanoparticles: new sensing approach based on plasmon resonance energy transfer. Sci Rep. 2015;5:10142.
32. Bu T, Zako T, Fujita M, Maeda M. Detection of DNA induced gold nanoparticle aggregation with dark field imaging. Chem Commun. 2013;49:7531–3.
33. Li K, Qin W, Li F, Zhao X, Jiang B, Wang K, Deng S, Fan C, Li D. Nanoplasmonic imaging of latent fingerprints and identification of cocaine. Angew Chem Int Ed. 2013;52:11542–5.
34. Poon C-Y, Wei L, Xu Y, Chen B, Xiao L, Li H-W. Quantification of cancer biomarkers in serum using scattering-based quantitative single particle intensity measurement with a dark-field microscope. Anal Chem. 2016;88:8849–56.
35. Guo L, Ferhan AR, Chen H, Li C, Chen G, Hong S, Kim DH. Distance-mediated plasmonic dimers for reusable colorimetric switches: a measurable peak shift of more than 60 nm. Small. 2013;9:234–40.
36. Lee K, Cui Y, Lee LP, Irudayaraj J. Quantitative imaging of single mRNA splice variants in living cells. Nat Nanotechnol. 2014;9:474.
37. Xiong B, Zhou R, Hao J, Jia Y, He Y, Yeung ES. Highly sensitive sulphide mapping in live cells by kinetic spectral analysis of single Au-Ag core-shell nanoparticles. Nat Commun. 2013;4:1708.
38. Hao J, Xiong B, Cheng X, He Y, Yeung ES. High-throughput sulfide sensing with colorimetric analysis of single Au–Ag core–shell nanoparticles. Anal Chem. 2014;86:4663–7.
39. Chen Z, Li J, Chen X, Cao J, Zhang J, Min Q, Zhu J-J. Single gold@ silver nanoprobes for real-time tracing the entire autophagy process at single-cell level. J Am Chem Soc. 2015;137:1903–8.
40. Zhou J, Yang T, He W, Pan Z, Huang CZ. Galvanic exchange process visualized on single silver nanoparticles via dark-field microscopic imaging. Nanoscale. 2018;10:12805.
41. Smith JG, Yang Q, Jain PK. Identification of a critical intermediate in galvanic exchange reactions by single-nanoparticle-resolved kinetics. Angew Chem. 2014;126:2911–6.
42. Bansal V, Jani H, Du Plessis J, Coloe PJ, Bhargava SK. Galvanic replacement reaction on metal films: a one-step approach to create nanoporous surfaces for catalysis. Adv Mater. 2008;20:717–23.
43. Zhang S, Geryak R, Geldmeier J, Kim S, Tsukruk VV. Synthesis, assembly, and applications of hybrid nanostructures for biosensing. Chem Rev. 2017;117:12942–3038.
44. González E, Arbiol J, Puntes VF. Carving at the nanoscale: sequential galvanic exchange and Kirkendall growth at room temperature. Science. 2011;334:1377–80.
45. Smith JG, Chakraborty I, Jain PK. In situ single-nanoparticle spectroscopy study of bimetallic nanostructure formation. Angew Chem Int Ed. 2016;55:9979–83.
46. Smith JG, Jain PK. The ligand shell as an energy barrier in surface reactions on transition metal nanoparticles. J Am Chem Soc. 2016;138:6765–73.

47. Liu Y, Huang CZ. Real-time dark-field scattering microscopic monitoring of the in situ growth of single Ag@ Hg nanoalloys. ACS Nano. 2013;7:11026–34.
48. Novo C, Funston AM, Mulvaney P. Direct observation of chemical reactions on single gold nanocrystals using surface plasmon spectroscopy. Nat Nanotechnol. 2008;3:598.
49. Lei G, Gao PF, Yang T, Zhou J, Zhang HZ, Sun SS, Gao MX, Huang CZ. Photoinduced electron transfer process visualized on single silver nanoparticles. ACS Nano. 2017;11:2085–93.
50. Xu D, Liu D, Xie T, Cao Y, Wang J-G, Ning Z-j, Long Y-T, Tian H. Plasmon resonance scattering at perovskite CH 3 NH 3 PbI 3 coated single gold nanoparticles: evidence for electron transfer. Chem Commun. 2016;52:9933–6.
51. Li Z, Fang Y, Wang Y, Jiang Y, Liu T, Wang W. Visualizing the bidirectional electron transfer in a Schottky junction consisting of single CdS nanoparticles and a planar gold film. Chem Sci. 2017;8:5019–23.
52. Pereira MLO, Grasseschi D, Toma HE. Photocatalytic activity of reduced graphene oxide–gold nanoparticle nanomaterials: interaction with asphaltene and conversion of a model compound. Energy Fuel. 2017;32:2673–80.
53. Li S, Du Y, He T, Shen Y, Bai C, Ning F, Hu X, Wang W, Xi S, Zhou X. Nanobubbles: an effective way to study gas-generating catalysis on a single nanoparticle. J Am Chem Soc. 2017;139:14277–84.
54. Jing C, Rawson FJ, Zhou H, Shi X, Li W-H, Li D-W, Long Y-T. New insights into electrocatalysis based on plasmon resonance for the real-time monitoring of catalytic events on single gold nanorods. Anal Chem. 2014;86:5513–8.
55. Jing C, Gu Z, Long Y-T. Imaging electrocatalytic processes on single gold nanorods. Faraday Discuss. 2016;193:371–85.
56. Wonner K, Evers MV, Tschulik K. Simultaneous opto-and spectro-electrochemistry: reactions of individual nanoparticles uncovered by dark-field microscopy. J Am Chem Soc. 2018;140:12658.
57. Badireddy AR, Wiesner MR, Liu J. Detection, characterization, and abundance of engineered nanoparticles in complex waters by hyperspectral imagery with enhanced darkfield microscopy. Environ Sci Technol. 2012;46:10081–8.
58. Théoret T, Wilkinson KJ. Evaluation of enhanced darkfield microscopy and hyperspectral analysis to analyse the fate of silver nanoparticles in wastewaters. Anal Methods. 2017;9:3920–8.
59. Mortimer M, Gogos A, Bartolomé N, Kahru A, Bucheli TD, Slaveykova VI. Potential of hyperspectral imaging microscopy for semi-quantitative analysis of nanoparticle uptake by protozoa. Environ Sci Technol. 2014;48:8760–7.
60. Sekine R, Moore KL, Matzke M, Vallotton P, Jiang H, Hughes GM, Kirby JK, Donner E, Grovenor CR, Svendsen C. Complementary imaging of silver nanoparticle interactions with green algae: dark-field microscopy, electron microscopy, and nanoscale secondary ion mass spectrometry. ACS Nano. 2017;11:10894–902.
61. Avellan A, Schwab F, Masion A, Chaurand P, Borschneck D, Vidal V, Rose J, Santaella C, Levard CM. Nanoparticle uptake in plants: gold nanomaterial localized in roots of Arabidopsis thaliana by X-ray computed nanotomography and hyperspectral imaging. Environ Sci Technol. 2017;51:8682–91.
62. Mehta N, Shaik S, Devireddy R, Gartia MR. Single-cell analysis using hyperspectral imaging modalities. J Biomech Eng. 2018;140:020802.
63. More SS, Beach JM, Vince R. Early detection of amyloidopathy in Alzheimer's mice by hyperspectral endoscopy. Invest Ophthalmol Vis Sci. 2016;57:3231–8.
64. Fu D, Yang W, Xie XS. Label-free imaging of neurotransmitter acetylcholine at neuromuscular junctions with stimulated Raman scattering. J Am Chem Soc. 2016;139:583–6.
65. Sorg BS, Moeller BJ, Donovan O, Cao Y, Dewhirst MW. Hyperspectral imaging of hemoglobin saturation in tumor microvasculature and tumor hypoxia development. J Biomed Opt. 2005;10:044004.

66. Misra SK, Ostadhossein F, Daza E, Johnson EV, Pan D. Hyperspectral imaging offers visual and quantitative evidence of drug release from zwitterionic-phospholipid-nanocarbon when concurrently tracked in 3D intracellular space. Adv Funct Mater. 2016;26:8031–41.
67. Gosnell ME, Anwer AG, Mahbub SB, Perinchery SM, Inglis DW, Adhikary PP, Jazayeri JA, Cahill MA, Saad S, Pollock CA. Quantitative non-invasive cell characterisation and discrimination based on multispectral autofluorescence features. Sci Rep. 2016;6:23453.
68. Chin JA, Wang EC, Kibbe MR. Evaluation of hyperspectral technology for assessing the presence and severity of peripheral artery disease. J Vasc Surg. 2011;54:1679–88.
69. Larsen EL, Randeberg LL, Aksnes A, Svaasand LO, Olstad E, Haugen OA. Hyperspectral imaging of atherosclerotic plaques in vitro. J Biomed Opt. 2011;16:026011.
70. Greenman RL, Panasyuk S, Wang X, Lyons TE, Dinh T, Longoria L, Giurini JM, Freeman J, Khaodhiar L, Veves A. Early changes in the skin microcirculation and muscle metabolism of the diabetic foot. Lancet. 2005;366:1711–7.
71. Liu L, Ngadi M. Detecting fertility and early embryo development of chicken eggs using near-infrared hyperspectral imaging. Food Bioprocess Technol. 2013;6:2503–13.
72. Chaudhari K, Pradeep T. Spatiotemporal mapping of three dimensional rotational dynamics of single ultrasmall gold nanorods. Sci Rep. 2014;4:5948.
73. Johnson WR, Wilson DW, Fink W, Humayun MS, Bearman GH. Snapshot hyperspectral imaging in ophthalmology. J Biomed Opt. 2007;12:014036.
74. Usenik P, Bürmen M, Fidler A, Pernuš F, Likar B. Evaluation of cross-polarized near infrared hyperspectral imaging for early detection of dental caries. In: Lasers in dentistry XVIII. Bellingham, WA: International Society for Optics and Photonics; 2012. p. 82080G.
75. Li Q, Wang Y, Liu H, Chen Z. Nerve fibers identification based on molecular hyperspectral imaging technology. In: Computer Science and Automation Engineering (CSAE), 2012 IEEE International Conference on. Washington, DC: IEEE; 2012. p. 15–7.
76. Benavides JM, Chang S, Park SY, Richards-Kortum R, Mackinnon N, MacAulay C, Milbourne A, Malpica A, Follen M. Multispectral digital colposcopy for in vivo detection of cervical cancer. Opt Express. 2003;11:1223–36.
77. Kong SG, Martin ME, Vo-Dinh T. Hyperspectral fluorescence imaging for mouse skin tumor detection. ETRI J. 2006;28:770–6.
78. Panasyuk SV, Yang S, Faller DV, Ngo D, Lew RA, Freeman JE, Rogers AE. Medical hyperspectral imaging to facilitate residual tumor identification during surgery. Cancer Biol Ther. 2007;6:439–46.
79. Akbari H, Uto K, Kosugi Y, Kojima K, Tanaka N. Cancer detection using infrared hyperspectral imaging. Cancer Sci. 2011;102:852–7.
80. Akbari H, Halig L, Schuster DM, Fei B, Osunkoya A, Master V, Nieh P, Chen G. Hyperspectral imaging and quantitative analysis for prostate cancer detection. J Biomed Opt. 2012;17:076005.
81. Renkoski TE, Utzinger U, Hatch KD. Wide-field spectral imaging of human ovary autofluorescence and oncologic diagnosis via previously collected probe data. J Biomed Opt. 2012;17:036003.
82. Afromowitz MA, Callis JB, Heimbach DM, DeSoto LA, Norton MK. Multispectral imaging of burn wounds: a new clinical instrument for evaluating burn depth. IEEE Trans Biomed Eng. 1988;35:842–50.
83. Siddiqi AM, Li H, Faruque F, Williams W, Lai K, Hughson M, Bigler S, Beach J, Johnson W. Use of hyperspectral imaging to distinguish normal, precancerous, and cancerous cells. Cancer Cytopathol Interdiscipl Intl J Am Cancer Soc. 2008;114:13–21.
84. Vetten MA, Tlotleng N, Rascher DT, Skepu A, Keter FK, Boodhia K, Koekemoer L-A, Andraos C, Tshikhudo R, Gulumian M. Label-free in vitro toxicity and uptake assessment of citrate stabilised gold nanoparticles in three cell lines. Part Fibre Toxicol. 2013;10:50.
85. Weinkauf H, Brehm-Stecher BF. Enhanced dark field microscopy for rapid artifact-free detection of nanoparticle binding to Candida albicans cells and hyphae. Biotechnol J Healthcare Nutr Technol. 2009;4:871–9.

86. Zuzak KJ, Naik SC, Alexandrakis G, Hawkins D, Behbehani K, Livingston EH. Characterization of a near-infrared laparoscopic hyperspectral imaging system for minimally invasive surgery. Anal Chem. 2007;79:4709–15.
87. Schols RM, Bouvy ND, van Dam RM, Stassen LP. Advanced intraoperative imaging methods for laparoscopic anatomy navigation: an overview. Surg Endosc. 2013;27:1851–9.
88. Akbari H, Kosugi Y, Kojima K, Tanaka N. Detection and analysis of the intestinal ischemia using visible and invisible hyperspectral imaging. IEEE Trans Biomed Eng. 2010;57:2011–7.
89. Akbari H, Kosugi Y, Kojima K, Tanaka N. Wavelet-based compression and segmentation of hyperspectral images in surgery. In: International Workshop on Medical Imaging and Virtual Reality. New York, NY: Springer; 2008. p. 142–9.
90. Akbari H, Kosugi Y, Kojima K, Tanaka N. Hyperspectral imaging and diagnosis of intestinal ischemia, Engineering in Medicine and Biology Society. In: EMBS 2008. 30th Annual International Conference of the IEEE. Washington, DC: IEEE; 2008. p. 1238–41.
91. Cha J, Broch A, Mudge S, Kim K, Namgoong J-M, Oh E, Kim P. Real-time, label-free, intraoperative visualization of peripheral nerves and micro-vasculatures using multimodal optical imaging techniques. Biomed Opt Express. 2018;9:1097–110.

Chapter 9
Additive Manufacturing Technologies Based on Photopolymerization

Haibo Ding, Xiangwei Zhao, and Zhongze Gu

Abstract The rapid progress of additive manufacturing (AM) allows the digital design and rapid prototyping of three-dimensional (3D) microstructures, which have promoted the development of optics, electronics, mechanics, and medicine. Among the current strategies for AM, photopolymerization, which takes advantage of the light reaction for photocurable polymers, has shown significant benefits for high-resolution printing of objects with complex geometrical configurations. In this book chapter, we review the development process of AM technologies based on photopolymerization. Digital projection lithography (DPL) and direct laser writing (DLW) are included to summarize the advantages and disadvantages in throughput and resolution. Finally, the current challenges of these emerging methods and their applications in biomedical engineering are presented.

Keywords Additive manufacturing · Photopolymerization · Digital projection lithography · Direct laser writing · Two-photon polymerization

9.1 Introduction

Advanced manufacturing methods have substantially satisfied the demands of both scientific research and industrial manufacturing. Unlike conventional manufacturing methods that require multiple processes, the emerging AM makes it possible to rapid prototyping of digital designs into real 3D objects on demand. Numerous techniques have been introduced into commercial 3D printers to satisfy industrial and individual consumers. Owing to the ability to shape the morphology of the functional materials, the 3D printers have demonstrated a series of applications in wearable devices, tissue engineering, robotics, and controlled microstructural architectures [1–4].

H. Ding · X. Zhao (✉) · Z. Gu (✉)
State Key Laboratory of Bioelectronics, School of Biological Science and Medical Engineering, Southeast University, Nanjing, China
e-mail: xwzhao@seu.edu.cn; gu@seu.edu.cn

X. Zhao, M. Lu (eds.), *Nanophotonics in Biomedical Engineering*,
https://doi.org/10.1007/978-981-15-6137-5_9

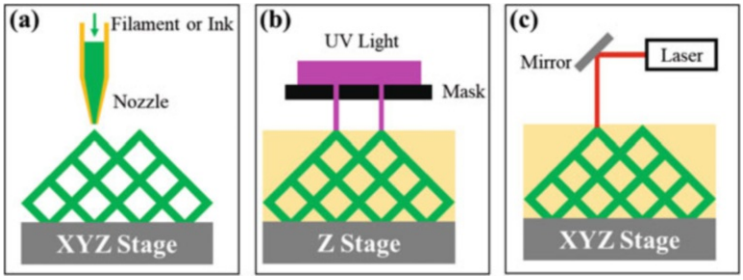

Fig. 9.1 Scheme of conventional AM methods. (**a**) ink-based 3D printing with a nozzle; (**b**) light-based 3D printing with photopolymerization in a plane; (**c**) light-based 3D printing with photopolymerization in a point

A massive effort has been launched on the invention of novel AM methods for different materials, aiming to the high throughput of specialized structures with high feature resolution. Ink- and light-based 3D printing methods are two basic strategies for AM [5]. By far, the most common AM strategy is the ink-based 3D printing, such as fused deposition modeling (FDM), direct ink writing (DIW), and electrohydrodynamic inkjet [6–8]. After transferring the materials into printable inks, a computer-controlled 3D translation stage is used to deposit the inks on the desired position through a nozzle (Fig. 9.1a). This simple setup brings about the apparent advantages of vast material choices, including polymers, metals, and composites with functional particles or fragment. Moreover, multimaterial printing could be realized by integrating multiple nozzles according to a well-designed formula [9]. However, these ink-based approaches have inherent limitations in printing resolution and molding quality. The printing resolution relies on the diameter of the nozzle, making it impossible to achieve printing resolution smaller than 1 μm. Besides, the ink-based 3D printing needs a solid supporting base for modeling so that it is challenging to generate suspending structures.

Thanks to the high average and peak powers in the focal volume of the light source, the interaction between the light and the materials could generate several types of precision microfabrication. For example, ablation results in laser drilling and laser cutting [10, 11], heating effects result in laser welding or state modification of the materials [12, 13], and chemical reactions result in polymerization of the photosensitive materials and photoreduction of metal ions [14, 15]. Therefore, materials can be removed, modified, or added in a point-by-point or line-by-line fashion following predetermined outlines. Among these processing methods, photopolymerization, which allows the solidification of a photocurable resin according to the projected area (Fig. 9.1b, c), is considered to be an ideal alternative for AM. Compared with the ink-based 3D printing, photopolymerization could implement the fabrication without the nozzle, leading to a significant increase in total process flexibility.

Figure 9.2 presents the similar polymer structures fabricated by both ink-based and light-based 3D printing methods. The fabrication resolution and suspending structures

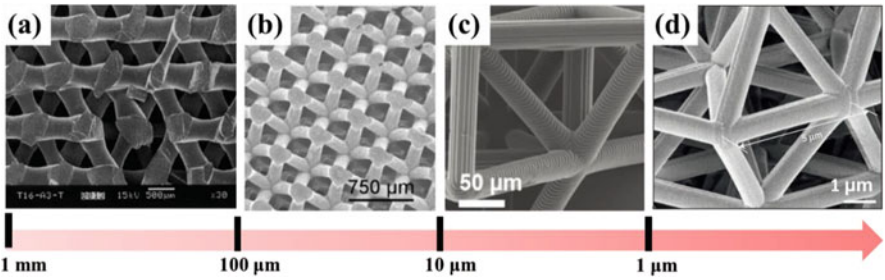

Fig. 9.2 Images of the microlattices fabricated by different methods: (**a**) FDM [6]; (**b**) self-propagating UV polymerization [16]; (**c**) DPL [17]; (**d**) TPP [18]

are the main obstacles for FDM. On the other sides, the photopolymerization methods provide a possibility of generating small structures even on the submicrometer scale. However, the high-resolution photopolymerization methods suffer from a shortage of printing speed and the overall size. Thus, researchers are motivated to improve the existing techniques and to find novel solutions for AM base on photopolymerization.

9.2 Brief Tutorial on Photopolymerization

Photopolymerization based on single-photon absorption and two-photon absorption are the most common mechanisms for AM. In single-photon polymerization (SPP), the emission spectrum from the light source requires to overlap the absorption band of the photoinitiator. After absorbing only one photon, the photoinitiator converts this light energy into chemical energy in the form of reactive intermediates, which initiates the polymerization of monomers and oligomers. As the polymerization occurring along the light path, SPP has been widely used to produce two-dimensional patterns with a customized mask or a mold (Fig. 9.3a). Compared to SPP, the two-photon polymerization (TPP) processes great advantage of confining polymerization within the focal volume in the nanometer scale. This nonlinear optical process requires a wavelength of the laser longer than the maximum absorption wavelength of the initiator [19, 20]. Due to the features of spatial coherence and temporal coherence, a laser can be focused in a tight spot and with pulse width as short as femtoseconds. Thus, the energy is transferred into the material in a time range shorter than the electron–phonon coupling time. Since the thermal effects are negligible, the crosslinking reaction of the monomers is achieved by a radical chain reaction initiated by the simultaneous absorption of two photons. These operations can be performed both on the interface and in the interior of a target material without physical contact between the optical probe and the substrate (Fig. 9.3b).

As described above, SPP struggles with true 3D components because of the preparation of the masks, the time-consuming process of mask alignment, and difficulties of creating high-aspect ratio features [21]. While arbitrary 3D

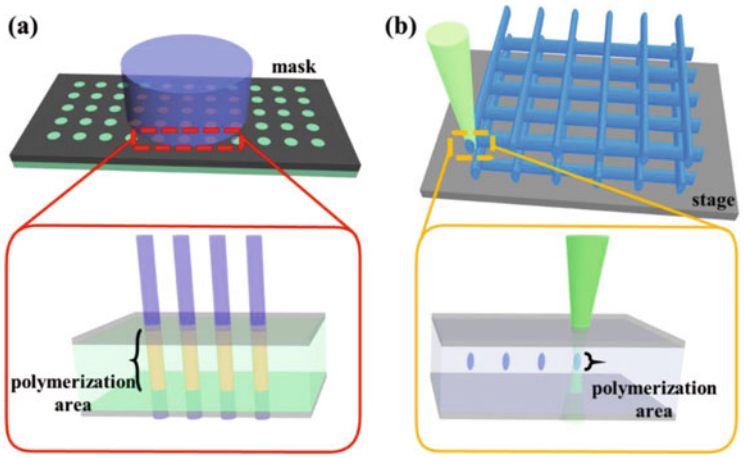

Fig. 9.3 Scheme of microfabrication based on different polymerization principles: (**a**) single-photon polymerization; (**b**) TPP

microstructures can be achieved by accurate positioning of the focal point in TPP. Recently, DPL has been developed to overcome the limitations of SPP in 3D printing and more advanced technologies have been demonstrated to expand the working range and throughput for TPP.

9.3 Digital Projection Lithography

DPL is a serial photopolymerization process which combines the high-throughput capability of mask photolithography and the design flexibility offered by the shape of the light source. Each polymerization is controlled by a dynamic projection setup which could be a digital micromirror device (DMD) with a micro-mirror array or a spatial light modulator (SLM) with a tunable liquid-crystal pattern. According to a predesigned sequence, the polymerized parts would assembly into the desired structures.

9.3.1 Projection Microstereolithography

A typical DPL apparatus is the projection microstereolithography that implements a layer-by-layer operation for the 3D microstructures [22–24]. Figure 9.4 illustrates the working principle of the whole process. First, the shapes of these constructed layers are determined by slicing the desired 3D model with a series of closely spaced horizontal planes. The electronic images of the slicing shape are transferred to the DMD to generate the corresponding digit mask. Then, the illuminated light is shaped

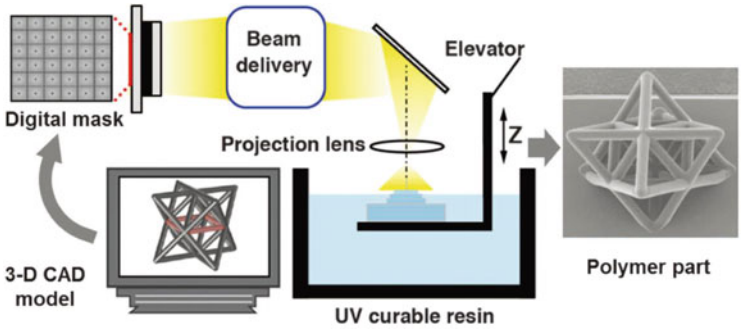

Fig. 9.4 Scheme of Projection microstereolithography, a layer-by-layer technique capable of fabricating arbitrary, microscale, 3D structures with a resolution of about 5 μm [17]

by the defined mask pattern and several lenses are used to adjust the final projection area on the surface of the curable resin. After one UV exposure on the layer, the elevator immerses the polymerized layers into the resin and there would be a new layer of resin on the surface. Finally, a microstructure with complex 3D architectures is realized by stacking all the layers from bottom to top. A developing step is necessary to remove all the unpolymerized resin.

Sun and co-workers established a process model to explain the underlying physical and chemical mechanisms, which also provides a guide to control the curing depth [22]. As shown in Fig. 9.5, the Gaussian distribution was approximately used to describe the intensity distribution of the projection light. Numerically, the intensity distribution at the image plane was the summation of each individual spotlight from the DMD. Thus the curing depth (C_d) could be calculated according to the "working curve equation":

$$C_d = D_p \ln\left(E_{max}/E_c^*\right) \tag{9.1}$$

where D_p is the light penetration depth of the resin, which is defined as the depth within the resin where irradiation drops to $1/e$ of the intensity on the surface. E_{max} is the peak value intensity distribution and E_c^* is the effective critical energy for polymerization. The experimental results were in good agreement with the numerical model that the curing depth is linearly proportional to the natural logarithm of UV exposure (Fig. 9.5c). On the other hand, the curing width increased rapidly when the exposure is larger than 665 mJ/cm^2 (Fig. 9.5d). This is because the curing width is mainly determined by the amount of UV exposure near the resin surface.

Moreover, the researcher also found that the existence of the photoinhibitor could be used to decrease the spatial resolution. By introducing 0.3% UV doping, the curing depth and width could be smaller at the same UV exposure. As shown in Fig. 9.5c, the curing depth of the resin was decreased from 163 to 45 μm.

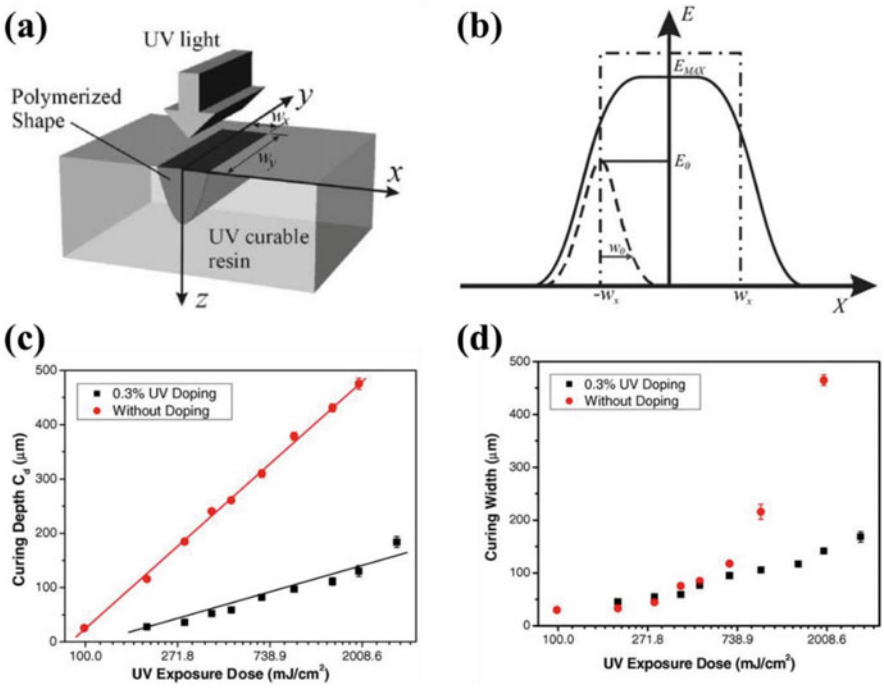

Fig. 9.5 (**a**) Schematic diagram of the projection UV light. (**b**) Schematic diagram of the distribution of light intensity. The dashed line represents the intensity distribution corresponding to a single-spot light source and the solid line represents the intensity distribution corresponding to the designed pattern along the *xz*-plane. The measured curing width (**c**) and depth (**d**) at different exposure dose [22]

9.3.2 Continuous Liquid Interface Production

The fabrication speed is a critical issue for the mass manufacturing of complex structures. For projection microstereolithography, each layer needs only one exposure and the exposure time is short in several seconds or milliseconds. But resin renewal and part movement are also essential operations for each layer and they cost another few seconds. The printing speed is restricted 1.2 mm/h when the slicing distance is 100 μm and the time for illumination, resin renewal, and part movement is 1 s.

Continuous liquid interface production (CLIP) was proposed by Tumbleston in 2016 [25]. Compared with the conventional projection microstereolithography, they increased the vertical printing speed 1000 times. The key technology of CLIP is controlled oxygen inhibition of free radical polymerization. Oxygen can either quench the photoexcited photoinitiator or create peroxides by combining with the free radical from the photocleaved photoinitiator [26], leading to incomplete cure and surface tackiness. In CLIP, an oxygen-permeable window was placed at the

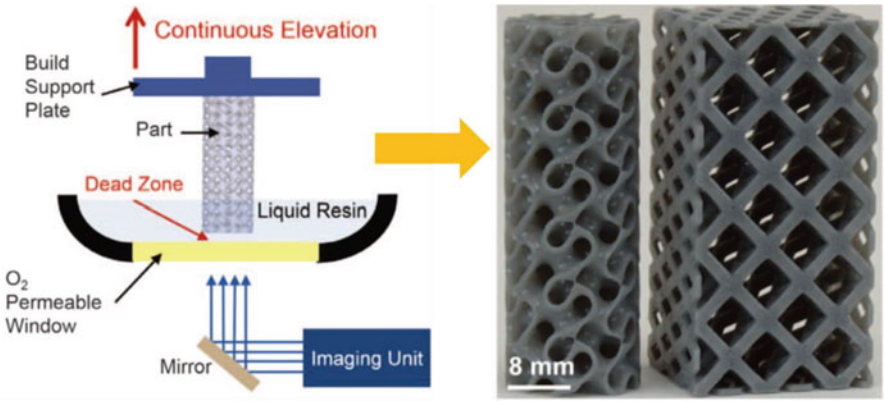

Fig. 9.6 Scheme of CLIP and the fabricated samples that were fabricated with a speed of 500 mm/h [25]

bottom of the liquid resin to create an oxygen-containing dead zone for polymerization (Fig. 9.6). The thickness of the dead zone depended on the incident photon flux, photoinitiator absorption coefficient, and resin curing dosage. The minimum thickness of the dead zone was 20–30 μm because smaller thickness would result in window adhesion-related defects. Above the dead zone, photopolymerization occurred with a certain thickness that relied on the exposure time, the resin absorption coefficient, and the three controlling parameters for the dead zone. The curing part is continuously drawn out of the resin bath and new resin would fill the area between the curing part and the dead zone constantly, leading to a nonstop production.

9.4 Direct Laser Writing

The miniaturization of common materials towards smaller scale contributes to improvements in their original capabilities [27]. In particular, some microstructures and nanostructures possess specific abilities based on their feature sizes or geometrical configurations. Thus, the fabrication resolution and molding quality are challenging for AM. DLW, which enables the polymerization in a confined zone, has attracted much attention in spite of its low throughput [28, 29]. Figure 9.7 presents a typical stereolithography system. Unlike the projection setups, selective photopolymerization in the resin is controlled by the scanning mirror and a translation stage. The polymerized size depends on the laser intensity and exposure time. Due to the intrinsic property of SPP, the resolution is still in micrometer scale and some excrescent polymerized points are inevitable.

Two-photon absorption enables the reaction in the focal spot of a laser with high light intensity. Polymerization converts the photocurable resins into the polymer

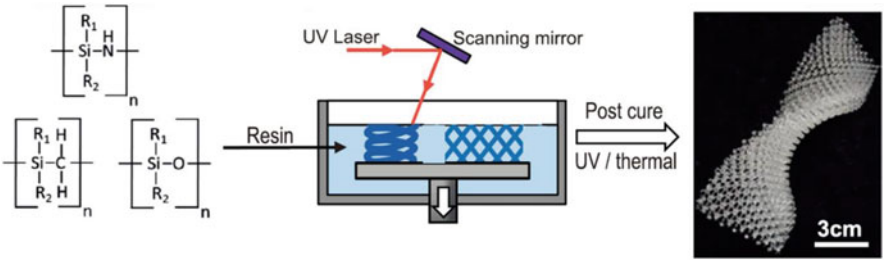

Fig. 9.7 Scheme of the stereolithography processing and the fabricated samples [29]

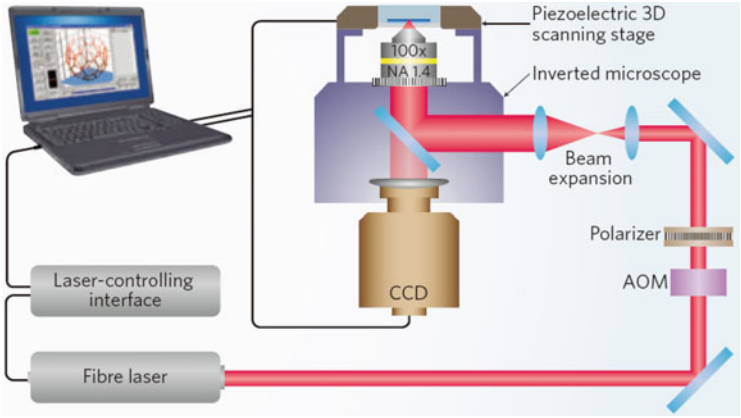

Fig. 9.8 Scheme of a typical TPP system [32]

network when the laser intensity reached the threshold [30–33]. Therefore, the confined reaction zone not only results in a fabrication resolution beyond the diffraction limit but also enables 3D nanostructures generated by accurate positioning of the focal spot. Figure 9.8 illustrates a typical TPP system from the Germany company Nanoscribe. The light source is a femtosecond (fs) laser with a wavelength in the near-infrared zone. The acoustooptical modulator (AOM) and polarizer are used to control the power and polarization of the incident light. With the optical lenses for beam expansion, the light is focused into the resin through the objective. Here, the feature size in TPP is restricted by the Abbe's law,

$$r = 0.61\frac{\lambda}{\mathrm{NA}} \tag{9.2}$$

where r is the radius of the focus spot, λ is the wavelength of the incident light, and NA is the numerical aperture (NA) of the objective. The effective polymerization voxel is smaller than the focal spot due to the threshold, providing a possibility of breaking the diffraction limit. This process would reduce the polymerization level and weaken the mechanical strength of the fabricated structures. Some advanced

TPP methods based on the stimulated-emission-depletion technique have demonstrated super-resolution 3D printing with a feature size down to 9 nm [34–36]. However, the available smallest feature size in TPP is still limited by the mechanical strength of the solidified material.

9.4.1 *Direct Laser Wring with a Continuous-Wave Laser*

An fs laser may be too expensive for some homemade system or individual users. The nonlinear response of SPP allows for DLW with a continuous-wave (CW) laser. This Schwarzschild-type nonlinearity was reported and demonstrated the ability for AM in 2000 [37]. Due to the reaction between oxygen molecules and the radicals, oxygen could inhibit the photopolymerization. When the intensity of the incident light is low, only the resin around the focus could selectively solidify, while oxygen molecules scavenge the radicals in the other regions. This incomplete polymerization would get strengthened with the suppression of effective exposure dose in the desired volume during the whole scanning. As a result, DLW with a CW laser has been a low-cost alternative for DLW with an fs laser [38, 39].

Mueller and coauthors found some photoresist compositions with the nonlinear absorption ability to increase the spatial resolution of DLW with a CW laser [40]. The pure monomer of pentaerythritol triacrylate and the commercial IP-Dip from Nanoscribe company were characterized to possess a nonlinear absorption for a 405 CW laser. The intensity distribution of the focus spot was calculated and measured (Fig. 9.9a), which was similar to the focal spot in TPP. By using these resins, they demonstrated point diameters as small as 50 nm, 2D line gratings with 110 nm lateral period, and 3D woodpile photonic crystals with 250 nm rod spacing. The printed micro-Eiffel Tower showed the potential to replace CLW with an fs laser (Fig. 9.9b).

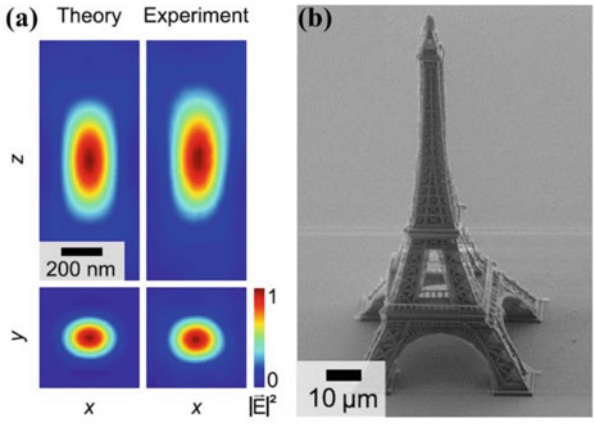

Fig. 9.9 (**a**) Calculated and measured focus of the 405 nm CW laser. (**b**) Image of the fabricated objects by DLW with the CW laser [40]

9.4.2 *Two-Photon Polymerization for Centimeter-Height Structures*

The spatial resolution is a common problem for both SPP and TPP. Due to the elongation of the focal spot along the propagation direction of the light, the plane resolution is always better than the axial resolution. This anisotropy of the polymerization may cause the anisotropy in mechanical stability or the other related properties [41, 42]. For TPP, the transverse superposition and optical compensation methods have applied to compensate the spherical aberration [43–45]. However, the effective depth for the above compensation strategies are limited at the micrometer scale and the high NA lenses usually have short working distances.

To fabricate a centimeter-height object with high spatial resolution, the simultaneous spatiotemporal focusing (SSTF) approach has been applied to TPP with an fs laser [46–48]. The core technique is to separate the spectral components of the incident light pulse spatially. As shown in Fig. 9.10a, a pair of gratings is added in the system to spatially chirp the fs laser and temporal focusing occurs during propagation toward the focal spot. All the frequency components overlap each other in both space and time domains at the focal plane (position 3 in Fig. 9.10a). Thus, the elongation of the focal spot along the axial direction is shortened to obtain an isotropic distribution of the laser, leading to an improvement for the symmetric shape of the polymerized voxel.

In 2018, Chu and coauthors manufactured a model of the Terra Cotta Warrior with a height of 1.3 cm [47]. A femtosecond laser amplifier (central wavelength 800 nm, repetition rate 1 kHz) and an objective (2×, NA = 0.35, working distance

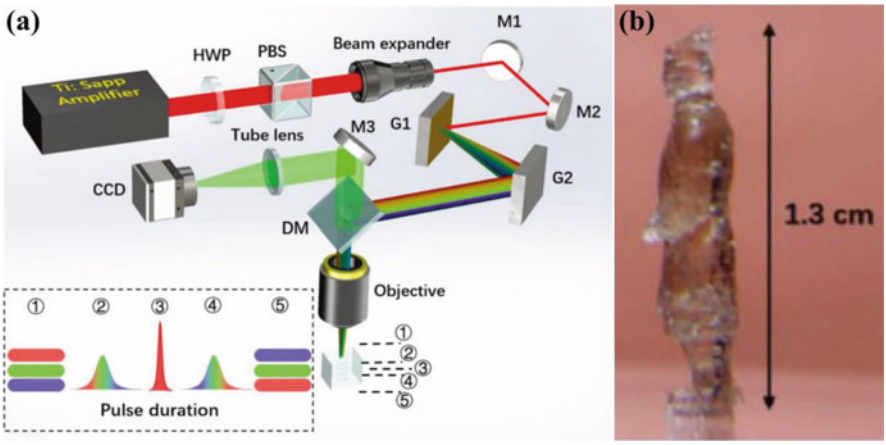

Fig. 9.10 (**a**) Scheme of the SSTF-TPP system. HWP, half waveplate; PBS, polarizing beam-splitter; M1–M3, reflective mirrors; G1 and G2, gratings; DM, dichroic mirror; and CCD, charge-coupled device. Inset: The evolution of the pulse duration when the light propagated in the focal volume. Positions 1 and 5 are far away from the focus, whereas positions 2 and 4 are within the Rayleigh range near the focus. (**b**) Image of the fabricated Terra Cotta Warrior [47]

2.0 cm) were used in their system. During the fabrication, the laser power was set at 5 mW, the thickness of the slicing layer was set at 30 μm, and the scan speed was 400 μm/s. It took about 15 h for the printing of the model (Fig. 9.10b).

9.4.3 Parallel Two-Photon Polymerization with Multifocal Arrays

There is always a trade-off between the resolution and the speed in AM methods. Especially for TPP, the structures need to be printed point-by-point with the small polymerized voxels each exposure. The velocity of the existing piezo stages could reach several hundred micrometers per second and the galvanometer mirror could improve the scanning speed. However, the working ranges of the piezo stages and galvanometer mirror are less than 300 μm. Besides, not all the resins could work under such high speed.

Parallel DLW with the multifocal array has been demonstrated with the generation of a multifocal spot array [49–53]. Microlens array, diffraction optical elements, and some other optical devices are employed to obtain programmable intensity distribution in the focus zone. In addition to controlling the intensity, the polarization states of each focal spot could also be individually controlled by using the SLM. Moreover, the generated multifocal arrays exist not only in a 2D focus plane but also in the 3D volume. Nowadays, parallel DLW has been improved to satisfy the AM for complex microstructures.

Geng and coauthors combined the TPP fabrication with a DMD scanner which generated multifocal array based on the binary holography [54]. The updating rate for the holography could reach 22.7 kHz. Figure 9.11a illustrated the whole setup. A blazed transmission grating and a high reflectivity mirror were placed in system to compensate angular dispersion of the incident laser on the DMD. The hologram images for the DMD were calculated by superposing the binary holograms for all the designed laser focus. For an objective (40×, NA = 1.3, working distance 0.22 mm), the work volume of the DMD scanner is calculated to be $103 \times 206 \times 524\ \mu m^3$ and the printing resolution is 130 nm and 270 nm in the lateral and axial directions, respectively. Due to the rapid updating rate of the DMD, an object whose size was smaller than the work volume could be achieved without the movement of the piezo stage. As shown in Fig. 9.11b, a woodpile scaffold ($36 \times 36 \times 20\ \mu m^3$) was fabricated under the three-focus mode. It cost 3.6 s for the 7200 hologram images at a frequency of 2 kHz. Compared with the conventional point-scanning-based parallel DLW, this optimized projection method for TPP provided a solution for complex overhanging structures.

In addition to the DMD, the phase-only SLM with liquid-crystal on silicon (Lcos) provides a more flexible way to generate the hologram for intricate patterns. For example, the Mathieu beams possess controllable parameters to obtain regular focus around a circle. The optical setup is similar to the TPP system with a DMD

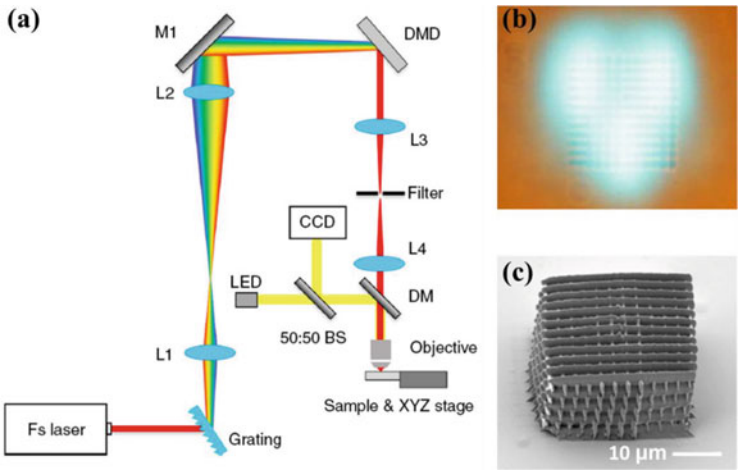

Fig. 9.11 (**a**) Scheme of the TPP setup with a DMD for multifocus processing. L1-L2, lens; M1, mirror; DM, dichroic mirror; BS, beam splitter. (**b**) Snapshots of the three-focus TPP fabrication. (**c**) SEM images of the woodpile structures printed by the three-focus TPP [54]

(Fig. 9.12a). Here, the number of focus is tuned by the feature parity and integer m (Fig. 9.12b) and the diameter of the circle pattern is tuned with the ellipticity q (Fig. 9.12c). Besides, the focal depth of the laser could be controlled by the focal length ratio of the *4f* system L1 and L2. By using this system for dynamic holographic fabrication, Wang and coauthors have fabricated microcages for trapping microbeads by projecting different hologram patterns along the axial direction [55]. The scanning speed was 50 μm/s, which reduced the fabrication time by two orders of magnitude.

9.5 Applications in Biomedical Engineering

These AM methods based on polymerization make it possible to fabricate functional devices for biomedical engineering including organ-on-a-chip [56, 57], biosensors [58, 59], and micromachines [60, 61].

The DLP methods have been applied for the rapid fabrication of microfluidics networks for the cell culture in vitro [62]. By using this method, a variety of channels, connectors, and functional scaffolds with feature size from several micrometers to millimeters could be achieved by the polymerization of biocompatible resins and hydrogels. Besides, the digital projection strategy allows the generation of specific patterns such as the arborescent and capillary-like networks shown in Fig. 9.13a. Due to the significant difference of the width of the trunk (>1100 μm) and the branch (~17 μm), the solution was able to fill the whole networks without an

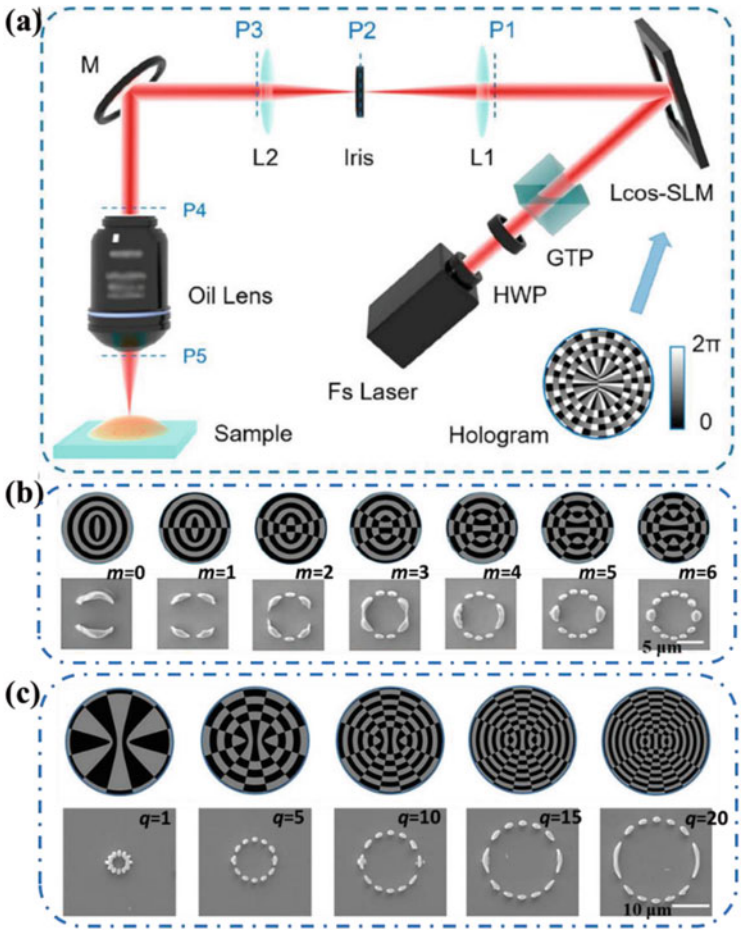

Fig. 9.12 (**a**) Scheme of the TPP setup with an SLM for parallel processing. HWP, half waveplate; GTP, Glan laser beam splitter; M, mirror; L1 and L2, lens. (**b**) Patterns made by Mathieu beams with different feature parity and integer m. (**c**) Patterns made by Mathieu beams with different ellipticity parameter q [55]

extra pump [63]. Moreover, the capillary-like system demonstrated a positive effect on the proliferation of lung cancer cells.

Unlike the DLP methods, DLW can be regarded as a pencil of light in three dimensions. Notably, the feature size based on confinement of the laser probe range from nanometer to micrometer, making it possible to fabricate functional devices. In this respect, TPP highlights its distinct advantage in building arbitrary 3D structures. Also, the improvement of feature size infuses new life into traditional devices and structures for the application in biomedical engineering.

An interesting application is 3D scaffolds for cell culture because they can provide a real 3D microenvironment for cell growth in vitro [2, 64]. Well-defined

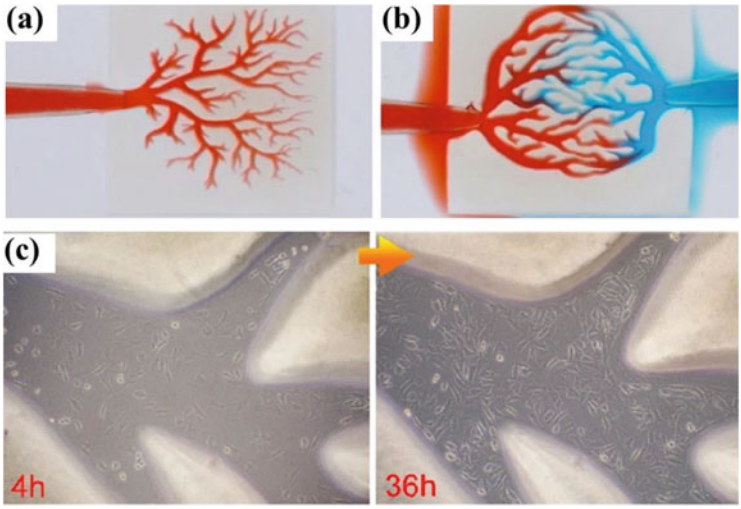

Fig. 9.13 Microstructures fabricated by DLP. (**a**) Image of the arborescent scaffold with the perfusion of red solution. (**b**) Image of the capillary-like scaffold with the perfusion of two dye solution. (**c**) Cell proliferation at 36 h in the capillary-line scaffold [63]

templates fabricated by DLW have a direct influence on proliferation, morphology, adhesion, and differentiation of the cells. A significantly higher proliferation was observed on hexagonal grids with 25 μm spaced posts compared to unstructured surfaces [65]. Besides, the bending property of the micropillars and suspended nanowires embedded in the scaffold offers a solution to measure the cell force (Fig. 9.14a) [66]. The distinctive performance of the hierarchical structures provides the possibility of investigating the influence of three-dimensionality and elasticity on the differentiation of individual cells and the formation of tissues. The study of cell culture in the 3D scaffolds can give the researchers a deep understanding of the influence of these physical parameters and promote the research in tissue engineering and regenerative medicine.

With the assistance of functional materials, miniaturized smart machines with micro/nanometer-sized moving parts have now been utilized for on-site, in vivo sensing, monitoring, analysis, and treatment in narrow enclosure, harsh environment, and even inside human body [67, 68]. A microtransporter that can actively collect, encapsulate, transport, and controllably release small agents has been created based on DLW with selective physical vapor deposition of magnetic materials at specific locations (Fig. 9.14b) [69]. The capacity of remotely activated loading and releasing was tested with polystyrene microbeads, biological materials, and smaller micromachines. Another example is an array of micropillars with spatial arrangements and pillar heights [70]. The micropillars can self-assemble into regular periodic structures with the assistance of controlled capillary forces in an evaporating liquid, which offers a capacity to trap and release micro-objects selectively. These compound micromachines and microrobots can be used to access remote

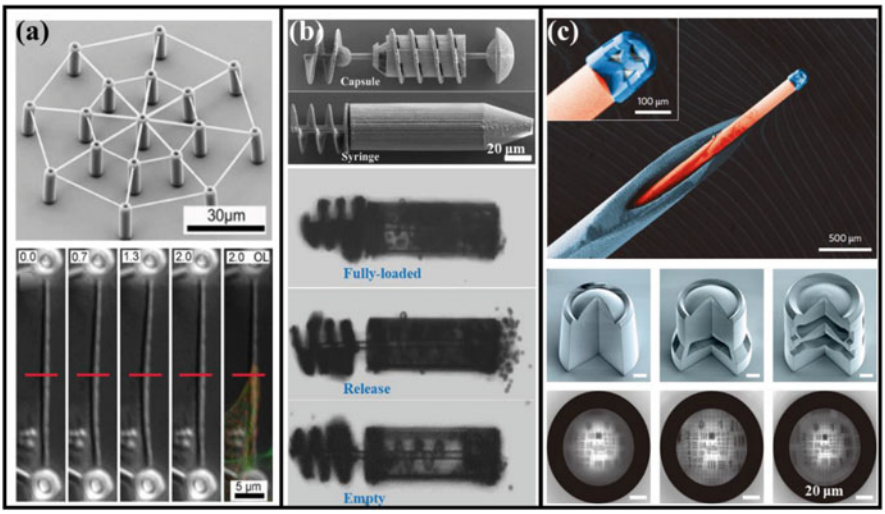

Fig. 9.14 Microstructures fabricated by DLW based on TPP. (**a**) Elastic fully 3D microscaffolds for cell force measurements [66]. (**b**) Microtransporter that can actively collect, encapsulate, transport, and controllably release micro- and nanoagents [69]. (**c**) Ultracompact multilens objectives on the end of optical fiber [71]

places of the body such as the peritoneal cavity, hepatic arteries, and the gastrointestinal tract for targeted delivery or to perform more complicated tasks such as mechanical removal of occlusions, collection of biological samples for diagnostic analysis, and generation of local fluid flows for mixing.

DLW has also been used in the fabrication of medical devices in the micrometer scale. An ultracompact compound lens system with numerous refractive surfaces was developed for endoscopic instruments and miniaturized microscopes [71]. The researchers took advantage of DLW for high optical quality with resolutions of up to 500 lp/mm (Fig. 9.14c). This method paves the way towards printed optical miniature instruments such as endoscopes, fiber-imaging systems for cell biology, new illumination systems, miniature optical fiber traps, integrated quantum emitters and detectors, and tiny drones and robots with autonomous vision.

9.6 Summary and Outlook

In this chapter, we have summarized the development of AM methods based on photopolymerization. These emerging fabrication methods enable high printing resolution in micrometer and nanometer scale depending on the initiation principle for polymerization (Fig. 9.15). The two-photon absorption provides a higher resolution than single-photon absorption under the same wavelength. Besides, the projection illumination mode possesses higher throughput than the single-point

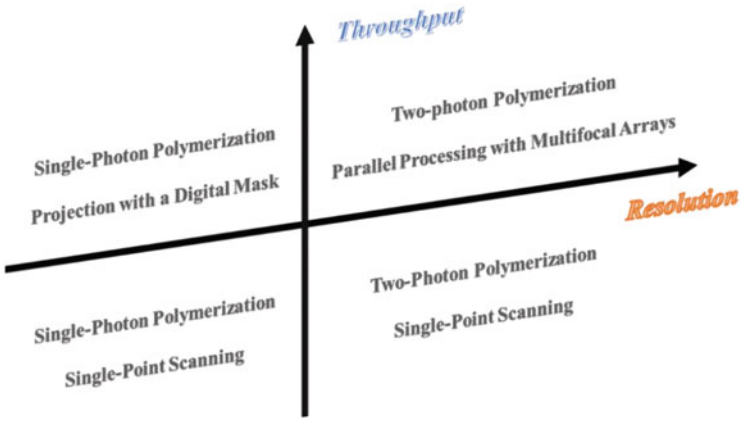

Fig. 9.15 Summary of the AM techniques based on photopolymerization

scanning mode. The desired object could be printed with a suitable photopolymerization method based on its whole size, feature size, and the geometrical configuration.

On the other hand, there remain problems that need to be solved. The metals and carbon materials possess specific optical, mechanical, and electrical properties. 3D printing of these materials has been demonstrated with the ink-based method, while it is impossible to polymerize them [72–74]. Some researchers have realized metal structures by using the polymer scaffolds as the sacrificial material. The polymer structures were fabricated to act as the template for metal coating. Owing to the roughness and conduction issue, the metal materials are still desired to be printed directly. The reduction induced by the photon reaction has attracted widespread attention recently [75–77]. Both the single-photon absorption and two-absorption have been studied for reducing metal. And they provide the potential for future AM methods for metals with the light.

Eventually, the goal of AM is to satisfy the demand for rapid prototyping of complex architectures. With the development of optical technique and material science, AM based on photopolymerization will present more robust functionality, which will benefit the individual user and commercial production.

References

1. Ahn BY, Duoss EB, Motala MJ, Guo X, Park SI, Xiong Y, Yoon J, Nuzzo RG, Rogers JA, Lewis JA. Omnidirectional printing of flexible, stretchable, and spanning silver microelectrodes. Science. 2009;323(5921):1590.
2. Kang HW, Lee SJ, Ko IK, Kengla C, Yoo JJ, Atala A. A 3D bioprinting system to produce human-scale tissue constructs with structural integrity. Nat Biotechnol. 2016;34(3):312.

3. Xu T, Zhang J, Salehizadeh M, Onaizah O, Diller E. Millimeter-scale flexible robots with programmable three-dimensional magnetization and motions. Sci Robot. 2019;4(29):eaav4494.
4. Hollister SJ. Porous scaffold design for tissue engineering. Nat Mater. 2005;4(7):518.
5. Truby RL, Lewis JA. Printing soft matter in three dimensions. Nature. 2016;540(7633):371.
6. Hutmacher DW, Schantz T, Zein I, Ng KW, Teoh SH, Tan KC. Mechanical properties and cell cultural response of polycaprolactone scaffolds designed and fabricated via fused deposition modeling. J Biomed Mater Res. 2001;55(2):203.
7. Gratson GM, Xu M, Lewis JA. Microperiodic structures: direct writing of three-dimensional webs. Nature. 2004;428(6981):386.
8. An BW, Kim K, Lee H, Kim SY, Shim Y, Lee DY, Song JY, Park JU. High-resolution printing of 3D structures using an electrohydrodynamic inkjet with multiple functional inks. Adv Mater. 2015;27(29):4322.
9. Liu W, Zhang YS, Heinrich MA, Ferrari FD, Jang HL, Bakht SM, Alvarez MM, Yang J, Li YC, Santiago GT, Miri AK, Zhu K, Khoshakhlagh P, Prakash G, Cheng H, Guan X, Zhong Z, Ju J, Zhu GH, Jin X, Shin SR, Dokmeci MR, Khademhosseini A. High performance graphene/Ni 2 P hybrid anodes for lithium and sodium storage through 3D yolk-shell-like nanostructural design. Adv Mater. 2017;29(3):1604630.
10. Wu D, Wu SZ, Xu J, Niu LG, Midorikawa K, Sugioka K. Hybrid femtosecond laser microfabrication to achieve true 3D glass/polymer composite biochips with multiscale features and high performance: the concept of ship-in-a-bottle biochip. Laser Photonics Rev. 2014;8 (3):458.
11. Liu XQ, Chen QD, Guan KM, Ma ZC, Yu YH, Li QK, Tian ZN, Sun HB. Dry-etching-assisted femtosecond laser machining. Laser Photonics Rev. 2017;11(3):1600115.
12. Li X, Zhang Q, Chen X, Gu M. Giant refractive-index modulation by two-photon reduction of fluorescent graphene oxides for multimode optical recording. Sci Rep. 2013;3:2819.
13. Skylar-Scott MA, Gunasekaran S, Lewis JA. Laser-assisted direct ink writing of planar and 3D metal architectures. PNAS. 2016;113(22):6137.
14. Kawata S, Sun HB, Tanaka T, Takada K. Finer features for functional microdevices. Nature. 2001;412(6848):697.
15. Cao YY, Takeyasu N, Tanaka T, Duan XM, Kawata S. 3D metallic nanostructure fabrication by surfactant-assisted multiphoton-induced reduction. Small. 2009;5(10):1144.
16. Jacobsen AJ, Barvosa-Carter W, Nutt S. Micro-scale truss structures formed from self-propagating photopolymer waveguides. Adv Mater. 2007;19(22):3892.
17. Zheng X, Lee H, Weisgraber TH, Shusteff M, DeOtte J, Duoss EB, Kuntz JD, Biener MM, Ge Q, Jackson JA, Kucheyev SO, Fang NX, Spadaccini CM. Ultralight, ultrastiff mechanical metamaterials. Science. 2014;344(6190):1373.
18. Bauer J, Schroer A, Schwaiger R, Kraft O. Approaching theoretical strength in glassy carbon nanolattices. Nat Mater. 2016;15(4):438.
19. Cumpston BH, Ananthavel SP, Barlow S, Dyer DL, Ehrlich JE, Erskine LL, Heikal AA, Kuebler SM, Lee IYS, McCord-Maughon D, Qin J, Röckel H, Rumi M, Wu XL, Marder SR, Perry JW. Two-photon polymerization initiators for three-dimensional optical data storage and microfabrication. Nature. 1999;398(6722):51.
20. LaFratta CN, Fourkas JT, Baldacchini T, Farrer RA. Multiphoton fabrication. Angew Chem Int Ed. 2007;46(33):6238.
21. Zheng X, Deotte J, Alonso MP, Farquar GR, Weisgraber TH, Gemberling S, Lee H, Fang N, Spadaccini CM. Design and optimization of a light-emitting diode projection micro-stereolithography three-dimensional manufacturing system. Rev Sci Instrum. 2012;83 (12):125001.
22. Sun C, Fang N, Wu DM, Zhang X. Projection micro-stereolithography using digital micro-mirror dynamic mask. Sensors Actuators, A. 2005;121(1):113.
23. Johnson DW, Sherborne C, Didsbury MP, Pateman C, Cameron NR, Claeyssens F. Macrostructuring of emulsion-templated porous polymers by 3D laser patterning. Adv Mater. 2013;25(23):3178.

24. Hegde M, Meenakshisundaram V, Chartrain N, Sekhar S, Tafti D, Williams CB, Long TE. 3D printing all-aromatic polyimides using mask-projection stereolithography: processing the nonprocessable. Adv Mater. 2017;29(31):1701240.
25. Tumbleston JR, Shirvanyants D, Ermoshkin N, Janusziewicz R, Johnson AR, Kelly D, Chen K, Pinschmidt R, Rolland JP, Ermoshkin A, Samulski ET, DeSimone JM. Continuous liquid interface production of 3D objects. Science. 2015;347(6428):1349.
26. Ligon SC, Husár B, Wutzel H, Holman R, Liska R. Strategies to reduce oxygen inhibition in photoinduced polymerization. Chem Rev. 2014;114(1):557.
27. Ding H, Zhang Q, Gu H, Liu X, Sun L, Gu M, Gu Z. Controlled Microstructural architectures based on smart fabrication strategies. Adv Funct Mater. 2020;30(2):1901760.
28. Melchels FPW, Feijen J, Grijpma DW. A review on stereolithography and its applications in biomedical engineering. Biomaterials. 2010;31(24):6121.
29. Eckel ZC, Zhou C, Martin JH, Jacobsen AJ, Carter WB, Schaedler TA. Additive manufacturing of polymer-derived ceramics. Science. 2016;351(6268):58.
30. Gattass RR, Mazur E. Femtosecond laser micromachining in transparent materials. Nat Photonics. 2008;2(4):219.
31. Maruo S, Fourkas JT. Recent progress in multiphoton microfabrication. Laser Photonics Rev. 2008;2(1–2):100.
32. Anscombe N. Direct laser writing. Nat Photonics. 2010;4:22.
33. Sugioka K, Cheng Y. Femtosecond laser three-dimensional micro- and nanofabrication. Appl Phys Rev. 2014;1(4):041303.
34. Li L, Gattass RR, Gershgoren E, Hwang H, Fourkas JT. Achieving lambda/20 resolution by one-color initiation and deactivation of polymerization. Science. 2009;324(5929):910.
35. Gan Z, Cao Y, Evans RA, Gu M. Three-dimensional deep sub-diffraction optical beam lithography with 9 Nm feature size. Nat Commun. 2013;4:2061.
36. Gan Z, Turner MD, Gu M. Biomimetic gyroid nanostructures exceeding their natural origins. Sci Adv. 2016;2(5):e1600084.
37. Maruo S, Ikuta K. Three-dimensional microfabrication by use of single-photon-absorbed polymerization. Appl Phys Lett. 2000;76(19):2656.
38. Galajda P, Ormos P. Complex micromachines produced and driven by light. Appl Phys Lett. 2001;78(2):249.
39. Thiel M, Fischer J, Freymann G, Wegener M. Direct laser writing of three-dimensional submicron structures using a continuous-wave laser at 532 nm. Appl Phys Lett. 2010;97 (22):221102.
40. Mueller P, Thiel M, Wegener M. 3D direct laser writing using a 405 Nm diode laser. Opt Lett. 2014;39(24):6847.
41. Turner MD, Saba M, Zhang Q, Cumming BP, Schröder-Turk GE, Gu M. Miniature chiral beamsplitter based on gyroid photonic crystals. Nat Photonics. 2013;7(10):801.
42. Huang L, Salter PS, Payne F, Booth MJ. Aberration correction for direct laser written waveguides in a transverse geometry. Opt Express. 2016;24(10):10565.
43. Wong S, Deubel M, Pérez-Willard F, John S, Ozin GA, Wegener M, Freymann G. Direct laser writing of three- dimensional photonic crystals with a complete photonic bandgap in chalcogenide glasses. Adv Mater. 2006;18(3):265.
44. Salter PS, Jesacher A, Spring JB, Metcalf BJ, Thomas-Peter N, Simmonds RD, Langford NK, Walmsley IA, Booth MJ. Adaptive slit beam shaping for direct laser written waveguides. Opt Lett. 2012;37(4):470.
45. Cumming BP, Debbarma S, Luther-Davis B, Gu M. Simultaneous compensation for aberration and axial elongation in three-dimensional laser nanofabrication by a high numerical-aperture objective. Opt Express. 2013;21(16):19135.
46. He F, Xu H, Cheng Y, Ni J, Xiong H, Xu Z, Sugioka K, Midorikawa K. Fabrication of microfluidic channels with a circular cross section using spatiotemporally focused femtosecond laser pulses. Opt Lett. 2010;35(7):1106.

47. Chu W, Tan Y, Wang P, Xu J, Li W, Qi J, Cheng Y. Centimeter-height 3D printing with femtosecond laser two-photon polymerization. Adv Mater Technol. 2018;3(5):1700396.
48. Sun B, Salter PS, Roider C, Jesacher A, Strauss J, Heberle J, Schmidt M, Booth MJ. Four-dimensional light shaping: manipulating ultrafast spatiotemporal foci in space and time. Light: Sci Appl. 2018;7(1):17117.
49. Kato J, Takeyasu N, Adachi Y, Sun HB, Kawata S. Multiple-spot parallel processing for laser micronanofabrication. Appl Phys Lett. 2005;86(4):044102.
50. Jesacher A, Booth MJ. Parallel direct laser writing in three dimensions with spatially dependent aberration correction. Opt Express. 2010;18(20):21090.
51. Lin H, Jia B, Gu M. Dynamic generation of debye diffraction-limited multifocal arrays for direct laser printing nanofabrication. Opt Lett. 2011;36(3):406.
52. Lin H, Gu M. Creation of diffraction-limited non-airy multifocal arrays using a spatially shifted vortex beam. Appl Phys Lett. 2013;102(8):084103.
53. Li X, Cao Y, Tian N, Fu L, Gu M. Multifocal optical nanoscopy for big data recording at 30 TB capacity and gigabits/second data rate. Optica. 2015;2(6):567.
54. Geng Q, Wang D, Chen P, Chen SC. Ultrafast multi-focus 3-D nano-fabrication based on two-photon polymerization. Nat Commun. 2019;10(1):2179.
55. Wang C, Yang L, Hu Y, Rao S, Wang Y, Pan D, Ji S, Zhang C, Su Y, Zhu W, Li J, Wu D, Chu J. Femtosecond mathieu beams for rapid controllable fabrication of complex microcages and application in trapping microobjects. ACS Nano. 2019;13(4):4667.
56. Derby B. Printing and prototyping of tissues and scaffolds. Science. 2012;338(6109):921.
57. Moroni L, Boland T, Burdick JA, Maria CD, Derby B, Forgacs G, Groll J, Li Q, Malda J, Mironov VA, Mota C, Nakamura M, Shu W, Takeuchi S, Woodfield TBF, Xu T, Yoo JJ, Vozzi G. Biofabrication: a guide to technology and terminology. Trends Biotechnol. 2018;36(4):384.
58. Wiesbauer M, Wollhofen R, Vasic B, Schilcher K, Jacak J, Klar TA. Nano-anchors with single protein capacity produced with STED lithography. Nano Lett. 2013;13(11):5672.
59. Gomez LPC, Spangenberg A, Ton XA, Fuchs Y, Bokeloh F, Malval JP, Bui BTS, Thuau D, Ayela C, Haupt K, Soppera O. Rapid prototyping of chemical microsensors based on molecularly imprinted polymers synthesized by two-photon stereolithography. Adv Mater. 2016;28(28):5931.
60. Tian Y, Zhang YL, Ku JF, He Y, Xu BB, Chen QD, Xia H, Sun HB. High performance magnetically controllable microturbines. Lab Chip. 2010;10(21):2902.
61. Vizsnyiczai G, Frangipane G, Maggi C, Saglimbeni F, Bianchi S, Leonardo RD. Light controlled 3D micromotors powered by bacteria. Nat Commun. 2017;8:15974.
62. Zhang R, Larsen NB. Stereolithographic hydrogel printing of 3D culture chips with biofunctionalized complex 3D perfusion networks. Lab Chip. 2017;17(24):4273.
63. Xue D, Wang Y, Zhang J, Mei D, Wang Y, Chen S. Projection-based 3D printing of cell patterning scaffolds with multiscale channels. ACS Appl Mater Interfaces. 2018;10(23):19428.
64. Morley CD, Ellison ST, Bhattacharjee T, O'Bryan CS, Zhang Y, Smith KF, Kabb CP, Sebastian M, Moore GL, Schulze KD, Niemi S, Sawyer WG, Tran DD, Mitchell DA, Sumerlin BS, Flores CT, Angelini TE. Quantitative characterization of 3D bioprinted structural elements under cell generated forces. Nat Commun. 2019;10(1):3029.
65. Hohmann JK, Freymann G. Influence of direct laser written 3D topographies on proliferation and differentiation of osteoblast-like cells: towards improved implant surfaces. Adv Funct Mater. 2014;24(42):6573.
66. Klein F, Striebel T, Fischer J, Jiang Z, Franz CM, Freymann G, Wegener M, Bastmeyer M. Elastic fully three-dimensional microstructure scaffolds for cell force measurements. Adv Mater. 2010;22(8):868.
67. Bozuyuk U, Yasa O, Yasa IC, Ceylan H, Kizilel S, Sitti M. Light-triggered drug release from 3D-printed magnetic chitosan microswimmers. ACS Nano. 2018;12(9):9617.
68. Jeon S, Kim S, Ha S, Lee S, Kim E, Kim SY, Park SH, Jeon JH, Kim SW, Moon C, Nelson BJ, Kim J, Yu SW, Choi H. Magnetically actuated microrobots as a platform for stem cell transplantation. Sci Robot. 2019;4(30):eaav4317.

69. Tottori S, Zhang L, Qiu F, Krawczyk KK, Franco-Obregón A, Nelson BJ. Magnetic helical micromachines: fabrication, controlled swimming, and cargo transport. Adv Mater. 2012;24 (6):811.
70. Hu Y, Lao Z, Cumming BP, Wu D, Li J, Liang H, Chu J, Huang W, Gu M. Laser printing hierarchical structures with the aid of controlled capillary-driven self-assembly. PNAS. 2015;112(22):6876.
71. Gissibl T, Thiele S, Herkommer A, Giessen H. Two-photon direct laser writing of ultracompact multi-lens objectives. Nat Photonics. 2016;10(8):554.
72. Deubel M, Freymann G, Wegener M, Pereira S, Busch K, Soukoulis CM. Direct laser writing of three-dimensional photonic-crystal templates for telecommunications. Nat Mater. 2004;3 (7):444.
73. Meza LR, Das S, Greer JR. Strong, lightweight, and recoverable three-dimensional ceramic nanolattices. Science. 2014;345(6202):1322.
74. Yee DW, Lifson ML, Edwards BW, Greer JR. Additive manufacturing of 3D-architected multifunctional metal oxides. Adv Mater. 2019;31(33):1901345.
75. Tabrizi S, Cao Y, Cumming BP, Jia B, Gu M. Functional optical plasmonic resonators fabricated via highly photosensitive direct laser reduction. Adv Optical Mater. 2016;4(4):529.
76. Yang X, Sun M, Bian Y, He X. A room-temperature high-conductivity metal printing paradigm with visible-light projection lithography. Adv Funct Mater. 2019;29(1):1807615.
77. Zeng Y, Du X, Hou W, Liu X, Zhu C, Gao B, Sun L, Li Q, Liao J, Levkin PA, Gu Z. UV-triggered polydopamine secondary modification: fast deposition and removal of metal nanoparticles. Adv Funct Mater. 2019;29(34):1901875.